DECARBURIZATION AND OXIDATION OF SOME IRON-BASE ALLOYS

A thesis submitted in fulfilment of the
requirements for the degree of

DOCTOR OF PHILOSOPHY

IN

CHEMISTRY

Shahreer Ahmad

Department of Chemistry
Aligarh Muslim University
Aligarh

1988-89

A. U. MALIK
M. Sc., Ph. D. (Alig.)
Ph.D. (Liverpool), D.Sc.(Alig.)

Professor of Chemistry

Dept. of Applied Chemistry
Zakir Husain College of
Engineering & Technology
Aligarh Muslim University
Aligarh-202001 (India)

Date 8th. Feb. 1989

This is to certify that the Ph.D. thesis entitled, 'Decarburization and Oxidation of Some Iron-base Alloys' which has been submitted by Mr. Shahreer Ahmad contains an original piece of research work. The entire work has been carried out under my supervision.

To the best of my knowledge and belief this work has not been submitted elsewhere for the award of any degree.

A. U. Malik

(A.U.MALIK)

ACKNOWLEDGEMENTS

I wish to express my profound gratitude to Professor A.U. Malik for his excellent guidance, constant support and trust throughout the course of this study. But for his keen interest and encouragement, the present thesis would not have seen the light of the day.

Sincere thanks are also due to Dr. Mohammad Ajmal for his persistent interest and encouragement at various levels. I am thankful to Professor K.T.Naseem, Chairman, Department of Applied Chemistry for providing research facilities.

I also wish to thank Drs. Nadeem A. Siddiqi, Sultan Ahmad and A. Jabbar Khan for their valuable suggestions and encouragement at all levels.

The present work was accomplished with the financial assistance of Department of Atomic Energy, Govt. of India. It also owes a great deal to entirely non-financial assistance of many others, friends and colleagues, my gratitude to them will perhaps best be expressed by leaving them unnamed. Mr. Masood Alam Malik deserves a word of praise for the expert typing of the manuscript.

A token of deep appreciation to Hina, Rubina, Shamim, Rais, Jamal and Akhtar for their friendly co-operation, help and interesting discussions, scientific and otherwise.

My gratitude, too, to my brothers, sisters and parents to whom this thesis is dedicated.

SHAHREER AHMAD

CONTENTS

LIST OF TABLES

ABSTRACT

The work described in this thesis deals primarily with the studies on high temperature oxidation, decarburization and decarburization-oxidation behaviour of iron-base alloys. Decarburization in a low oxygen potential atmosphere such as H_2-H_2O is a conventional technique to produce low carbon steels for electromagnetic application. Decarburization is also important in liquid sodium or liquid sodium and lithium cooled nuclear power plants. High temperature oxidation of steels involve scaling (formation of oxide layer) and decarburization (carbon loss) during oxidation; in such a type of decarburization disruption of otherwise protective scales occurs resulting in faster oxidation rates. Oxidation of steels is a common phenomenon in high temperature applications such as boilers, tubes, evaporators, condensers, reheaters and other components in power generating plants and in similar applications. It has been shown that the dispersion of transition metal carbide(s) lowers greatly the oxidation rates of steels. Also, the presence of transition metal oxide or rare earth oxide influences significantly the oxidation rates of steels.

The development of some new type of high temperature materials such as oxide-dispersion strengthened or carbide dispersion strengthened alloys or ceramic metal composite materials made it necessary to study the oxidation and decarburization behaviour under simulated conditions of energy

generation or conversion units, chemical plants, desalination plants, petroleum refinary plants etc.

The multiphase alloy systems used for the oxidation and decarburization studies have been chosen taking into consideration the importance of above mentioned materials in high temperature applications. The alloy system consist of plain iron-carbon alloys, commercial alloy steels, transition metal carbide dispersed iron-base sintered alloys, rare earth oxide and reactive-oxide-containing transition metal carbide dispersed iron-base sintered alloys and chromium-containing carbide-dispersed iron-base sintered alloys. The entire studies were focussed primarily on the role of carbide dispersoids on the oxidation/decarburization behaviour of iron-base alloys in absence or presence of reactive metal oxide additions.

Chapter I

Chapter I includes a brief literature survey pertaining to the high temperature oxidation and decarburization of iron-base alloys. Effects of various alloying additions, chromium, carbon and other reactive elements and their oxides have been dealt in detail.

Reference from research papers, reports, reviews and conference proceedings are cited and special emphasis has been laid to the work which has direct or indirect bearing on the studies described in this thesis. It is possible that some

results of important or remarkable studies might have left unquoted in the introduction quite inadvertently yet there was absolutely no intention to undermine those works.

Chapter II

Chapter II describes the materials, instrumental facilities and methods/procedures used and followed during the course of this study.

While the model Fe-C alloys were casted, the carbide-dispersed iron-base alloys, with or without alloying additions, were prepared by standard compacting and sintering techniques. Some structural and heat resistant alloy steels used during the oxidation and decarburization studies were commercially procured.

The oxidation, decarburization, and oxidation of decarburized alloys were carried out in O_2 (1 atm.) and H_2-H_2O ($P_{O_2} \sim 10^{-19}$ atm.) atmospheres. Argon (g) and nitrogen (g) were used during sintering. All the gases were of 99.9 % purity.

The oxidation kinetic studies were carried out in an all glass-laboratory fabricated apparatus using a quartz helical-cathetoscope arrangement for measuring weight changes. The same apparatus was used for decarburization studies in water-saturated H_2(g).

The microstructural studies were carried out using

Photometallurgical Microscope and Scanning Electron Microscope. The constituents in the oxidized/decarburized alloys were identified by X-ray diffraction analysis.

Chapter III

Chapter III includes the studies on the decarburization and oxidation behaviour of plain carbon steels (containing 0.1, 0.8 and 1.2 wt. % carbon) at 700, 800, 900 and 1000°C. The oxidation studies were carried out in O_2(g) at 1 atm. pressure and decarburization studies were performed in H_2-H_2O atmosphere ($p_{O_2} \sim 10^{-19}$ atm.).

The kinetics of the oxidation of plain and decarburized iron-carbon alloys were measured. The weight gain versus time plots were found to be generally parabolic indicating the operation of a diffusion controlled mechanism during oxide growth.

The oxidized, decarburized, decarburized-oxidized and plain specimens (in as cast condition) were examined under photometallurgical and scanning electron microscopes. The presence of different constituents in the matrix and/or scales were identified by conventional X-ray diffraction analysis.

The morphological features of the scales on plain carbon steels were similar irrespective of carbon contents. The oxide scales found on decarburized-oxidized alloys were quite similar to those formed on undecarburized-oxidized alloys. However, the scales formed on decarburized-oxidized alloys were relatively

thicker, porous and more fragile.

The presence of carbon greatly lowers the oxidation rates of the alloy,however, the dependence on carbon content was some what complex. At 700°C, Fe-1.2C alloy has the highest oxidation rate and 0.1 % C alloy has the lowest oxidation rate. However, at higher temperatures the behaviour is reversed and Fe-0.1C alloy has the highest oxidation rate. Such a behaviour can be explained on the basis of alloy phase structure and morphology of the oxide scales.

The steels decarburized in H_2-H_2O showed well defined decarburized layers, the thickness of decarburized layer increases with increase in alloys carbon content or exposure time. The decarburized layers were ferritic in nature.

Chapter IV

This chapter contains the results of the oxidation and decarburization studies carried-out on Fe-10MC, where MC is a transition metal carbide e.g. TiC, VC, NbC, TaC, Cr_7C_3, MoC, WC or Fe_3C-10 wt. %. The main aim of the investigation was to examine the behaviour of carbide dispersion during decarburization or/and oxidation.

Three different types of studies were carried out :

(i) the alloys were decarburized in H_2-H_2O ($p_{O_2} \sim 10^{-19}$ atm.) at 900°C for 6-7 hrs.,

(ii) the alloys were decarburized for 6 hrs. and were then oxidized in O_2(g) (1 atm.) at 900°C, the kinetic of oxidation was studied,

(iii) the alloys were oxidized in O_2(g) (1 atm.) for 8 hrs. and during this period oxidation kinetic was also measured.

The morphology of the oxide scales and nature of the alloy substrates or decarburized layers were studied through microstructural investigations involving optical and scanning electron microscopes.

The different constituents present in the oxide scales were identified by X-ray diffraction analysis.

The weight gain versus time plots obtained during the oxidation of Fe-1OMC alloys, were usually parabolic indicating the operation of a diffusion controlled mechanism during oxidation. The oxidized alloys invariably form multilayered oxide scales, the innermost layers mainly consist of spinal or mixed oxide followed by porous layers containing oxides of iron, Fe_2O_3 constituting the outermost layer, the carbides were also incorporated in the inner scales. In some alloys, a metal oxide layer containing M_2O_x was also present.

The oxide scales formed on predecarburized-oxidized alloys were much thinner than the corresponding undecarburized oxidized alloys although the composition and structure of the

scales were not much different.

The oxidation rates of undecarburized Fe-1OMC alloys arranged according to decreasing parabolic rates follows the sequence :

$$VC < NbC < Cr_7C_3 < TaC < MoC < TiC < WC < Fe_3C$$

The plain Fe-1OMC alloys showed a dispersion of carbides in the ferrite matrix. On decarburization H_2-H_2O atmosphere, the microstructure of decarburized Fe-1OMC alloys showed a marked increase in the amount of ferrite and a corresponding decrease in the carbide concentration. The decarburization rate (in terms of wt. loss/area) follow the sequence:

$$TaC < TiC < Fe_3C < NbC < Cr_7C_3 < WC < VC < MoC$$

The decarburization during oxidation of Fe-1OMC alloys occurred due to decomposition of carbide and its extent depends upon the thermal stabilities of different carbides in presence of an oxidant. The thermal stabilities of different carbides was compared in terms of the standard free energy of the oxidation reactions. The calculated values of ΔG^o can be arranged in the following sequence (in increasing order) :

$$WC > MoC \sim TiC > Fe_3C > TaC > Cr_7C_3 \sim NbC > VC$$

The sequence was similar to the oxidation rate sequence with the notable exception of Fe_3C.

The values of parabolic rate constants, Kp for the oxidation of decarburized Fe-10MC alloys follow the sequence (in increasing order) :

$TiC > TaC > Cr_7C_3 > MoC > Fe_3C > WC > NbC > VC$

With a few exceptions, the rate constant sequence was quite similar to that observed for the oxidation of undecarburized Fe-10MC alloys. The oxidation rates of decarburized Fe-10MC alloys were about 2-3 magnitude lower than the corresponding undecarburized alloys. Probably two factors were responsible for a phenomenal lowering in the oxidation rates of decarburized alloys. Firstly, a thin protective oxide film was formed during decarburization in H_2-H_2O atmosphere, which retards the mobility of carbon atoms and secondly, the presence of a fine carbide dispersion in an austenitic matrix which considerably reduces the level of decarburization during oxidation and in consequence assists in retaining the integrity of oxide scales.

Chapter V

Chapter V deals with the decarburization and oxidation studies on Cr-containing carbide-dispersed iron-base alloys. Alloys of the general composition Fe-10MC-0.1C-20Cr containing 10 wt. % of the carbide : TiC, Cr_7C_3, NbC or WC ; 0.1 wt. % carbon and 20 wt. % chromium were prepared by sintering. The alloys were oxidized and decarburized in O_2 (1 atm.) and

H_2-H_2O ($p_{O_2} \sim 10^{-19}$ atm.), respectively at 900°C.

All the alloys oxidized followed a parabolic rate law indicating a diffusion controlled mechanism operated during oxidation. The WC-containing alloy oxidized at the lowest rate and Cr_7C_3-containing alloy at the fastest rate. There were three important morphological features of the oxidized alloys. An internal Cr_2O_3 was formed as a separate phase along with a ferritic phase, Cr_7C_3 was present as a dispersion but mainly concentrated at the ferritic polygonal grain boundaries and a $Cr_2O_3/FeO.Cr_2O_3$ layer was present invariably at the alloy/scale interface. These three factors were probably responsible for relatively low oxidation rates of those alloys.

In decarburized alloys there was no well defined decarburized layer but there were evidence of decarburization from microstructure. The microstructure showed the presence of 2 phase, the light phase represented ferrite and a dark phase represented Cr-rich iron solid solution, the carbide particles were dispersed in both the phases. Some Cr was oxidized to Cr_2O_3 in the ferritic phase.

The decarburized Fe-10MC-0.1C-20Cr alloys were further oxidized at 900°C in O_2 (1 atm.). With the exception of NbC-containing alloys, the decarburized alloys oxidized at a slightly higher rate than the undecarburized alloy. The formation of a protective chromium oxide layer seems to restrict greatly the oxidation rates of undecarburized alloys. However,

it is to be noted that the values of oxidation rates of undecarburized and dedarburized Fe-10MC-0.1C-20Cr alloys were very similar.

Chapter VI

Chapter VI describes the influence of rare earth oxide additions on the oxidation and decarburization behaviour of carbide-dispersed iron-base sintered alloys.

Alloys of the general composition : Fe-10MC-0.1C-1.0RE_2O_3 containing 10 weight % of metal carbide (Cr_7C_3, NbC or WC), 1.0 wt. % of rare earth oxide (La_2O_3, Pr_2O_3, or Y_2O_3) and 0.1 wt. % of carbon were prepared by compacting and sintering techniques.

The weight gain vs time plots obtained during the kinetics of oxidation of plain as well as decarburized alloys were parabolic indicating the growth of oxide layers through diffusion.

The Fe-10MC-0.1C-1.0RE_2O_3 sintered alloys have agglomeration of carbides at the grain boundaries. During decarburization this agglomeration remains undisturbed. On oxidation, internal oxidation of the carbide depleted phase occurs and the oxidation product, FeO was present either admixed with carbide or as a discrete phase adjacent to the grain boundaries. Oxidation rates of Fe-10MC-0.1C-RE_2O_3 sintered alloys were largely dependent on the extent of internal oxidation. Thus WC-

containing alloys have relatively very little internal oxidation rates. The oxidation rates of Fe-10MC-0.1C-1.0RE_2O_3 in undecarburized and decarburized states were much lower than the corresponding Fe-10MC alloys. This showed that the presence of rare earth oxides played an important role in restricting the oxidation rates of the alloy. However the oxidation rates of RE_2O_3-containing alloys were slightly higher than the corresponding 20 % Cr-containing alloys (Chapter V). It was obvious from these observations that the presence of internal Cr_2O_3 network at the grain boundaries limits the transportation of Fe or any element and therefore restricts the oxidation rates. In WC-containing alloys, the higher thermodynamic stability of WC towards oxidation plays an important role.

The influence of RE_2O_3 on the oxidation of alloys was not fully understood, but they do play some role in lowering the oxidation rates either affecting the mobility of carbon or providing more adherent nonporous oxide scales.

Chapter VII

The influence of a reactive oxide (TiO_2 or ZrO_2) on the decarburization and oxidation behaviour of carbide-dispersed iron-base sintered alloys has been discussed in this chapter.

Sintered alloys of the general composition : Fe-10MC-

0.1C-1.0MO_2 (where MC is NbC, Cr_7C_3 or WC and M is Cr, Nb or W and M´ is Zr or Ti) were decarburized in H_2-H_2O ($p_{O_2} \sim 10^{-19}$ atm.) and oxidized in O_2 (1 atm.).

In general, the weight gain Vs time plots were parabolic, indicating the diffusion-controlled growth of oxide scales. The oxidation rates of undecarburized Fe-10WC-0.1C-1.0ZrO_2/TiO_2 alloys were the lowest and the corresponding NbC-containing alloys have the highest rate. A similar trend was observed in Fe-10MC and Fe-10MC-0.1C-1.0RE_2O_3 alloy system. In the decarburized-oxidized state, Fe-10WC-0.1C-1.0ZrO_2 alloy has the lowest oxidation rate and Fe-10NbC-0.1C-1.0TiO_2 has the highest rate. In general, NbC-containing alloys have invariably higher oxidation rates than other carbide-containing alloys.

In most cases, the oxidation rates of Fe-10MC-0.1C-1.0ZrO_2/TiO_2 were very slightly higher than the corresponding rare earth oxide-containing alloys. However, like RE_2O_3-containing alloys, ZrO_2/TiO_2-containing alloys in undecarburized and decarburized states have oxidation rates much lower than (1-2 order of magnitude) than the corresponding Fe-10MC alloys (Chapter IV).

The results of oxidation kinetic and morphology of the oxidized alloys indicate that the presence of ZrO_2 or TiO_2 in the matrix greatly restricts the oxidation rates of Fe-10MC alloys like the corresponding RE_2O_3-containing alloys. ZrO_2

or TiO_2 inclusions act as deterents to the transport of metal during oxidation. The rare earth oxides have a slight edge over TiO_2 or ZrO_2 as far as adherence and compactness of the scales are concerned.

Chapter VIII

This chapter describes the oxidation and decarburization behaviour of some industrial steels, viz. silver steel, die steel, high speed steel (HSS) containing 18 and 6 wt. % W, EN-36, EN-31, EN-24 and EN-9, at 900°C in 1 atmospheric oxygen and H_2-H_2O mixture ($p_{O_2} \sim 10^{-19}$ atm.) respectively.

The phase structure of the alloys and morphology of the oxide scales have been investigated on the basis of optical and scanning electron microscopic studies.

The oxidation kinetic in general followed a parabolic rate law. With a few exceptions, the oxidation rates of undecarburized alloy steels are slightly lower than the predecarburized-oxidized steels. Amongst the undecarburized and predecarburized alloy steels, EN-9 has the highest oxidation rate followed by EN-31 alloy steel, high speed steel (18 % W) and die-steels, the latter showed the lowest rate. The increasing oxidation rate sequence for the different alloys:

EN-9 > EN-31 > silver steel > EN-24 > EN-36 > high speed steel (6 W) > die-steel > high speed steel (18 W).

The alloy steels on decarburization showed a well defined decarburized layers and an increase in the ferrite contents of the alloys. The tickness of the decarburized layer increases with increasing carbon contents. However a deviation was found in some cases probably due to the varying concentration of the carbides like Cr_7C_3, MoC or WC in the alloy matrix.

The alloy phase structure and the morphology of the oxide scales seem to influence the oxidation rates of the alloys. The alloys forming chromia scales and containing dispersion of carbides in the matrix have relatively lower oxidation rates. The plain carbon steel (EN-9) or low chromium steels (EN-24, -31 and -36) form copious oxide scales mainly comprised of iron oxides.

A plot of parabolic rate constant, Kp Vs (Cr+C) % for different alloy showed that, with some exception, the oxidation rate decreases with increasing (Cr+C) % content, this indirectly indexed the influence of chromium carbide and other transition metal carbides on the oxidation rates of the alloys.

The carbon loss sequence for different alloys during a 4 hr. decarburization run in H_2-H_2O atmosphere was :

High speed steel (18 % W) < EN-31 < high speed steel (6 % W) < EN-24 < silver steel < EN-9 ∽ EN-36 < die steel

Alloys containing no or very small carbide concentration showed

well defined decarburized layer. The decarburized layer was usually ferrite containing dispersion of carbides.

The oxidation rates of the decarburized alloys were slightly higher than the undecarburized alloys. This could be explained on the basis of the oxidation of decarburized layer which was ferritic in nature, the layer oxidizes at a much higher rate than the carbide dispersed ferrite matrix present in the undecarburized alloys. Such a behaviour has also been reported in decarburized carbide dispersed Fe-5M-C alloys (where M is a transition metal), which oxidize at a much higher rate than the corresponding undecarburized alloys. However, a reverse behaviour has been observed in case of Fe-10MC iron-base sintered alloys, where decarburized alloys have higher oxidation rates.

CHAPTER I

INTRODUCTION

1.1 Oxidation

1.1.1 Oxidation of Metals

Due to their typical electronic configurations almost all the metals (with the possible exception of gold) have the tendency to react with the environment at ambient temperatures forming metal oxides. The rate of oxide formation increases with increasing temperature. The oxide forms on the metal may be continuous or discontinuous, adhered or unadhered and porous or non porous. The oxide scales which are compact, non-porous and adhered to metal or alloy are called protective scales. A limited number of metals such as Cr, Al, Si, Ti etc. form protective oxide films in true sense. A crude way of determining the tendency of a metal to form protective oxide scales is to test by Pilling and Bedworth criterion where the ratio of the volume of oxide to the volume of the metal consumed should be greater than 1. However, factors such as surface condition of the metal, mechanical and thermal stresses, nature of the oxidant etc. also influence greatly the protective nature of the oxide film.

The selection of a vast number of structural materials for high temperature applications is based upon the formation of a protective oxide film(s), this film once formed acts as

an impervious barrier against further oxidation provided the integrity of the film is maintained. A selected band of materials fulfil this condition and include metals such as Cr, Al, Si, Ti, Ni etc. or the alloys based on these metals or the alloys containing these metals as major alloy additions.

The oxidation kinetic of a metal or an alloy forming a protective oxide film is usually governed by a parabolic rate law. The oxide growth on a metal occurs through cation and anion diffusion. As early as Wagner proposed his parabolic equation for the oxidation of metals. When a metal is exposed to oxygen, reaction will take place provided the oxygen pressure is greater than the pressure required for the metal oxide equilibrium, namely

$$M + 1/2\ O_2 = MO \qquad (1)$$

and

$$(P_{O_2})^{1/2}_{M\text{-}MO} = \exp\ (+\ \Delta G^{o}_{MO}/RT) \qquad (2)$$

where $(P_{O_2})_{M\text{-}MO}$ is the oxygen pressure of the metal oxide equilibrium, ΔG^{o}_{MO} is the standard free energy of formation of the oxide MO, and T is the absolute temperature. The equilibrium oxygen pressure for most metals with the exception of precious metals are very small at the temperatures and consequently the thermodynamic conditions are favourable for oxide formation in many gas environments encountered in

practice. Oxide scales are therefore developed upon metals exposed to oxygen at elevated temperatures. When these scales are macroscopically dense, exhibit predominant electronic conditions and adheres uniformally to the metal surface, the oxidation rate expressed in terms of specimen weight change (the oxidation may also be expressed in terms of oxide scale thickness or thickness of metal consumed) is given by

$$\frac{d(\Delta m/A)}{dt} = \frac{K_p}{\Delta m/A} \qquad (3)$$

where Δm is weight change, A is the specimen area, t is time and K_p is the parabolic rate constant. The important feature of this relationship is that the oxidation rate decreases with time since the oxide scale acts as a barrier which inhibits oxidation by separating the reactants. If the oxide scale is non-protective, it does not inhibit subsequent oxidation and the oxidation rate is given by

$$\frac{d(\Delta m/A)}{dt} = K_l \qquad (4)$$

where K_l is linear rate constant. The oxides of metal follow other rate laws in addition to the parabolic (eqn. 3) and linear (eqn. 4) expressions[1]. However, when one is primarily concerned with oxidation resistance, consideration of these two rate laws is sufficient.

In considering the oxidation of alloys, eqn. (1) and (2) must be modified as follows :

$$M_i + 1/2\ O_2 = M_iO \qquad (5)$$

$i = 1,2, \ldots$ number of elements in alloy

and

$$(P_{O_2})^{1/2}_{M_i-M_iO} = \frac{\exp\ (+\Delta G^{o}_{M_iO}/RT)}{a_{M_i}} \qquad (6)$$

where a_{M_i} is the activity of M_i in the alloy. Hence upon exposure to oxygen, oxides of all elements in the alloy will be formed providing the oxygen pressure in the gas is greater than the equilibrium pressure defined by eqn. (6). Even though numerous oxide phases are usually formed upon alloys during the initial stages of oxidation, there is competition between the elements for oxygen since some of the oxides are more stable than others. Hence it is necessary to consider reactions such as

$$M_1O + M_2 = M_2O + M_1 \qquad (7)$$

with

$$\frac{a_{M_1}}{a_{M_2}} = \exp\ [(\Delta G^{o}_{M_1O} - \Delta G^{o}_{M_2O}/RT)] \qquad (8)$$

Equation (8) shows that the thermodynamic conditions for oxide formation are controlled by the activities of the metallic components in the alloy, the pressure of the oxygen in

the gas and the relative affinities of the metallic elements for oxygen. As a result of this competition between the elements in the alloy for oxygen, there is a tendency for the alloy eventually to become covered with most thermodynamically stable oxide. This is an especially fortunate circumstance because it permits the selective oxidation of essentially one element in the alloy. The oxide scales that are formed on alloys are very often composed of layers with the more thermodynamically stable oxides close to the alloys. Even when only one oxide scale is evident upon an alloy, examination of the scale during the very early stages of oxidation often shows the formation of the less stable oxides. The oxidation of alloys often therefore consist of a transient stage during which a variety of oxides are formed[2,3]. This initial stage is followed by another stage where only the thermodynamically stable phases continue to grow. Kinetic factors play a significant role in determining which of the oxide phases continue to grow.

During the very early stages of oxidation virtually all oxides are formed. As oxidation continues diffusion begins to take place and displacement reactions begin to occur. The important diffusion species are oxygen into the alloy and the outward diffusion of elements in the alloy. In case where oxygen diffuses rapidly compared to the metallic elements, the volume fraction of oxide is approximately equal

to that of the element in the alloy because the element is converted to oxide in situ with virtually no diffusion. On the other hand, when oxygen diffusion is slow compared to that of elements in the alloy, the volume fraction of the oxide can be substantially greater than that of the element in the alloy because of diffusion of the element from the interior towards the oxidation front. When the volume fraction of a given oxide achieves some critical value it is more favourable to form additional oxide via lateral growth rather than to form new oxide deeper within the alloy, and hence for such critical volume fractions the oxide will then develop a continuous layer over the surface of the alloy. In summary, the development of oxides on alloys can be described as sequential process. Initially many oxides are formed but then the more thermodynamically stable phases gradually predominate. In order to have total dominance of an oxide over the surface of the alloy, this oxide must be more stable than any other of the oxides, and the kinetics of formation for this oxide must be such that lateral growth is favoured as opposed to the formation of a discontinuous subscale.

1.1.2 Protective and Nonprotective Scales

Rate of reaction in the later stages of oxidation depends on whether the thick film or scale remains continuous and protective as it grows, or whether it contains cracks and

pores and is relatively non-protective. Because reaction product films are usually brittle and lack ductility, the initiation of cracks depends in some measure on whether the film is formed in tension favouring fracture or in compression favouring protection. This situation in turn depends on whether the volume of reaction product is greater or less than the volume of metal from which the product forms[4]. If

$$Md/nmD > 1 \qquad (9)$$

a protective scale forms.

Where M is the molecular weight and D the density of scale, m and d are the atomic weight and density of a metal respectively, and n is the number of metal atoms in a molecular formula of scale substance.

1.1.3 Internal and Intergranular Oxidation

The formation of oxidation products within alloys occurs in two forms, which may be identified by the terms internal oxidation and intergranular oxidation. The term internal oxidation is characterized by the formation of oxidation products at a reaction front that advances uniformly into the alloy, independent of microstructural features such as grain boundaries. The oxidation products may be present as either discrete precipitates or continuous rods, plates etc. In the case of intergranular oxidation, formation of

oxidation products along alloy grain boundaries occurs to a greater depth than in the interiors of the alloy grains. Heterogeneous precipitation of oxidation products along alloy grain boundaries within the zone of internal oxidation does not in itself constitute intergranular oxidation. The oxidation products in either case may be oxides, sulfides or carbides or combinations of two or more such compounds. Formation of both the external and internal (intergranular) oxidation products usually occurs simultaneously. Intergranular oxidation often accompanies with void formation by various mechanism such as vacancy injection from the scale, the Kirkendall effect and creep-type processes.

Wagner's classical model for internal oxidation of binary alloys by a single oxidant[5], which has been reviewed and extended by others[6-10] provides a valuable basis for describing the kinetic of internal oxidation and includes several special cases.

(a) The flux of the solute is significant relative to that of the oxidant.

(b) The flux of the solute being oxidized is negligible relative to the flux of the oxidant.

This model also provides a basis for understanding the transition from internal to external oxidation of alloys.

Wagner was also able to explain quantitatively, based

on his model for binary alloys, how the addition of a third element could promote the formation of an external scale[11]. Although this model provides some guidelines for understanding the effects of a third element on the transition from internal to external oxidation it does not seem to apply to all cases. A case in point is the failure of Mn to promote external Al_2O_3 scales on Fe-Al alloys[12].

Wagner's model does not take into account the effects of a number of variables that may have an important effect on the process of internal oxidation. These include alloy microstructure (grain size, dislocation, density, presence of second phase particles etc.) mechanical properties of alloy, the presence of more than one oxidant, and diffusion of metal and/or oxidant along alloy/product interphase boundaries and through the oxidation product itself. Work by Shida et al.[13] suggests, for example, that stresses generated by intergranular oxidation may facilitate further intergranular oxidation by wedging open grain boundaries of alloys that do not easily undergo plastic deformation. The exact mechanism is, however, not clear and the effects of stresses on internal and intergranular oxidation generally are not known. It has been suggested recently that stresses generated in the zone of internal oxidation of Ag-Pd-In-Sn alloys give rise to a vacancy flux (Nabarro-Herring Creep) that yields a layer of Ag-Pd alloy on the surface of the internally oxidized alloy.[14]

The formation of metallic particles on the surfaces of other alloys that have experienced internal oxidation seems to occur in the absence of stresses[15,16].

Whittle et al.[17] have developed a quantitative model to account for diffusion of oxidant through an internal oxidation zone by more than one path, i.e., diffusion in the alloy, diffusion along the alloy/product interphase boundary, and diffusion within the oxidation product. It appears that interphase diffusion may be a major factor in determining the kinetics and morphology of internal oxidation. Interphase diffusion probably also plays a significant role in intergranular penetration.

Very little is known about the mechanism of intergranular oxidation. Perhaps this is because it occurs rarely, except for oxidation of solutes present in alloy at low concentrations. The formation of intergranular silica occurs, for example, during the oxidation of stainless steels containing less than 1 wt. % silicon. The use of very fine grained alloys (< 10 μm) to promote formation of closed grain boundary loops of silica may provide an effective means for inhibiting carbon penetration into such alloys. Thus, further studies of the mechanisms of intergranular oxidation seem warranted. The work of Shida et al.[13,18] has defined a significant number of cases of internal and intergranular oxidation. The shape morphology, size and disposition of oxide

precipitates require further understanding, following up the work of Bohm and Kahlweit.[19].

1.1.4 Oxidation of Iron

When iron is exposed to oxygen at temperatures higher than 560°C, a relatively complex reaction system is involved due to the formation of multilayered scale comprising of wustite (FeO), magnetite (Fe_3O_4) and haematite (Fe_2O_3). The Fe-O diagram[20] (Fig. 1.1) shows that at temperatures above

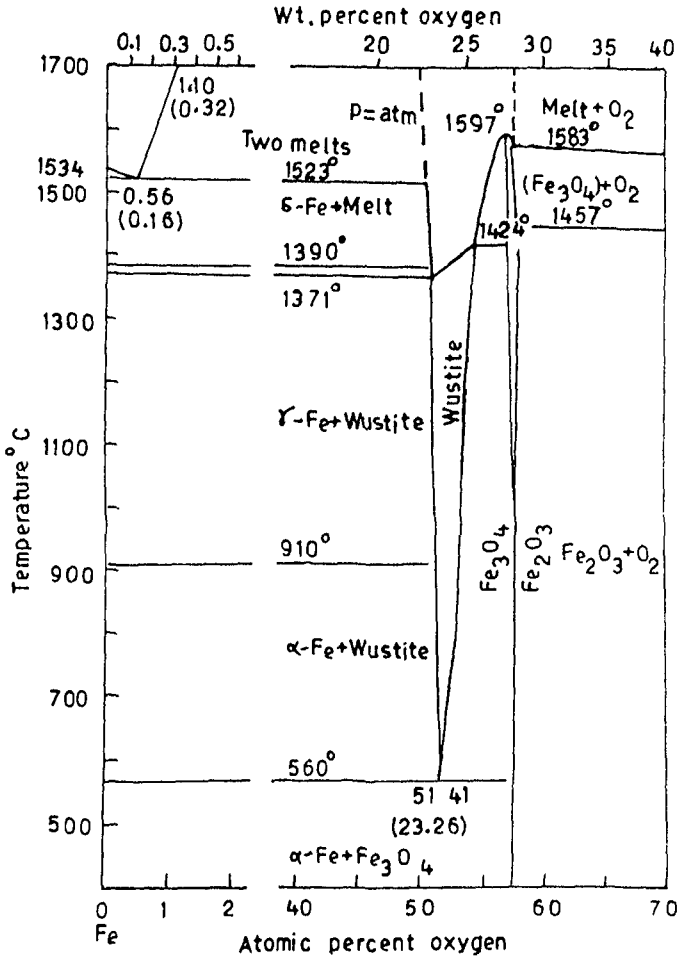

Fig. 1.1 Iron Oxygen phase diagram[20].

560°C, iron forms three oxides, the lowest valency oxide, FeO (wustite), has a NaCl type cubic structure and is metal deficient of the order of 5-12 % of iron vacancies. Being cation conducting it grows entirely by the diffusion of iron and appears in the form of innermost layer. The second oxide, Fe_3O_4 (magnetite), has a spinel type structure and is an excess oxygen compound. It grows largely by oxide ion diffusion with an appreciable contribution from iron ion diffusion (12 %). The highest valency oxide, Fe_2O_3 (hematite), which forms outermost layer of the multilayer scale has rhombohedral crystal structure. It is slightly oxygen deficient, metal excess and largely grows by oxide ion diffusion.

The relative percentage of FeO, Fe_3O_4 and Fe_2O_3 in the scales vary with temperature[21] (Fig. 1.2), duration of

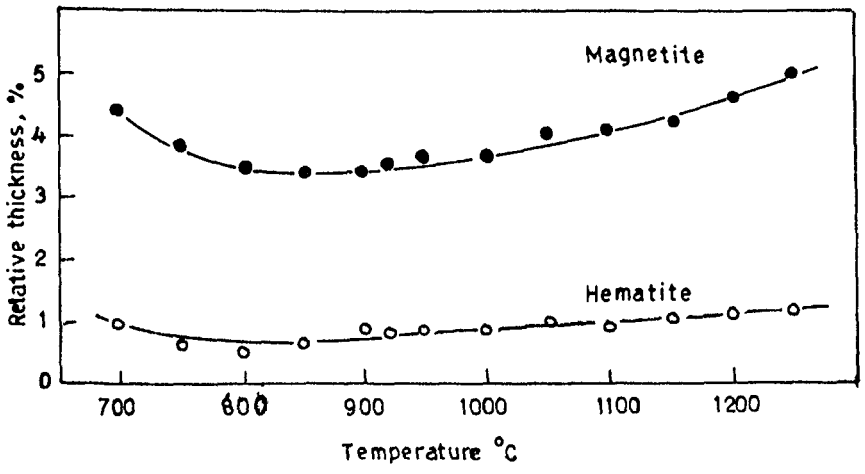

Fig. 1.2 Relative thickness of Fe_2O_3 and Fe_3O_4 in the scaling of iron in air.

oxidation and nature of oxidizing gas. However, above 600°C, FeO is the predominant species and since FeO has more defective structure than either of the two oxides, iron oxidizes much more rapidly above this temperature. Since the three oxides are formed simultaneously upon the iron surface and the ratio of thickness of three layers is reported to be dependent of time and temperature, the mechanism of oxidation is not simple and requires several mechanistic approaches at various stages of oxidation. Below 560°C, FeO is unstable and if any is formed above this temperature it decomposes at room temperature into Fe_3O_4 plus Fe.

1.1.5 Oxidation of Iron-Base Alloys

Failure of pure iron to form sufficiently protective oxide layer suitable for practical applications at temperatures above 500°C, demands the presence of an alloying element which has a higher oxygen affinity than iron and where oxide grows at a low rate. Generally, Cr or in some cases Al or Si serve this purpose, and when present in sufficient concentrations, protective scales of Cr_2O_3, Al_2O_3 or SiO_2 are formed exclusively.

At low alloying concentrations, the oxide scales are still similar to those on pure iron, with the alloying element remaining in solution in wustite and other oxides. The defect concentration may be modified, usually increased, resulting in

change in oxidation rate. At higher concentrations, the composition range of FeO becomes restricted and eventually disappears as a single phase. Compound oxides with spinel structure are formed of the general type $Fe(FeM)O_4$ where M is the alloying element. Often these spinels can exist over a range of composition and usually their appearance in the scale results in a decrease in the overall oxidation rate. At higher concentration still a complete selective oxidation may occur with a maximum reduction in the overall oxidation rate.

Rahmel[22] proposed a reaction mechanism for the oxidation of dilute binary iron alloys with alloying additions which are less noble than iron, e.g., V, Cr, Si and Mo. Initially these alloys oxidize like pure iron resulting in the formation of iron oxides. Subsequently oxygen dissolves in the alloy phase causing internal oxidation, and because of the preferential oxidation of iron, the alloying addition is enriched at the metal/oxide interface. As the oxide of alloying addition is formed, this reacts with FeO to form $Fe(FeM)O_4$, giving two phase inner layer.

Fig.(1.3) shows the effect of common alloying elements on the oxidation of iron[23]. The factor F represents relative weight increment after 4 hrs. of oxidation at 890°C.

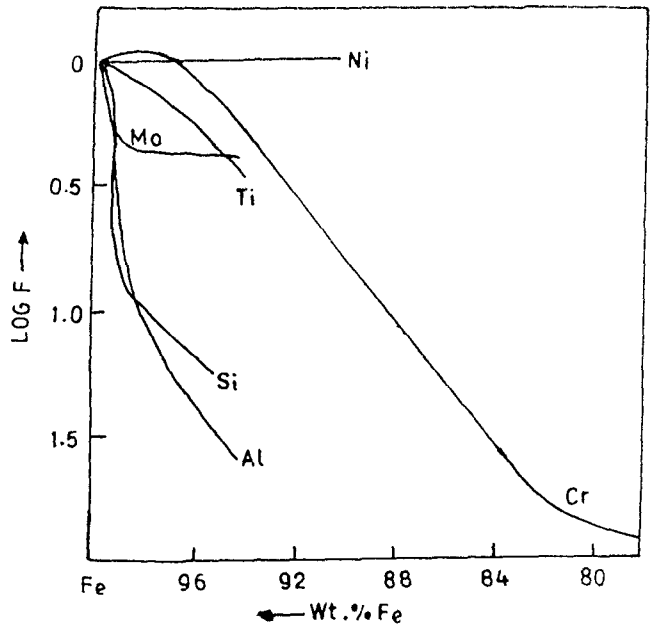

Fig. 1.3 Effect of Common alloying elements on oxidation of iron[23].

1.1.6 Oxidation of Fe-Cr Alloys

Protection of the metallic materials in hostile environments such as found in energy generating and energy conversion units might be achieved by growing compact and stable oxide scales. Alloying with chromium improves the oxidation resistance of iron at high temperatures. The magnitude of this improvement depends primarily on the Cr concentration. Above 570°C, iron forms three oxides : $Fe_{1-x}O$, Fe_3O_4, and Fe_2O_3 of which ($Fe_{1-x}O$) constitutes more than 90 % of the oxide scale[24]. Alloying with chromium supresses the formation of wustite. Seybolt[25] showed Cr_2O_3 is the stable oxide

when the Cr concentration at the alloy/oxide interface exceeds 13 wt. %. At lower Cr contents the oxidation behaviour of Fe-Cr alloys is very complex, scales consisting of $(Fe,Cr)_3O_4$ spinel and various other Fe- and Cr- oxides[26-28] are formed. Coplan and Cohen[29] and others have reported that Fe alloys containing more than 16-20 % Cr show excellent oxidation resistance.

Kahveci[30] investigated the oxidation behaviour and microstructure on Fe-3 wt. % Cr alloy at 800°C in dry air at atmospheric pressure. A change in the oxidation kinetic was caused by micro-chemical and micro-structural development in the oxide scale. Several layers developed in the oxide scale, consisting of an innermost layer of $(Fe,Cr)_3O_4$ spinel, an intermediate layer of $(Fe,Cr)_2O_3$ sesquioxide, and the outer layers of Fe_2O_3, hematite, each with different morphologies. Wustite ($Fe_{1-x}O$) and distorted cubic oxide (γ-$(Fe,Cr)_2O_3$) were observed during the initial parabolic oxidation only.

Fe-Cr alloys containing less than 20 wt. % Cr exhibit several types of scaling behaviour when oxidized in air at high temperatures. Thick stratified layers of complex Cr, Fe oxides grow at randomly distributed sites on the alloy surface[31]. They are non-protective and allow the rapid diffusion of reactants through the oxide barrier. Whittle and Wood[32] studied the oxidation of Fe-Cr alloys containing 22-68 wt.% Cr in oxygen at 800-1200°C. The oxidation decreases with

increasing Cr contents and the oxide growth is diffusion controlled. Bernes[33] on the basis of radio isotopic exchange studies, using O^{18}, showed that bulk oxygen diffusion plays a negligible role in the oxidation reaction and cation transport always dominate the scale growth mechanism. Skeldon and coworkers[34] investigated the growth mechanism of Cr_2O_3 scale formed on pure chromium oxidized at 950°C in oxygen at 1 atm. using isotopic tracer techniques. They proposed, initially oxide growth occurs entirely by cation diffusion, with new oxide being formed at the oxide-gas interface. Then at a time that is not the same for all parts of the scale, the growth mechanism changes to one in which new oxide is formed within the outer part of the scale.

Kurod et al.[35], investigated the oxides formed on Fe and Fe-Cr alloys containing 3-18 wt. % Cr at 700-800°C and $\backsim 10^{-3}$ Pa of O_2, by Electron Microscopy. On Fe and Fe-3 wt.% Cr, wustite and magnetite particles nucleated and grew out of the surface. On the alloys containing > 9 wt. % Cr, the $(Fe,Cr)_3O_4$ spinel nucleated and grew into the metal. Gardiner et al.[36] used Raman microscopy to study the nature of corrosion products formed on Fe-Cr alloys containing 2-18 wt. % Cr in air at 400-850°C. The oxides Fe_2O_3, Fe_3O_4, Cr_2O_3, and $FeCr_2O_4.Fe_2O_3$ and Fe_3O_4 were formed exclusively on pure Fe and the 2 and 5 wt. % Cr alloys at all temperature and on 14 wt. % Cr alloy at 400°C. The 14 and 18 wt. % Cr alloys formed scales

containing Cr_2O_3 and $Fe.Cr_2O_4$ at higher temperatures (600-850°C). Choi and Stringer[37] showed that Fe-Cr alloys which seem to form protective oxide films in atmospheres containing S and O under short term laboratory tests could be non-protective under long term exposure test due to accelerated corrosion rates caused by breakway corrosion. The breakway involves the development of a critical microstructure characterized by considerable intrusions of relatively coarse Cr_2O_3 fingers into the metal substrate. The intrusions also involve the progressive oxidation of CrS. This also causes the oxide fingers to be porous, allowing gaseous species easy access to the reaction front.

1.1.7 Effect of Reactive Elements on the Oxidation Behaviour of Fe-Cr alloys

The improvement in oxidation resistance of high temperature alloys as a result of additions of rare earth elements, other reactive metals, or dispersions of oxides, has been known for many years. Two effects seem to be most important: first, the adhesion between scale and alloy is markedly improved and this increases the alloys resistance to thermal cycling exposure, secondly, in most cases the actual growth rate of the oxide is also reduced. Cr_2O_3 and Al_2O_3 are generally regarded as the best protective oxides : diffusion through them is relatively slow in comparison with most other oxides,

and since they are also stable, relatively little difficulty exists in selecting an alloy which contains sufficient chromium or aluminium to provide, by selective oxidation, a protective Cr_2O_3 or Al_2O_3 scale under various service environments.

It was discovered over 50 years ago that additions of rare earth metals as a melt deoxidant to nichrome (Ni-20 wt. % Cr) heating elements produced substantial increase in their life time to failure in cyclic heating and cooling tests[38], the protective oxide was more adherent. Yttrium and scandium additions were included in the original patent, and it was also shown that by the combined addition of rare earths, alkaline earths and carbon, the life of heat resistant alloys could be further improved. The amounts of the additions were such that 0.01-0.5 wt. % rare earth, about 0.001-0.05 % Ca and upto about 0.25 wt. % C remained in the finished alloy. Pfeil[39] indicated that elements from Groups II, III, IV and V of the Periodic Table could be used although their effectiveness decreased on passing from group II to group V, but increased with increasing atomic mass within a particular group.

Francis and Whitlow[40] suggested that the oxidation rate of an Fe-25Cr alloy is approximately parabolic, that of an Fe-25Cr-IV alloy is asymptotic, and after an initially fast rate of attack slows down very rapidly. Wood and

Boustead[41] indicated similar behaviour of Gd and Y additions to Fe-27Cr alloy. However, Y was not able to prevent breakway attack in Fe-16Cr alloys at 1200°C, or during thermal cycling[42], Zirconium[41] and Gadolnium[42], however, tended to increase the time breakway. A 3 wt. % (by volume) addition of Y_2O_3 as a fine oxide dispersion was more effective and rapid breakway oxidation of Fe-16Cr at 1100°C was never observed. Goncel et al.[43] have studied the effects of TiO_2, HfO_2 and TiN dispersions on the oxidation behaviour of both ferritic and austenitic stainless steels. Each addition reduced the overall oxidation rate but the oxide dispersions were generally much better than the nitride, and HfO_2 better than TiO_2.

It has been well known that small additions of reactive elements such as Y, Al and Si, singly or together, to Fe-Cr, Ni-Cr and Co-Cr alloys play a crucial role in improving their oxidation resistance. Although various hypothesis and explanations on improving mechanism have been proposed, the mechanism has not been clearly understood. The significant mechanisms proposed are as follows:

(a) The oxide layer of the reactive element formed beneath the scale as a physical barrier to inhibit the diffusion of metal from alloy to scale and reduces the rate of scale growth[44-51].

(b) Diffusion of the elements (Y, Al or Si) is enhanced by changing the properties of the base alloy[52] such as an expansion of the lattice by the addition of elements with a large atomic volume. It promotes the formation of the protective Cr_2O_3 scale or the protective internal oxidation layer of the reactive element added together with rare earths.

(c) A complicated alloy scale interface formed by preferential oxidation at grain boundary improves the scale adherence, so called "key-on" effect[52-54].

(d) Internal oxide particles act as vacancy sinks and absorb inward flowing vacancies, thus preventing void formation at the alloy-scale interface[55-57].

(e) Dissolution of additive elements into scale improves the sintering and plasticity of the scale and consequently prevents the mechanical failure of the scale[57-58].

Wright and Wilcox[42] had studied the oxidation resistance of Fe-16Cr alloy containing 0.05 wt. % Zr at 1100°C and 1200°C and reported only a slight effect of zirconium. Moroishi et al.[59] studied the effect of C, Zr, Ti and Nb on the oxidation resistance of Fe-17Cr steels upto 1000°C. They found that Zr improves the oxidation resistance of the alloy to a great extent.

Miner and Nagarajan[60] oxidized a series of iron-base alloys containing 18 wt. % C and 0.5 to 2 wt. % Si in

air, in a H_2/H_2O environment ($P_{O_2} = 10^{-18}$ atm.) and corroded in a $H_2/H_2O/H_2S$ environment ($P_{O_2} = 10^{-18}$ atm., $P_{S_2} = 10^{-6}$ atm.) after pre-oxidizing in air. They reported that, (i) the silicon containing alloys form a subscale of silica when subjected to oxidation in air or a low P_{O_2} environment, and it may be continuous in the 2 % silicon containing alloy, (2) in the low P_{O_2} environment, the amount of iron in the surface scale is relatively low compared to the surface scale produced in air, and (3) pre-oxidation improves the corrosion resistance (in a coal gasifier environment) of these alloys, but, sulfer diffuses through the Cr_2O_3-rich layer. The establishment of a silica rich subscale may be necessary to achieve corrosion resistance.

The effect of finely distributed stable oxides such as Y_2O_3, CeO_2 or other rare earth metal oxides on high temperature oxidation behaviour of alloys based Ni-Cr, Co-Cr or Fe-Cr have been well documented[61-71]. Similar dispersions in pure Cr were also shown to modify the oxidation rate[56-72].

Nagai et al.[73-75] reported the oxidation behaviour of Fe-20Cr alloys with single additions of rare earths and some active elements and suggested that these elements had two main beneficial effects to reduce the oxidation rate. The first effect is the stabilization of the Cr_2O_3 scale by dissolving the additive element in the scale, which was followed by a drop in the dissociation oxygen pressure of the scale, stronger

the affinity for oxygen of the alloying element, the greater was the extent of the first effect. The second effect is the formation of a dense internal oxidation beneath the scale. In Fe-20Cr alloys, 0.7 wt. % La was found beneficial and with 0.68 wt. % Si addition gives better oxidation resistance than others (Y, Gd, Al, Zr, Ti)[76]. They further studied the effect of La or Y with Al[77] or Si[78] and reported that the oxidation resistance of the alloys, Si with La extremely improved, the improving effect of the simultaneous additions of rare earths with Si was more effective than that of rare earths with Al.

Nagai et al.[79] reported the isothermal oxidation resistance of Fe-20Cr sintered and hot rolled alloys with 1.0 wt.% dispersoid of Y_2O_3, La_2O_3, Al_2O_3, TiO_2, SiO_2 or Cr_2O_3 in air at 1000, 1100 and 1200°C. The effect of La_2O_3 and Y_2O_3 dispersoids was excellent, while SiO_2 reduced the rate, the dispersoids, TiO_2 and Cr_2O_3 showed no beneficial effect on the oxidation resistance except for the oxidation after 10 h at 900°C, however, Al_2O_3 slightly increases the oxidation resistance. They[80] further studied the effect of dispersion and superficial application of various rare earth oxides (Y_2O_3, La_2O_3, CeO_2, Eu_2O_3, Gd_2O_3) on the isothermal oxidation of Fe-20Cr sintered alloys at 1200°C in air. The dispersion of La_2O_3, Y_2O_3 and Gd_2O_3 greatly reduced the oxidation, while the effect of Eu_2O_3 dispersion was less than of the other oxides. The dispersion of CeO_2 suppresses the spalling of the scale.

Whittle and Stringer[81] suggested that carbides or even intermetallic compounds may be used for the development of high temperature resistant alloys and generalized the following important factors :

(a) the dispersoid must be very stable so that it does not dissociate or dissolve in the matrix, and it is better if it does not oxidize,

(b) it is also better if the dispersoid does not contain the constituent that is going to form the protective scale, and

(c) it is possible to disperse the phase within the matrix in the right configuration.

The influence of carbon on Fe-Cr alloys is very little known. Malik and Whittle[82] reported that the carbon content decreased the oxidation rate of Fe-C steels with respect to pure Fe. By contrast, the higher content of C increases the oxidation rates of Cr-containing Fe-C alloys[83]. Hajduga and Kucera[84] reported the primary stage oxidation of Fe-Cr alloys containing 13 wt. % Cr and 0.15-1.63 wt. % carbon at 1100°C for 3 hr in 4.8 % O_2-1.2 % N_2-94 % He. It was found that the oxidation rate increased with increasing carbon content in the alloys. The measured time variation of CO_2 evolution showed that, during the first period of oxidation (0-40 min.), a compact surface layer of FeO formed, which prohibited the free transfer of CO_2 into the streaming oxidation atmosphere.

The measurable CO_2 evolution started between 40 and 50 min., and the most rapid evolution occurred in the internal t = 60-90 min. of oxidation. This effect corresponds well to scale layer damage and to the maximum O_2 absorption.

1.1.8 Effect of Alloying Element

The effect of different alloying elements on the oxidation of iron is described briefly as follows :

Silicon : Addition of 2-3 wt. % Si or more markedly reduces the oxidation rate of iron. A SiO_2-rich inner layer is apparently formed which restricts the diffusion rate of Si and hinders Fe^{+2} diffusion through the SiO_2 layer. The lower Fe-Si alloys are subjected to internal oxidation. By controlling the oxygen potential initially it is possible to oxidize Si selectively to SiO_2 at the surface to form a protective layer but in normal conditions iron oxidizes as well to replace protective SiO_2 by much less protective spinel $2FeO.SiO_2$.

Chromium : The addition of small amounts of chromium (< 3 wt. %) somewhat increases the oxidation rate of iron at least for short exposures, but for longer exposures the rate is gradually reduced. The kinetics of oxidation is governed by the formation of spinel layer, $Fe.Cr_2O_4$ at the base of the alloy together with layers of pores.

At higher chromium contents the oxidation rate falls

at any given temperature. In such alloys a protective scale of doped Cr_2O_3 is formed in the initial stages but less strongly adhered as interfacial discontinuities and growth stresses increase. The underlying metal layer, depleted in Cr, is then much less resistant to oxidation and alloy subsequently may show breakway oxidation behaviour.

Nickel : Small additions of Ni have very little effect on the oxidation resistance of iron. There is slight improvement with alloys of higher Ni content. For example, alloy with 32-40 wt. % Ni oxidize 30-40 times less than pure iron or about the same extent as pure Ni.

The oxidation of Fe-Ni alloys (containing upto 36 wt. % Ni) proceeds in two stages : in the first stage oxide grows due to the diffusion of Fe^{2+} ions and in the second stage the diffusion of oxygen is more rapid than the diffusion of cation due to accumulation of Ni at the metal surface[85]. Only alloys containing 42 wt. % or more Ni, were found to have Ni in the scale in the form of a spinel $NiFe_2O_4$ next to the alloy[86]. The rate controlling step in the oxidation of these alloys is the diffusion of cations across the spinel which is likely to be less than the diffusion in iron oxides, and would account for the improved resistance of these alloys.

Tungsten : Addition of W in iron has an adverse effect on the high temperature oxidation resistance properties of

iron[23]. This is mainly due to the relatively low melting point of WO_3 (m.p. 1470°C) causing catastropic oxidation. Scheill[87] observed the formation of double oxide $FeO-WO_3$ in a Fe-4 wt. % W alloy, the compound accumulates in the inner scale layer and this probably reduces the tendency of WO_3 to escape from the oxide layer. Similar behaviour has been observed by Malik et al.[88] for Fe-5 wt. % W alloy in the temperature range 650-850°C.

Titanium: Oxidation resistance of iron is slightly improved[89] by the small addition of Ti upto 6 wt. %. The titanium is found in the form of a double oxide $FeO.TiO_2$ near the oxide/metal interface.

Vanadium : Vanadium causes adverse effect on the oxidation resistance of iron due to the presence of low melting point compound V_2O_5 thus causing catastropic oxidation[23].

1.1.9 Oxidation of Fe-C Alloys

It is a well known fact that iron containing even relatively low carbon contents does not form a sufficiently protective scale suitable for practical applications at temperatures above 500°C. The presence of carbon in minimal amount ($\sim$ 0.1 wt. %) is beneficial under high temperature conditions but at higher contents the blistering and cracking of the otherwise protective scales invariably occur due to the evolution of carbonaceous gases. This provides easy passage

for the transport of oxidizing gases through the pores and voids in the scales resulting in direct contact between metal and the gas. Consequently the alloy oxidizes at a faster rate. At temperatures above 600°C, the oxidation is even faster due to the growth of wustite.

Numerous studies[89-96] have been reported on the oxidation behaviour of iron-carbon alloys. Wagner[97] gave two general reaction sequences during oxidation of a metal carbon alloys : (i) diffusion of carbon to the metal/scale interface where it reacts with the scale to produce gaseous carbon oxides which may accumulate and cause rupture of the scale and (ii) diffusion of carbon through the scale to react with oxygen at the scale/gas interface. The second sequence would allow decarburization to take place without scale rupture. On the other hand, Langer and Trenkler[98] have suggested that both carbon and iron may diffuse sufficiently and rapidly through the scale to react with the gaseous reactants at the oxide/gas interface.

Malik and Whittle[99] studied the influence of carbon on the oxidation behaviour of iron-base alloys in the temperature range 600-850°C and under flowing air. The oxidation kinetics was supplemented by total loss measurements during oxidation. The values of parabolic rate constants, Kp for Fe-5M-1.2C follow the sequence

Fe-Cr-C > Fe-C > Fe-Ti-C > Fe-Ta-C > Fe-Nb-C >
Fe-V-C > Fe-W-C

The order gave an indication about the relative stability of the various carbides towards oxidation.

1.2 Decarburization

1.2.1 Decarburization of Iron-Base Alloys

The carbon loss from the surface layers of alloy in presence of an oxidizing atmosphere (wet H_2 or O_2 at low potential) is termed as decarburization. Oxidation of carbon is the most important reaction in steel making, because it controls the rate of production. In some industrial units working under low oxygen potential atmospheres, the loss of carbon may result in unsatisfactory performance of engineering components. For example, the decarburization softens the surface layers, the wear resistance is decreased and, in many instances there can be a serious drop in fatigue life. However the decarburization of steel by wet hydrogen at high temperature is an accepted technique in research as well as in industry. For example, this technique is used commercially in processing low carbon steels for magnetic applications.

It has been frequently reported[100] that the decarburization of steels is greatly enhanced by the presence of water vapour in hydrogen. During recent years, the decarburization of steels in low oxygen potential atmospheres has been a

subject of intensive studies.

At high temperature carbon usually reduces the oxidation resistance of steels due to the evolution of oxides of carbon which disrupt the otherwise protective scales. However, it could be prevented by introducing metals which can bind carbon in the form of stable carbides. A parallel situation arises in decarburization too. If the carbon is present in the matrix as stable carbide dispersion then most probably the carbon loss due to decarburization can be prevented or can be reduced to the maximum extent. Very limited attention has been paid on this aspect of the problem and scant information is available regarding the role of carbides during decarburization. The decarburization study of iron-base alloys containing carbide dispersion in H_2-H_2O atmospheres is thus an interesting area of research like its oxidation counterpart. Moreover, such study would be helpful in comparing the oxidation and decarburization capability of the alloy with the same phase structure in the oxidizing and decarburizing conditions. Since it is not surprising if an industrial alloy subjected to high temperature oxidation conditions could also be used under decarburizing atmospheres.

The decarburization of iron carbon alloys depends upon special factors namely

i) temperature

ii) nature of the gas used for decarburization

iii) carbon content

iv) period of decarburization

v) number and nature of the phases present at the decarburization temperature

vi) rate of scaling if any

vii) nature of the alloying elements if any.

1.2.2 Mathematical Evaluation of Decarburized Layer Thickness

Preliminary calculations[101] on the low carbon portion of the Fe-C phase diagram (Fig. 1.4) show that the critical temperature is in between 727° and 905°C. In this range, the alloy contains two phases during heat treatment, ferrite and austenite. Decarburization[102] therefore occurs by the process termed 'diffusion accompanied by a phase change'. For intermediate stages of decarburization, the carbon concentration profile in a flat plate is shown in Fig. 1.5. The carbon content increases linearly from zero at the surface to a value, C_B, at the two phase boundary. C_B is known from the phase diagram (Fig. 1.4). At the interface where $x = \xi$, the carbon content increases to Ci, the initial concentration in the alloy.

Smith[103] has derived an equation which describes the rate of movement of the boundary. With a rearrangement of terms, Smith's equation may be written as follows :

$$\frac{\xi}{t} = \frac{6\ Dc_B}{3C_i - 2C_B}$$

where D is the diffusion coefficient of carbon in α iron and t is the reaction time in seconds.

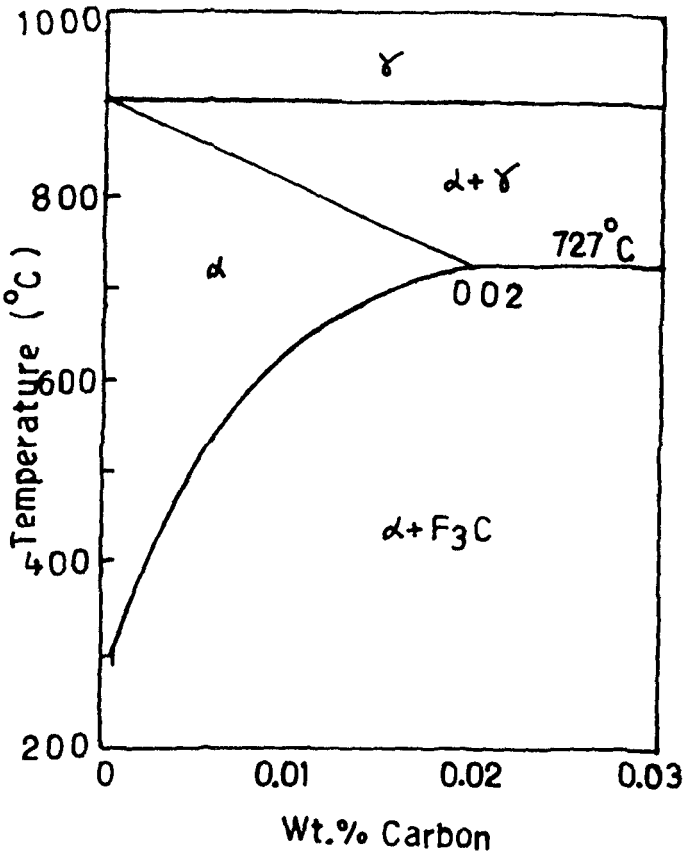

Fig. 1.4 Low temperature portion of iron side of Fe-C phase diagram[101].

The average concentration in the specimen, C,can be evaluated as a function of ξ by integrating under the carbon concentration profile in Fig. 1.5.

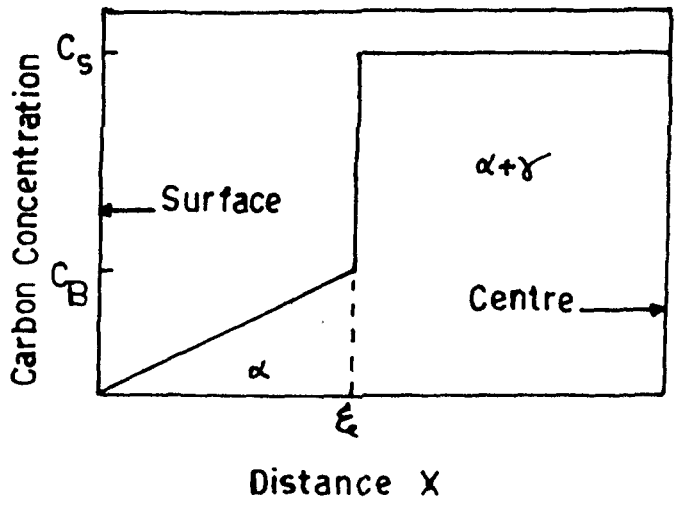

Fig. 1.5 Carbon concentration profile in a flat plate of low carbon steel after partial decarburization at temperatures between 727° and 905°C[102].

Wagner[104-105] derived mathematical equations for evaluating decarburized layer thickness in steel with respect to the number of phases present at the decarburization temperature. If decarburization of a steel involves two phases at the given temperature then the following three cases are possible (Fig. 1.6).

(i) A sample having a composition within the $\alpha+\gamma$ field and in the temperature range 723 to 910°C, is exposed to a decarburizing atmosphere so that only α-phase is stable at the surface;

(ii) A steel sample with a composition in the ($\gamma+Fe_3C$) field decarburized by an atmosphere in which austenite with a

definite carbon concentration is stable (especially 910°C); (iii) A steel with a composition (α+Fe_3C) below 723°C decarburized by an atmosphere in which only α-phase is stable.

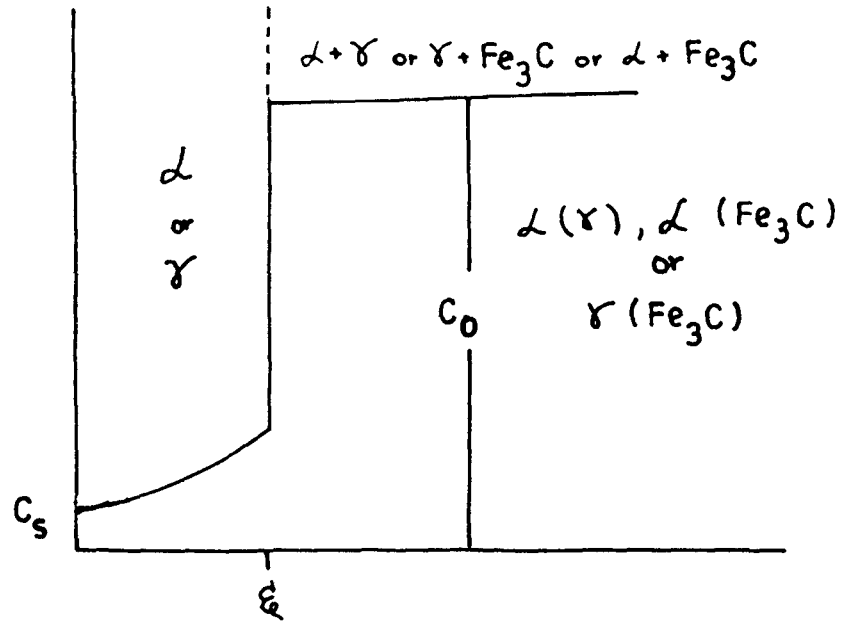

Fig. 1.6 Decarburization of steel[104].

At the distance x = ξ (depending upon time, t) the concentration of carbon in the surface reaches the limit of existence with the second phase present in the bulk alloy.

In deriving an equation for calculating the decarburization layer thickness, Wagner made the following assumptions: (i) the diffusion coefficient is independent of concentration, (ii) due to the high rate constants for phase boundary reactions

the partition equlibria are virtually established, and

(iii) heterogeneous region of the sample can be characterized by its average concentration. The equation is applicable only to dilute solutions particularly to Fe-C system and can be represented as

$$\frac{C_s - \overset{*}{C}}{\overset{*}{C} - C_o} = \sqrt{\pi}\, r\, e^{\gamma^2}.\mathrm{erf}\, \gamma \qquad (10)$$

where, $\overset{*}{C}$ is the equilibrium concentration of carbon between the surface, phase and the other phase in the bulk alloy. C_o and C_s are the initial and surface concentrations, respectively γ is the dimensionless parameter to be defined as

$$\xi = 2\sqrt{Dt} \qquad (11)$$

ξ is the decarburized layer thickness in time, t and D is the diffusion coefficient of carbon in the surface phase.

From equation (10) the unknown parameter, γ can be determined by plotting right hand member as a function of γ. The value of γ, for unknown value of left hand member can be read.

Wagner also derived an equation applicable to decarburization process involving an conversion of one phase into another phase. For example, between 723° and 910°C a sample containing γ-phase is decarburized so α phase is formed at the surface.

In a decarburizing atmosphere consisting of H_2 and H_2O flowing over with such a rate that no CO accumulates then the activity of carbon at the surface can safely be assumed as equal to zero.

The parameter γ can be determined by the relation

$$\frac{C_s - C^{\alpha(\gamma)}}{\pi^{1/2}\gamma\, e^{\gamma^2}\cdot \mathrm{erf}\gamma} = (C^{\alpha(\gamma)} - C^{\gamma(\alpha)}) + \frac{C^{\gamma(\alpha)} - C_o}{\sqrt{\pi}\gamma\cdot \psi^{1/2} e^{\gamma^2\psi}\, \mathrm{erfc}\gamma\psi^{1/2}} \quad (12)$$

where $\psi = D^{\alpha}/D^{\gamma}$ and ξ is defined by the equation (11).

Birks[106] considered decarburization with simultaneous scaling at temperature above 910°C when the steel remains austenitic throughout and decarburization model can be represented as given in Fig. 1.7.

Two simultaneous processes are in progress : the alloy surface is continually oxidized to form a scale while carbon is oxidized to form CO and CO_2, the scale is permeable to these gases which escape to the atmosphere. The carbon concentration profile in the metal varies from low surface concentration to the original carbon content within the metal.

At a time t, scaling has consumed a thickness X of metal. To calculate the depth of decarburization, Birks[106] applied Fick's Second Law to determine the distribution of carbon in the metal.

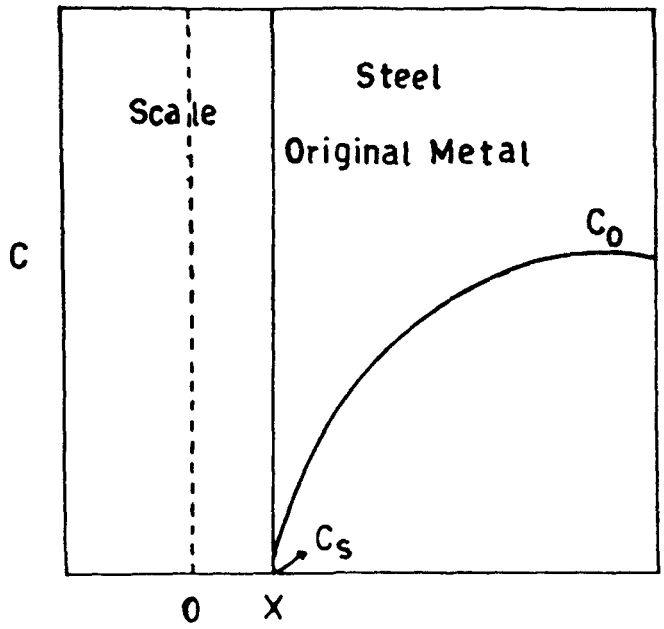

Fig. 1.7 Model for decarburization above 910°C[106].

$$\frac{dc}{dt} = D \frac{d^2c}{dx^2} \quad \text{for} \quad x > X \tag{13}$$

$$C = Co \text{ for } x > 0 \; ; \; t = o \tag{14}$$

$$C = Cs \quad \text{for } x = X \; ; \; t > o \tag{15}$$

Assuming that (i) decarburization does not extend to the centre of the specimen (ii) diffusion coefficient of carbon in austenite phase is independent of composition and (iii) enhanced diffusion down to grain boundaries is neglected, the solution of equation (13) at constant temperature reads :

$$\frac{C_o - C}{C_o - C_s} = \frac{\mathrm{erf}_c\left[\frac{x}{2\sqrt{2}}/DT\right]}{\mathrm{erf}_c\left[\frac{K_c}{2D}\right]^{1/2}} \qquad (16)$$

K_c is corrosion constant and defined as $K_c = X^2/2t$. Equation (16) gives the carbon content of the metal phase ($x > X$) as a function of time and position.

1.2.3 Decarburization Without Scaling

Grabke and Tuber[107] studied the decarburization kinetics of α and γ iron in H_2O-H_2 mixtures in the temperature range between 600 and 1000°C by resistance-relaxation measurements on 10 µm thick iron foils. The decarburization proceeds predominantly according to

$$[C] + \{H_2O\} = \{CO\} + [H_2] \qquad (17)$$

$$[C] + 2\{H_2\} = \{CH_4\} \qquad (18)$$

the reaction according to equation (18) can be neglected at $p_{H_2O}/p_{H_2} > 0.01$. The kinetics is governed by the supply and diffusion of H_2O in the gas phase or with low carbon concentrations and high gas velocities by the surface reaction. To establish the rate law of the reversible reaction :

$$\{CO\} + \{H_2\} \rightleftharpoons [C] + \{H_2O\} \qquad (19)$$

The rate then reads

$$\nu = K \frac{P_{CO}}{1+K_o P_{H_2O}/P_{H_2}} - K'' \frac{a_c K_o P_{H_2O}/P_{H_2}}{1+K_o P_{H_2O}/P_{H_2}} \qquad (20)$$

It shows that the elementary step $\{CO\} = [C] + O_{ad}$ is rate controlling, whereas the average with adsorbed oxygen is adjusted by the equilibrium $\{H_2O\} = \{H\} + O_{ad}$. The reaction (19) is very fast as compared with decarburization by CH_4-H_2 mixtures, the kinetics and the steady state carbon activity are mainly governed by the reaction (19).

Gosh[108] studied the kinetics of decarburization of Fe-C melts (4.0-0.2 % C) at temperatures 1545, 1600 and 1650°C under partial pressures of oxygen of 0.25 atm. and 1.0 atm. It was observed that the rate of decarburization was not effected by temperature at 1.0 atm. of oxygen at flow rates of 6.0 and 8.3 lit/min. However, the rate was found to increase with temperature at 0.25 atm. of oxygen. The effect of the amount of Fe-C alloy on decarburization rate was also investigated. He reported that the weight of melt does not appear to effect significantly the rate of carbon decrease at 0.25 atm. of oxygen. Further more, the amount of liquid steel affects the induction stirring of the melt but does not affect rate of carbon decrease. He also studied the kinetics of decarburization of liquid Fe-C metls (0.1 and 0.07 % C) at temperatures between 1550 and 1650°C, under a partial pressure of 0.25 atm. of oxygen. The flow rate was maintained at 8.3

lit/min. Increase of temperature appears to increase the rate of decarburization. The rate of decarburization was independent of partial pressure of oxygen and the flow rate of the oxidizing gas atmosphere. The rate of carbon decrease was found to increase as the size of the melt was reduced. On the basis of these observations, he concluded that the diffusion of carbon in the melt is the rate controlling step.

Grievson [109] studied the kinetics of decarburization of Fe-0.98 % C alloy at 1000°C in low oxygen potential atmospheres and pure hydrogen. The results of decarburization in pure hydrogen indicate that reaction follows a linear rate law until the carbon concentration in the specimen was reduced to about 0.5 %, below 0.5 % level the reaction rate was found to be dependent on carbon concentration.

With H_2O-H_2 mixtures, a rapid increase in reaction rate is observed so that reaction becomes diffusion controlled for water vapour partial pressure at 0.5 mm or above. Similar reaction rates were observed for various water vapour-hydrogen ratios until a water vapour pressure of about 20 mm. Above 200 mm of water vapour partial pressure, a reduction in reaction rate is observed and decarburization reaction becomes chemical reaction controlled. The authors suggested that the rate controlling mechanism involves the dissociation of an active complex $[H_2O]$, and oxygen absorption is important since surface active sites are available for absorption of water

vapour. After long reaction times, the decarburization rate ceases to be linear indicating the equivalence of the chemical reaction rate and diffusion control (at low carbon concentration).

Swisher[110] determined the optimum temperature for decarburizing low carbon steels in wet hydrogen for alloys containing about 0.1 % C. He found 813°C to be ideally suited for maximum decarburization.

Recently Hajduga and Kucera[111] studied the heating effect of steels containing 12.77-13.22 % Cr and 0.15-1.63 % C in a flowing atmosphere of O-N-He at 1100°C for 3 hrs the steels containing 0.08-12.77 % Cr and 0.1-1.63 % C were oxidized in ambient air at temperatures of 900, 1000, and 1200°C and reported the following :

(1) the surface layers are carbon depleted (2) decarburization occurs in all the steels independent of Cr and C content (3) lowering of the carbon concentration results in grain growth (4) the higher oxidation temperature leads to a higher degree of decarburization for the same heating time (5) longer heating times result in higher decarburization at the same temperature and (6) decarburization in ambient air occurs about one order of magnitude more intensively than in the flowing atmosphere.

1.2.4 Decarburization with Simultaneous Scaling

Trenkler et al.[112] studied the decarburization

behaviour of Fe-C and Fe-C-X alloys with simultaneous scaling of the metal surface in the temperature range of 900-1200°C using flue gas (15 % CO_2 + 10 % H_2O + N_2). The alloying element was either a carbide former e.g., Cr, W, V and Mo or Si and Ni which increases the activity of carbon in the γ-phase. For plain iron carbon alloys, the depth of decarburized layer increases with time and temperature at corresponding carbon contents. Increasing the alloy carbon content, otherwise under similar conditions, produces only a limited increase in the total decarburized depth, but a large increase in the apparent decarburization under comparable conditions, the thickness of the oxidized metal decreases with carbon content, whilst the decarburization depth increases, from which it follows that decarburization and oxidation follow different rate laws.

It can be assumed that the carbon exchange at the metal/gas, and in particular at metal/scale interface has a large influence on the carbon loss. Initially, the carbon present over the entire sample surface can be lost without any diffusion, and the decarburization proceeds rapidly. As oxidation commences, the area available for carbon loss decreases, and more carbon is transported to the interface by surface and volume diffusion than can be oxidized. As oxidation proceeds and the scale increases in thickness, release of the gaseous reaction product and ingress of oxidizing gases through the

scale are certainly hindered.

The addition of alloying element Cr, V, Mo and W does not show any significant effect on the rate of decarburization when compared with corresponding Fe-C alloys. Si and Ni additions increase the carbon activity in γ-phase, and thus only γ-phase is found in the decarburized state. With low silicon additions (upto 0.4 %) the apparent decarburization is only trivially greater than with pure Fe-C alloys and the Si content remains unaltered in the decarburized zone. With higher silicon contents, a definite silicon enrichment at the surface was observed and with a high silicon contents (4.2 % Si), a significantly more rapid increase of surface carbon is noticed in comparison with corresponding iron-carbon alloys resulting in a greater decarburization ratio if compared with corresponding Fe-C alloy; exceptional behaviour may be expected only in those cases where abnormal change in scaling rate takes place.

1.2.5 Effect of Alloying Elements

The addition of alloying elements can effect the decarburization by influencing (i) ferrite-austenite transformation temperature (ii) the activity of carbon in solution (iii) the diffusion coefficient of C in solution and (iv) the scaling characteristic of iron. Birks[106] considered the following general cases :

(a) If the alloying element is nobler than iron, e.g., Ni, Cu, Sn, etc., the distribution of the element in the matrix is not expected to be changed due to the absence of scale.

(b) When the alloying element is less noble than iron, then possibility of internal oxidation arises and an external oxide scale may also be formed under circumstances which are normally protective to iron. If either type of oxide formation occurs, the concentration of alloying element is reduced at the metal surface, and so the effect on decarburization behaviour will be reduced. If the scaling rate (due to formation of external scale) is increased, then in absence of other factors, the observed depth of decarburization will be reduced.

(c) When alloying element is a carbide former then the decarburization mechanism also involves the dissolution of carbide particles in the matrix. The decarburization might be accelerated if oxidation of alloying element occurs, since then both this element and carbon are continually being removed from solution in the matrix.

The effect of some common alloying elements are as follows :

Nickel : It concentrates at the scale/metal interface and, though the scaling rate may not be greatly affected, the solubility of carbon in the surface layers may be reduced thus restricting carbon diffusion outwards and reducing the depth of decarburization.

Silicon : This element concentrates in the scale and forms $FeO.SiO_2$, fayalite which reduces the scaling rate. This should lead to deeper observed decarburization. Si also increases the activity of carbon and therefore increases the tendency of carbon to diffuse out to the scale/metal interface. Thus the general effect of Si is to increase decarburization.

Chromium : In general, the presence of chromium reduces the scaling rate. The formation of stable carbide $(Fe,Cr)_7C_3$ introduces the possibility of a slow carbide decomposition step into the mechanism. At decomposition temperatures, due to almost complete solubility of carbides in the matrix the activity of carbon will be reduced resulting in the reduction of the diffusion rate to the surface. Therefore, there are two conflicting factors. The lower scaling rate would tend to increase the observed decarburization whereas reduction of carbon activity would tend to lower it. The latter factor may perhaps be expected to predominant and reduce decarburization.

1.3 Statement of the Problem

The work described in this thesis includes the following studies.

(i) Oxidation kinetic measurements for decarburized and undecarburized

(a) Fe-C (C is 0.1, 0.8 and 1.2 wt. %),

(b) Fe-10MC (MC is TiC, VC, Cr_7C_3, NbC, TaC, MoC, WC or Fe_3C 10 wt. %),

(c) Fe-10MC-0.1C-20Cr (MC is TiC, NbC, Cr_7C_3 or WC 10 wt. %),

(d) Fe-10MC-0.1C-1.0RE_2O_3 (MC is NbC, Cr_7C_3 or WC 10 wt. % and RE_2O_3 is La_2O_3, Pr_2O_3 or Y_2O_3 1.0 wt. %),

(e) Fe-10MC-0.1C-1.0MO_2 (MC is NbC, Cr_7C_3 or WC 10 wt. % and M is Zr or Ti 1.0 wt. %) alloys.

(f) and some low alloy steels as EN-9, EN-24, E-31, EN-36, silver steel, die-steel and high speed steels (18 and 6 wt. %) in 1 atmospheric oxygen.

(ii) The decarburization studies of above mentioned alloys in H_2-H_2O at 900°C for 2-6 hrs.

(iii) The oxidation kinetic studies of the decarburized alloys at 900°C for 6-12 hrs. in 1 atmospheric oxygen.

(iv) Morphological studies of the oxidized/decarburized/ decarburized-oxidized alloys. The studies have been carried out by applying the techniques of Optical and Scanning Electron Microscopy.

(v) The identification of the different constituents is dtermined by X-ray diffraction analysis.

CHAPTER II

MATERIALS AND METHODS

The studies described in this thesis are concerned with the effect of transition metal carbide(s) dispersions on the oxidation and decarburization behaviour of iron-base alloys.

Five different types of alloys were prepared :

i) Plain carbon steels,
ii) Iron base alloys containing carbide,
iii) Iron-base alloys containing carbide, carbon and rare earth oxides,
iv) Iron-base alloys containing carbon, chromium and carbide, and
v) Some commercial ferritic, and low alloy steels.

2.1 Materials

The transition metal carbide powders were CERAC, USA products, their specific and spectrographic analysis data are given in tables 2.1 and 2.2, respectively. The transition metal oxides of 99.9 % purity were obtained from LEICO industries, New York and Central Drug House (CDH) India. The high purity iron and iron-carbon powders ASC 100.29 were the gifts from M/S Sintermetallwerk, GmbH, Krebsöge, FRG and M/S Högnäs, Sweden. The iron powder ASC 100.29 contains 0.01 % C.

Table 2.1

Specific analysis and property of the metal carbides

Carbide	% purity	Mesh size	Crystal structure	Average particle size (microns)	% carbon (Theo.)	% carbon (found)
TiC	99.5	325	Cubic	1.55	20.05	19.34
VC	99.5	325	Cubic	5.59	19.08	17.32
Cr_7C_3	99.5	325	Hexagonal	-	9.01	8.79
NbC	99.5	325	Cubic	-	11.45	11.00
TaC	99.5	325	Cubic	1.57	6.22	6.20
MoC	99.0	325	Orthorhombic	-	11.06	11.13
WC	99.5	Less than 1 micron	Hexagonal	0.73	6.13	6.13
Fe_3C	99.5	325	Orthorhombic	-	6.69	6.78

Table 2.2

Spectrographic Analysis of the metal carbides in wt. %

Elements	TiC	VC	Cr_7C_3	NbC	TaC	MoC	WC	Fe_3C
Ag	-	-	-	0.001	-	-	-	-
Al	0.03	0.10	0.05	0.01-0.10	0.001	0.01	-	-
B	-	-	-	-	-	<0.001	-	-
Ca	0.02	-	0.001	0.01-0.10	0.01	0.01	-	0.001
Co	-	-	-	-	-	0.08	0.01	-
Cr	-	0.05	-	0.001	-	0.05	0.002	0.001
Cu	0.001	0.001	-	0.01	0.01	<0.001	-	0.001
Fe	0.10	0.15	0.001	0.01-0.10	0.001	0.01	0.01	-
In	-	-	0.001	-	-	-	-	-
Mg	0.05	0.001	0.01	0.01	0.001	<0.001	-	<0.001
Mn	0.001	0.001	0.05	0.01	0.001	<0.001	-	-
Mo	-	-	0.005	-	-	-	0.01	-
Ni	0.03	<0.001	0.001	-	-	0.01	0.002	0.001
Si	0.10	0.10	0.001	0.01-0.10	<0.001	0.01	-	0.01
Ti	-	0.01	0.001	-	0.01	0.001	-	-
Zr	-	0.05	-	-	-	-	-	-
Ta	-	-	-	0.05	-	-	-	-

Commercially available ferritic steels, low and high alloy steels and special purpose steels were obtained from various sources and were used for the oxidation, decarburization and decarburization-oxidation studies. The nominal composition of the steels is given in table 2.3.

Table 2.3

Composition of the low alloyed steels in wt. %

Alloy	Ni	Cr	C	Mo	W	V
HSS 18% W	-	4	0.75	-	18	1
HSS 6% W	-	4	0.80	5	6	2
EN-24	1.5	5	0.45	-	-	-
Silver Steel	-	1	1.00	0.1	-	-
EN-31	-	1	1.00	-	-	-
EN-36	3	1	0.18	-	-	-
Die-Steel	-	12	2.00	-	-	-
EN-9	-	-	0.45	-	-	-

2.2 Alloy Preparation

2.2.1 Plain Fe-C Alloys

Model Fe-C alloys (C is 0.1, 0.8 and 1.2 weight %) were prepared by melting in a high frequency induction furnace under a vacuum of 10^{-4} to 10^{-5} torr followed by casting into rectangular cross sectional moulds (Courtesy : University

of Liverpool, England). The electrolytic iron used had the following analysis : C < 0.01, Si < 0.02, P < 0.05, S < 0.007, B < 0.004, Cu < 0.01 weight %. The nominal composition of the alloys is given in table 2.4.

2.2.2 Carbide Dispersed Alloys

Transition metal carbide dispersed iron-base alloys were consist of (i) Fe-10 wt. % MC where MC : TiC, VC, NbC, TaC, Cr_7C_3, MoC, WC or Fe_3C (ii) Fe-10MC-0.1C-20Cr where MC:TiC, NbC, Cr_7C_3 or WC (iii) Fe-10MC-0.1C-1.0RE_2O_3 where MC:NbC, Cr_7C_3 or WC, RE_2O_3:La_2O_3, Pr_2O_3 or Y_2O_3 and (iv) Fe-10MC-0.1C-1.0$M\dot{O}_2$ where MC:NbC, Cr_7C_3 or WC, $M\dot{O}_2$:TiO_2 or ZrO_2. The alloys were synthesised by the combination compacting and sintering techniques. The nominal compositions of the alloys is given in table 2.4.

As a typical example, the tablets of Fe-10MC alloys of diameter 1.4 cm were prepared by intimately mixing the calculated amounts of iron and metal carbide powders in an agate mortar. The total amount of the mixture used for each tablet was about 2.0 gm. The mixture was put in a steel die and was compacted at 13 tons./cm^2 with a hydraulic press. The tablets were sintered in a quartz tube placed in a tubular furnace under H_2(g) atmosphere at 1200°C for 2 hrs., and subsequently annealed in a N_2(g) atmosphere at 1000°C for about 1.5 hrs. (Fig. 2.1).

Alloys of the general compositions : Fe-10MC-0.1C-

Table 2.4

Composition of the alloys fabricated

Serial Number	Iron wt. %	Carbon wt. %	Carbide 10 wt. %	Rare Earth 1.0 wt.%	Other wt. %
1	Balance	0.1,0.8,1.2	-	-	-
2	Balance	-	TiC,VC,NbC,TaC Cr_7C_3,MoC,WC,Fe_3C	-	-
3	Balance	0.1	TiC,NbC,Cr_7C_3,WC	-	20Cr
4	Balance	0.1	NbC	La_2O_3,Pr_2O_3,TiO_2, Y_2O_3,ZrO_2	-
5	Balance	0.1	Cr_7C_3	La_2O_3,Pr_2O_3,TiO_2, Y_2O_3,ZrO_2	-
6	Balance	0.1	WC	La_2O_3,Pr_2O_3,TiO_2, Y_2O_3,ZrO_2	-

1.0RE_2O_3/MO_2 and Fe-10MC-0.1C-20Cr were prepared by a similar procedure.

2.3 Specimen Preparation

Steel specimens of 15 x 15 x 1.5 mm size or 12.0 mm diameter and 1.5 mm thickness were cut from steel sheets or steel rods. A 0.4 mm suspension hole was drilled near the middle of one end of the specimen. The specimens were sealed in a quartz tube and annealed at 900°C for 4 hrs. The annealed specimens were then polished sequentially with 180, 320 and 600 grade SiC papers. The specimens were washed with water and alcohol and degreased with CCl_4.

The sintered alloys do not require any surface preparation and were used as such for decarburization and oxidation experiments.

2.4 Gases Used

High purity (99.9 %) hydrogen, argon, nitrogen and oxygen gases were used for sintering, decarburization and oxidation experiments.

2.5 Apparatus

A laboratory fabricated helical thermal balance attached with a cathetometer was used for decarburization and oxidation experiments (Fig. 2.2), the specimen was suspended to a quartz helix in the reaction tube. A Sartorius Elec-

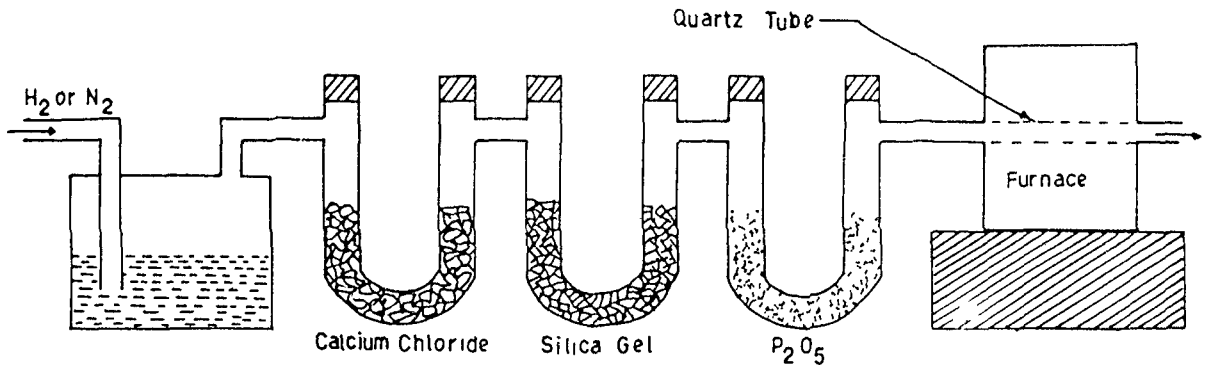

Fig. 2.1 Schematic diagram showing the set-up used for sintering

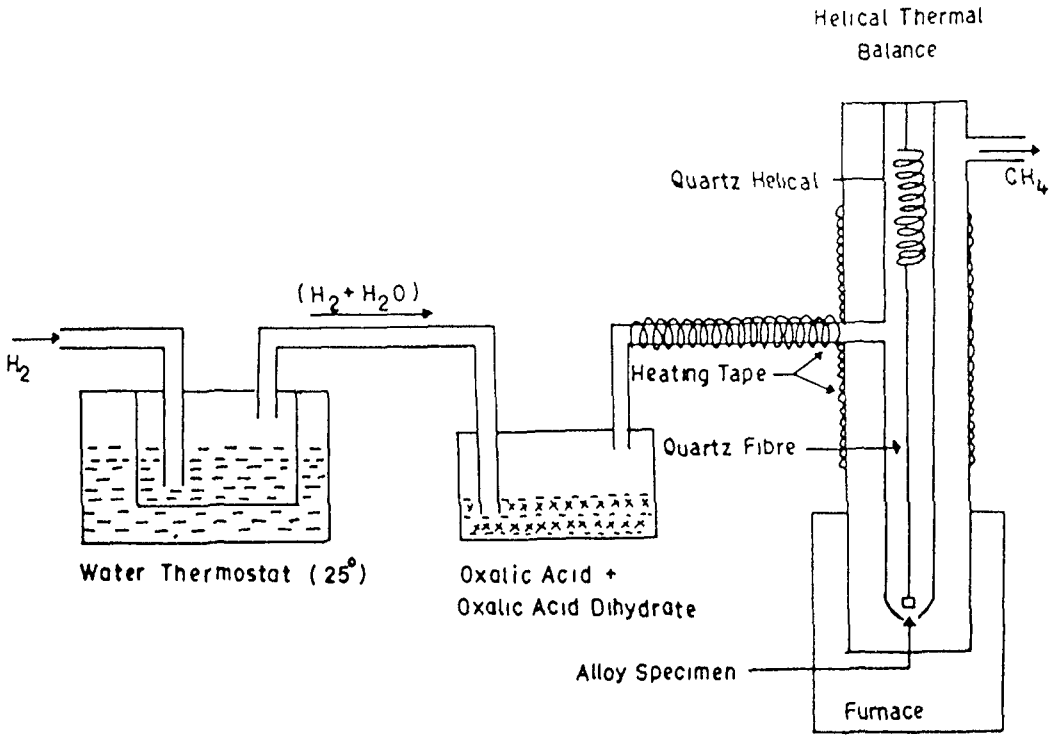

Fig. 2.2 Schematic diagram showing the apparatus used for oxidation and decarburization experiments

tronic Microbalance Model 4410-MP8 with a sensitivity of 1 μg attached with a pen ink recorder was used for oxidation kinetic measurements (Fig. 2.3). The specimen was suspended to the right pan of the balance through a quartz fibre, with a platinum loop at the end. After the balance has been poised, the hot furnace (set at desired temperature) was raised around the sample and the oxidation or decarburization commenced.

2.5.1 Decarburization Experiments

Hydrogen gas saturated with water was used for decarburization experiments. By passing $H_2(g)$ (flow rate : 100 ml/min.) through a mixture of oxalic acid/oxalic acid dehydrate at 25°C, a ratio of $P_{H_2O}/p_{H_2} = 4 \times 10^{-3}$ is obtained in the flowing gas which corresponds to $P_{O_2} \sim 10^{-19}$ atm. at 900°C[113]. Pure Argon was used for flushing the apparatus before and after the decarburization run. Fig. 2.2 and 2.3 represents a schematic diagram of the apparatus used during decarburization experiments.

2.5.2 Oxidation Experiments

The oxidation kinetic experiments were carried out at 900°C in 1 atm. pure and dried oxygen in the same reaction tube as described for decarburization experiments.

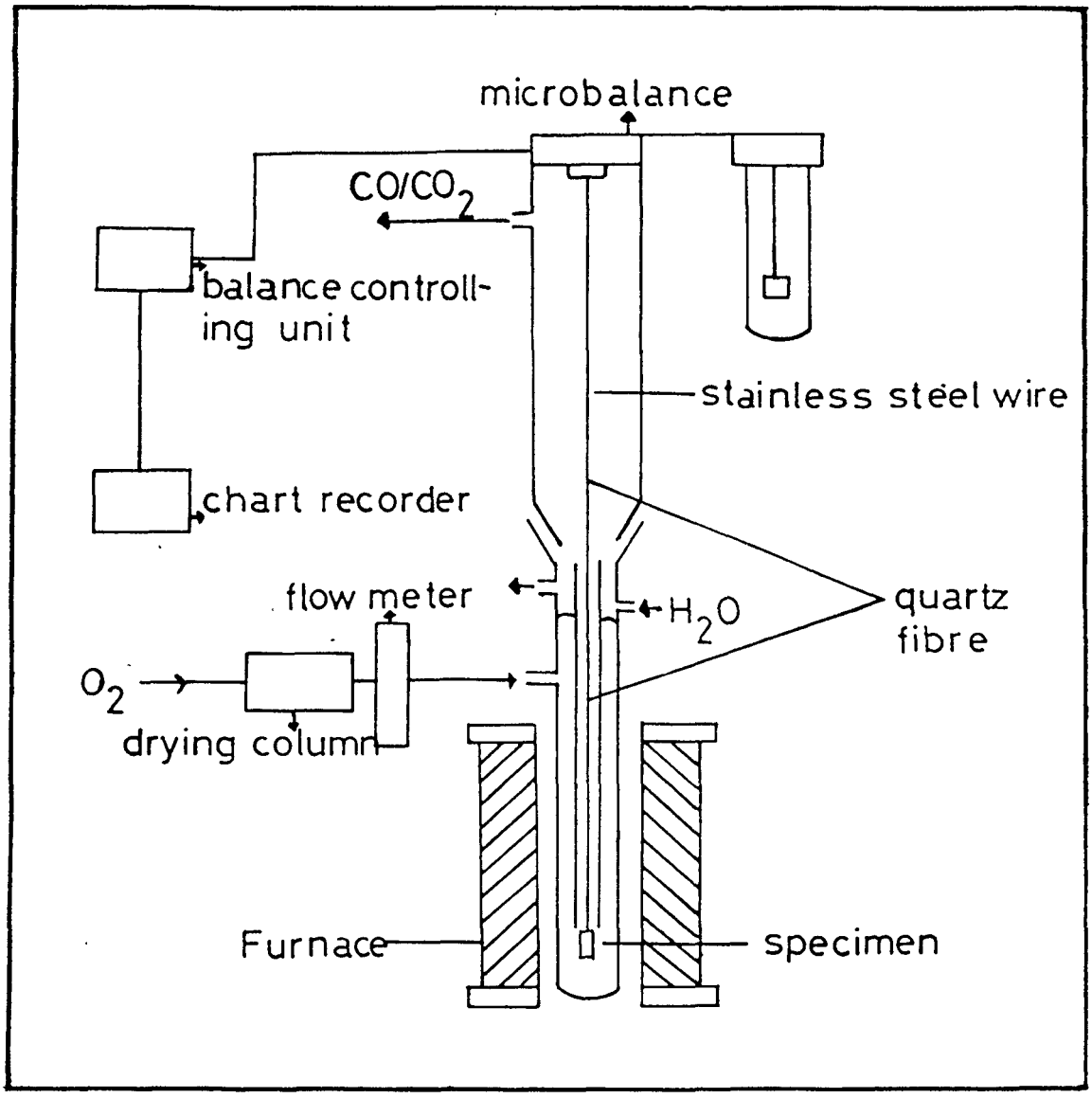

Fig. 2.3 Schematic diagram of the apparatus used for oxidation kinetic measurements.

2.6 Metallographic Studies

Metallographic studies were carried out using a Lietz Metallux 2 photometallurgical microscope. The specimens for metallographic studies were mounted in moulds using Araldite as a cold setting resin. The specimens were gritted sequentially on 180-360, and 800 SiC papers followed by polishing on varying grades of diamond pastes. Kerosene oil was used as a lapping liquid.

2.7 Scanning Electron Microscopic Studies

Polished specimens were coated with gold film of ~ 500 A^{o} thickness using a Edwards sputter coater, and were examined under a JEOL JSM-35C and PHILIPS PSEM 5000 Scanning Electron Microscope. The desired regions of the scales and the substrate were photographed at an appropriate magnification.

2.8 X-ray Diffraction Analysis

The presence of different constituents in the matrix and/or scales was identified by conventional X-ray diffraction analysis. The X-ray diffractograms were obtained by a X-ray diffractometer, using CuKα, CoKα or FeKα radiations with an appropriate filter.

CHAPTER III

DECARBURIZATION AND OXIDATION OF Fe-C ALLOYS

The experimental details have already been referred in Chapter II.

3.1 RESULTS

3.1.1 Oxidation Kinetics

The oxidation kinetic measurements were carried out at four different temperatures i.e. 700, 800, 900, 1000°C in 1 atm. O_2 for 24 hrs.

The weight gain vs time plots for the oxidation of plain carbon steels at 700, 800, 900 and 1000°C in O_2 (1 atm.) are shown in Figure 3.1. The steels oxidized at a much slower rate than pure iron. The weight gain^2 vs time plots are shown in figure 3.2. The weight gain vs time plots are parabolic and weight gain^2 vs time plots are linear indicating the growth of oxide scales by a diffusion controlled mechanism. The values of parabolic rate constant Kp for the oxidation of Fe-C alloys at different temperatures are given in table 3.1.

3.1.2 Oxidation Kinetics of Decarburized Alloys

The decarburization studies of Fe-C alloys was carried out in $H_2(g)$ saturated with water flowing at a rate of 100 ml/min. through a mixture of oxalic acid/oxalic acid dehydrate for 2-3 hrs. in the same apparatus used for oxidation studies.

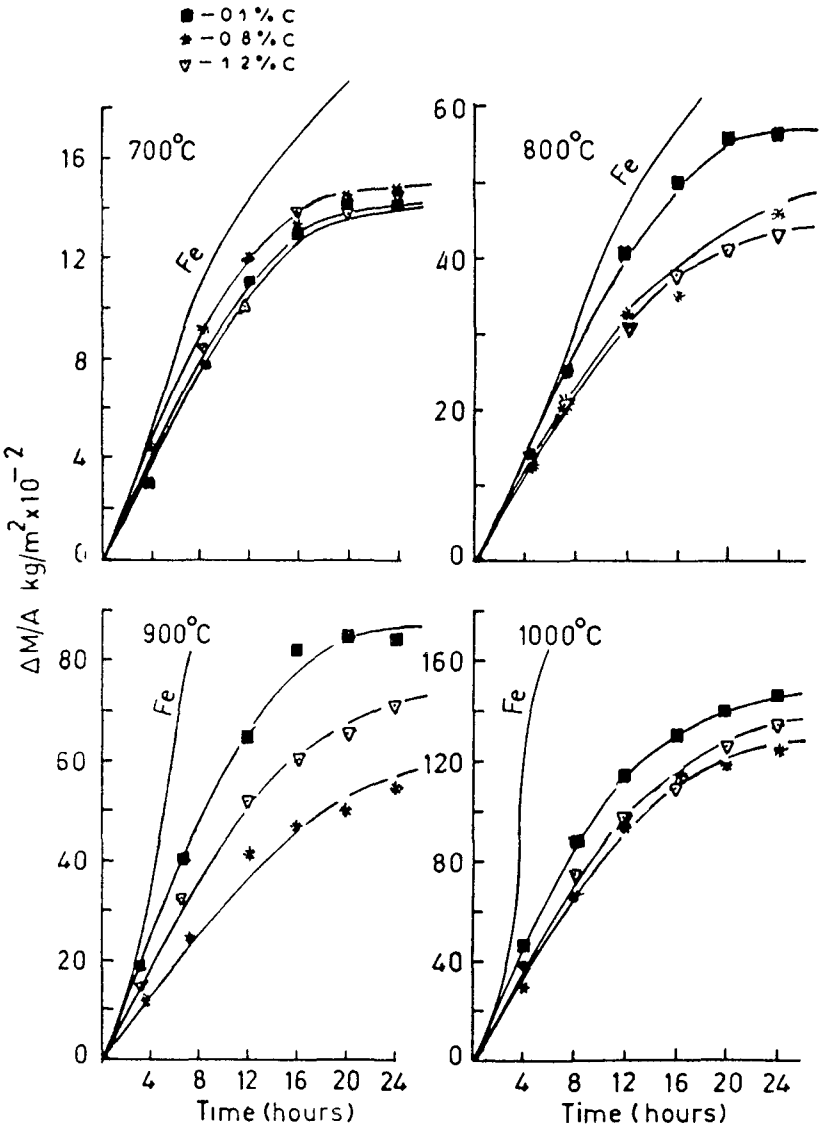

Fig. 3.1 Plots of weight gain Vs time for the oxidation of Fe-C alloys

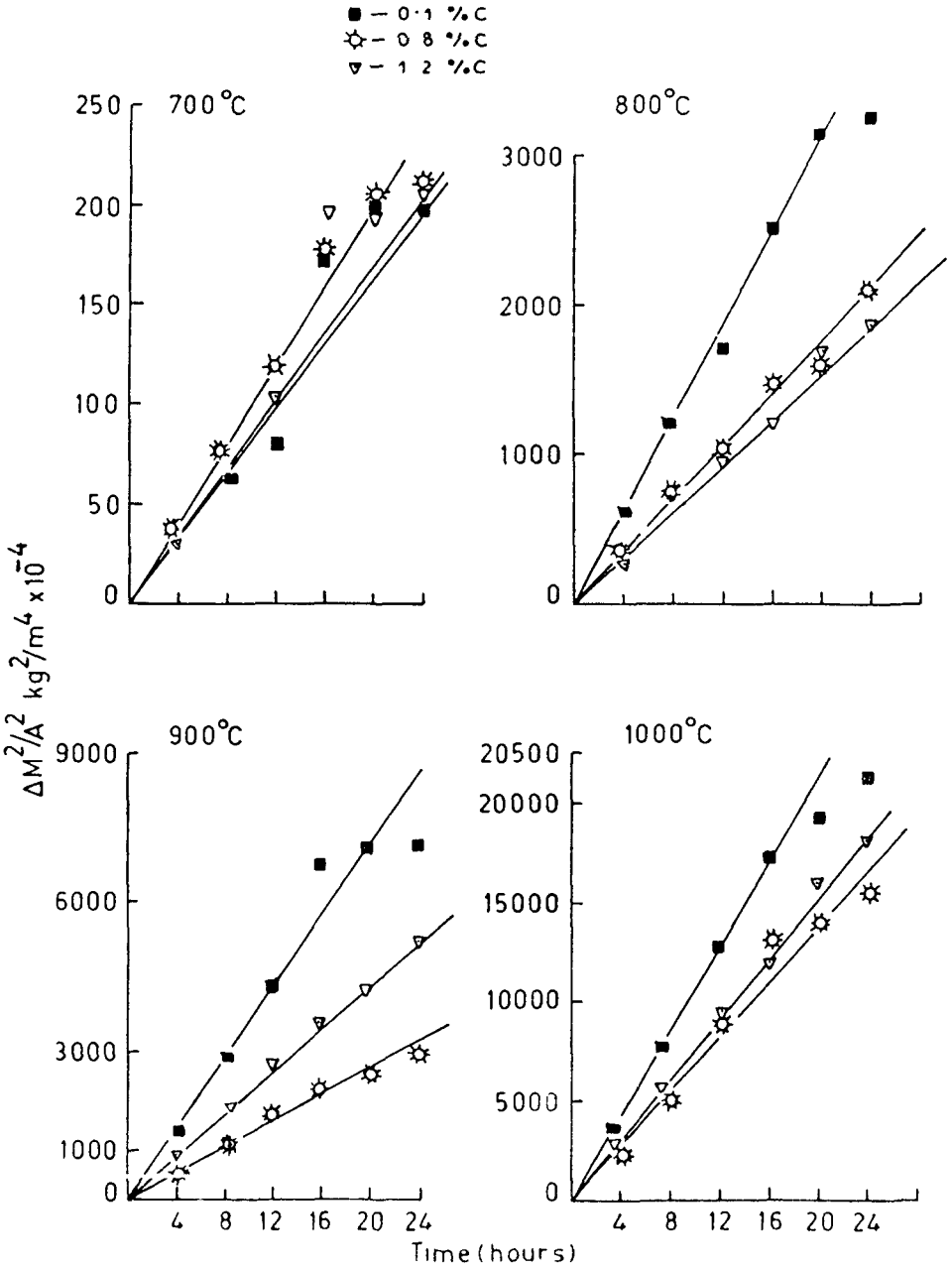

Fig. 3.2 Plots of weight gain^2 Vs time for the oxidation of Fe-C alloys.

Table 3.1

Parabolic rate constants for the oxidation of Fe-C alloys at 900°C in $Kg^2.m^{-4}.Sec^{-1} \times 10^{-6}$.

Alloy	700°C	800°C	900°C	1000°C
Fe-0.1C	0.22	4.44	9.95	30.38
Fe-0.8C	0.27	2.43	3.47	18.92
Fe-1.2C	0.23	2.08	5.56	20.66

Table 3.2

Parabolic rate constants for the oxidation of predecarburized Fe-C alloys at 900°C in $Kg^2.M^{-4}.Sec^{-1} \times 10^{-6}$.

Alloy	Undecarburized	Predecarburized
Fe-0.1C	9.95	53.47
Fe-0.8C	3.47	5.69
Fe-1.2C	5.56	1.56

The oxidation kinetic of decarburized alloys was carried out at 900°C in O_2 (1 atm.) for 6 hrs using the same apparatus as that used for previous oxidation/decarburization studies. In most cases, the decarburized alloys are oxidized by a diffusion controlled mechanism as indicated by the parabolic nature of weight gain vs time plots (Fig. 3.3-3.5) and linear nature of weight gain^2 vs time plot (Fig. 3.6). The values of parabolic rate constant, K_p for the oxidation of decarburized alloys at 900°C in 1 atm. O_2 are given in table 3.2.

3.1.3 Metallographic Studies

The oxidized, decarburized and decarburized-oxidized specimens were mounted, using Araldite as a cold setting resin. The mounted specimens were hand abraded on 180-, 380- and 600 grade silicon carbide papers and were polished sequentially with 40 μ, 8 μ, 6 μ and 1 μ grade diamond pastes using refined mobile oil as a lapping liquid. Metallographic examination of polished cross-section of the specimens were carried out using a Lietz Metallux-2 photometallurgical microscope. Figures 3.7-3.12 present some typical optical and scanning electron photomicrographs of Fe-C alloys oxidized in O_2 (1 atm.) at 4 different temperatures. The morphological features of the scales on plain carbon steels are similar irrespective of the carbon content. The scales are separated from the alloys substrate due to decarburization during oxida-

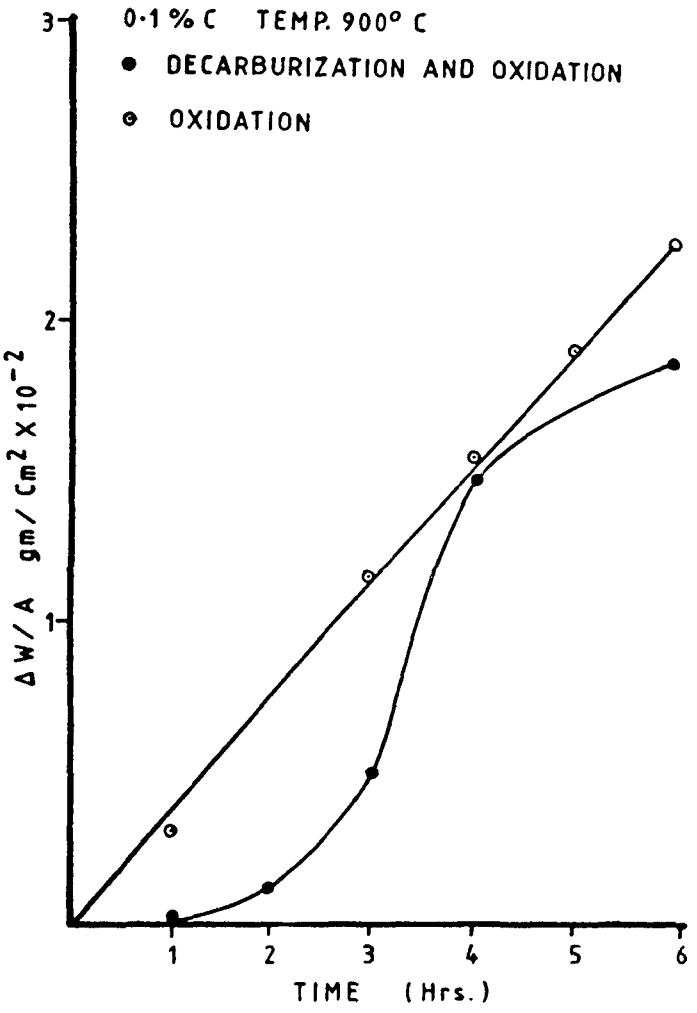

Fig. 3.3 Plots of weight gain Vs time for the oxidation of predecarburized Fe-0.1C alloy at 900°C.

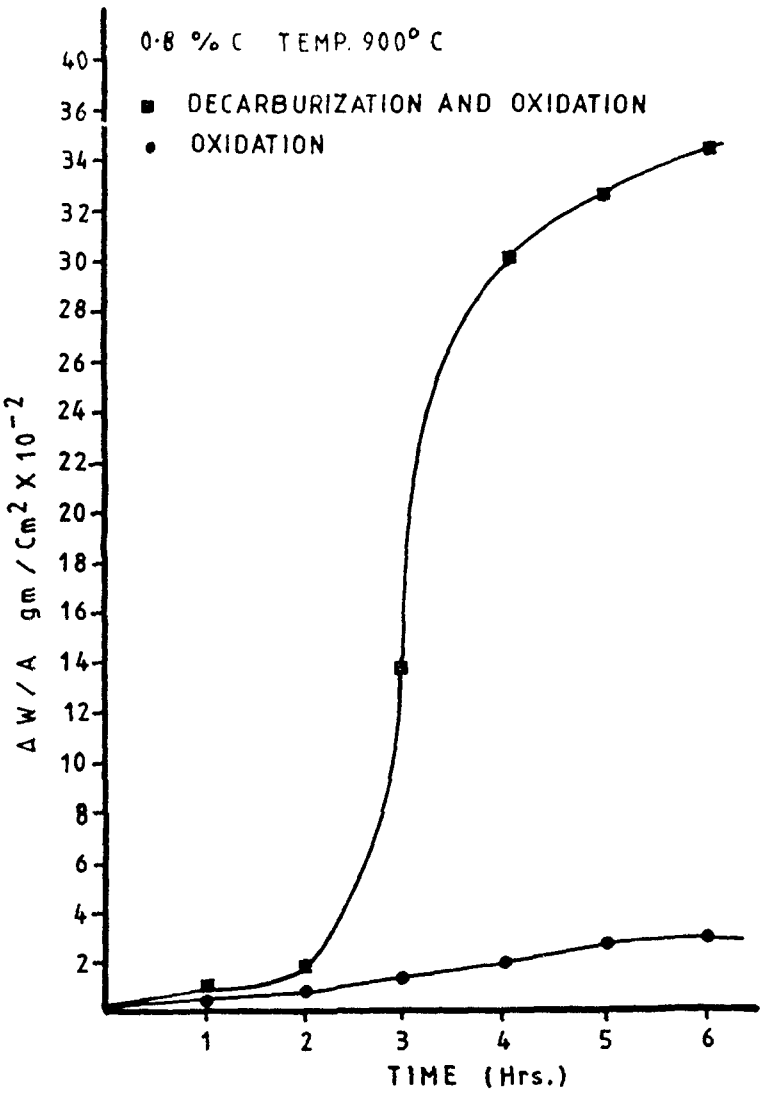

Fig. 3.4 Plots of weight gain Vs time for the oxidation of predecarburized Fe-0.8C alloy at 900°C.

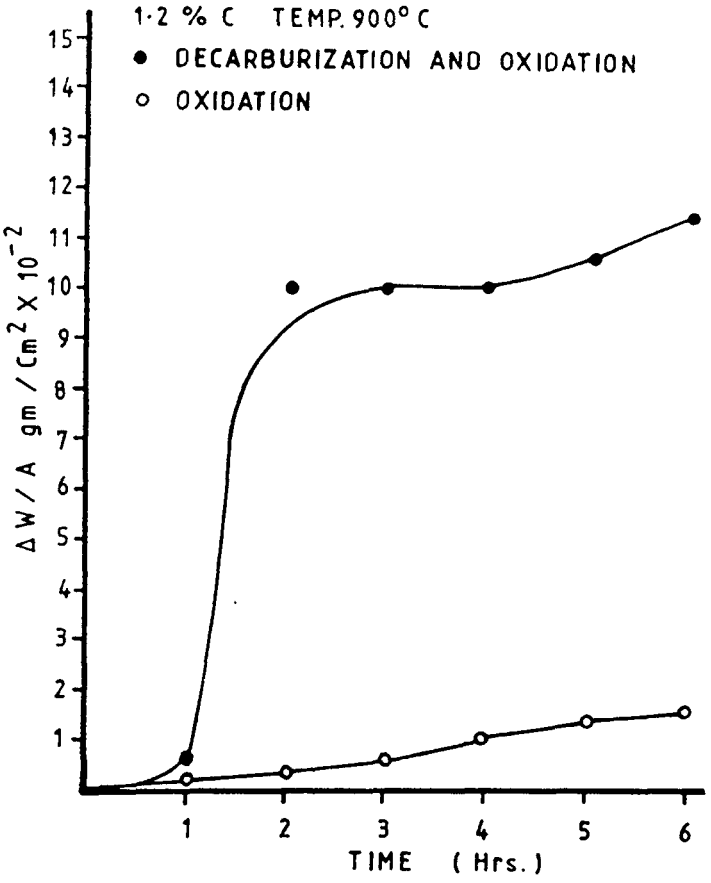

Fig. 3.5 Plot of weight gain Vs time for the oxidation of predecarburized Fe-1.2C alloy at 900°C.

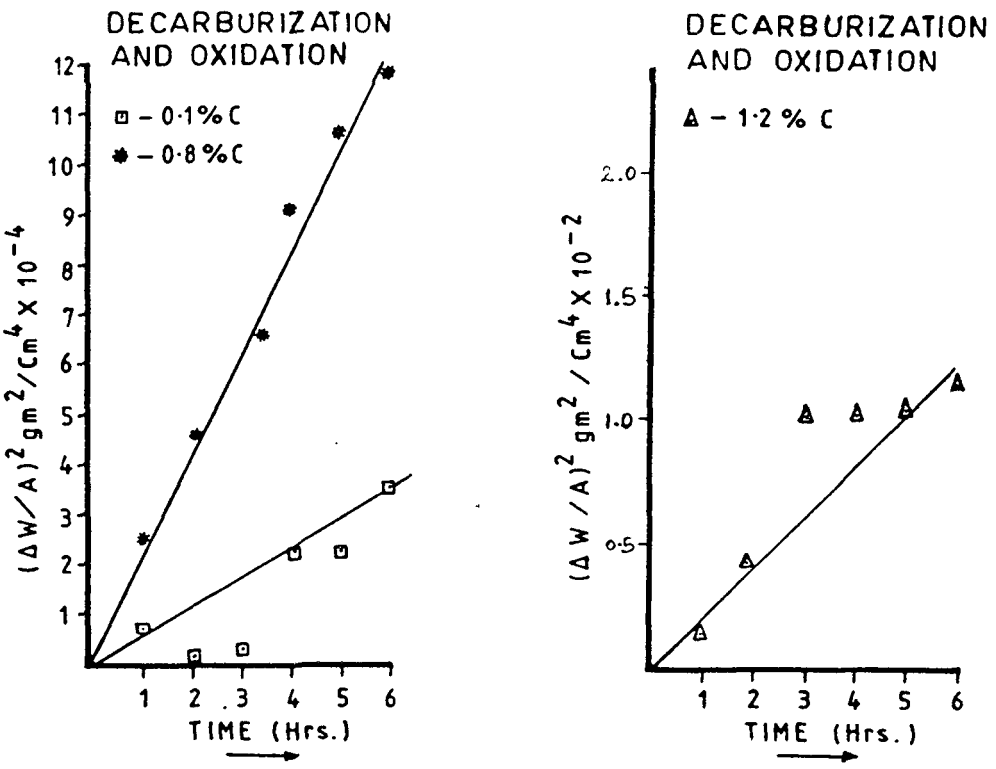

Fig. 3.6 Plots of weight gain^2 Vs time for the oxidation of predecarburized Fe-C alloys at 900°C.

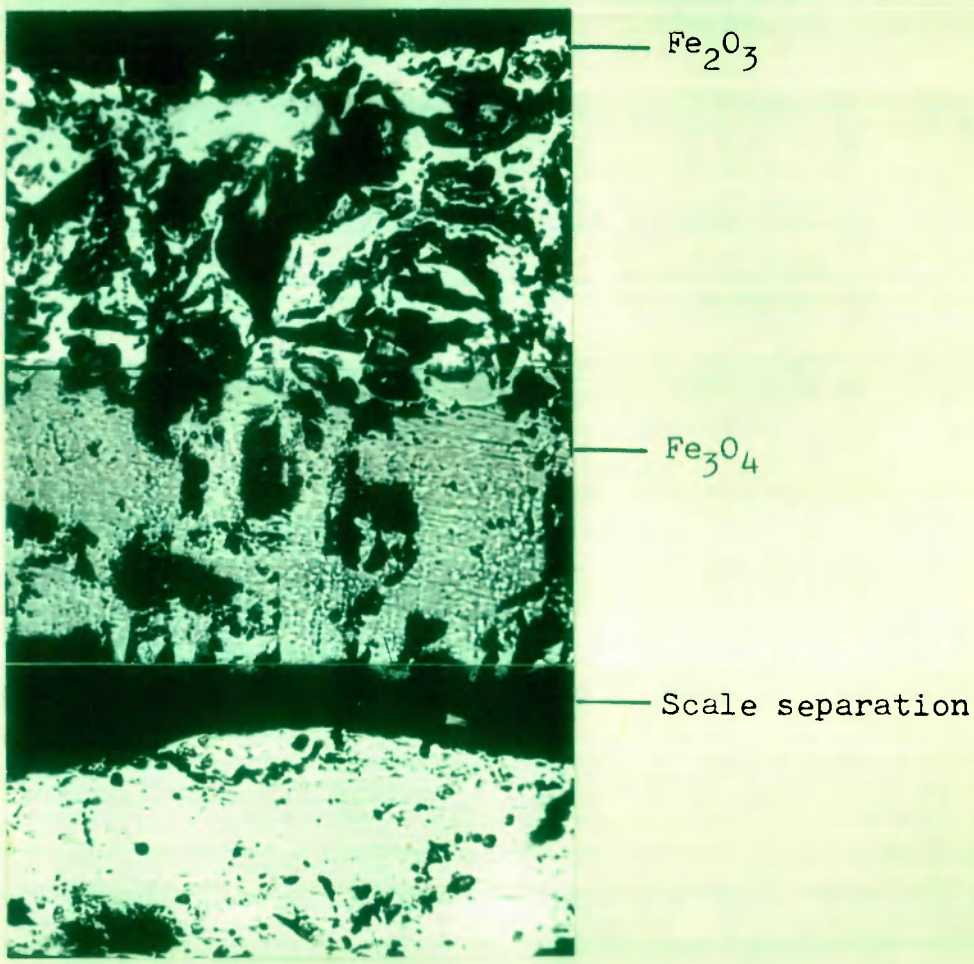

Fig. 3.7 Photomicrograph of cross-section of Fe-0.1C alloy, oxidized at 800°C for 24 hrs. X 100

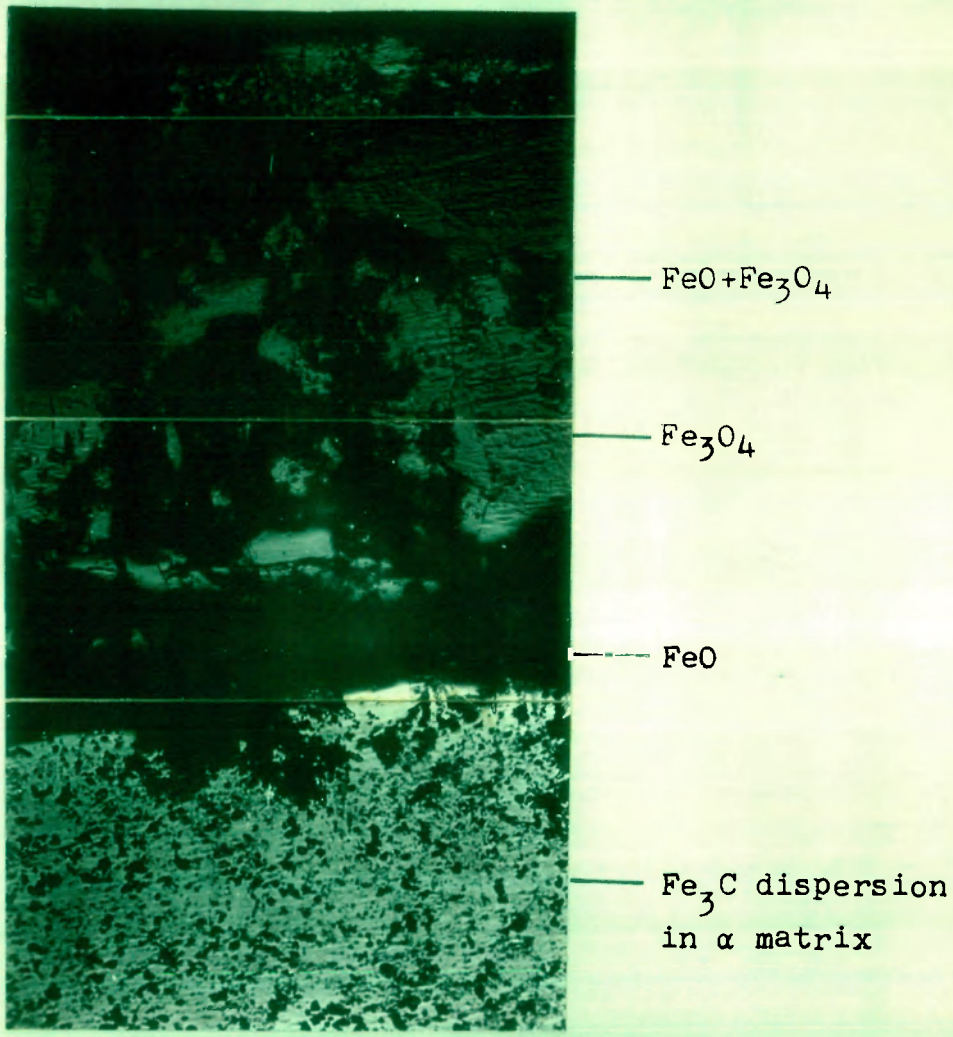

Fig. 3.8 Photomicrograph of cross-section of Fe-0.8C alloy, oxidized at 800°C for 24 hrs. X 100

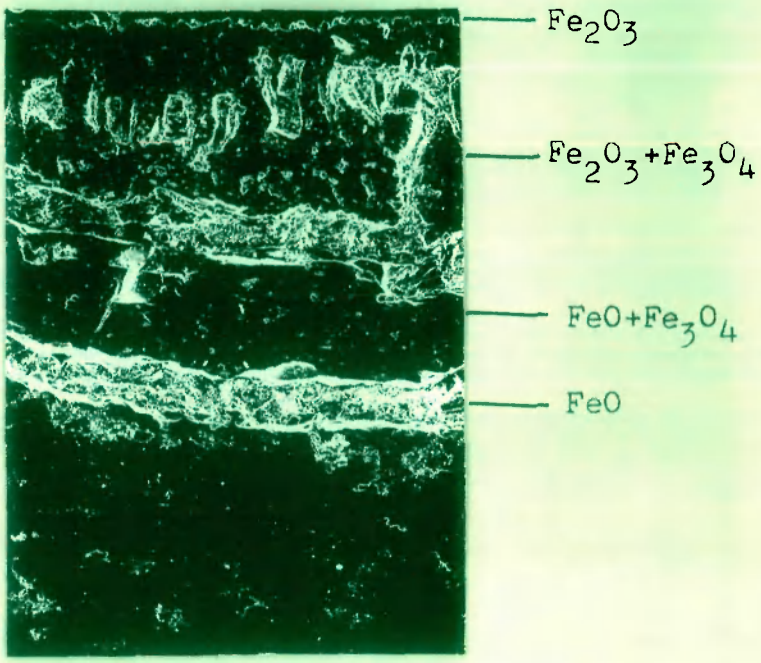

Fig. 3.9 SEM picture of Fe-0.1C alloy, oxidized at 900°C for 24 hrs. X 60

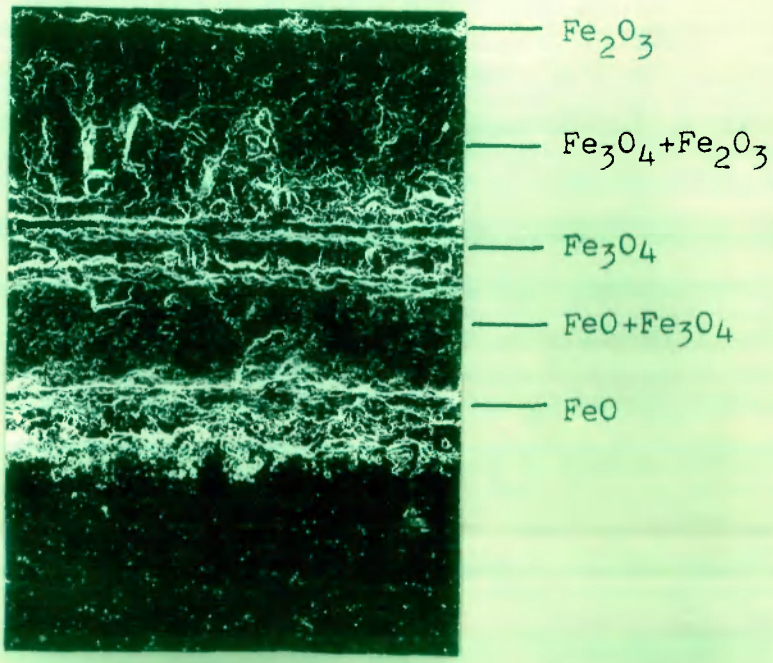

Fig. 3.10 SEM picture of Fe-0.8C alloy, oxidized at 900°C for 24 hrs. X 75

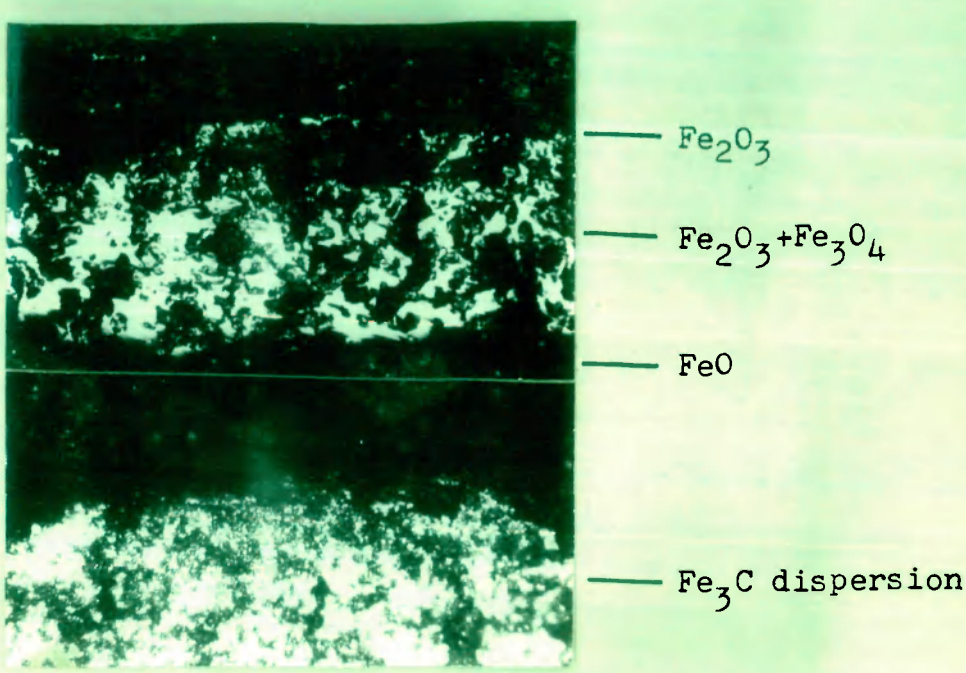

Fig. 3.11 Photomicrograph of cross-section of Fe-1.2C alloy, oxidized at 700°C for 24 hrs. X 100

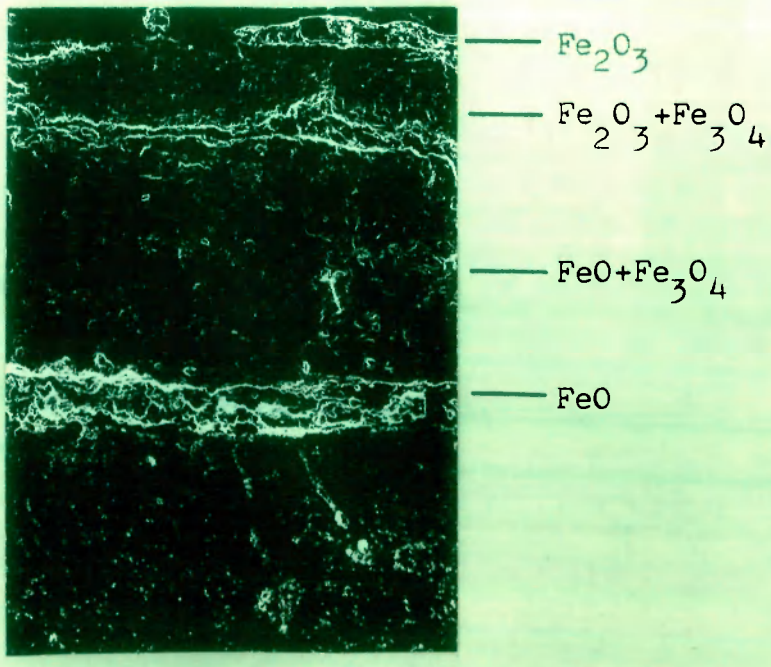

Fig.3.12 SEM picture of Fe-1.2C alloy, oxidized at 900°C for 24 hrs.

tion in O_2. A relatively thin irregular layer of wustite is invariably present in the inner scales. Due to separation and or/disruption of the outer scales, the wustite (FeO) scale come into contact with O_2 and oxidized to higher oxides of iron e.g. Fe_3O_4 and Fe_2O_3. The outer scales of oxidized alloys became porous as a result of the penetration of CO/CO_2(g) produced during oxidation.

Figures 3.13-3.18 show some photomicrographs of plain (undecarburized) carbon steels and decarburized steels in wet hydrogen (H_2-H_2O) at 900°C. The decarburized steels show well defined ferrite decarburized layers, the thickness of decarburized layer increases with increase in alloys carbon content, exposure time or temperature.

Figures 3.19-3.21 show some typical optical and scanning electron photomicrographs of decarburized-oxidized Fe-C alloys. The morphology of the oxide scales found on decarburized-oxidized alloys is quite similar to that of the scales formed on undecarburized-oxidized alloys. However, the scales formed on decarburized-oxidized alloys are relatively thicker, porous and more fragile.

3.2 DISCUSSION

The presence of carbon greatly lowers the oxidation rates of the alloy, however, the dependence on carbon content is some what complex. Considering the oxidation of plain

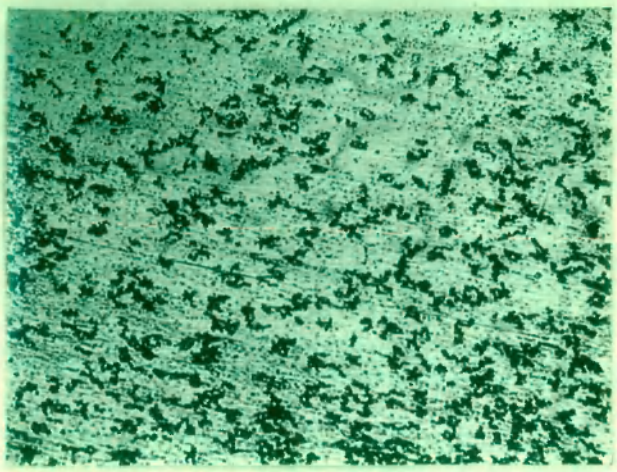

Fig. 3.13 Photomicrograph of cross-section of Fe-0.1C alloy. X 120

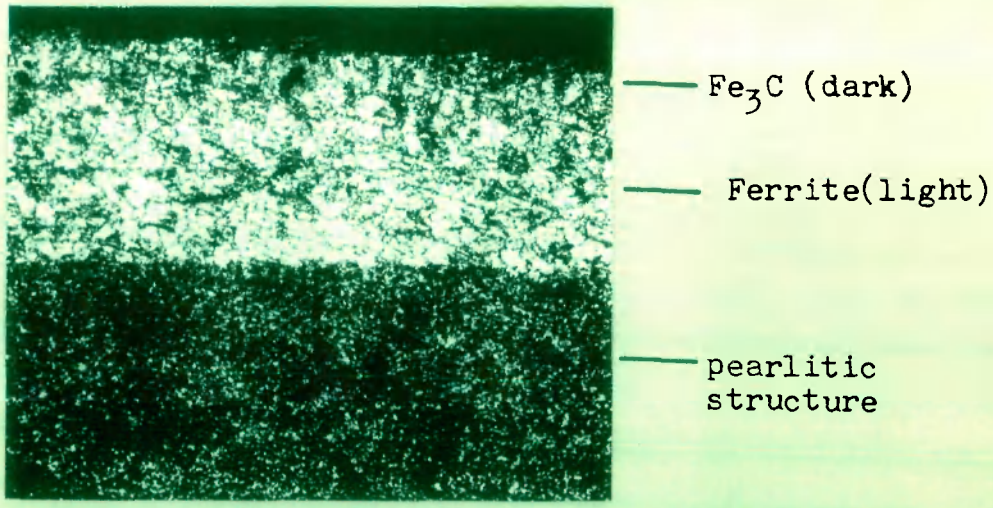

Fig. 3.14 Photomicrograph of cross-section of Fe-0.1C alloy, decarburized at 900°C for 2 hrs. X 120

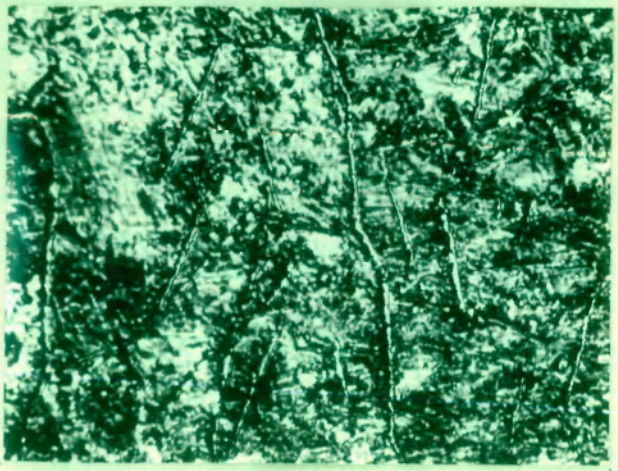

Fig. 3.15 Photomicrograph of cross-section of Fe-0.8C alloy. X 120

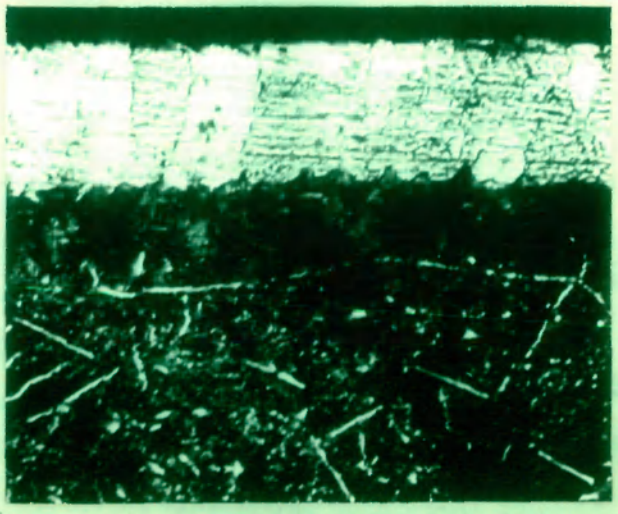

Fig. 3.16 Photomicrograph of cross-section of Fe-0.8C alloy, decarburized at 900°C for 1 hr. X 120

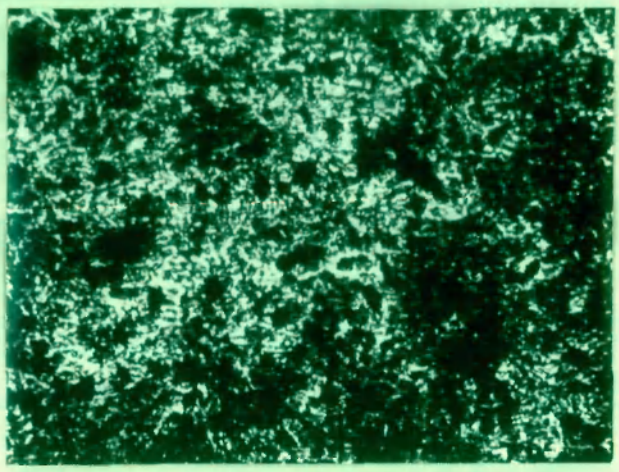

Fig. 3.17 Photomicrograph of cross-section of Fe-1.2C alloy. X 120

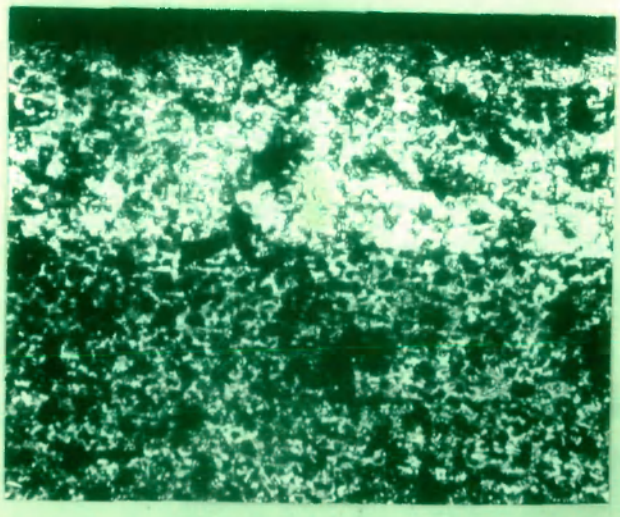

decarburized layer

Fig. 3.18 Photomicrograph of cross-section of Fe-1.2C alloy, decarburized at 900°C for 1 hr. X 120

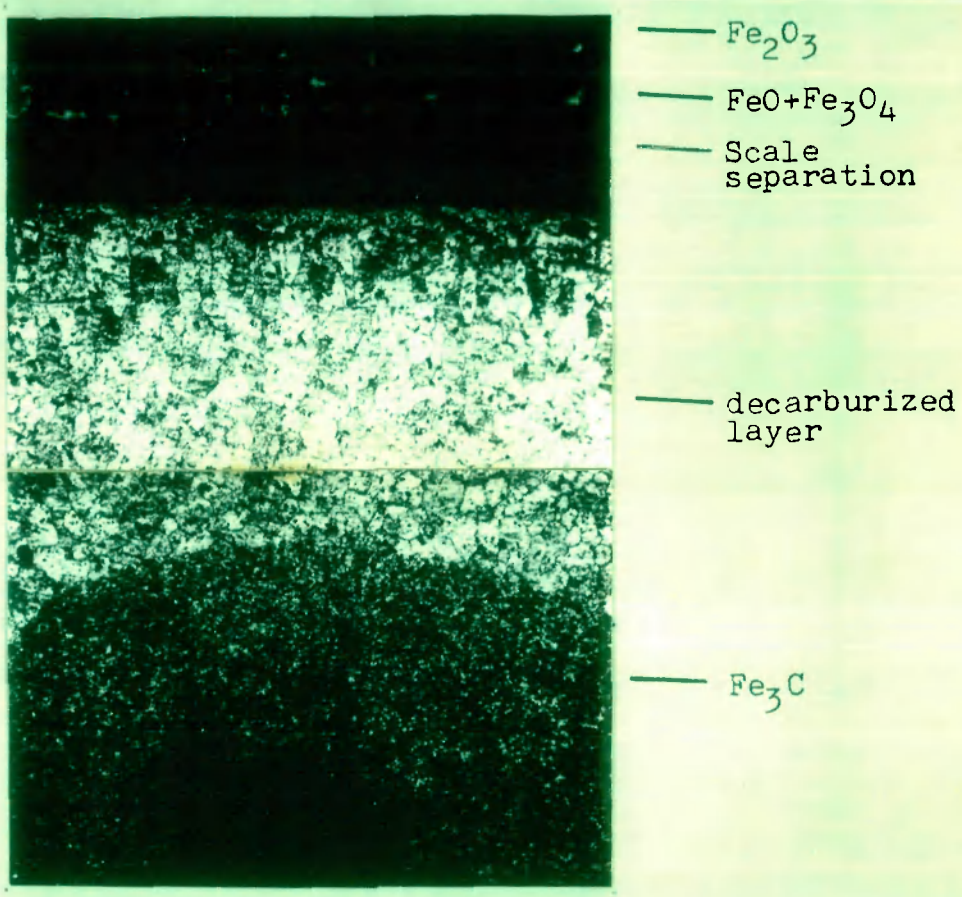

Fig.3.19 Photomicrograph of cross-section of predecarburized Fe-0.1C alloy, oxidized at 900°C for 6 hrs. X 120

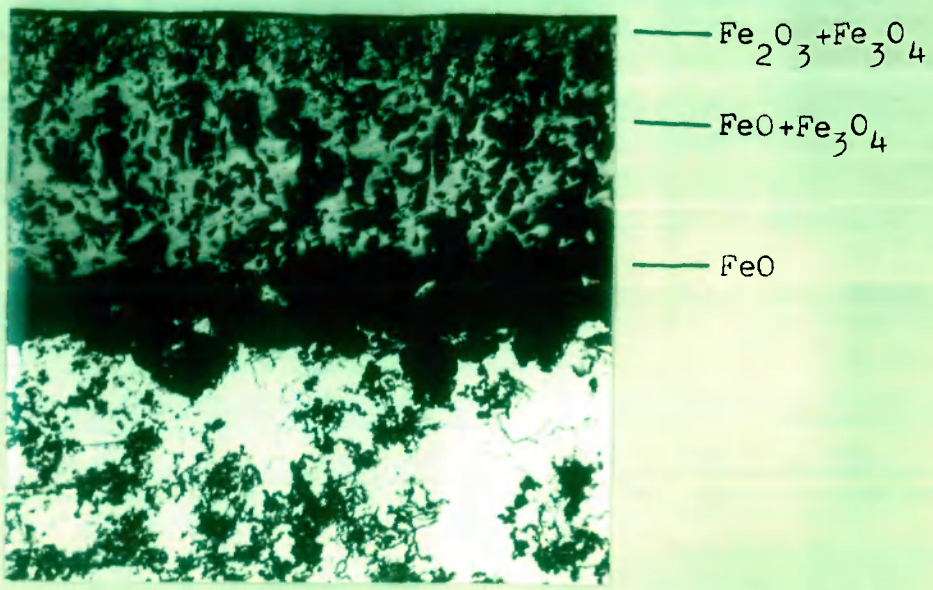

Fig. 3.20 Photomicrograph of cross-section of predecarburized Fe-0.8C alloy, oxidized at 900°C for 6 hrs. X 120

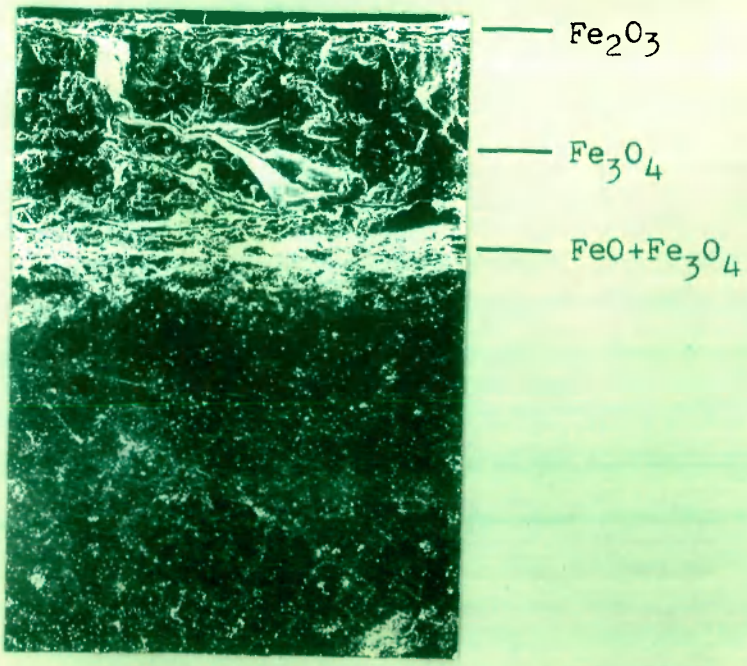

Fig. 3.21 SEM picture of predecarburized Fe-1.2C alloy, oxidized at 900°C for 6 hrs. X 80

carbon steels, at 700°C, Fe-1.2C alloy has the highest oxidation rate and 0.1 % C alloy has the lowest oxidation rate. However, at higher temperatures, the situation is reversed and 0.1 % C steel has the highest oxidation rates. Although at a definite temperature, the oxidation rates are similar at varying carbon contents, but even then the behaviour can be satisfactorily explained on the basis of phase structure and morphology of the scales. At 700°C the alloy structure consists of α-ferrite in case of 0.1 % C and $\alpha + Fe_3C$ at higher carbon content. At temperatures in the range of 800-1000°C, the structures are $\alpha + \gamma$ (0.1 % C), γ(0.4 and 0.8 % C) and $\gamma + Fe_3C$ (1.2 % C). At low temperature (700°C) there is a sufficient carbon available for decarburization in case of 1.2 % C and therefore, the oxidation rate is highest. However, at higher temperatures the presence of Fe_3C is perhaps responsible for lower oxidation rates of high carbon alloys.

The morphological features of the scales on plain carbon steels are similar. The scales are separated from the alloy due to decarburization. A relatively thin layer of wustite is invariably present. Due to separation and/or disruption of the scales, the wustite (FeO) scales would come into contact with O_2 and oxidized to higher oxides of iron: Fe_3O_4 and Fe_2O_3. The copious oxide scales containing Fe_3O_4 and Fe_2O_3 are found. Due to disruption or cracking of the

scales, fresh alloy surface comes into contact with O_2 and oxide growth on alloy is rate controlling factor. After sufficient exposure time, the healing of the disrupted scales is not ruled out. The outer scales are porous due to evolution of carbonaceous gases. The substrate shows dispersion of cementite (Fe_3C) in a ferrite matrix.

Considering the oxidation of decarburized plain carbon steels at 900°C; the oxidation rate of the decarburized alloy increases with increasing carbon content of the alloy. Further more, the oxidation rates of the decarburized Fe-1.2C is much lower than the undecarburized alloys. The metallographic studies show the oxidation of ferrite layer of decarburized alloy. The scales are separated from the alloy matrix partially due to decarburization and partially due to polishing artifacts. The matrix of the oxidized-decarburized alloy show the dispersion of coarse polygonal shaped carbide particles. Due to diffusion of iron and simultaneous decarburization, the matrix is depleted in dissolved carbon (or ferrite) and cementite seems to be the dominant and discrete phase. Since the cementite dispersion acts as an obstacle for the transport of iron during oxidation, the oxidation rates of decarburized steels are lower than undecarburized steels.

CHAPTER IV

DECARBURIZATION AND OXIDATION OF Fe-10MC ALLOYS

The experimental details containing material specifications, apparatus and procedures have already been given in Chapter II.

Transition metal carbide dispersed iron-base (Fe-10MC, where MC is TiC, VC, Cr_7C_3, NbC, TaC, MoC, WC or Fe_3C 10 wt. %) alloys were prepared by sintering in H_2 atmosphere at 1200°C and annealed in N_2 atmosphere at 1000°C for 1.5 hr. Each sintered alloy exhibits uniform and homogeneous textured surface. The microstructure shows 2-phase structure in which carbide particles are dispersed in an iron-rich matrix.

A laboratory fabricated helical thermal balance attached with a cathetometer was used for oxidation kinetics measurements of decarburized and undecarburized Fe-10MC alloys at 900°C for 6-9 hrs. in 1 atm O_2. The decarburization (H_2-H_2O) experiments were carried out at 900°C for 6-7 hrs.

4.1 Results

4.1.1 Microstructural Studies

Figures 4.1 to 4.8 show some typical optical and scanning electron photomicrographs of the cross sections of decarburized-carbide-dispersed iron-base sintered alloys. The photomicrographs show invariably a 2-phase structure containing dispersion

of fine grained carbide particles in a ferrite matrix.

TiC-dispersed alloy shows dispersion of grey irregular shaped grains in a ferrite matrix (Fig. 4.1). The decarburized alloy (Fig. 4.2) shows a marked increase in ferrite and a corresponding decrease in the carbide concentration. A decrease in porosity of the structure as a result of decarburization is also indicated. Similar behaviour has also been observed in VC-, NbC- and TaC-dispersed alloys. Figure 4.3 shows scanning electron photomicrograph of a cross-section of NbC-dispersed alloy decarburized at 900°C, the decarburized alloy shows the presence of NbC dispersoids in a ferrite matrix. A thin layer of Nb- rich iron oxide $FeO.Nb_2O_5$ is also shown. Figures 4.4 and 4.5 show optical photomicrographs of the cross-sections of WC-dispersed alloy in undecarburized and decarburized states, respectively. There is considerable depletion of carbide particles and increase in ferrite concentration, a situation which is also encountered in MoC-dispersed alloys. The Cr_7C_3- dispersed alloy is greatly affected on decarburization; a ferritic structure in which needle shaped carbides are dispersed is shown in figures 4.6 and 4.7. Figure 4.8 shows scanning electron photomicrograph of the decarburized alloy showing more details of the carbide morphology and oxide scales formed during decarburization. A uniform porous scale of $FeO.Cr_2O_3$ is present, the scale is detached from the alloy perhaps during polishing, some of the carbide is also incorporated into the scale.

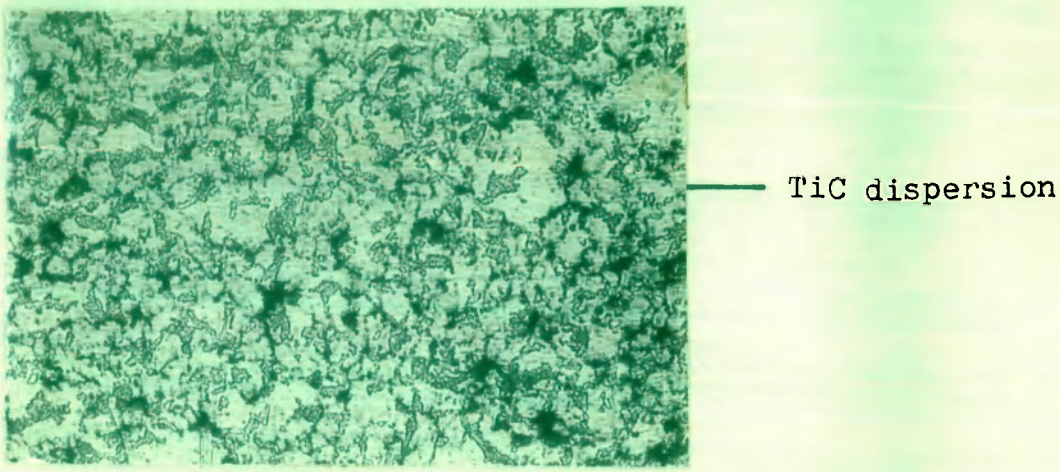

Fig. 4.1 Photomicrograph of a cross-section of Fe-10TiC dispersed alloy, undecarburized X 120

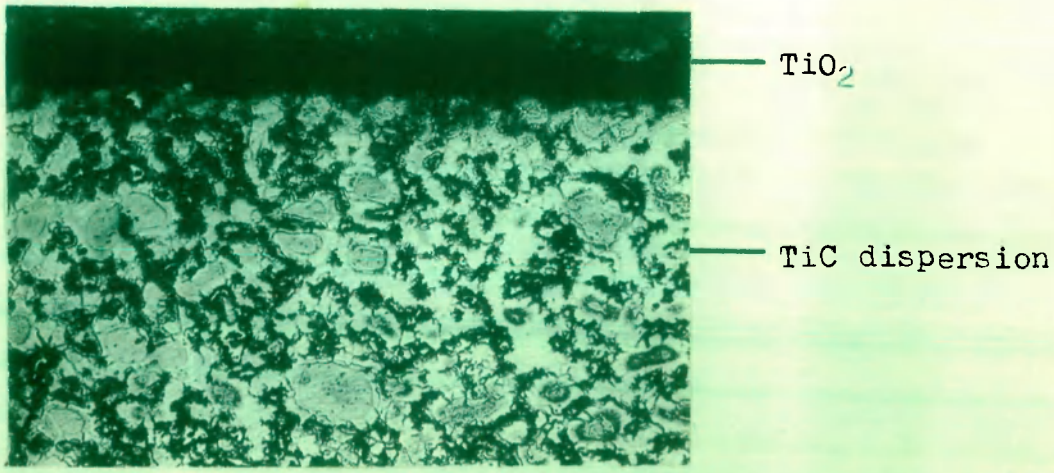

Fig. 4.2 Photomicrograph of a cross-section of Fe-10TiC dispersed alloy, decarburized at 900°C for 6 hrs. X 120

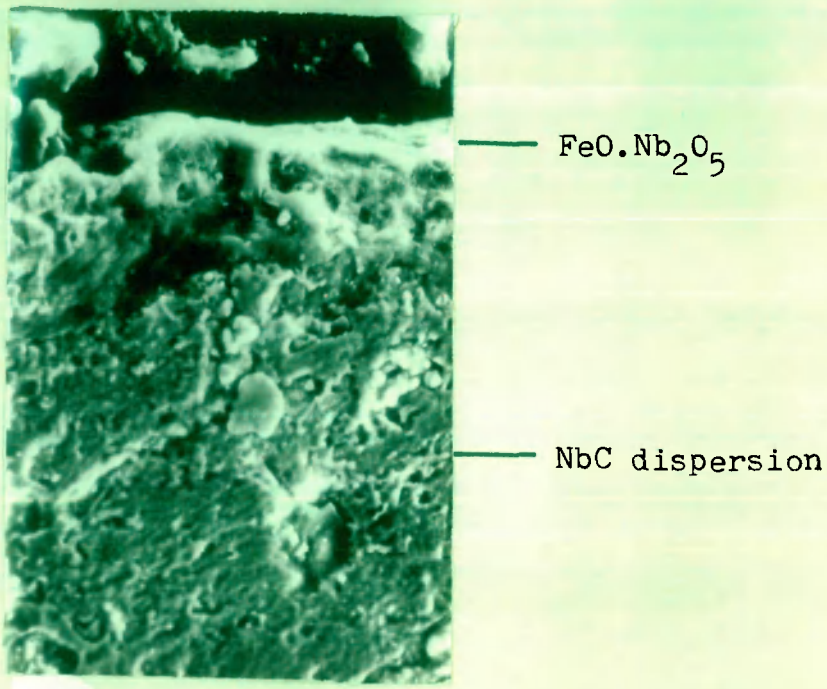

Fig. 4.3 SEM picture of Fe-10NbC dispersed alloy, decarburized at 900°C for 6 hrs.

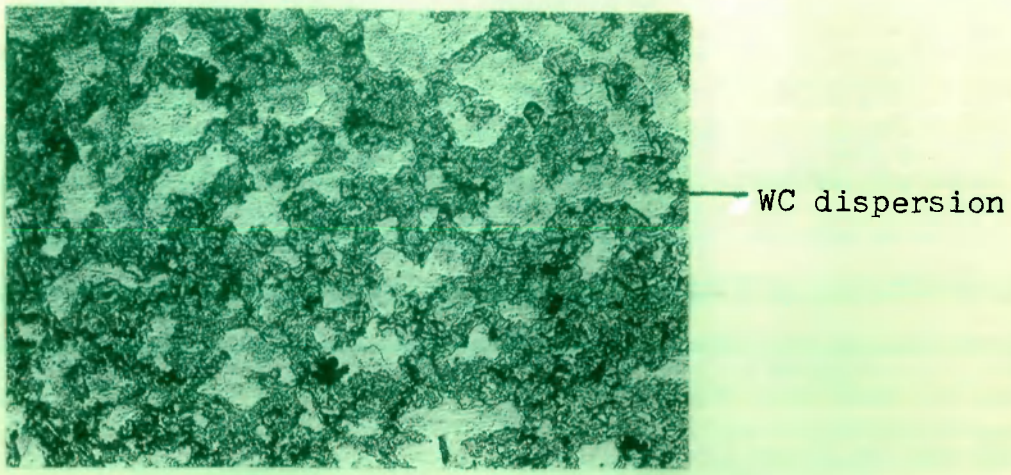

Fig. 4.4 Photomicrograph of a cross-section of Fe-10WC dispersed alloy, undecarburized.
X 120

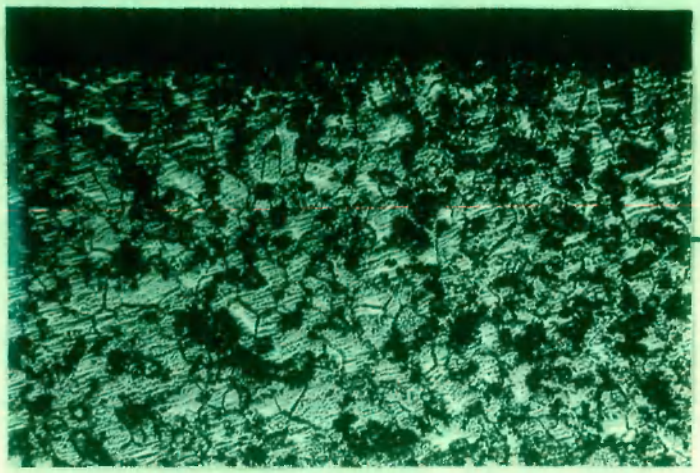

Fig. 4.5 Photomicrograph of a cross-section of Fe-10WC dispersed alloy, decarburized at 900°C for 6 hrs. X 120

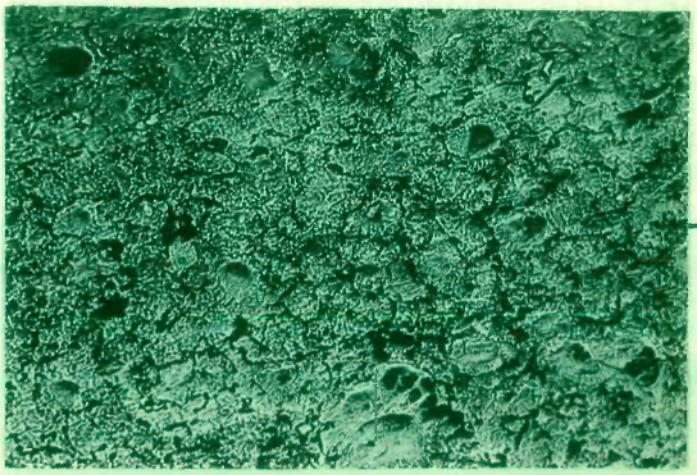

Fig. 4.6 Micrograph of a cross-section of Fe-10Cr_7C_3 dispersed alloy, undecarburized. X 120

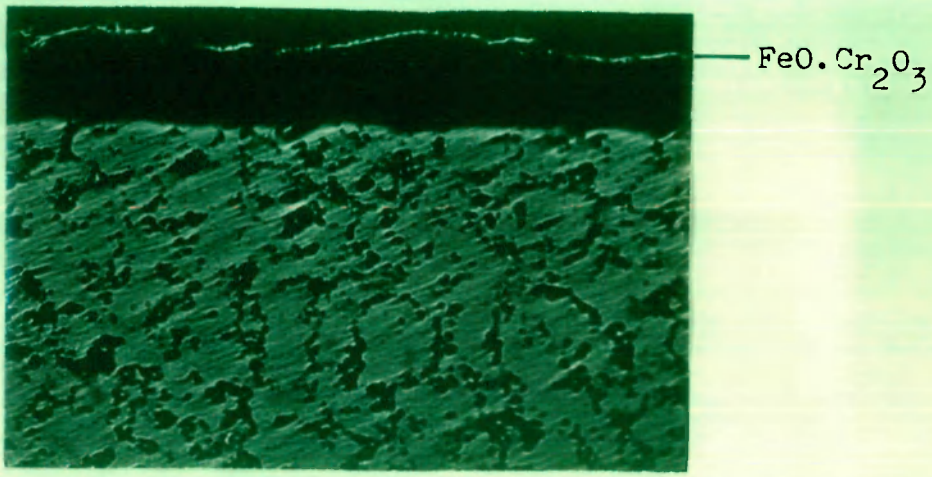

Fig. 4.7 Photomicrograph of a cross-section of Fe-10Cr_7C_3 dispersed alloy, decarburized at 900°C for 6 hrs. X 120

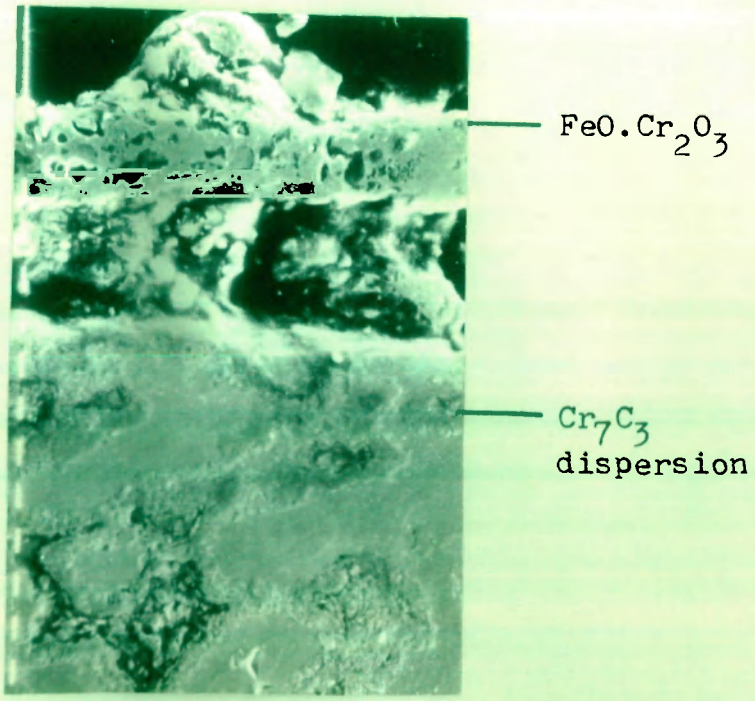

Fig. 4.8 SEM picture of Fe-10Cr_7C_3 dispersed alloy, decarburized at 900°C for 6 hrs.

4.1.2 Oxidation Kinetics

Figures 4.9 and 4.10 show weight gain vs time and weight gain^2 vs time plots, respectively for the oxidation of carbide dispersed iron based sintered alloys at 900^{o}C in 1 atm. oxygen. The oxidation seems to follow a parabolic rate law as indicated by the linear nature of weight gain^2 vs time plots. Figure 4.11 shows weight gain vs time for the oxidation of decarburized carbide-dispersed alloys at 900^{o}C. The majority of the alloys oxidize by a parabolic rate law but a few of them show deviation from parabolic rate law which is indicated by the breaks in the weight gain^2 vs time plots (Fig. 4.12).

Table 4.1 lists the values of parabolic rate constants for the oxidation of carbide dispersed iron-base alloys and oxidation of corresponding decarburized alloys. The oxidation rate of undecarburized carbide-dispersed alloys are about 2-3 magnitude higher than the corresponding decarburized alloys. Amongst the undecarburized alloys, VC-dispersed alloy has the highest oxidation rate followed by NbC-dispersed alloy, Fe_3C-dispersed alloy showing the lowest rate. Amongst the decarburized alloys, TiC-dispersed alloy has the highest oxidation rate followed by TaC-dispersed alloys, the lowest oxidation rate is observed for VC-dispersed alloy followed by NbC-dispersed alloys.

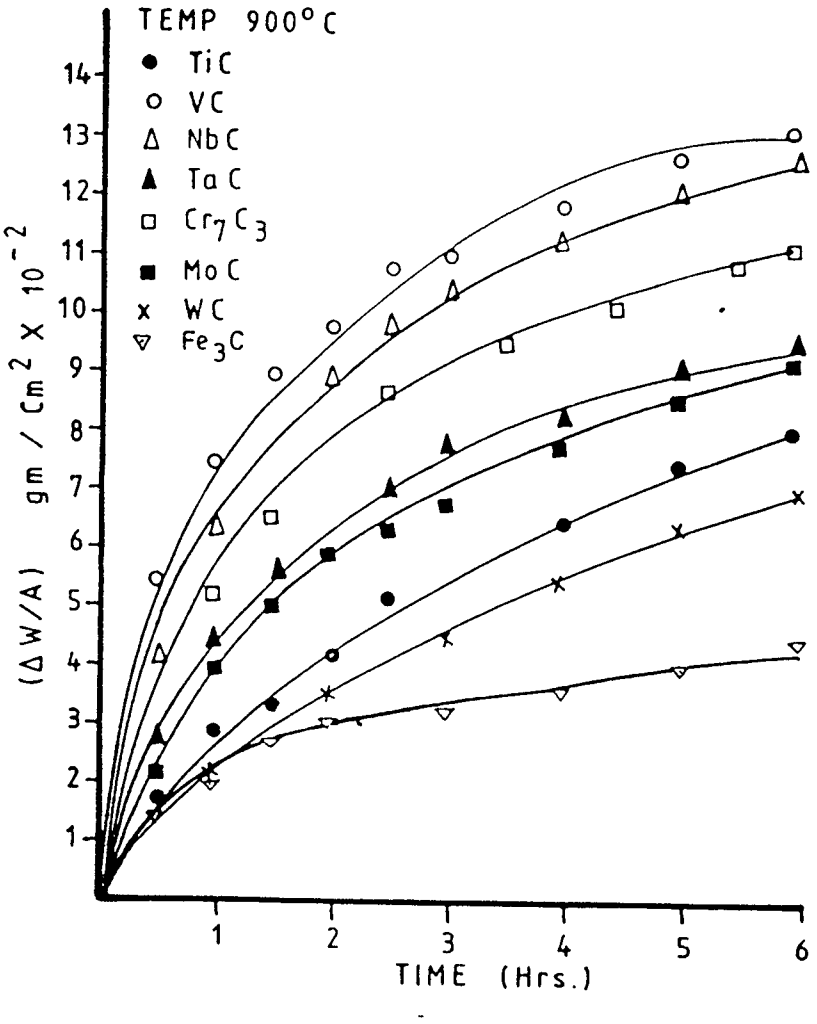

Fig. 4.9 Plots of weight gain Vs time for the oxidation of carbide dispersed iron-base alloys at 900°C

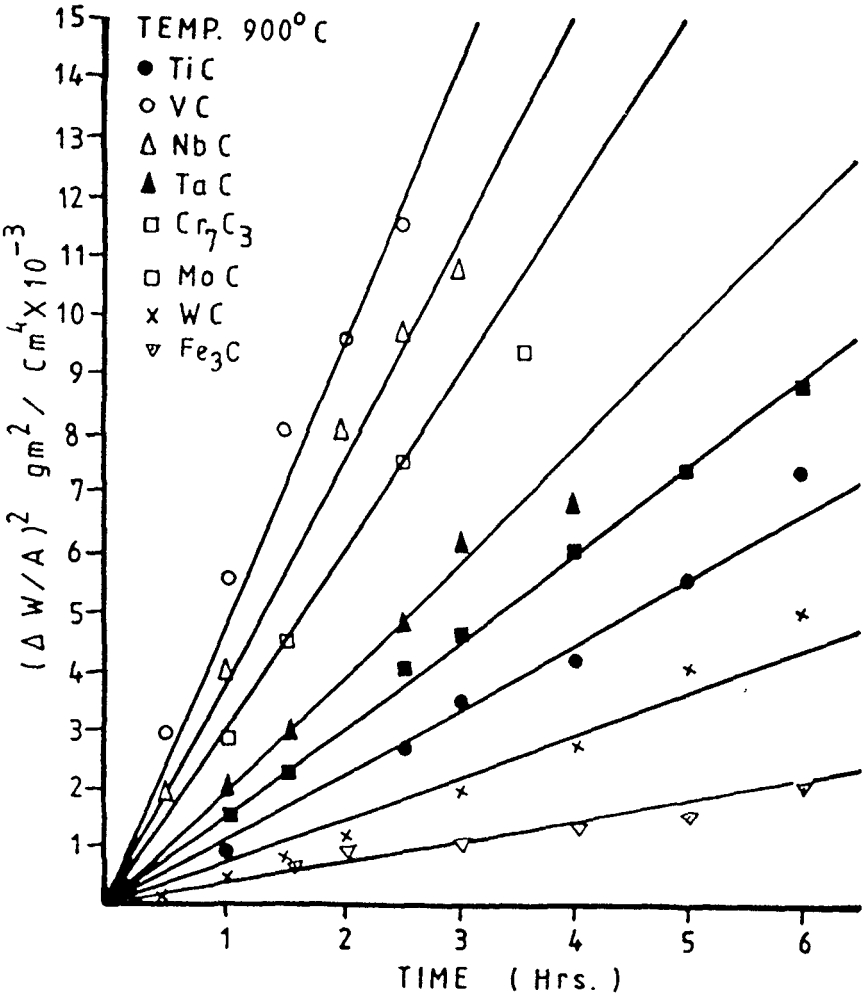

Fig.4.10 Plots of weight gain^2 Vs time for the oxidation of carbide dispersed iron-base alloys at 900°C.

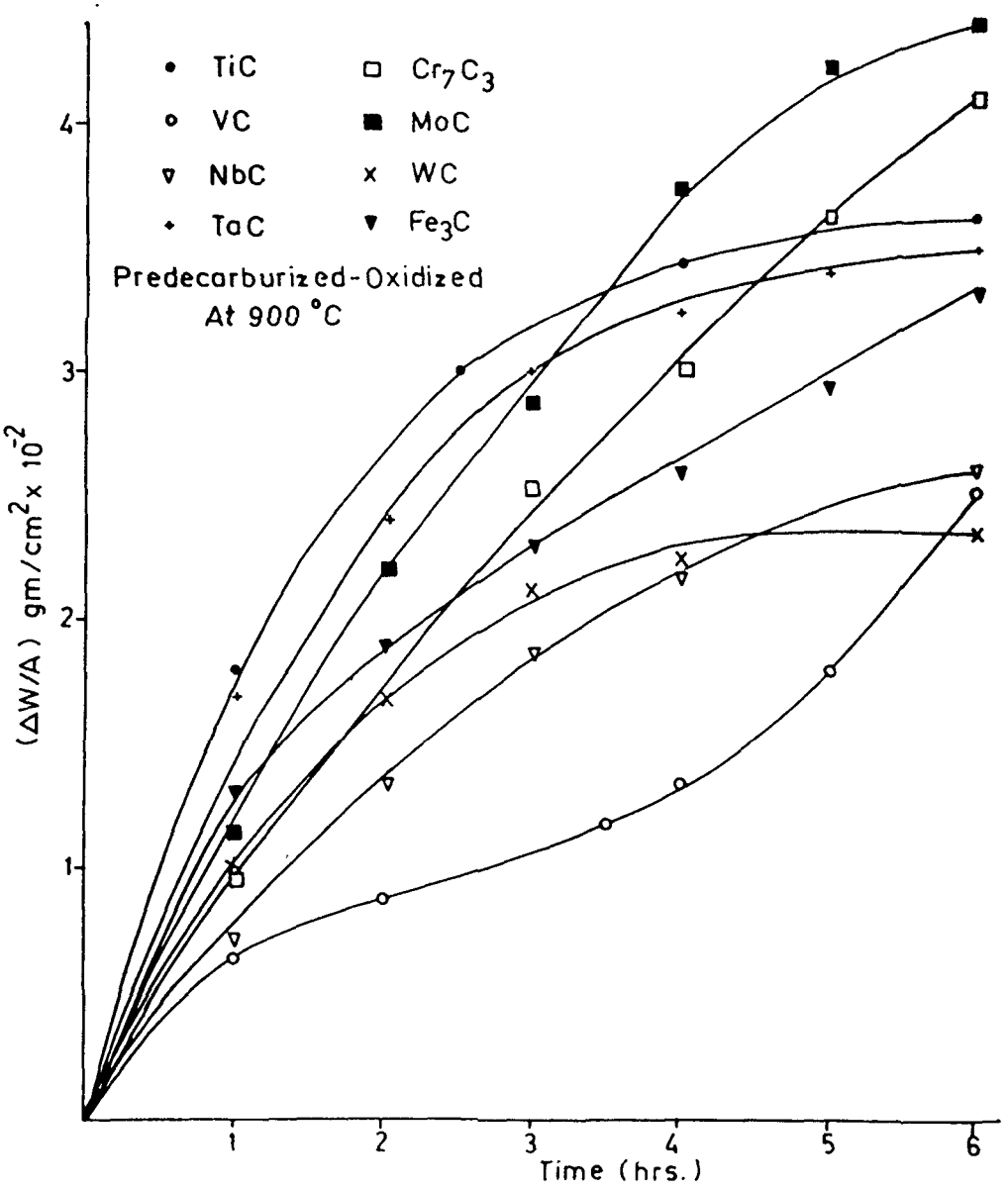

Fig. 4.11 Plots of weight gain VS time for the oxidation of decarburized carbide-dispersed alloys at 900°C.

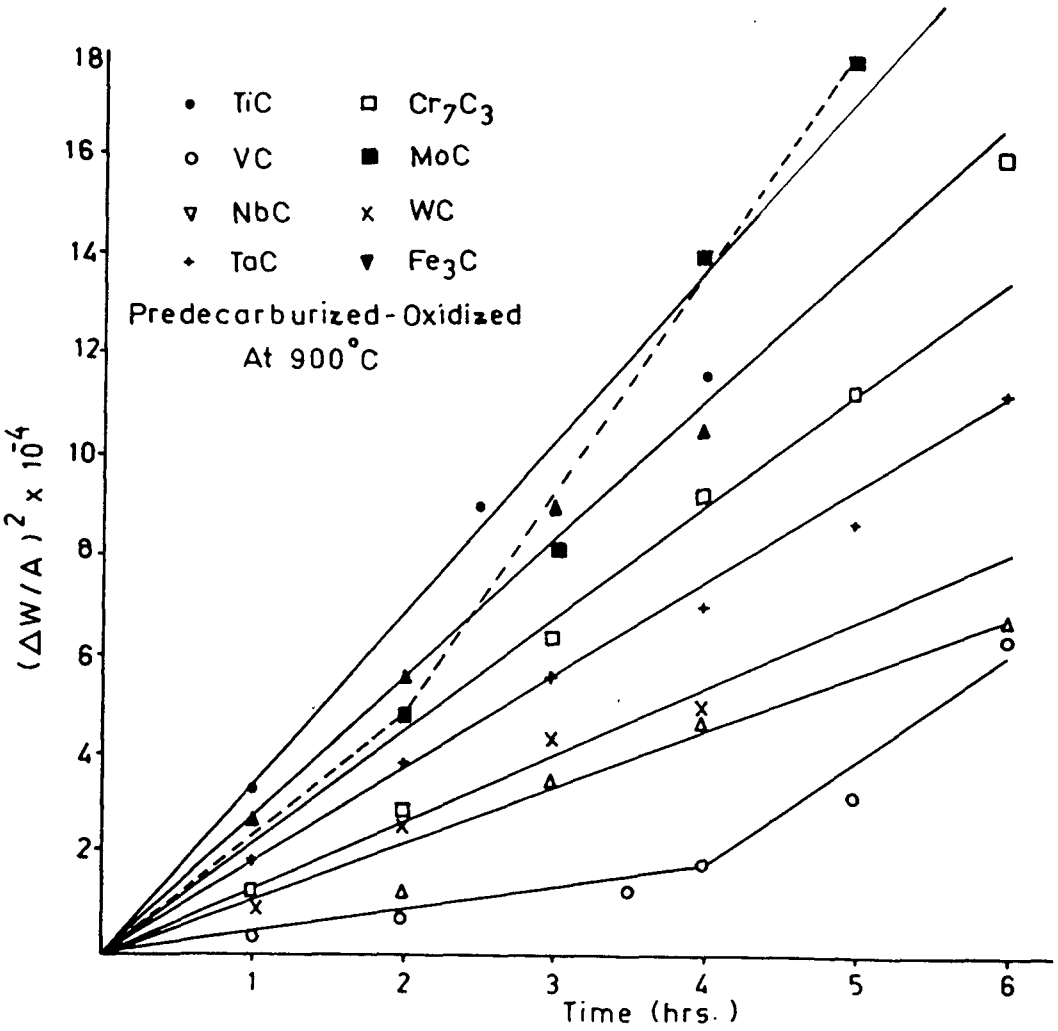

Fig.4.12 Plots of weight gain^2 time for the oxidation of decarburized carbide-dispersed alloys at 900 °C .

Table 4.1

Values of the parabolic rate constant, Kp for the oxidation at 900°C of alloys in $Kg^2.m^{-4}.Sec^{-1} \times 10^{-6}$

Alloy (wt.%)	Undecarburized	Predecarburized	
		K_{p_1}	K_{p_2}
Fe+10TiC	30.9	9.4	-
Fe+10VC	130.1	0.8	5.8
Fe+10NbC	105.0	3.1	-
Fe+10TaC	54.0	7.7	-
Fe+10Cr_7C_3	63.4	6.2	-
Fe+10MoC	44.0	5.3	12.5
Fe+10WC	20.3	3.6	-
Fe+10Fe_3C	9.8	5.1	-

4.1.3 Morphology of the Oxide Scale

Figures 4.13 to 4.16 show optical and scanning electron photomicrographs of the cross section of oxidized Fe-10MC-dispersed iron-base sintered alloys at 900°C. The oxidized alloys invariably form multilayered oxide scales, the innermost layers mainly consist of spinel or mixed oxide followed by porous layers containing oxides of iron, Fe_2O_3 forming outermost layer, the carbides are also incorporated in the inner scales. In some alloys, a metal oxide layer containing M_2O_x is also present.

Figure 4.13 shows scanning electron photomicrograph of the NbC-dispersed alloy in the oxidized condition, a multilayered oxide scale is present, the NbC dispersion remains largely unaffected. A similar structure is observed in TaC-dispersed alloy but due to decarburization the scales are detached from the substrate (Fig. 4.14). In Cr_7C_3-dispersed alloy, the scales are broken due to decarburization, some Cr_7C_3 is also incorporated into the scales (Fig. 4.15). WC-dispersed alloy on oxidation forms a multilayered scale in which inner layers of the scales contain WO_3, the carbide net work is affected only feably on oxidation (Fig. 4.16).

The oxide scales formed on predecarburized-oxidized alloys are much thinner than the corresponding undecarburized-oxidized alloys although the composition and structure of the scales are not much different.

The optical photomicrograph of a cross section of predecarburized-oxidized WC-dispersed alloy shows the presence of a multilayered scale in which the inner layer contains $WO_3/FeO.WO_3$ (Fig. 4.17) comparing with the undecarburized-oxidized alloy, the carbide grains are coarsened, the scales are less porous and more compact and the outer layer containing Fe_2O_3 is missing. The scanning electron photomicrograph is shown in Figure 4.18. The scanning electron photomicrograph of predecarburized-oxidized TaC-dispersed alloy shows stratified layers of Ta-rich iron oxide scales (Fig. 4.19) which are

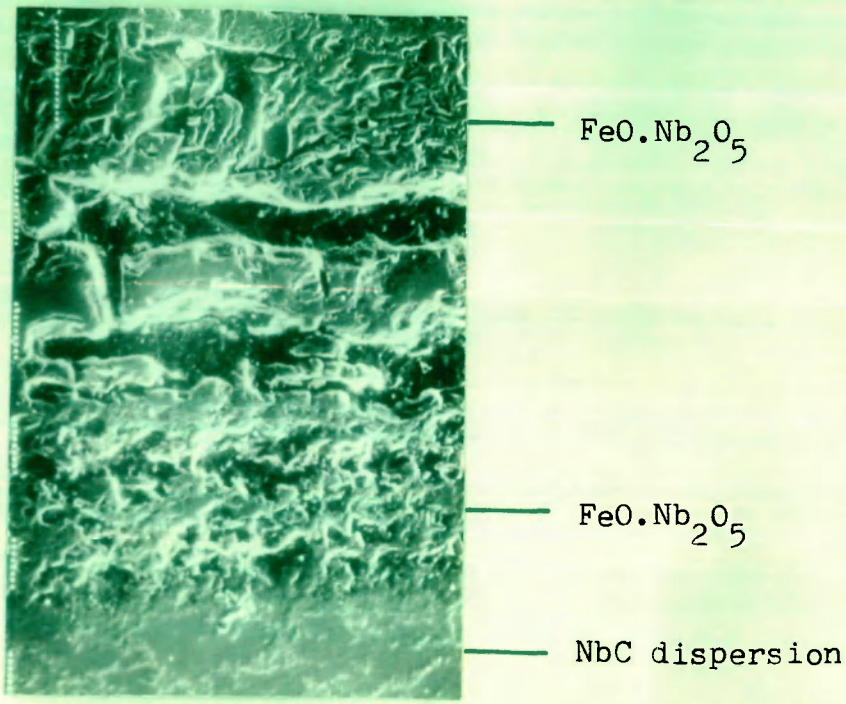

Fig. 4.13 SEM picture of Fe-10NbC dispersed alloy, oxidized at 900 C for 6 hrs.

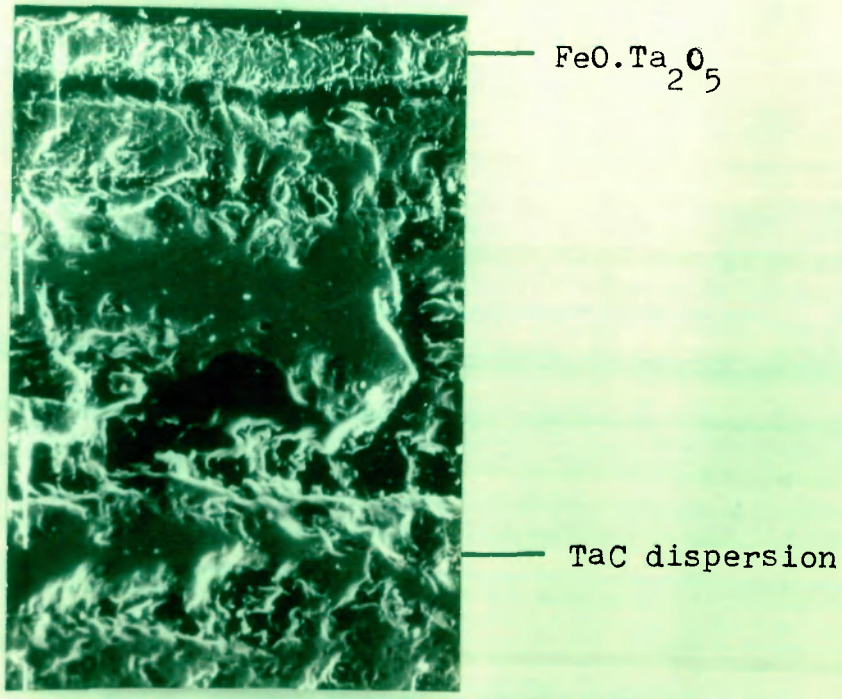

Fig.4.14 SEM picture of Fe-10TaC dispersed alloy, oxidized at 900°C for 6 hrs.

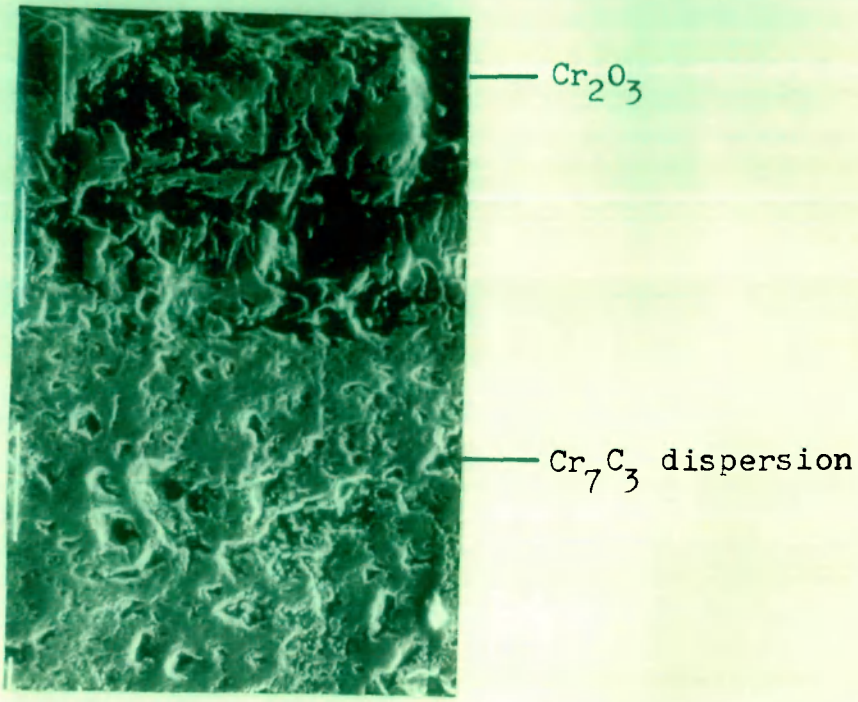

Fig.4.15 SEM picture of Fe-10Cr_7C_3 dispersed alloy, oxidized at 900°C for 6 hrs.

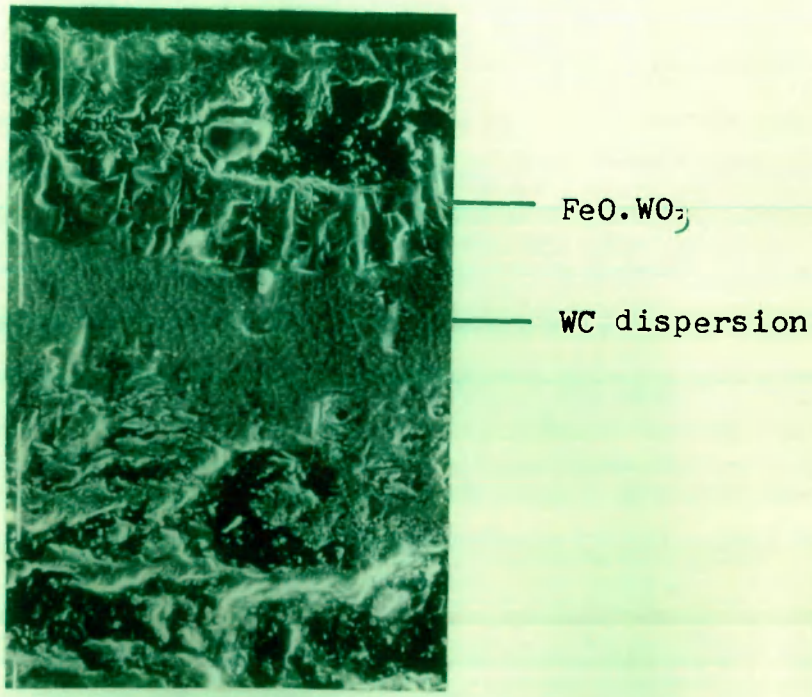

Fig. 4.16 SEM picture of Fe-10WC dispersed alloy, oxidized at 900°C for 6 hrs.

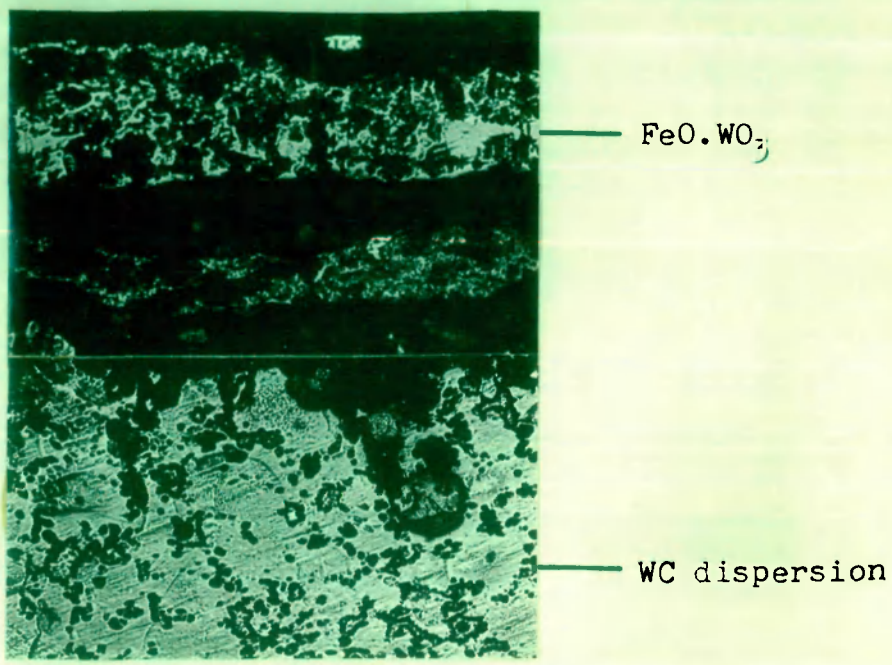

Fig. 4.17 Photomicrograph of a cross-section of predecarburized Fe-10WC dispersed alloy, oxidized at 900°C. X 100

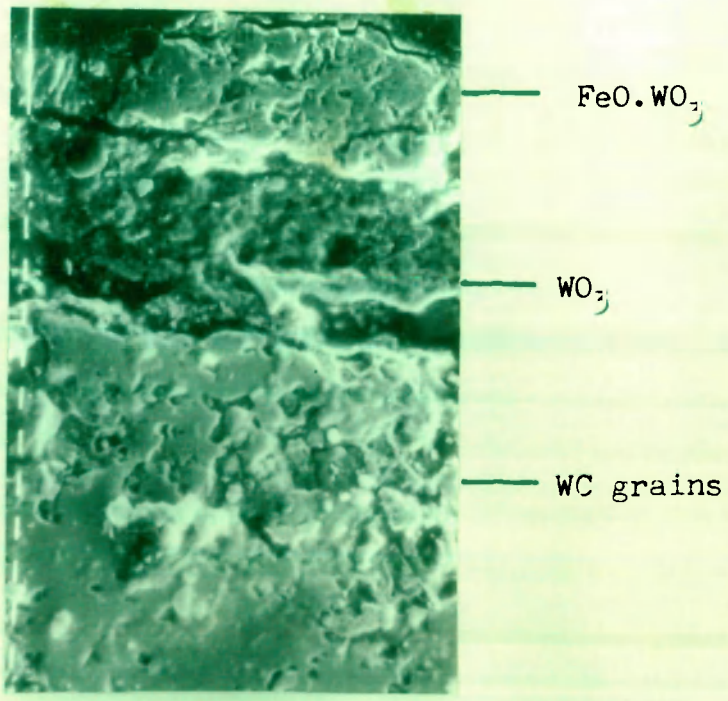

Fig. 4.18 SEM picture of predecarburized Fe-10WC dispersed alloy, oxidized at 900°C.

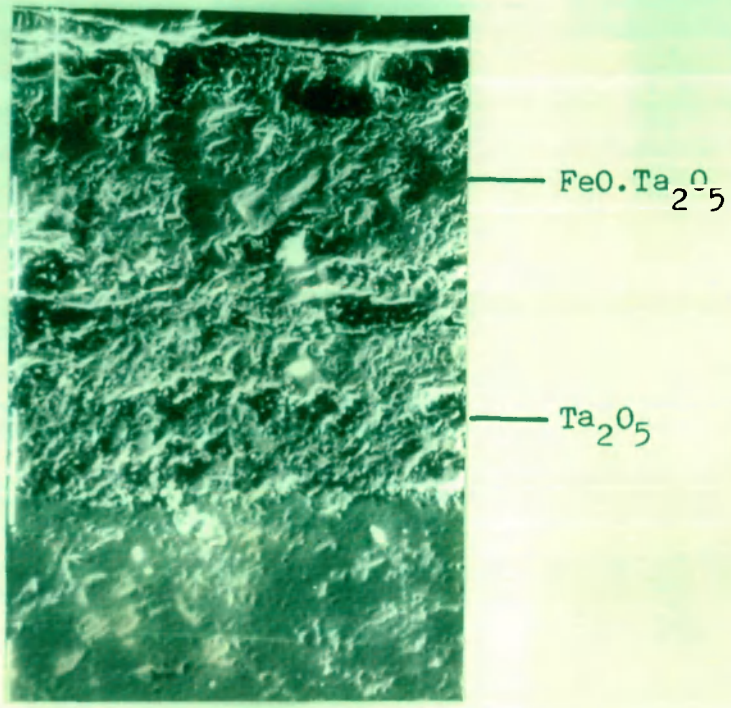

Fig. 4.19 SEM picture of predecarburized Fe-10TaC dispersed alloy, oxidized at 900°C for 6 hrs.

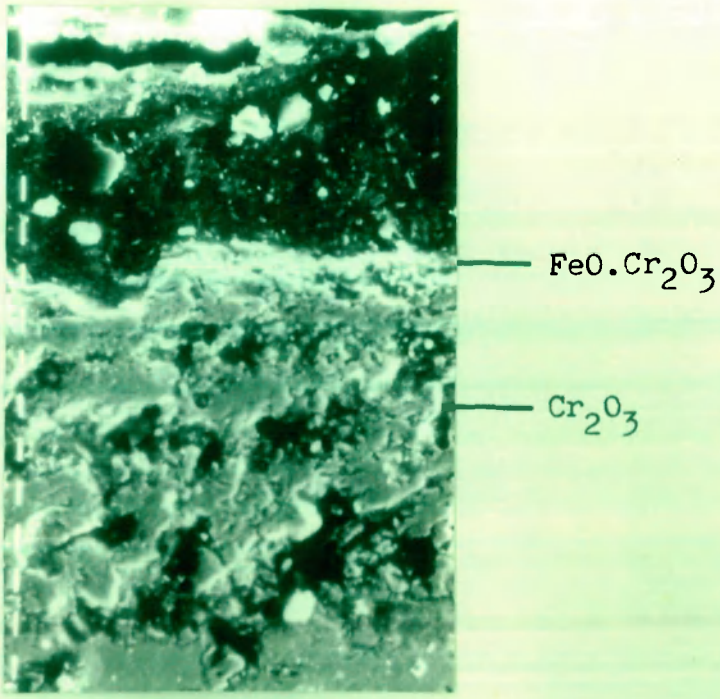

Fig. 4.20 SEM picture of predecarburized $Fe10Cr_7C_3$ dispersed alloy, oxidized at 900°C for 6 hrs.

much thinner than the corresponding undecarburized-oxidized alloy. The Cr_7C_3-dispersed decarburized-oxidized alloy shows coarsening of carbon grains and presence of a thick Cr-rich layer of $FeO.Cr_2O_3$ in which Cr_7C_3 is also incorporated (Fig. 4.20). Figures 4.21 and 4.22 show respectively the optical micrographs of the cross sections of predecarburized-oxidized TiC and MoC-dispersed alloys at 900°C. The inner layers contain $FeO.TiO_2$ and $FeO.MoO_3$, respectively and the layers are much thinner than the corresponding undecarburized-alloys. In Ti-containing alloys, the inclusion of TiC in the scales is also indicated.

4.2 Discussion

The carbide dispersed iron based sintered alloys on oxidation at 900°C obey a parabolic rate law. For different alloys, the oxidation rate sequence at 900°C is as follows :

$$VC > NbC > Cr_7C_3 > TaC > MoC > TiC > WC > Fe_3C$$

During oxidation of the alloy in oxygen at 900°C a pure oxide/spinel film is formed on the surface of the alloy in the initial stages which acts as a protective layer, this film is liable to be broken due to decarburization and/or insufficient plastic flow of the oxide layer. The decarburization during oxidation occurs due to the decomposition of carbide and its extent depends upon the thermal stabilities of different carbides in presence of an oxidant. The thermal stabilities

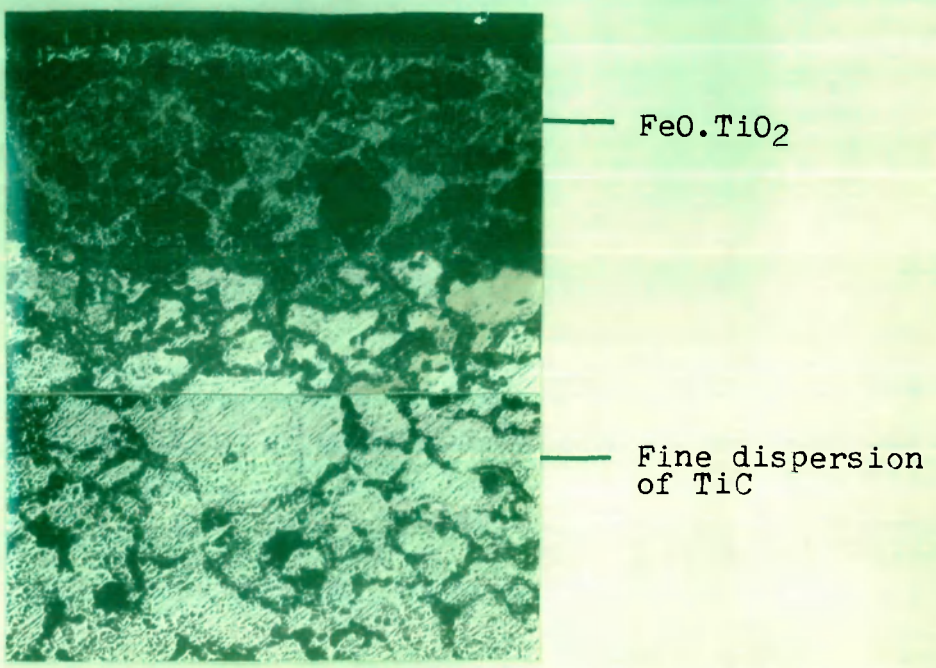

Fig. 4.21 Photomicrograph of a cross-section of predecarburized Fe-10TiC dispersed alloy, oxidized at 900°C for 6 hrs.
X 100

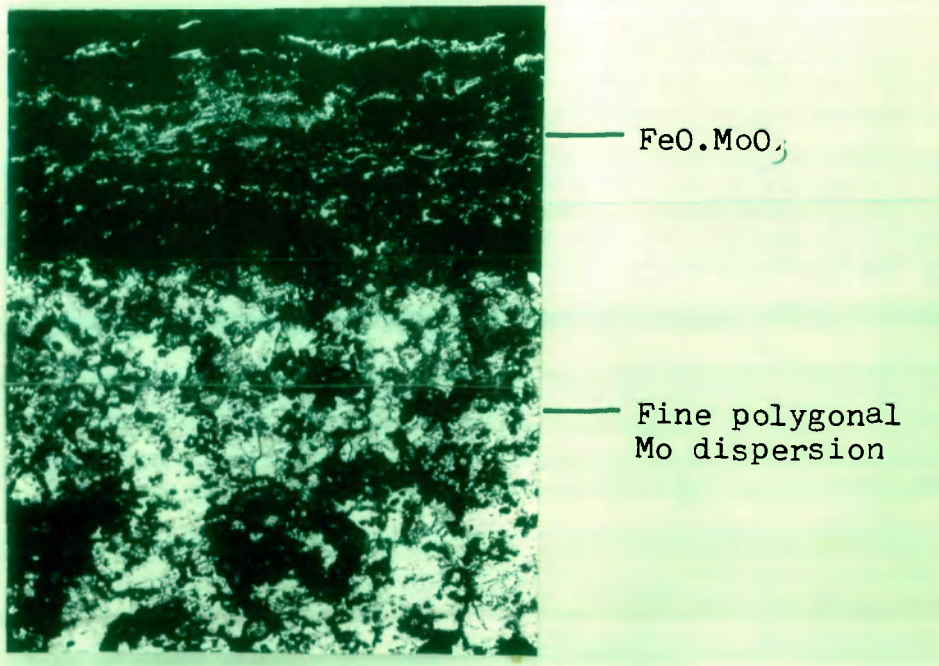

Fig.4.22 Photomicrograph of a cross-section of predecarburized Fe-10MoC dispersed alloy, oxidized at 900°C for 6 hrs.
X 100

of different carbides is compared in terms of ΔG^{o} (Kcal/mole) of the oxidation reactions (Table 4.2) and the calculated values can be arranged in the following sequence of increasing free enthalpies :

$$WC > MoC \backsim TiC > Fe_3C > TaC > Cr_7C_3 \quad NbC > VC$$

The sequence is similar with the oxidation rate sequence with a notable exception of Fe_3C.

Table 4.2

ΔG^{o} for the oxidation of carbide into oxide at 900°C in Kcal/g.at.C

Reaction	ΔG^{o}
$TiC + 3\ O \rightarrow TiO_2 + CO$	-261.0
$VC + 7/2\ O \rightarrow 1/2\ V_2O_5 + CO$	-119.7
$NbC + 7/2\ O \rightarrow Nb_2O_5 + CO$	-135.0
$TaC + 7/2\ O \rightarrow Ta_2O_5 + CO$	-147.0
$1/3Cr_7C_3 + 9/2\ O \rightarrow 7/6Cr_2O_3 + CO$	-135.0
$MoC + 4\ O \rightarrow MoO_3 + CO$	-261.0
$WC + 4\ O \rightarrow WO_3 + CO$	-281.0
$Fe_3C + 4\ O \rightarrow 3FeO + CO$	-187.0

The different oxidation rates for the iron-metal carbide alloy systems are also attributed to the varying degree of mobility of carbon which is apparently associated with the carbide

forming capacity of the metal[114]. For example, Cr-containing alloy has considerably higher oxidation rate than W-containing alloy since W is a stronger carbide former than Cr.

The morphology of the scales explains to some extent the oxidation behaviour of carbide-dispersed alloys. The NbC- and TaC dispersed alloys which have comparatively high oxidation rates form disrupted and porous scales (Figs. 4.13 and 4.14) whereas the scales formed on WC- dispersed alloys, are relatively more compact and less porous (Fig. 4.16). In case of NbC-, VC-, TaC- and Cr_7C_3- dispersed alloys, the oxide film is formed in the early stages but due to decarburization this film is broken, and the fresh alloy is exposed to oxygen resulting in higher oxidation rates for the alloys. In WC- and TiC- dispersed alloys, the oxide films formed are more integrated perhaps due to their high plasticity and low decarburization resulting in comparatively low oxidation rates.

During decarburization of carbide dispersed iron-base sintered alloys in a H_2-H_2O atmosphere ($\backsim P_{O_2} = 10^{-19}$ atm) at 900°C[113], most of the alloys show weight gain except MoC- and VC-dispersed alloys, the latter show weight losses although no decarburized layer is present (Table 4.3). The decarburization rates (in terms of weight loss/area) follow the sequence :

$$TaC > TiC > Fe_3C > NbC > Cr_7C_3 > WC > VC > MoC$$

During decarburization, a thin oxide film is invariably

Table 4.3

Weight loss or gain/area after a 6 hr decarburization run in H_2-H_2O atmosphere at 900°C

Alloy (wt %)	$Kg/m^2 \times 10^{-2}$
Fe + 10 TiC	+5.0
Fe + 10 VC	-1.5
Fe + 10 NbC	+3.9
Fe + 10 TaC	+8.2
Fe + 10 Cr_7C_3	+3.8
Fe + 10 MoC	-8.6
Fe + 10 WC	+1.0
Fe++ 10 Fe_3C	+4.8

formed even at a very low oxygen potential ($\sim 10^{-19}$ atm), the film is relatively thick in case of TaC-, TiC- and Fe_3C-containing alloys and thinnest in case of VC- and WC-containing alloys. As a result of decarburization, some transformation of carbide into austenite occurs providing a coarsened austenitic structure containing a fine dispersion of carbide. The structure of the alloy is more homogenized and degree of porosity is significantly decreased as a result of decarburization (Table 4.4). The microstructure of decarburized alloy can be compared with the oxidized alloy where similar changes have been shown in the matrix. This led to the contention

Table 4.4

Degree of porosity of undecarburized and decarburized alloys

Alloy (wt.%)	Plain % porosity	Decarburized % porosity	Reduction in % porosity on decarburization
Fe + 10 TiC	2.81	0.58	43.77
Fe + 10 VC	11.13	7.03	36.83
Fe + 10 NbC	6.32	2.81	55.53
Fe + 10 TaC	6.01	3.21	48.08
Fe + 10 Cr_7C_3	2.10	1.23	41.42
Fe + 10 MoC	1.56	1.17	25.00
Fe + 10 WC	2.03	1.17	42.36
Fe + 10 Fe_3C	1.40	0.31	77.85

that the mobility of carbon did play an important role during decarburization (at low p_{O_2}) and oxidation (at 1 atm. O_2), the alloys containing strong carbide forming elements e.g., W,V and Mo have much lower oxidation or decarburization rate than the alloys containing relatively weak tendency to form carbide such as Cr.

Considering the oxidation of predecarburized-iron-base sintered alloy, the parabolic rates follow the sequence :

$$TiC > TaC > Cr_7C_3 > MoC > Fe_3C > WC > NbC > VC$$

With a few exceptions, the rate sequence is quite similar to

that observed for the oxidation of undecarburized iron-base sintered alloys. The oxidation rates of predecarburized alloys are about 2-3 magnitude lower than the corresponding undecarburized alloys. Two factors seem to be responsible for a drastic lowering in the oxidation rate of decarburized alloys. Firstly, a thin protective oxide film is formed during decarburization in H_2-H_2O atmosphere, which retards the mobility of carbon atoms and secondly, the presence of a fine carbide dispersion in an austenitic matrix which considerably reduces the level of decarburization during oxidation and in consequence assists in retaining the integrity of oxide scales.

CHAPTER V

DECARBURIZATION AND OXIDATION OF Fe-10MC-0.1C-20Cr ALLOYS

The experimental details containing material specifications, apparatus and procedures have already been given in Chapter II.

Chromium- and iron-containing transition metal carbide dispersed iron based alloys : Fe-10MC-0.1C-20Cr (where C is 0.1 wt. %; MC is TiC, WC, Cr_7C_3 or NbC 10 wt. %, and Cr is 20 wt. %) were prepared by sintering. Tablets of 1.4 cm diameter were prepared by mixing carbon (0.1 wt. %), metal carbide (10 wt. %), chromium (20 wt. %) and iron (balance) powders in an agat mortar. The total amount of material used for each tablet was about 2.0 g. The mixture was put in a steel mould and was compacted at 15 tons/cm^2 using a hydraulic press. The green tablets were sintered in a quartz tube placed in a glober tubular furnace under dried hydrogen atmosphere at 1200°C for 2 hrs. and subsequently annealed under nitrogen atmosphere at 1000°C. Each sintered alloy was examined under a photometallurgical microscope and invariably shows a homogeneous 2-phase microstructure.

The sintered alloys were subjected to oxidation (1 atm. O_2), decarburization (H_2-H_2O) and decarburization-oxidation studies at 900°C on a laboratory fabricated helical thermal balance.

5.1 Results

5.1.1 Oxidation kinetics

Weight gain Vs time and weight gain^2 Vs time plots for the oxidation of undecarburized Fe-10MC-0.1C-20Cr alloys at 900°C in 1 atm. O_2 have been shown in figures 5.1 and 5.2, respectively. Furthermore, the alloys have been decarburized in wet hydrogen (H_2-H_2O) at 900°C for 2 hrs. followed by oxidation at the same temperature in 1 atm. O_2, the weight gain Vs time and weight gain^2 Vs time plots for the oxidation of decarburized-oxidized alloys are given in figures 5.3 and 5.4 respectively. In both the conditions, the weight gain Vs time plots are parabolic and weight gain^2 Vs time plots are linear. Therefore, the oxidation of undecarburized as well as decarburized alloys seem to proceed by a diffusion-controlled mechanism. The values of parabolic rate constant, Kp are listed in Table 5.1. A glance on the values of rate constant of different alloys indicates that Fe-10WC-0.1C-20Cr has the lowest oxidation rates in undecarburized and decarburized states. However, in an undecarburized state, Fe-10Cr_7C_3-0.1C-20Cr has the highest oxidation rate whereas in the decarburized state, the corresponding NbC-containing alloy has the highest oxidation rates although the oxidation rates of the alloys in both the states differ only marginally.

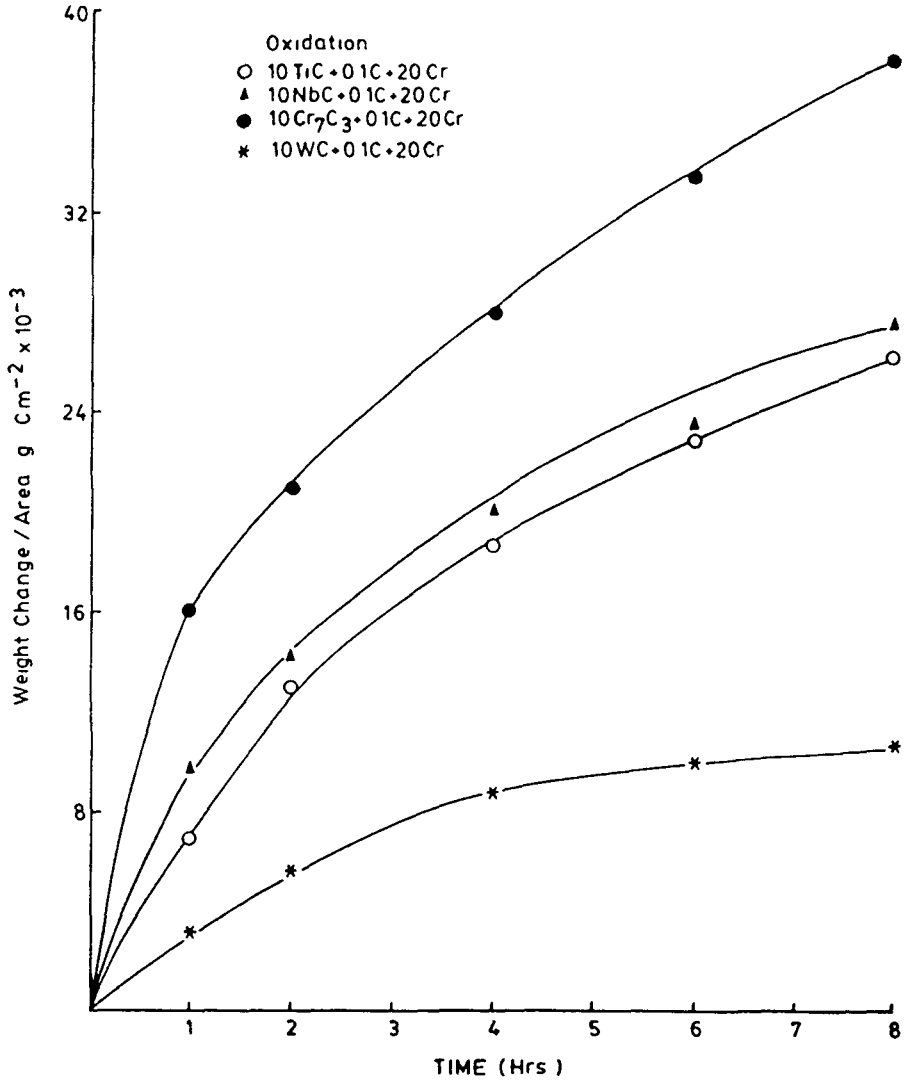

Fig. 5.1 Plots of weight gain Vs time for the oxidation of Fe-10MC-0.1C-20Cr alloys at 900°C for 8 hrs.

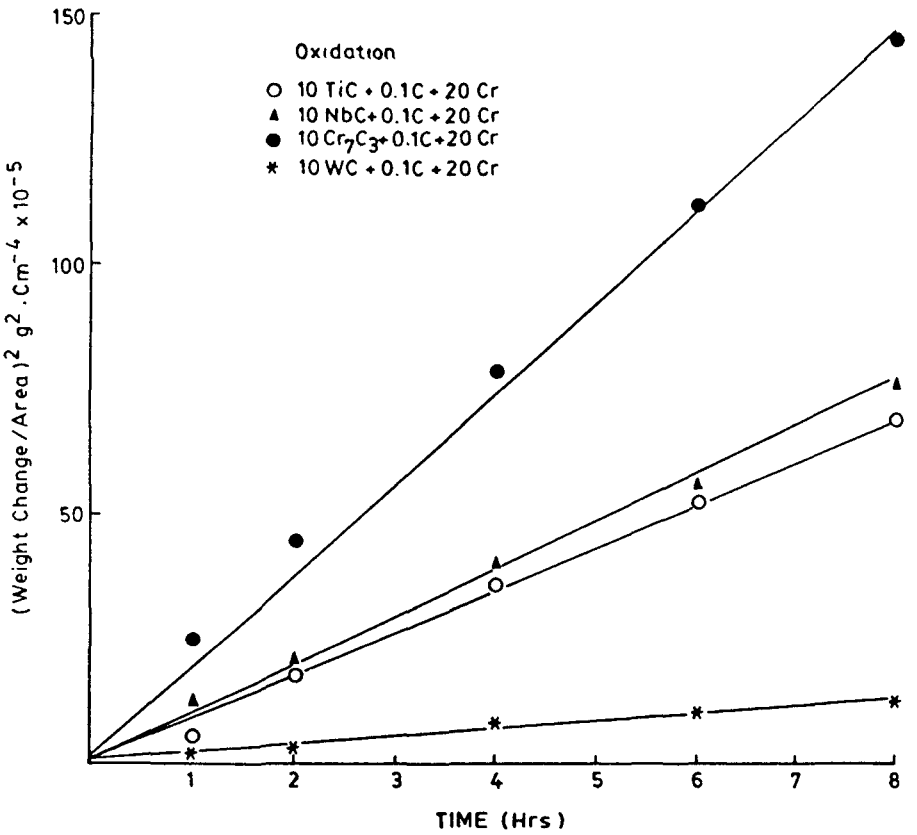

Fig. 5.2 Plots of weight gain^2 Vs time for the oxidation of Fe-10MC-0.1C-20Cr alloys at 900°C for 8 hrs.

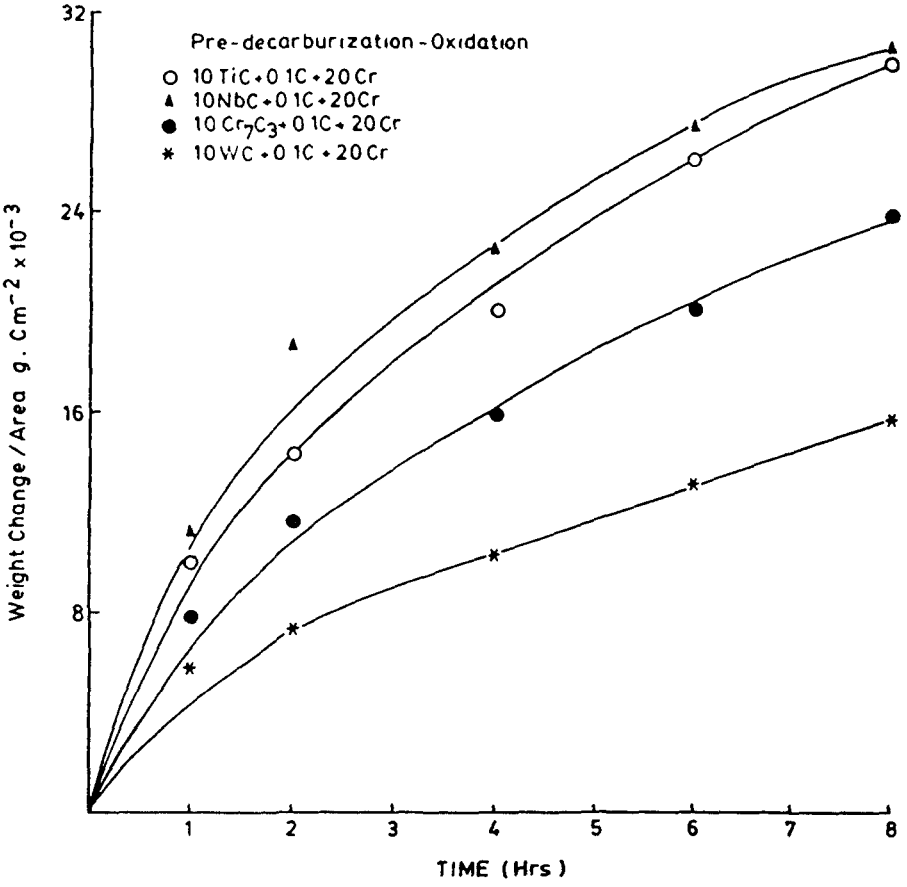

Fig. 5.3 Plots of weight gain Vs time for the oxidation of decarburized Fe-10M-0.1C-20Cr alloys at 900°C for 8 hrs.

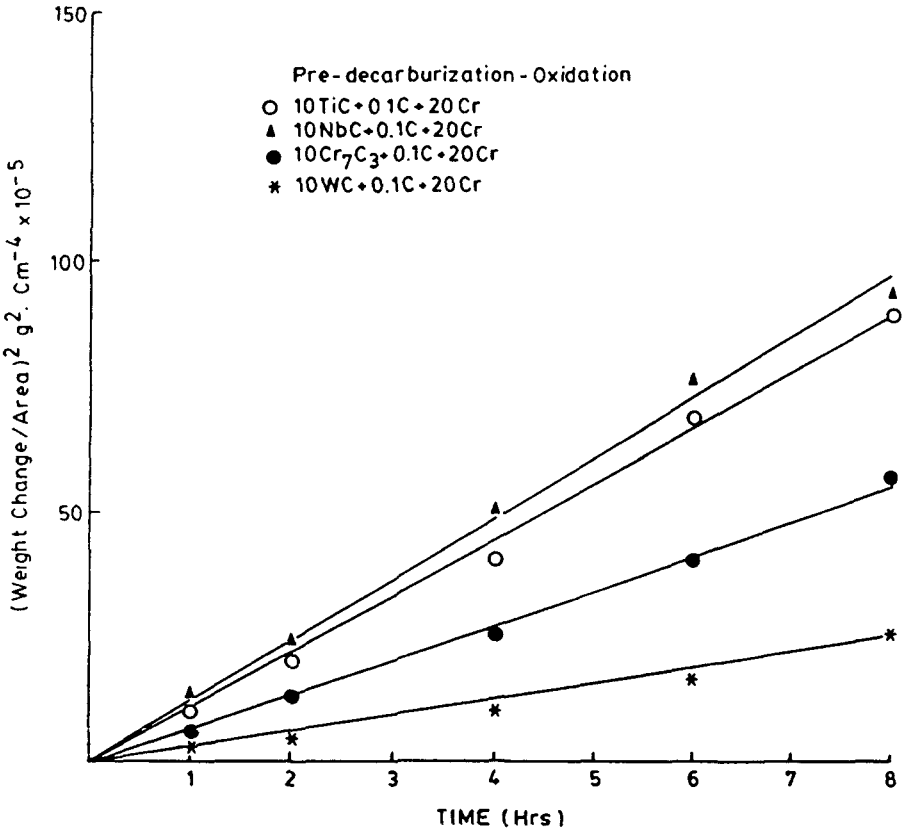

Fig. 5.4 Plots of weight gain^2 Vs time for the oxidation of decarburized Fe-10M-0.1C-20Cr alloys at 900°C for 8 hrs.

Table 5.1

Values of parabolic rate constants Kp for the oxidation of undecarburized and predecarburized Fe-10MC-0.1C-20Cr alloys at 900°C in $Kg^2.m^{-4}.Sec.^{-1}x10^{-7}$

Alloy (wt.%)	undecarburized	predecarburized
Fe-10TiC-0.1C-20Cr	23.43	30.65
Fe-10NbC-0.1C-20Cr	25.93	33.34
Fe-10Cr_7C_3-0.1C-20Cr	50.93	19.26
Fe-10WC-0.1C-20Cr	4.81	8.80

5.1.2 Metallographic Studies

5.1.2.1 Fe-10TiC-0.1C-20Cr Alloy

Figure 5.5 shows an optical micrograph of sintered Fe-10TiC-0.1C-20Cr alloy. The micrograph shows the presence of polygonal ferrite in a Cr-rich iron matrix porous in nature. The alloy on oxidation forms an internal Cr_2O_3 sorrounding the ferrite polygonals, TiC is segregated at the grain boundaries (Fig. 5.6). The oxides are the result of preferential oxidation of Cr in the matrix. The thick inner oxide scales largely contain $FeO.Cr_2O_3$ and Cr_2O_3. Due to the presence of carbon, some decarburization occurred during oxidation resulting in the evolution of CO/CO_2 and consequently in the formation of porous scales.

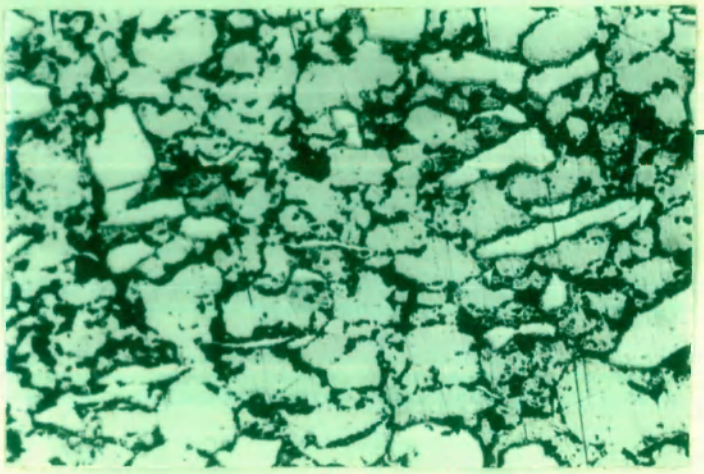

Fig. 5.5 Photomicrograph of a cross-section of Fe-10TiC-0.1C-20Cr alloy undecarburized. X 120

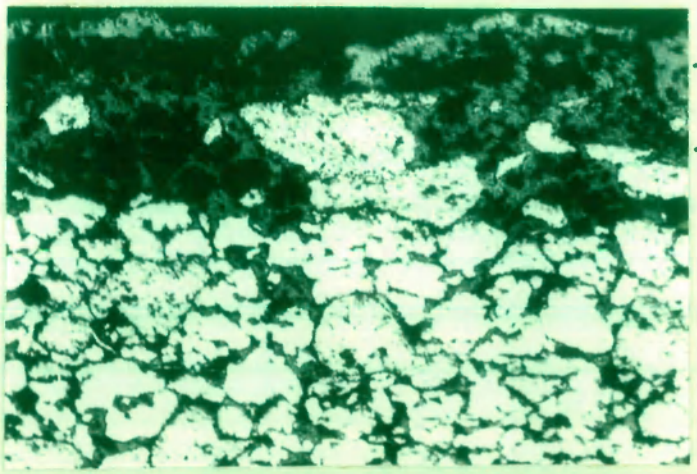

Fig. 5.6 Photomicrograph of a cross-section of Fe-10TiC-0.1C-20Cr, oxidized at 900°C for 8 hrs. X 120

Figure 5.7 shows a photomicrograph of TiC-containing sintered alloy decarburized in wet hydrogen (H_2-H_2O) for 2 hrs. at 900°C. There is quite a bit similarity between undecarburized and decarburized alloys, the only significant difference is the greater porosity of the decarburized alloy. The microstructure of decarburized-oxidized Fe-10TiC-0.1C-20Cr alloy is very similar to that of the corresponding undecarburized-oxidized alloy albeit the scales are less thicker and relatively less porous (Fig. 5.8). The scanning electron photomicrograph of decarburized-oxidized alloy shows the dispersion of TiC in the matrix in conjunction with internal Cr_2O_3 (Fig. 5.9). The incorporation of TiC in the innermost layers of the chromia scales is also apparent. The inner layers of the oxide scales are mainly comprised of $FeO.Cr_2O_3$ and the outer layers contain Fe_2O_3, the middle layers of the scale show a sort of denderite growth of iron oxide, Fe_3O_4 in which Cr_2O_3 and TiO_2 are also incorporated.

5.1.2.2 Fe-10NbC-0.1C-20Cr Alloy

Figure 5.10 shows a photomicrograph of Fe-10NbC-0.1C-20Cr sintered alloy. The microstructure contains coarsened polygonal grains of ferrite. In oxidized condition at 900°C, the photomicrograph (Fig. 5.11) exhibits internal Cr_2O_3 particles which are segregated at the grain boundaries of ferrite matrix. The NbC grains are dispersed in a ferrite matrix. A relatively thick layer of Cr_2O_3 is present in the inner scale

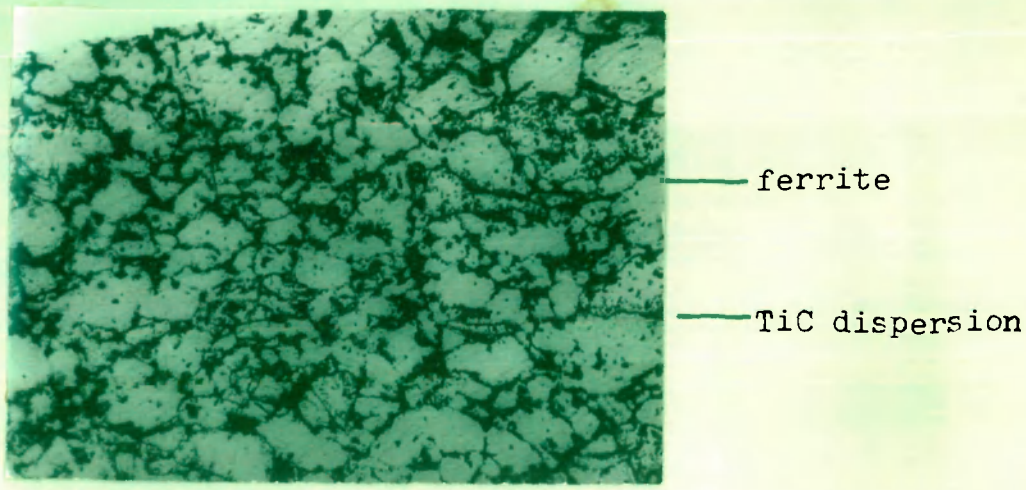

Fig. 5.7 Photomicrograph of a cross-section of Fe-10TiC-0.1C-20Cr alloy, decarburized at 900°C for 2 hrs. X 120

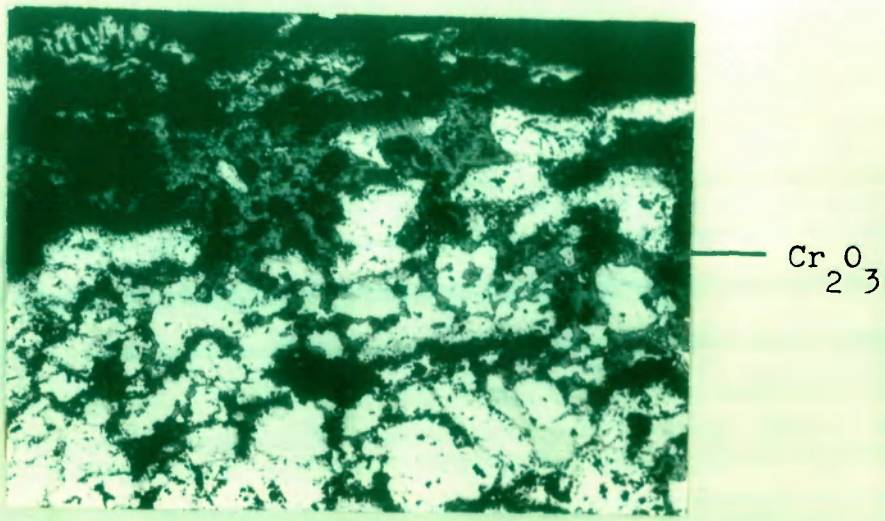

Fig.5.8 Photomicrograph of a cross-section of predecarburized (2 hrs) Fe-10TiC-0.1C-20Cr alloy, oxidized at 900°C for 8 hrs. X 120

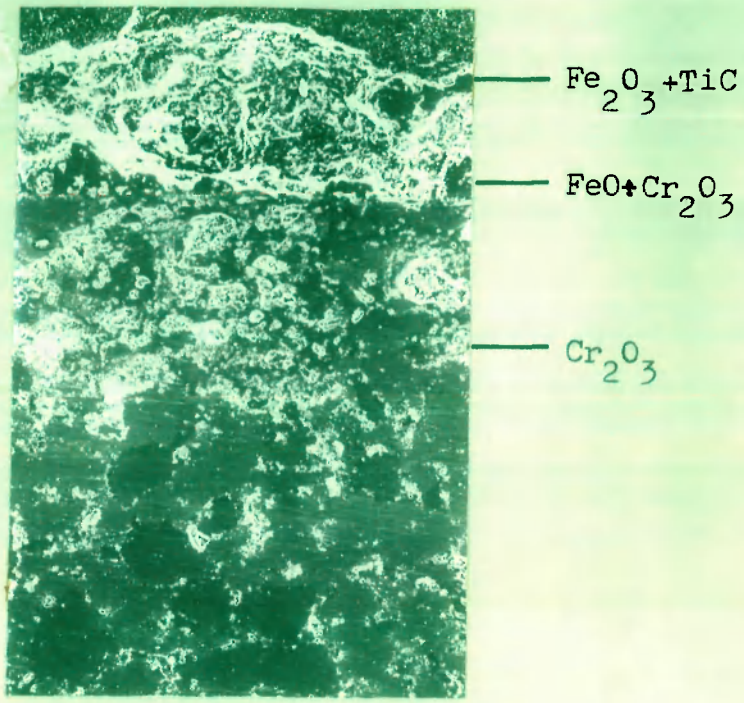

Fig. 5.9 SEM picture of predecarburized (2 hrs) Fe-10TiC-0.1C-20Cr alloy, oxidized at 900°C for 8 hrs.
X 120

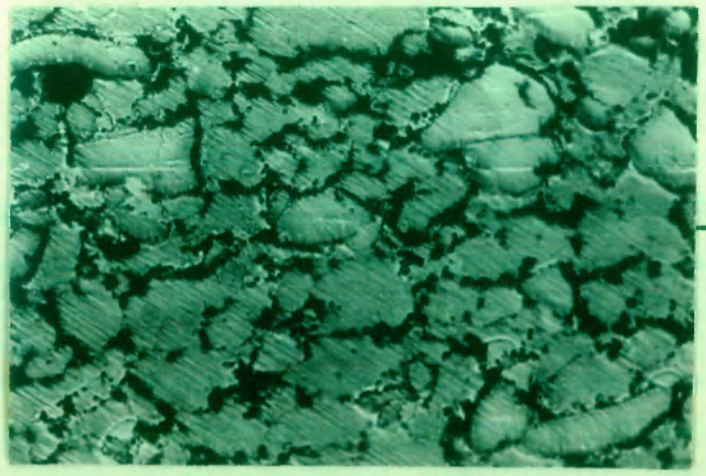

Fig. 5.10 Photomicrograph of a cross-section of Fe-10NbC-0.1C-20Cr alloy, undecarburized
X 120

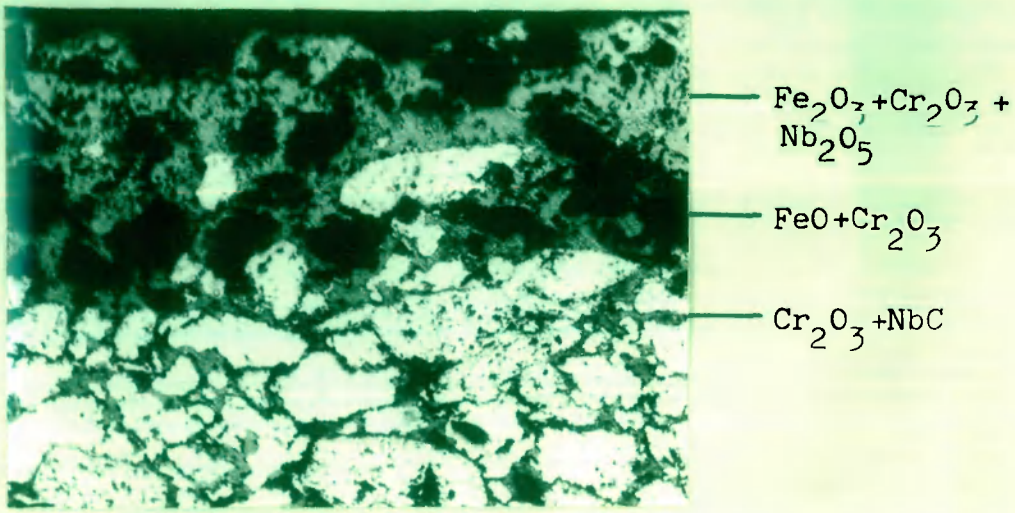

Fig. 5.11 Photomicrograph of a cross-section of Fe-10NbC-0.1C-20Cr alloys, oxidized at 900°C for 8 hrs. X 120

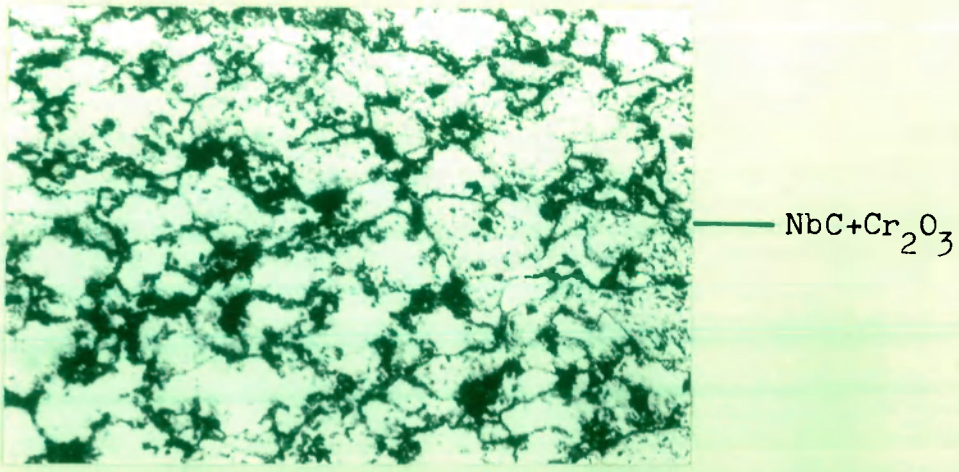

Fig. 5.12 Photomicrograph of a cross-section of Fe-10NbC-0.1C-20Cr alloys decarburized at 900°C for 2 hrs. X 120

in which some NbC is also incorporated. The outer scales are mainly comprised of iron oxides containing Cr_2O_3 and Nb_2O_5 inclusions.

The optical micrograph (Fig. 5.12) of sintered Fe-10NbC-0.1C-20Cr alloy decarburized in wet hydrogen (H_2-H_2O) shows the presence of polygonal grains of ferrite in which NbC is present as a dispersed phase. The structure is porous and internal Cr_2O_3 formed during decarburization is present at the grain boundaries. Figure 5.13 shows a photomicrograph of the decarburized-oxidized sintered alloy. The oxide scales are almost entirely consisted of Cr_2O_3 in which NbC is incorporated and like undecarburized-oxidized alloy, presence of internal Cr_2O_3 grains can be seen at the ferrite interstices.

5.1.2.3 Fe-10WC-0.1C-20Cr Alloy

The photomicrograph of sintered Fe-10WC-0.1C-20Cr alloy (Fig. 5.14) shows the presence of polygonal ferrites in a Cr-enriched matrix, the WC particles are present rather ununiformly at the grain boundaries. Figure 5.15 shows the photomicrograph of the same alloy oxidized at 900°C for 8 hrs. in 1 atm. O_2. Chromium is internally oxidized to Cr_2O_3 and is present with WC at the grain boundaries. A layer of $FeO.Cr_2O_3$ is present in the inner scales in which some WC particles are also incorporated, the outer layers of the scales contain Fe_2O_3 in which some Cr_2O_3 is also present. The scales are comparatively less

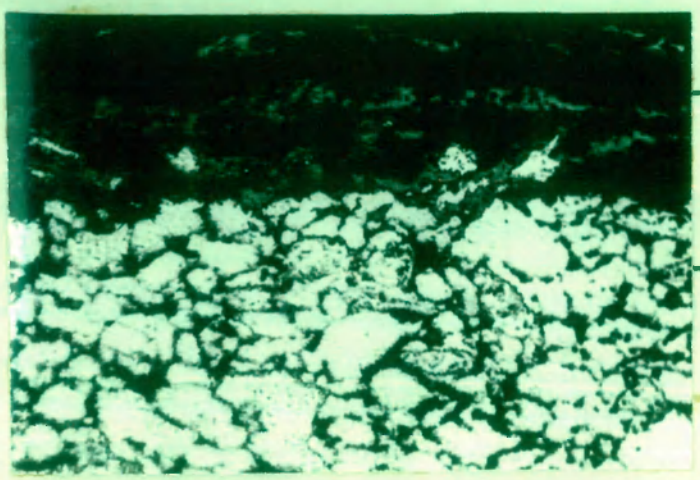

Fig. 5.13 Photomicrograph of a cross-section of predecarburized (2 hrs.) Fe-10NbC-0.1C-20Cr alloys, oxidized at 900°C for 8 hrs.
X 120

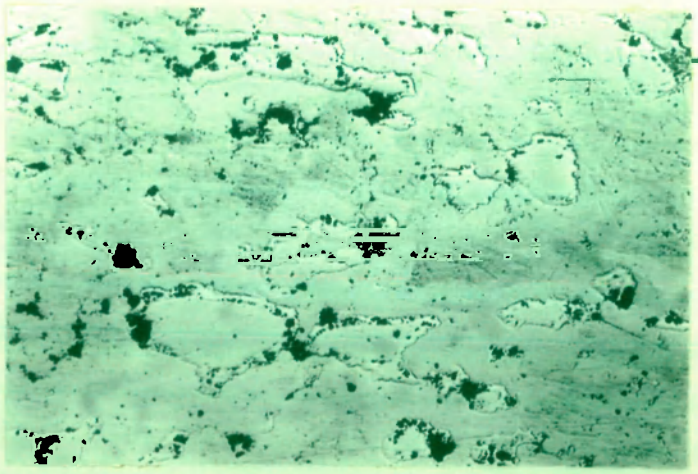

Fig. 5.14 Photomicrograph of a cross-section of Fe-10WC-0.1C-20Cr alloy, undecarburized
X 120

porous than the scales of TiC- and NbC-containing iron-base alloys. The scanning electron photomicrograph of oxidized alloy shows the presence of a relatively nonporous and more adherent scales (Fig. 5.16). The innermost layer of the scales are comprised of Cr_2O_3 and outermost contains Fe_2O_3 incorporating some Cr_2O_3. The middle portion of the scales show denderite of iron oxide(s) in which WO_3 and Cr_2O_3 particles are also participated. Figure 5.17 shows a photomicrograph of Fe-10WC-0.1C-20Cr sintered alloy decarburized in wet hydrogen at 900°C for 2 hrs. By and large WC does not seem to be much affected but some Cr present in the matrix got oxidized internally at the grain boundaries. In the decarburized-oxidized condition (Fig. 5.18), the inner scales are largely consisted of Cr_2O_3 followed by thicker but porous layers of wustite containing Cr_2O_3 and WO_3. The porosity is perhaps developed due to evolution of CO/CO_2 during oxidation.

5.1.2.4 Fe-10Cr_7C_3-0.1C-20Cr Alloy

Figure 5.19 represents a photomicrograph of sintered Fe-10Cr_7C_3-0.1C-20Cr alloy in as cast condition, the microstructure indicates the presence of 2 phases : a polygonal ferritic phase (light) and a Cr_7C_3-rich iron solution phase (dark) separated by well defined boundaries. When this alloy is oxidized at 900°C for 8 hrs. (Fig.5.20), the innermost layers of the porous oxide scales are consisted of Cr_2O_3 whereas the

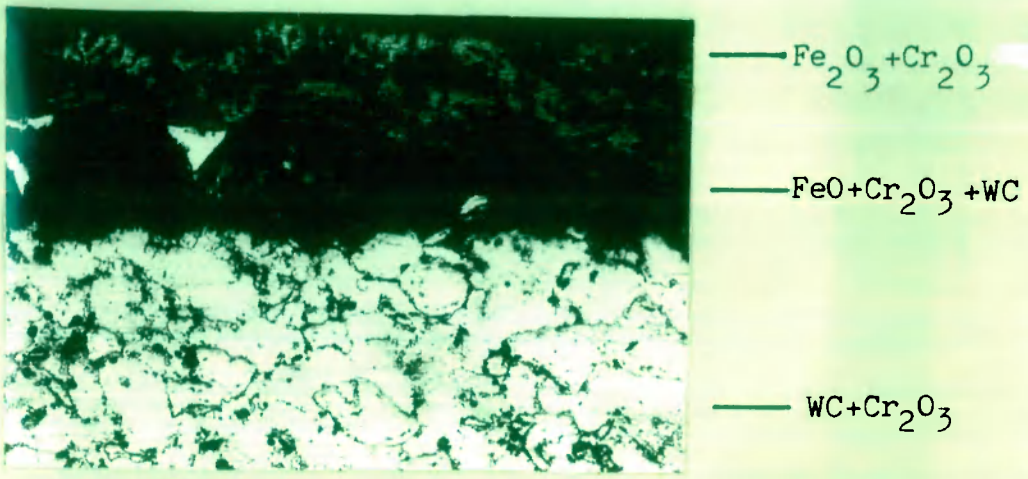

Fig. 5.15 Photomicrograph of a cross-section of Fe-10WC-0.1C-20Cr alloy oxidized at 900°C for 8 hrs. X 120

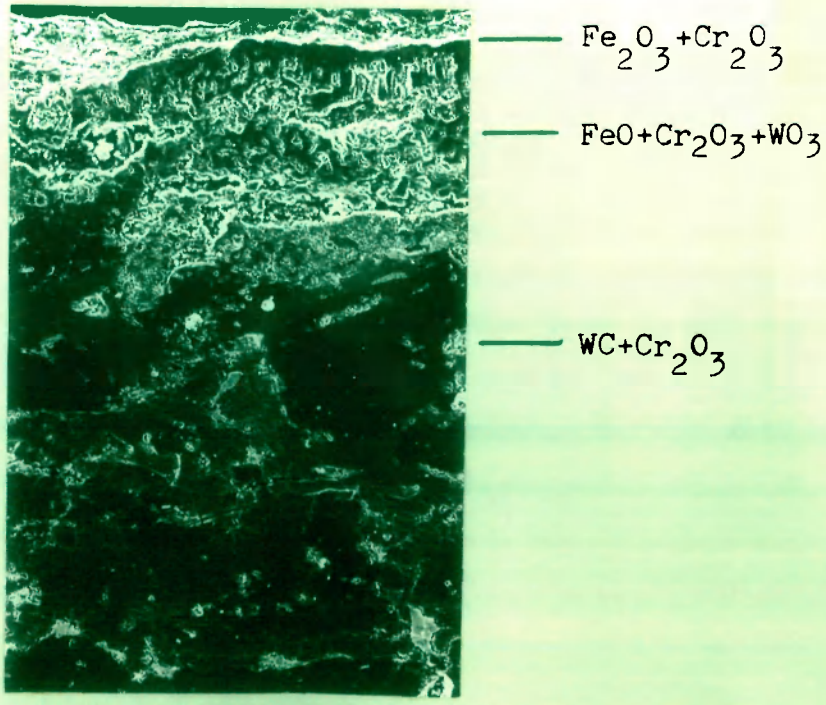

Fig. 5.16 SEM picture of Fe-10WC-0.1C-20Cr alloy, oxidized at 900°C for 8 hrs. X 100

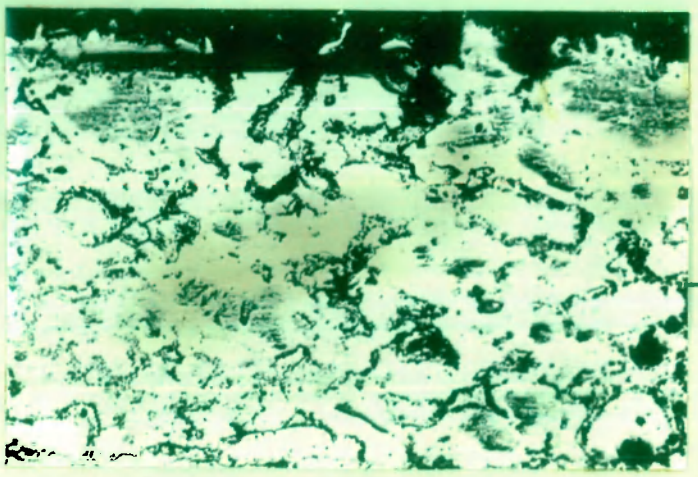

Fig. 5.17 Photomicrograph of a cross-section of Fe-10WC-0.1C-20Cr alloy, decarburized at 900°C for 2 hrs. X 120

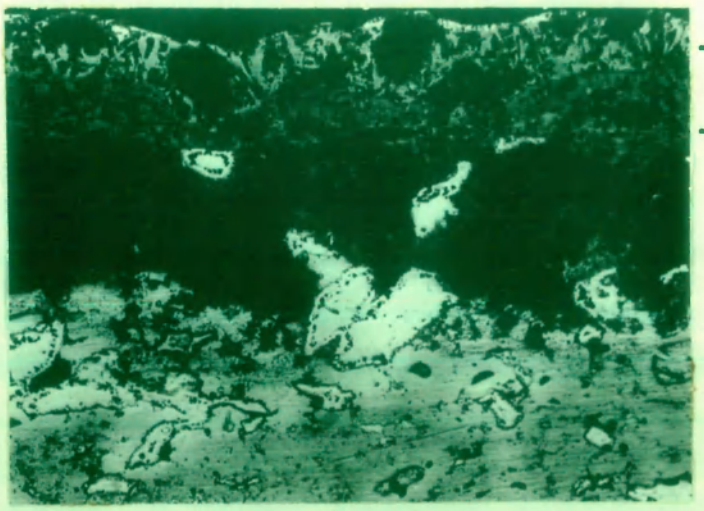

Fig. 5.18 Photomicrograph of a cross-section of predecarburized (2 hrs.) Fe-10WC-0.1C-20Cr alloy, oxidized at 900°C for 8 hrs. X 120

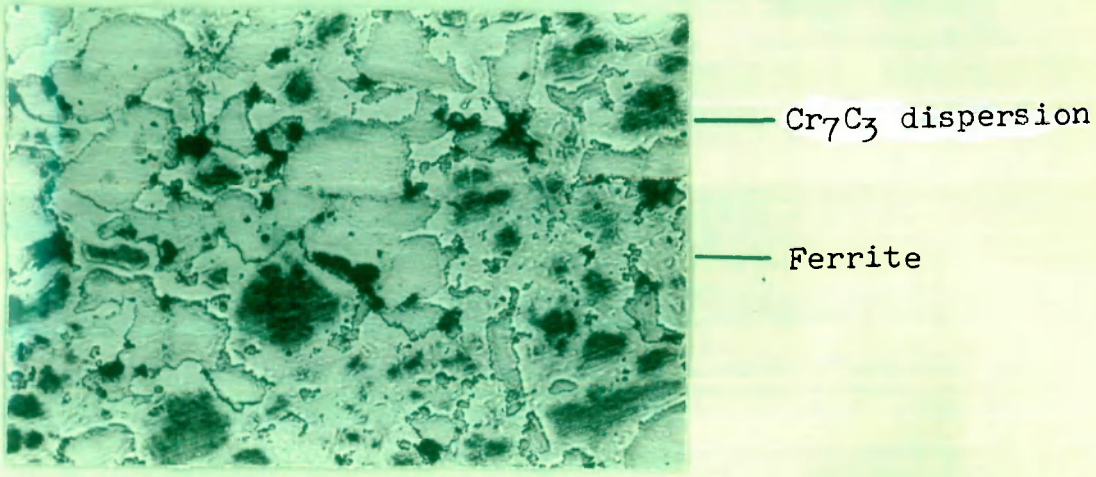

Fig.5.19 Photomicrograph of a cross-section of Fe-10Cr_7C_3-0.1C-20Cr alloy, undecarburized. X 120

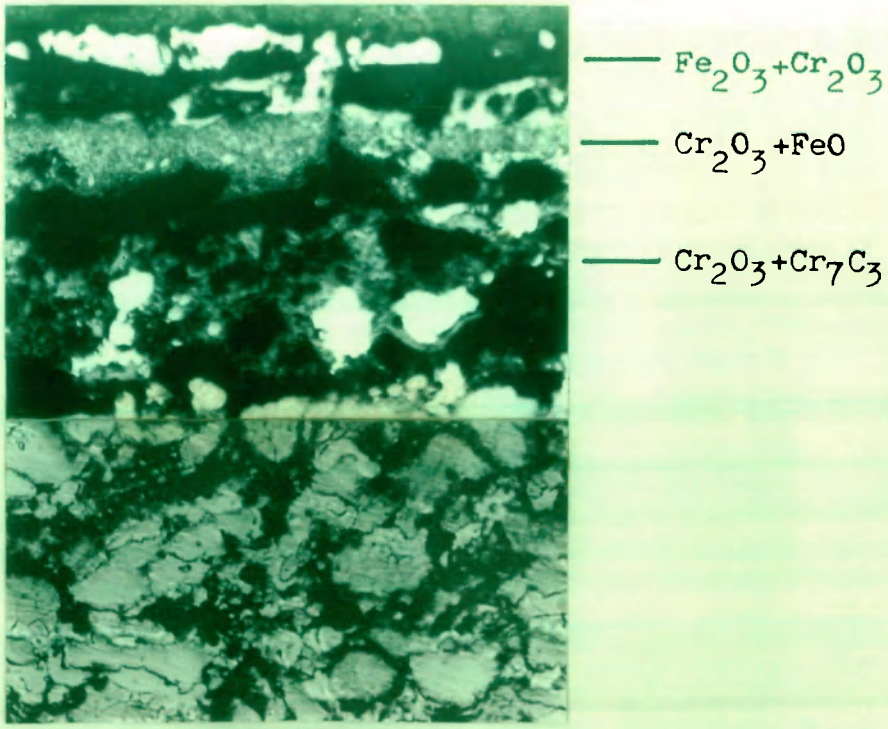

Fig.5.20 Photomicrograph of a cross-section of Fe-10Cr_7C_3-0.1C-20Cr alloy, oxidized at 900°C for 8 hrs. X 400

outer scale contains Fe_2O_3. The middle layers of the scales are nonporous and contain mainly the spinel $FeO.Cr_2O_3$. The inner chromia scales have incorporated some Cr_7C_3. The scanning electron photomicrograph of the oxidized alloy (Fig. 5.21) shows the presence of a dark phase which entirely consists of internal oxide, Cr_2O_3 with dispersion of Cr_7C_3 particles. This phase co-exists with a light ferritic phase, the Cr_7C_3 particles are concentrated at the grain boundaries of this phase.

The decarburized Fe-10Cr_7C_3-0.1C-20Cr in its microstructure (Fig. 5.22) shows the presence of 2 phases : the light phase representing ferrite and a dark phase representing Cr-rich iron solid solution, the Cr_7C_3 particles are dispersed in both the phases. Some Cr is oxidized to Cr_2C_3 in the Cr-rich phase. The Cr-rich phase is much more porous than the ferritic phase. Figures 5.23 and 5.24 show optical and scanning electron photomicrographs, respectively of Fe-10Cr_7C_3-0.1C-20Cr decarburized in H_2-H_2O atmosphere for 2 hrs. followed by oxidation in 1 atm. O_2 for 8 hrs. The alloy matrix of decarburized-oxidized alloy shows the presence of internal Cr_2O_3 phase along with light ferritic phase. Cr_7C_3 grains are segregated at the ferritic grain broundaries. The thicker inner scale is largely consisted of $Cr_2O_3/Cr_2O_3.FeO$. Due to decarburization and subsequent exposure of FeO to oxygen, some Fe_2O_3 is formed in the inner

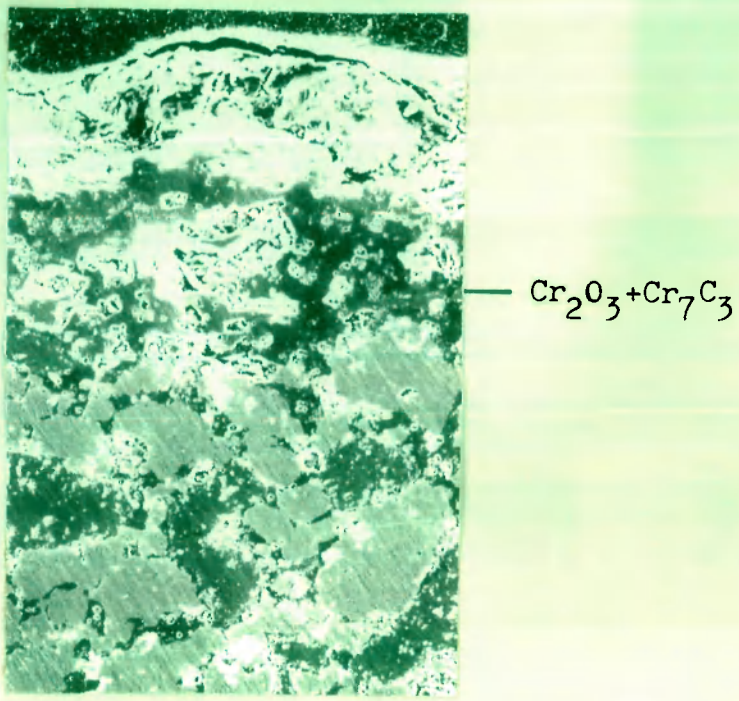

Fig. 5.21 SEM picture of Fe-10Cr_7C_3-0.1C-20Cr alloys, oxidized at 900°C for 8 hrs. X 200

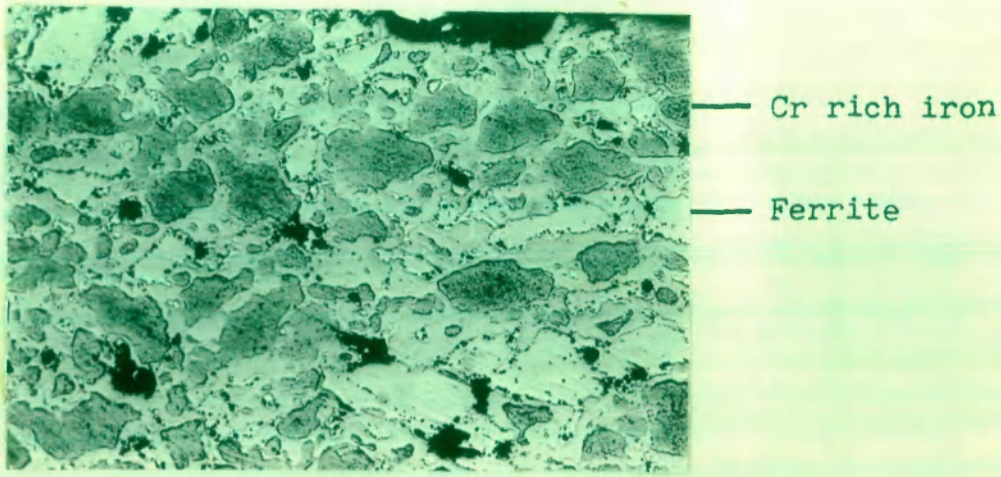

Fig. 5.22 Photomicrograph of a cross-section of Fe-10Cr_7C_3-0.1C-20Cr alloy, decarburized at 900°C for 2 hrs. X 120

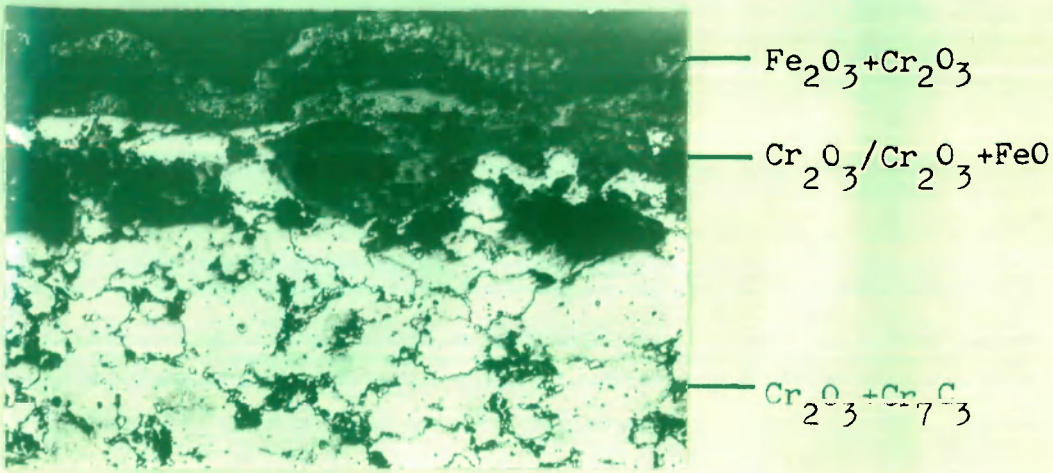

Fig. 5.23 Photomicrograph of a cross-section of predecarburized (2 hrs.) Fe-10Cr_7C_3-0.1C-20Cr alloy, oxidized at 900°C for 8 hrs. X 120

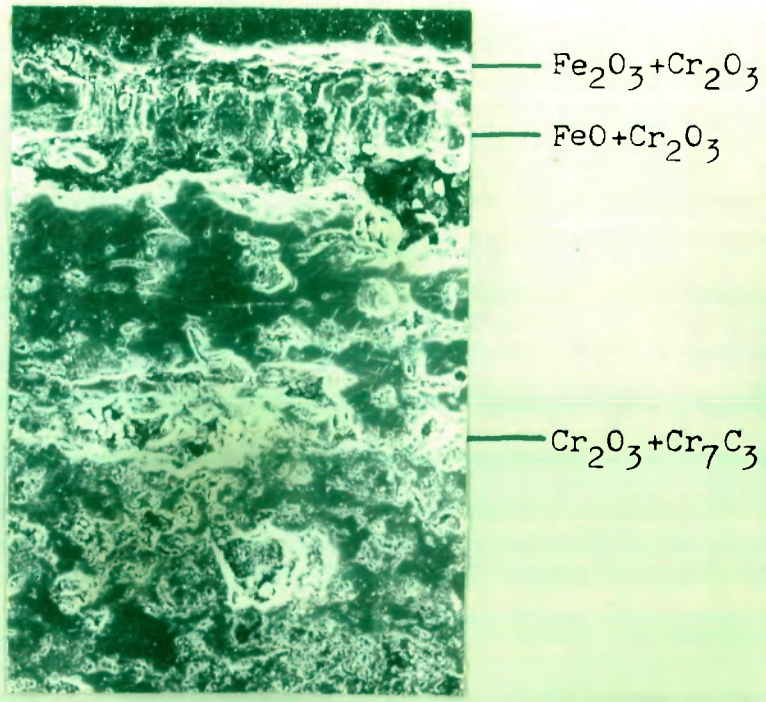

Fig. 5.24 SEM picture of predecarburized (2 hrs.) Fe-10Cr_7C_3-0.1C-20Cr alloy, oxidized at 900°C for 8 hrs. X 100

scales. The outer scales contain Fe_2O_3 in which some Cr_2O_3 is also included.

5.2 Discussion

The oxidation behaviour of iron-based sintered alloys of the composition : Fe-10MC-0.1C-20Cr was studied in the normal (undecarburized) state in 1 atm. O_2 at 900°C. The alloys oxidized following a parabolic rate law indicating a diffusion controlled mechanism operated during oxidation. The WC-containing alloy oxidized at the slowest rate and Cr_7C_3-containing alloy at the fastest rate. There are three important morphological features of the oxidized alloys. An internal Cr_2O_3 is formed as a separate phase along with a ferritic phase, Cr_7C_3 is present as a dispersion but mainly concentrated at the ferritic polygonal grain boundaries, $Cr_2O_3/FeO.Cr_2O_3$ layer is present invariably at the alloy/scale interface. These three factors seem to be responsible for relatively low oxidation rates of Fe-10MC-0.1C-20Cr alloys. This contention is further evident from the fact that Fe-10MC alloys (Chapter IV) have oxidation rates at least one order of magnitude higher than the latter. During oxidation of Fe-10MC-0.1C-20Cr, the carbide is largely remained unaffected which is shown by the incorporation of the carbides in the scales. Due to presence of carbon, some decarburization occurs during oxidation, resulting in the disruption of the protective film.

Fe-10MC-0.1C-20Cr alloys are decarburized in low oxygen potential atmosphere ($\backsim 10^{-19}$) of O_2 at 900°C, although there is no well defined decarburized layer but there is evidence of decarburization from microstructures. The decarburized alloys were further oxidized at 900°C in 1 atm. O_2. With the exception of NbC-containing alloys, the decarburized alloys oxidize at a slightly higher rate than the undecarburized alloy. This could be attributed to the highly porous structure of the decarburized alloys. But it is to be noted that there is only marginal difference in the oxidation rates of decarburized and undecarburized Fe-10MC-0.1C-20Cr alloys. In Fe-10MC system (Chapter IV), an opposite behaviour is observed, the oxidation rates of undecarburized alloys are atleast one order of magnitude higher than the decarburized alloys. The oxidation behaviour of decarburized Fe-10MC alloy has been explained firstly on the basis of the formation of a thin protective film during decarburization in H_2-H_2O atmosphere which retards the mobility of carbon atoms and secondly, the presence of a fine carbide dispersion in an austenitic matrix which considerably reduces the level of decarburization during oxidation and in consequence assists in retaining the integrity of oxide scales. In Fe-10MC-0.1C-20Cr system, these factors are valid but unlike Fe-10MC, the undecarburized alloys in addition also have a protective chromium oxide layer which drastically restricts the oxidation rates. This is

reflected by the values of oxidation rates of undecarburized and decarburized Fe-10MC-0.1C-20Cr alloys which are very similar.

CHAPTER VI

DECARBURIZATION AND OXIDATION OF Fe-10MC-0.1C-1.0RE_2O_3 ALLOYS

Niobium carbide (NbC), tungsten carbide (WC) or chromium carbide (Cr_7C_3) (10 weight %) dispersed iron-base alloys containing 0.1 weight % carbon and 1.0 weight % rare earth oxide viz La_2O_3, Pr_2O_3 or Y_2O_3 were prepared by compaction and sintering techniques. The details of experimental procedure are given in Chapter II.

The annealed samples were changed to required size and were placed into reaction tube for oxidation, decarburization and decarburization-oxidation experiments. The oxidation kinetics of the alloys were measured on Sartorius Electronic Microbalance (Model 4410-MP8) in presence of pure oxygen under 1 atmospheric pressure at 900°C for 8 hrs. and decarburization in H_2-H_2O atmosphere at 900°C for 2 hrs.

The morphology of the oxidized/decarburized alloys was studied using optical and scanning electron microscopes. The identification of the various constituents present in the scales/substrate was made by using X-ray diffraction analysis. The details are given in Chapter II.

6.1 Results

6.1.1 Oxidation Kinetics

Weight gain Vs time plots for the oxidation of a series

of iron-base sintered alloys of the general composition Fe-10MC-0.1C-1.0RE_2O_3 (MC is NbC, WC or Cr_7O_3-10 wt. %, C is 0.1 wt. % and RE_2O_3 is La_2O_3, Pr_2O_3 or Y_2O_3-1.0 wt. %) are shown in figures 6.1-6.3. All the alloys were oxidized under one atmospheric oxygen gas at 900°C for 8 hrs. Figures 6.4-6.6 show plots of weight gain^2 Vs time for the same alloys. In general, the weight gain Vs time plots are parabolic and weight gain^2 Vs time plots are linear, indicating the diffusion controlled growth of oxide scales. Table 6.1

Table 6.1

Values of parabolic rate constants Kp for the oxidation of undecarburized and predecarburized Fe-10MC-0.1C-1.0RE_2O_3 alloys at 900°C in $Kg^2.m^{-4}.Sec^{-1} \times 10^{-6}$.

Alloy (wt. %)	undecarburized	predecarburized
Fe-10WC-0.1C-1.0La_2O_3	2.40	8.70
Fe-10WC-0.1C-1.0Pr_2O_3	0.36	2.77
Fe-10WC-0.1C-1.0Y_2O_3	0.26	0.35
Fe-10NbC-0.1C-1.0La_2O_3	25.69	31.60
Fe-10NbC-0.1C-1.0Pr_2O_3	27.78	31.81
Fe-10NbC-0.1C-1.0Y_2O_3	28.47	10.42
Fe-10Cr_7C_3-0.1C-1.0La_2O_3	10.01	6.81
Fe-10Cr_7C_3-0.1C-1.0Pr_2O_3	10.40	10.42
Fe-10Cr C -0.1C-1.0Y O	13.89	9.55

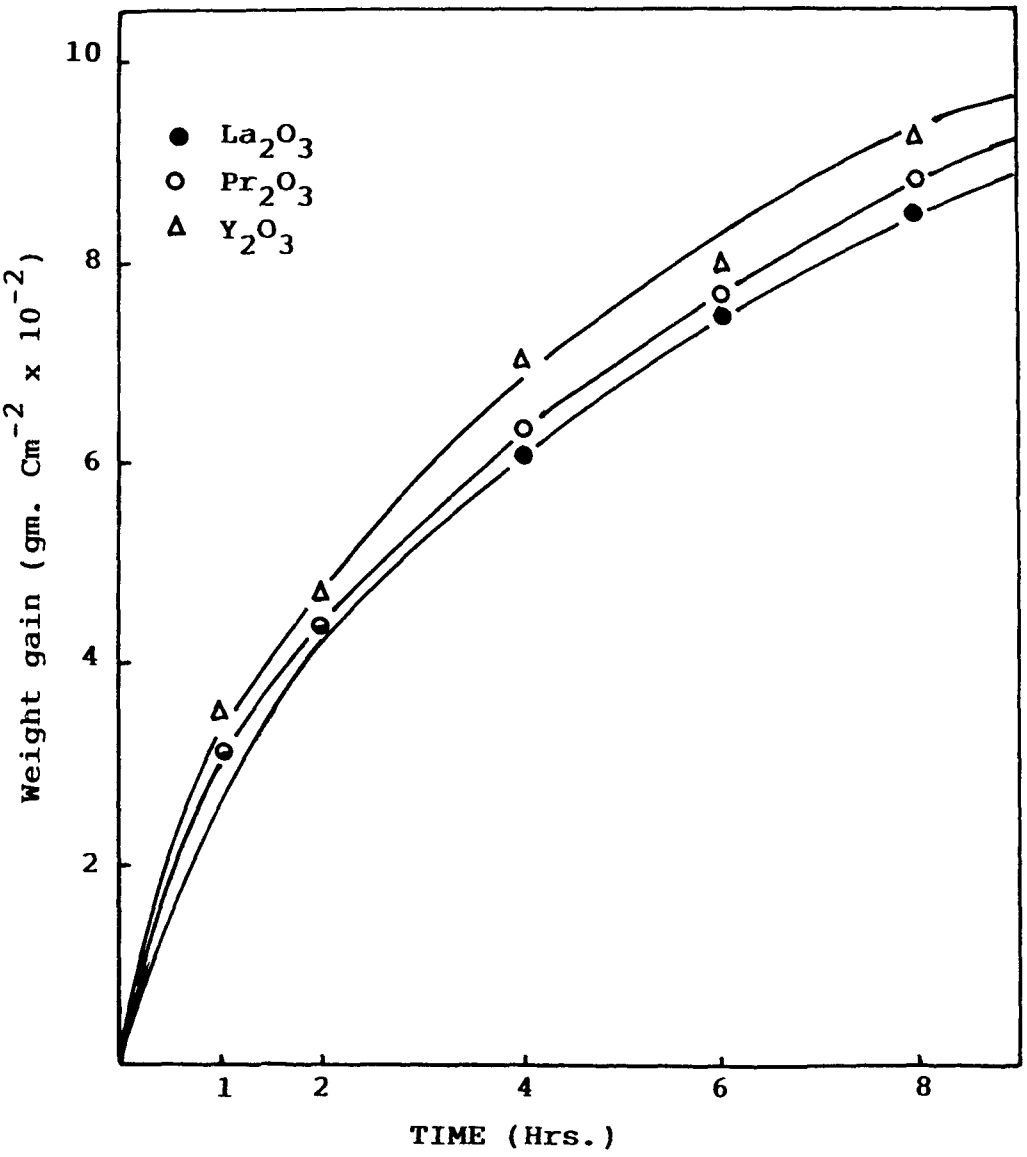

Fig. 6.1 Plots of weight gain Vs time for the oxidation of Fe-10NbC-0.1C-1.0RE_2O_3 alloys at 900°C.

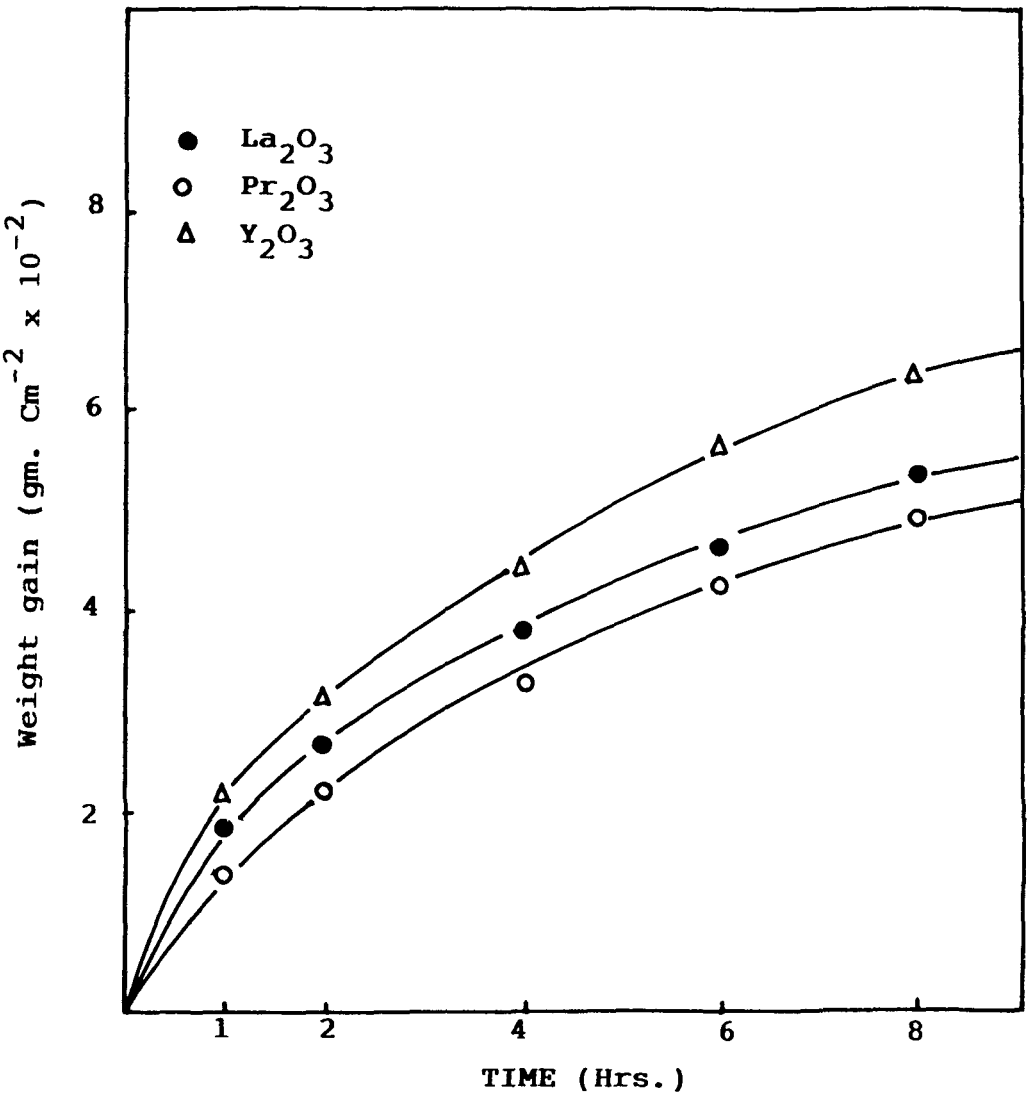

Fig. 6.2 Plots of weight gain Vs time for the oxidation of Fe-10Cr_7C_3-0.1C-1.0RE_2O_3 alloys at 900°C.

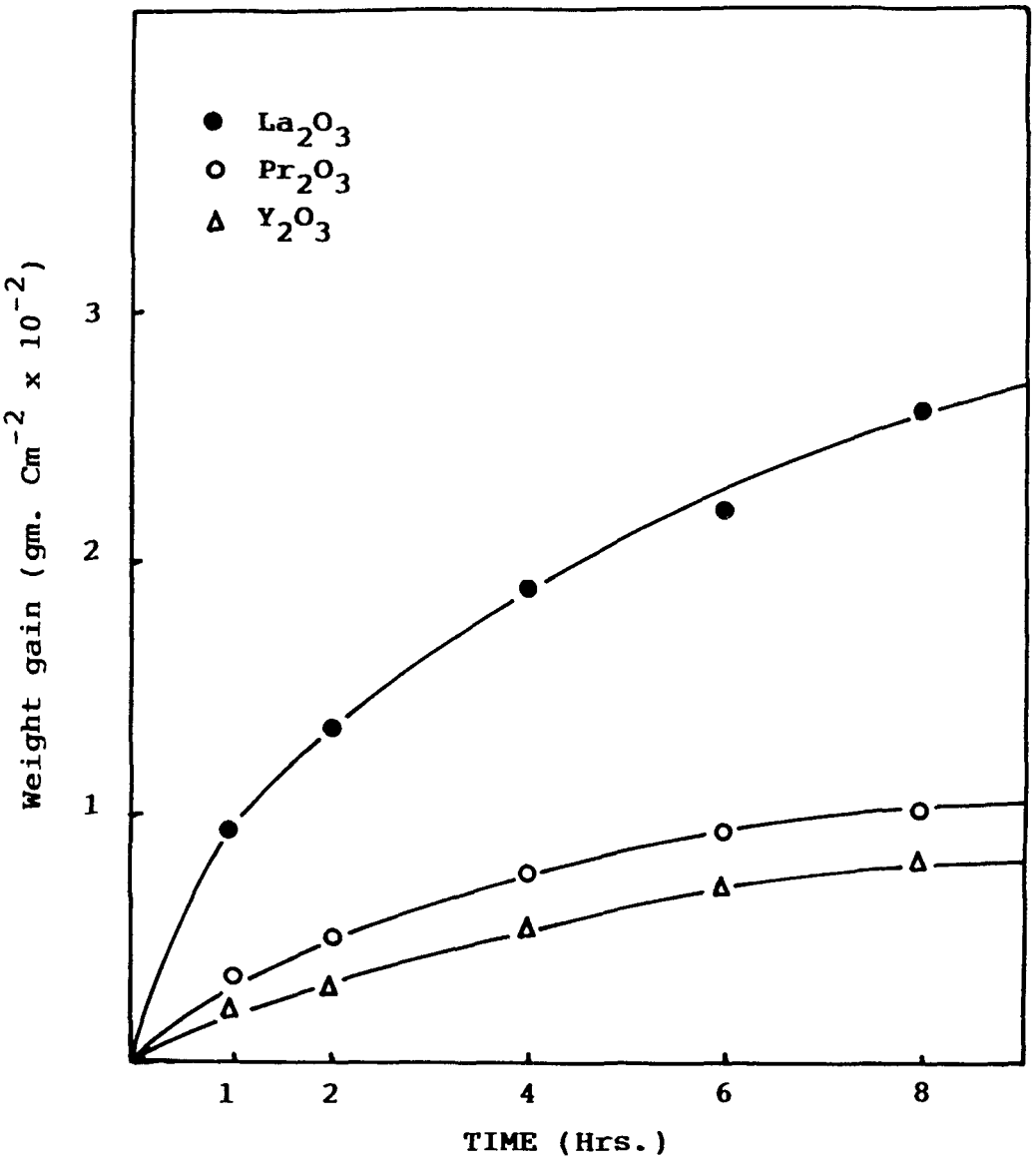

Fig. 6.3 Plots of weight gain Vs time for the oxidation of Fe-10WC-0.1C-1.0RE_2O_3 alloys at 900°C.

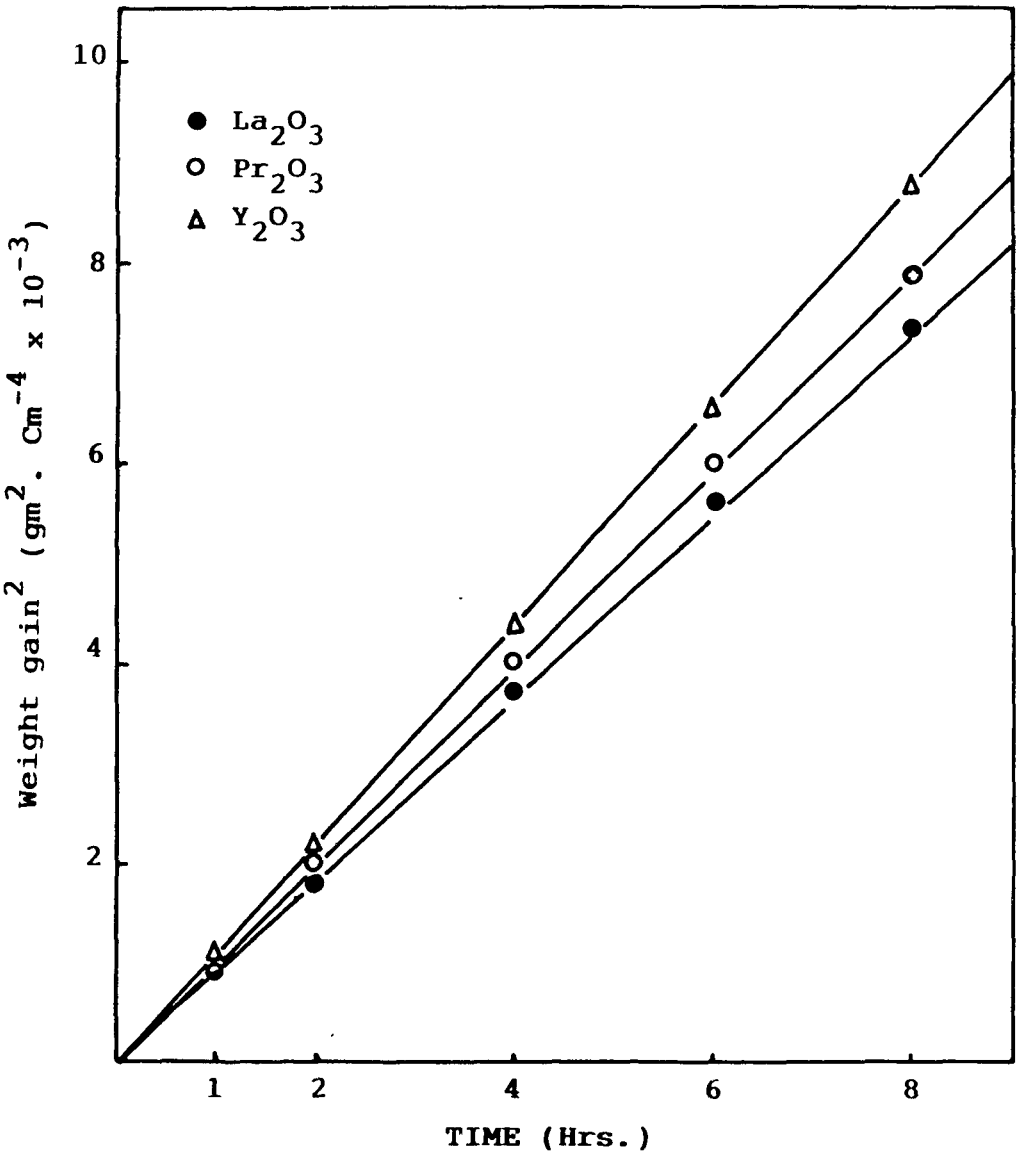

Fig. 6.4 Plots of weight gain^2 Vs time for the oxidation of Fe-10NbC-0.1C-1.0RE_2O_3 alloys at 900°C.

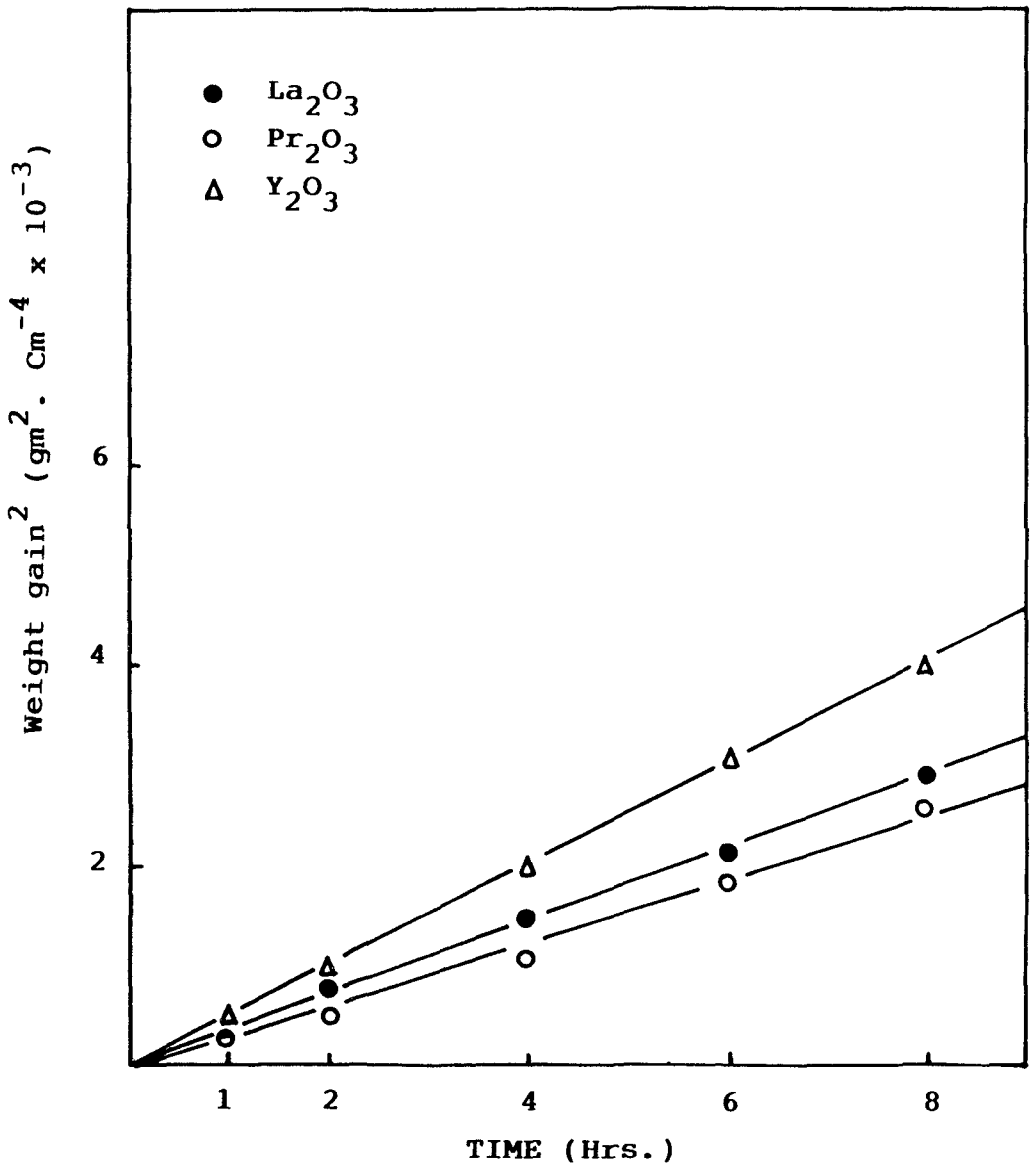

Fig. 6.5 Plots of weight gain^2 Vs time for the oxidation of Fe-10Cr_7C_3-0.1C-1.0RE_2O_3 alloys at 900°C.

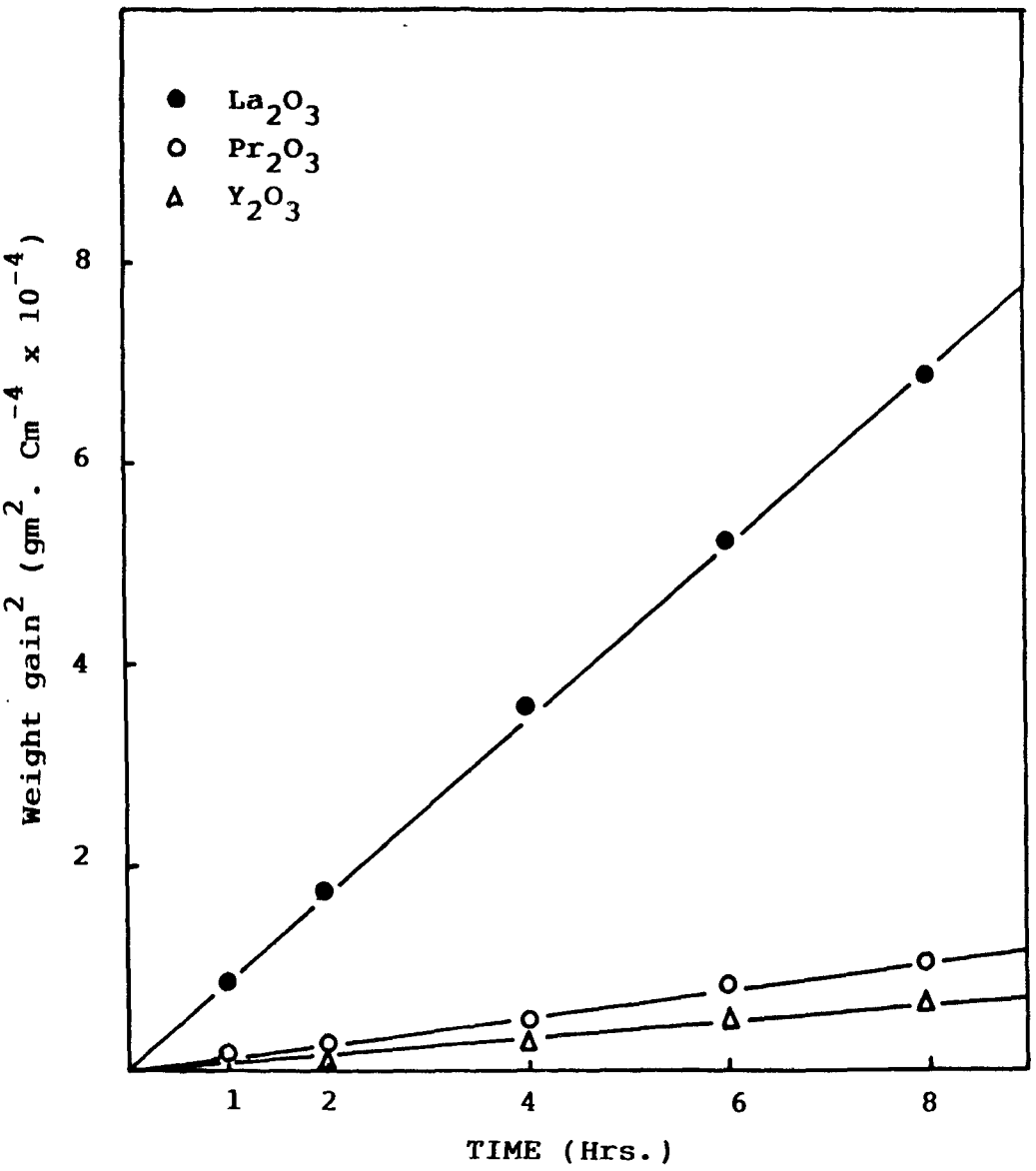

Fig. 6.6 Plots of weight gain^2 Vs time for the oxidation of Fe-10WC-0.1C-1.0RE_2O_3 alloys at 900°C.

lists the values of parabolic rate constant, Kp for the oxidation of Fe-10MC-0.1C-1.0RE_2O_3 at 900°C.

The alloys Fe-10MC-0.1C-1.0RE_2O_3 were decarburized in wet hydrogen (H_2-H_2O) for 2 hrs. at 900°C and were subsequently oxidized in O_2(g) at the same temperature for 8 hrs. The weight gain Vs time and weight gain^2 Vs time plots are shown in Figures 6.7-6.9 and 6.10-6.12 respectively. The decarburized alloys are also seemed to follow a parabolic rate law during oxidation indicating the operation of a diffusion controlled mechanism during oxide growth. The values of rate constant are given in Table 6.1.

6.1.2 Metallographic Studies

6.1.2.1 Fe-10NbC-0.1C-1.0RE_2O_3 Alloys

Figures 6.13-6.14 show photomicrographs of Pr_2O_3 and Y_2O_3 containing iron-base sintered alloys of the general composition : Fe-10NbC-0.1C-1.0RE_2O_3 in as-cast condition. The photomicrographs show the presence of polygonal ferritic grains and the carbides at the grain boundaries. Rare earth oxide particles are also present as inclusions particularly in the ferrite phase. On decarburization in wet hydrogen (H_2-H_2O), there is much more segregation of carbides at the polygonal interstices (Figs. 6.15 and 6.16) otherwise the microstructures of decarburized and undecarburized alloys look the same.

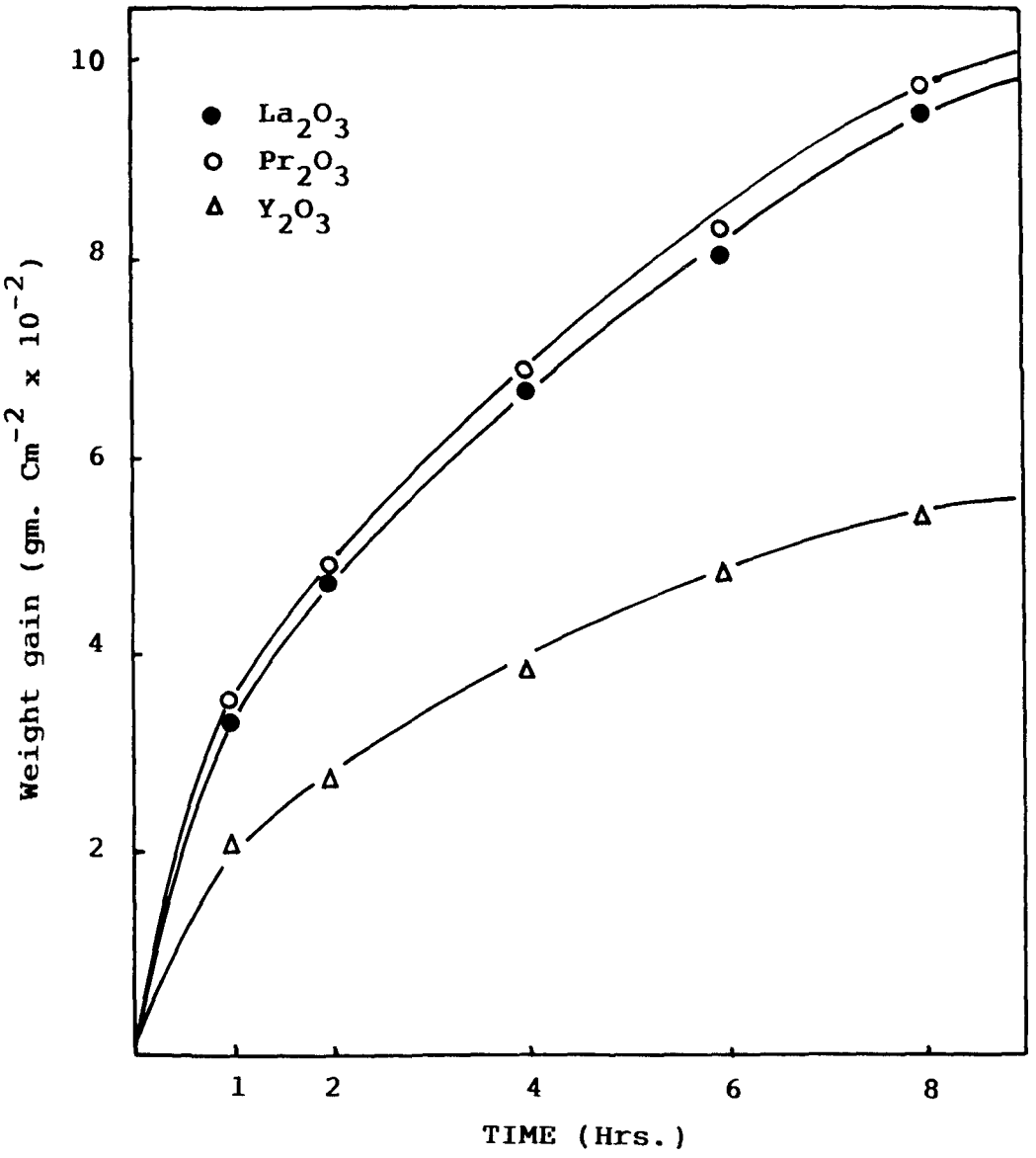

Fig 6.7 Plots of weight gain Vs time for the oxidation of decarburized Fe-10NbC-0.1C-1.0RE_2O_3 alloys at 900°C.

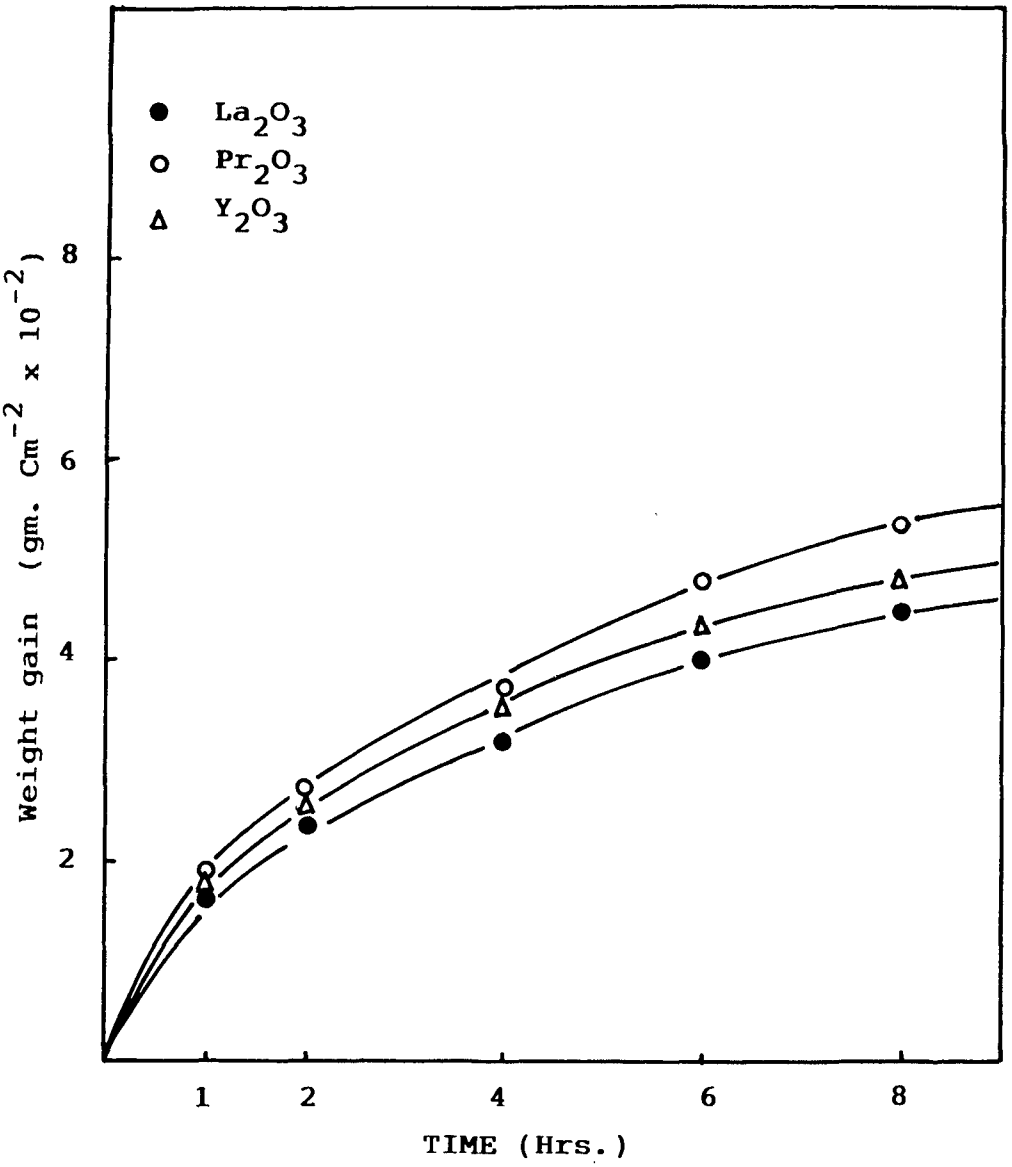

Fig. 6.8 Plots of weight gain Vs time for the oxidation of decarburized Fe-10Cr_7C_3-0.1C-1.0RE_2O_3 alloys at 900°C.

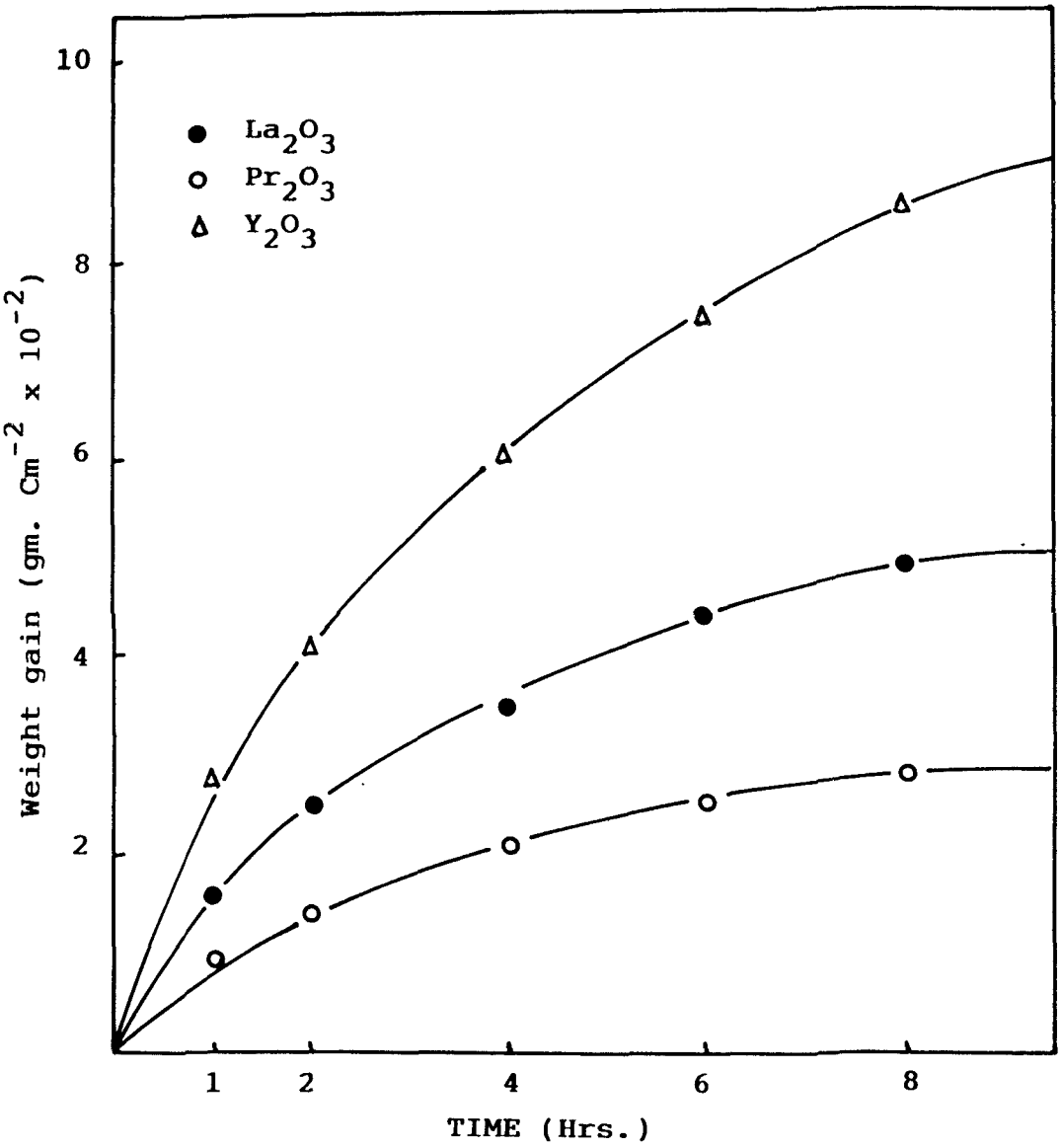

Fig. 6.9 Plots of weight grain Vs time for the oxidation of decarburized Fe-10WC-0.1C-1.0RE_2O_3 alloys at 900°C.

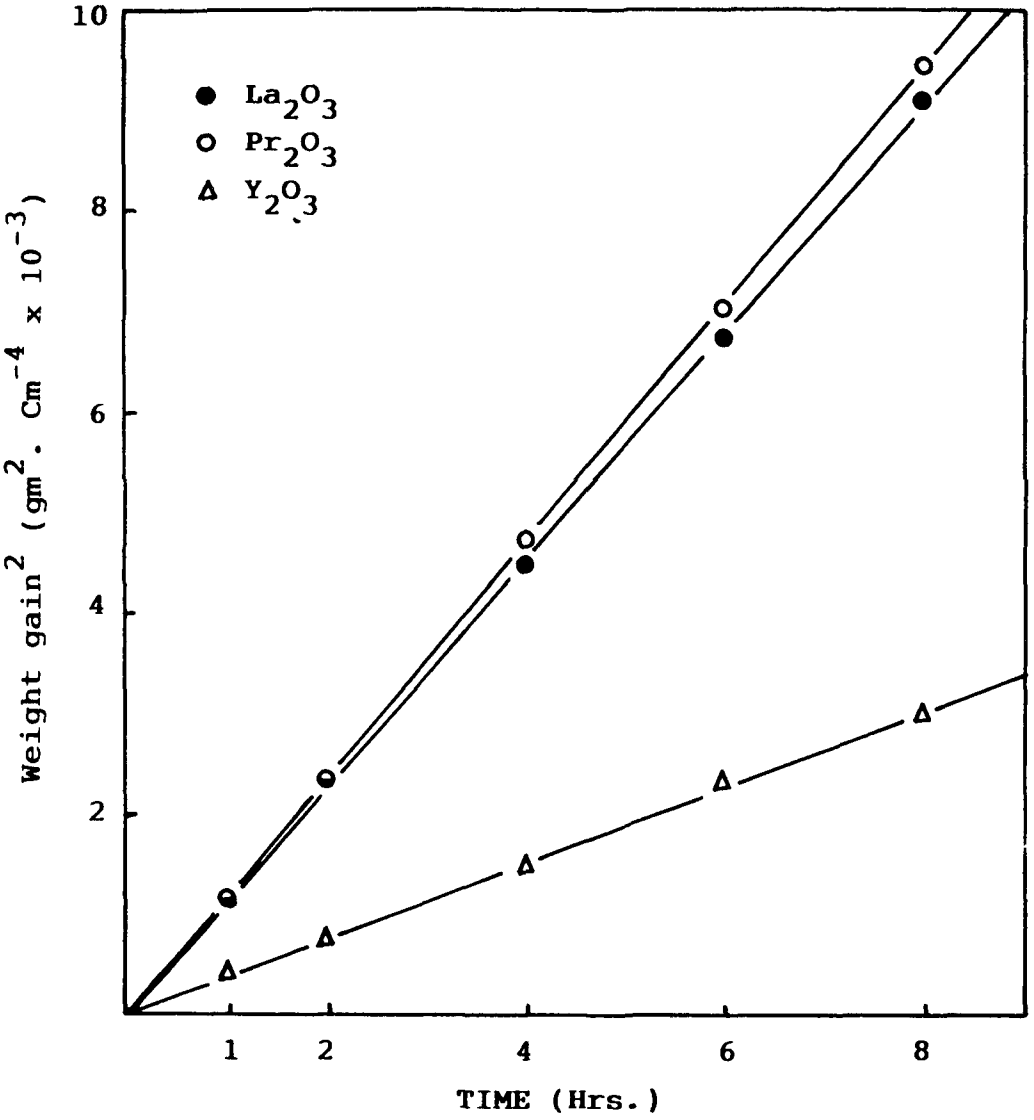

Fig. 6.10 Plots of weight gain^2 Vs time for the oxidation of decarburized Fe-10NbC-0.1C-1.0RE_2O_3 alloys at 900°C.

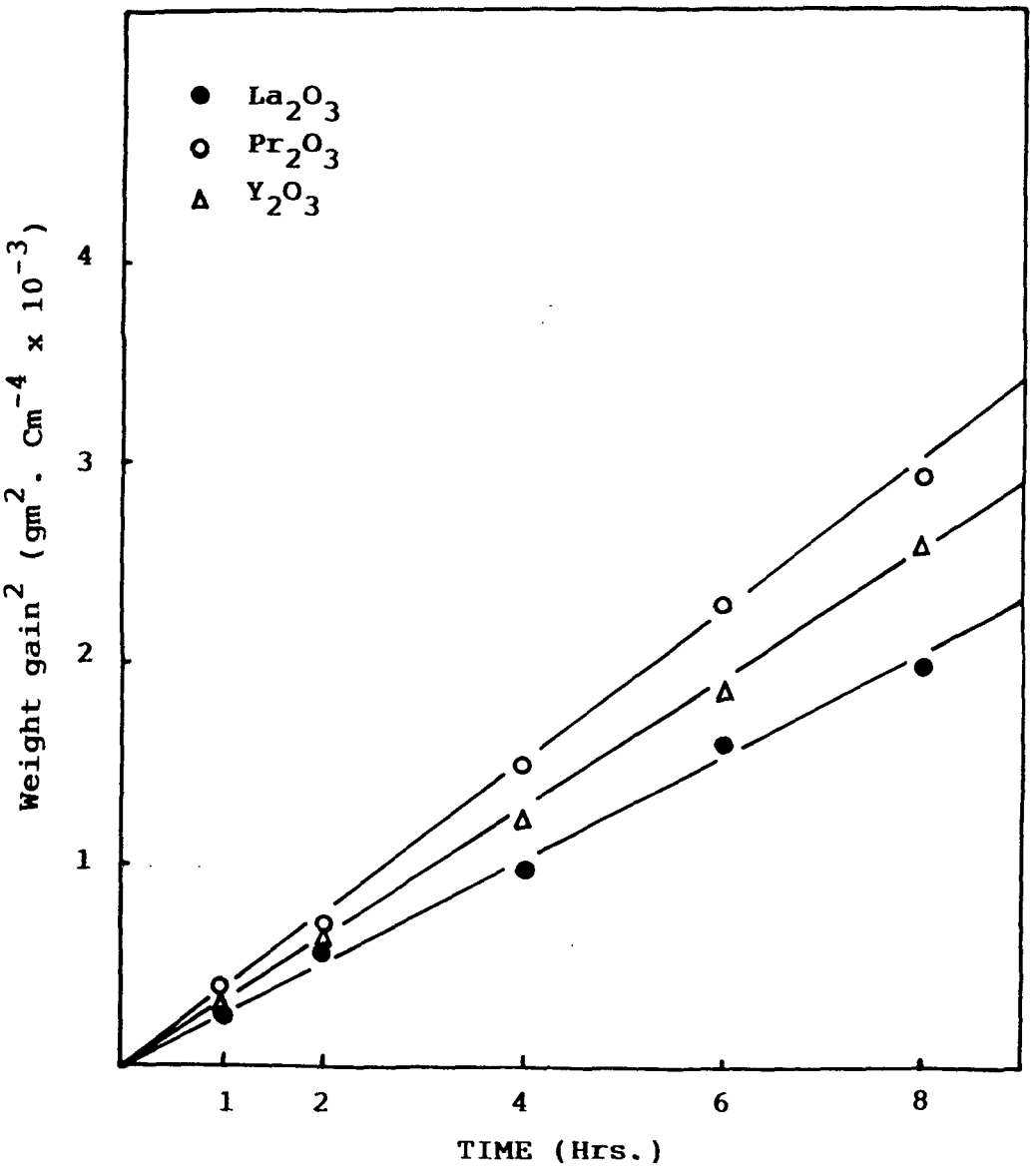

Fig. 6.11 Plots of weight gain^2 Vs time for the oxidation of decarburized Fe-10Cr_7C_3-0.1C-1.0RE_2O_3 alloys at 900°C.

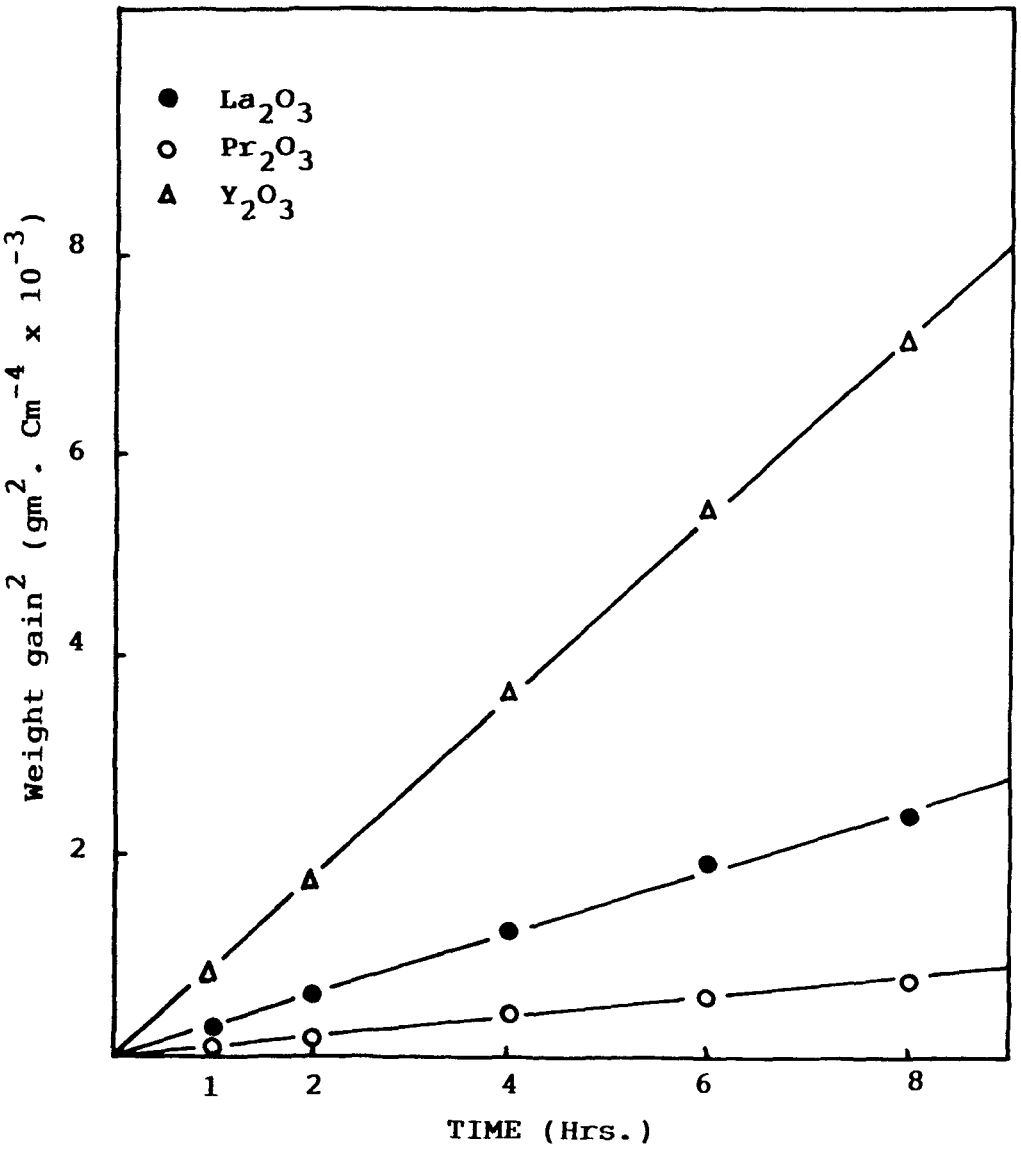

Fig. 6.12 Plots of gain^2 Vs time for the oxidation of decarburized Fe-WC-0.1C-1.0RE_2O_3 alloys at 900°C.

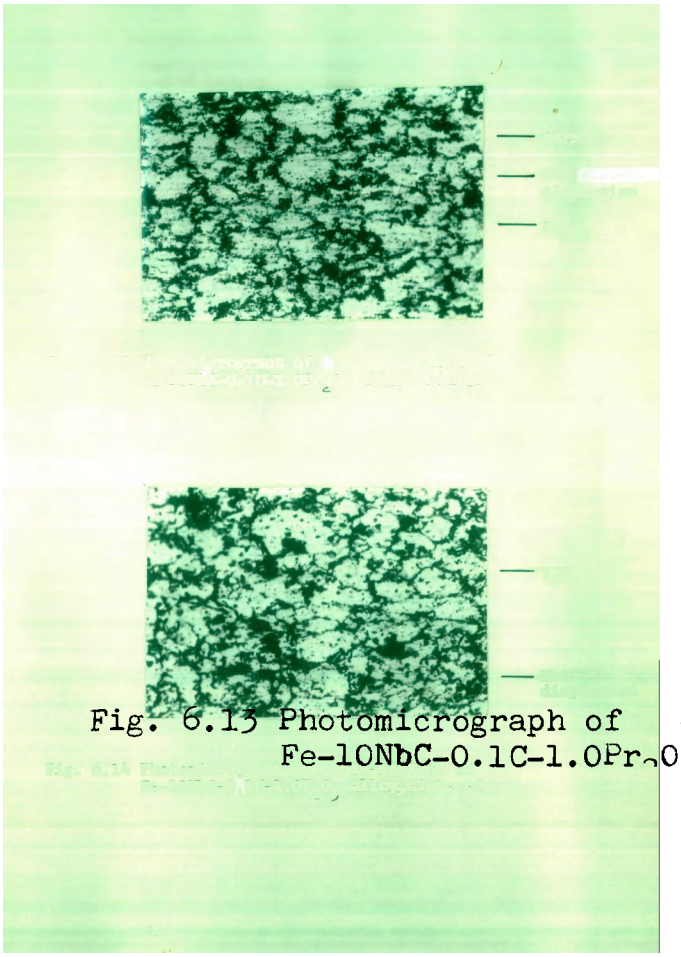

Fig. 6.13 Photomicrograph of cross-section of Fe-10NbC-0.1C-1.0Pr_2O_3 alloy, sintered. X 120

Fig. 6.14 Photomicrograph of cross-section of Fe-10NbC-0.1C-1.0Y_2O_3 alloy, sintered. X 120

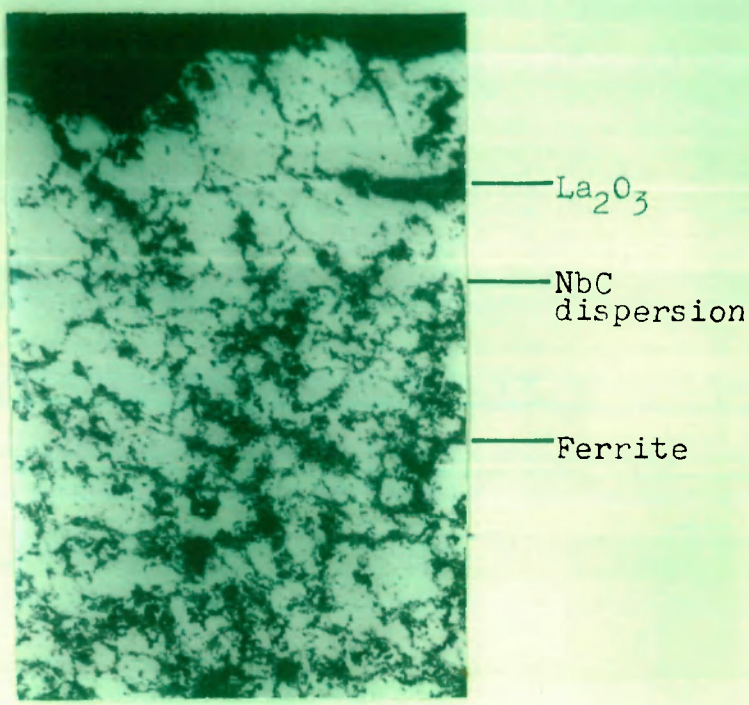

Fig. 6.15 Photomicrograph of cross-section of Fe-10NbC-0.1C-1.0La_2O_3 alloys, decarburized at 900°C for 2 hrs.
X 120

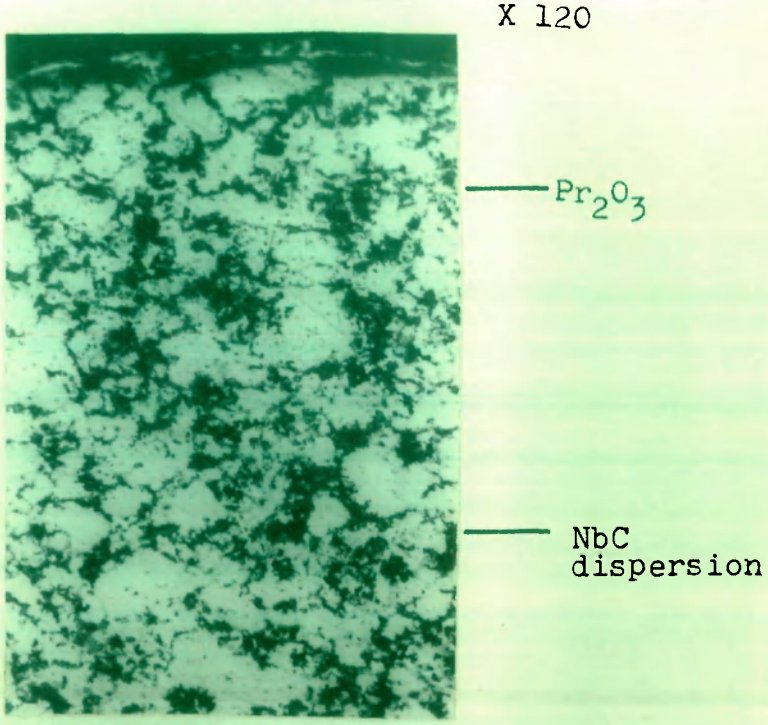

Fig. 6.16 Photomicrograph of cross-section of Fe-10NbC-0.1C-1.0Pr_2O_3 alloy, decarburized at 900°C for 2 hrs.
X 120

Figure 6.17 shows a photomicrograph of Fe-10NbC-0.1C-1.0 La_2O_3 oxidized at 900°C for 8 hr. the dark carbide particles consisting with the polygonal ferrite grains are remained almost unaffected but there is internal oxidation of iron at the ferrite/carbide interface and grey FeO particles are found at the ferrite grain boundaries. The scales are mainly consisted of iron oxides with Fe_2O_3 present in the outer scales. The rare earth oxide is incorporated with the internal oxides as well as with the inner scales. Figure 6.18 shows a scanning electron micrograph of the same alloy in the decarburized and oxidized condition. A net work of internal oxide particles sorrounding the polygonal grains can be seen. The scales are uniform and adhered containing oxides of iron; the wustite is oxidized to Fe_2O_3 due to penetration of O_2 through porous scales and Fe_2O_3 is present at localized sites in the scale.

Figures 6.19 and 6.20 show scanning electron and optical photomicrographs of Fe-10NbC-0.1C-1.0Pr_2O_3 alloy in decarburized-oxidized and oxidized condition. Almost similar morphologies are observed as those found in La_2O_3-containing alloys. The Y_2O_3-containing alloy in the decarburized and oxidized conditions (Fig. 6.21) show a denser net work of carbide grains in which internal oxide particles are incorporated otherwise the features are similar to those observed in corresponding Pr_2O_3-and La_2O_3-containing alloys.

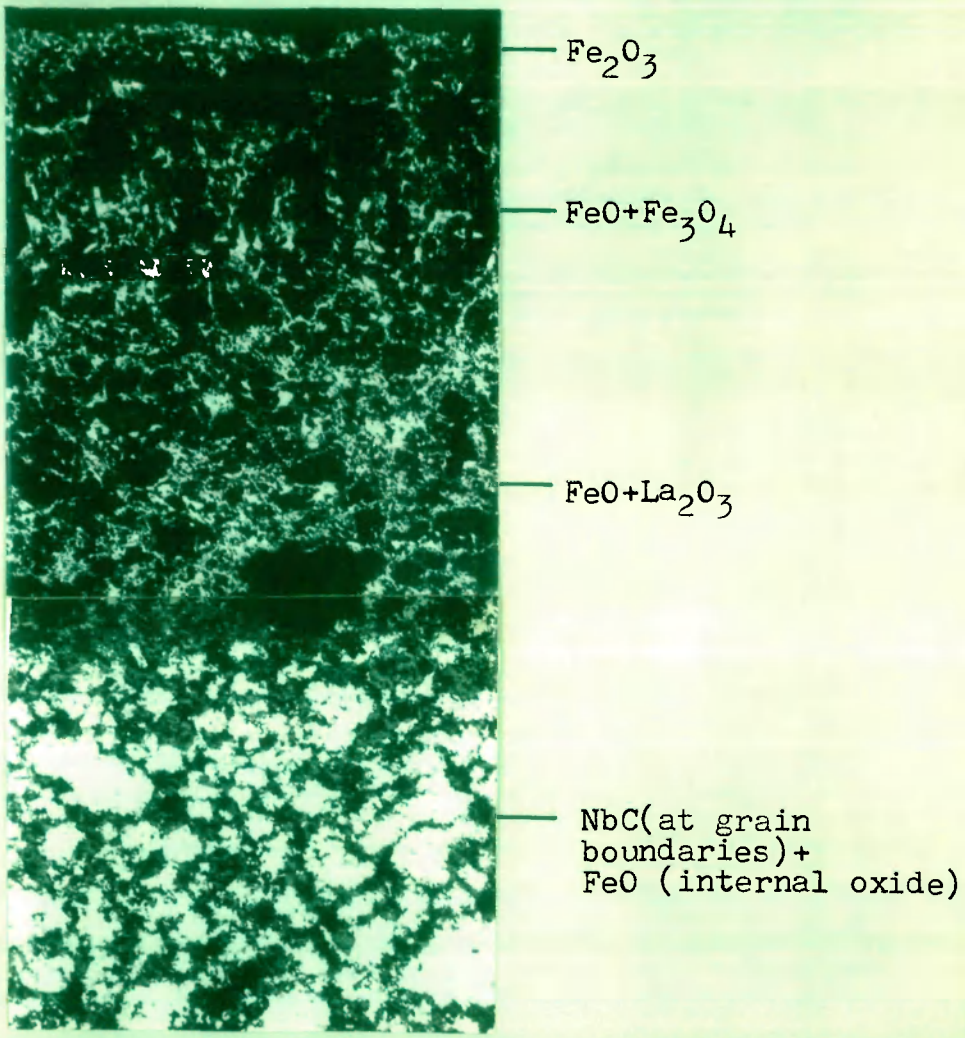

Fig. 6.17 Photomicrograph of cross-section of Fe-10NbC-0.1C-1.0La_2O_3 alloy, oxidized at 900°C for 8 hrs. X 120

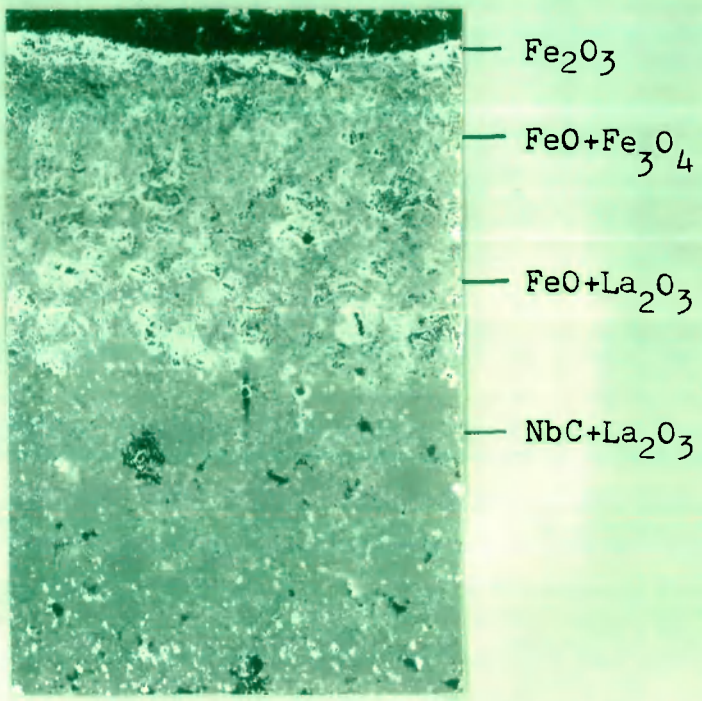

Fig. 6.18 SEM picture of Fe-10NbC-0.1C-1.0La_2O_3 alloy, oxidized at 900°C for 8 hrs.
X 80

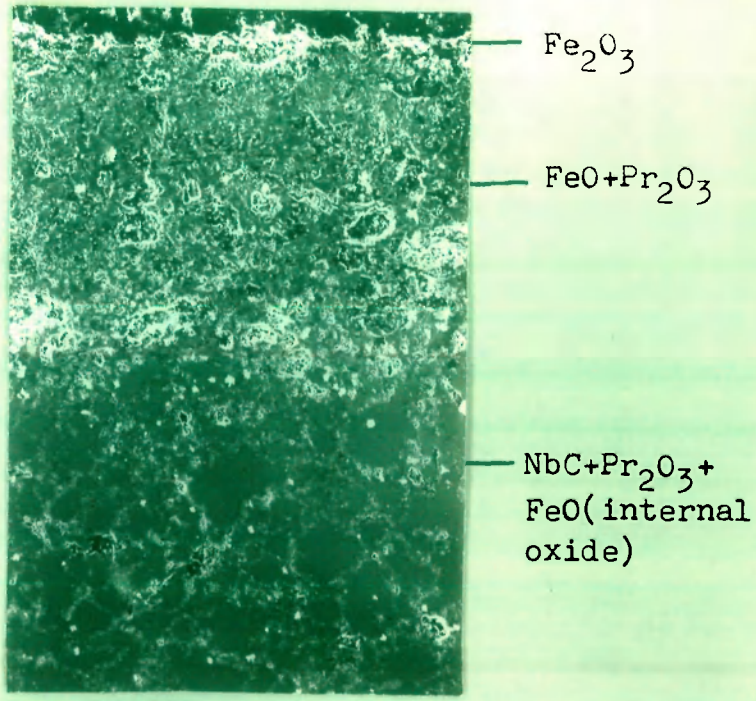

Fig. 6.19 SEM picture of predecarburized Fe-10NbC-0.1C-1.0Pr_2O_3 alloy, oxidized at 900°C for 8 hrs.
X 100

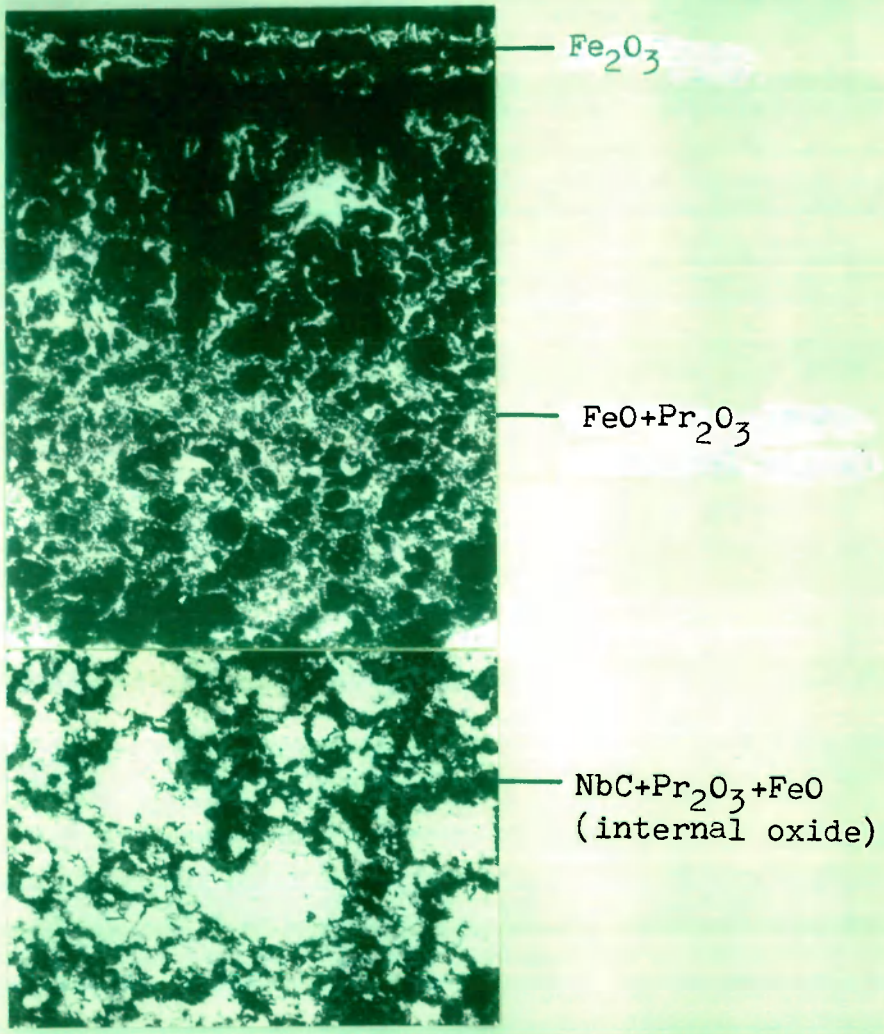

Fig. 6.20 Photomicrograph of cross-section of Fe-10NbC-0.1C-1.0Pr_2O_3 alloy, oxidized at 900°C for 8 hrs. X 120

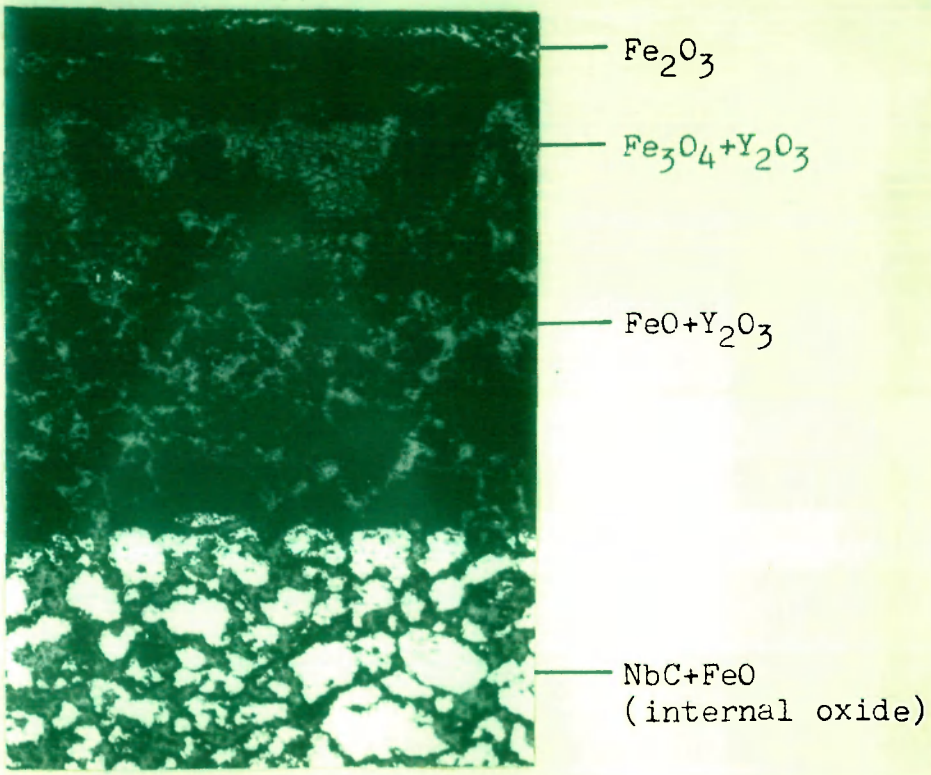

Fig. 6.21 Photomicrograph of a cross-section of predecarburized Fe-10NbC-0.1C-1.0Y_2O_3 alloy, oxidized at 900°C for 8 hrs.
X 120

6.1.2.2 Fe-10Cr_7C_3-0.1C-1.0RE_2O_3 Alloys

Figures 6.22-6.24 show photomicrographs of La_2O_3-, Pr_2O_3- and Y_2O_3- containing iron-base sintered alloys in as-cast condition. The photomicrographs show a dispersion of Cr_7C_3 particles in a ferrite matrix, the RE_2O_3 are also present as dispersed phase but it is difficult to identify these particles in the photomicrograph. In the decarburized state, the amount of ferrite is enhanced and segregation of carbide along the grainboundary is more clearly observed (Figs. 6.25).

Figure 6.26 shows a scanning electron photomicrograph of the Y_2O_3-containing alloy oxidized at 900°C. At the ferrite grain boundaries some of the Cr_7C_3 is oxidized to Cr_2O_3 and appears as a net work along with Cr_7C_3. The iron oxide scales contain inclusions of Cr_2O_3. The decarburized-oxidized alloy shows (Fig. 6.27) similar features although the scales are more thicker and porous. The Pr_2O_3-containing alloy in oxidized condition shows oxide network in the matrix formed due to selective oxidation of Cr_7C_3 into Cr_2O_3 (Fig. 6.28). The inner scales contain Cr_2O_3 and $FeO.Cr_2O_3$ and outer scales contain a relatively thick layer of Fe_2O_3, the middle layers have inclusions of Cr_2O_3 in Fe_2O_3/Fe_3O_4 scales. Figure 6.29 shows a scanning electron photomicrograph of La_2O_3-containing alloy decarburized and oxidized at 900°C. The interesting features of the oxide scale is that FeO and Cr_2O_3 are present

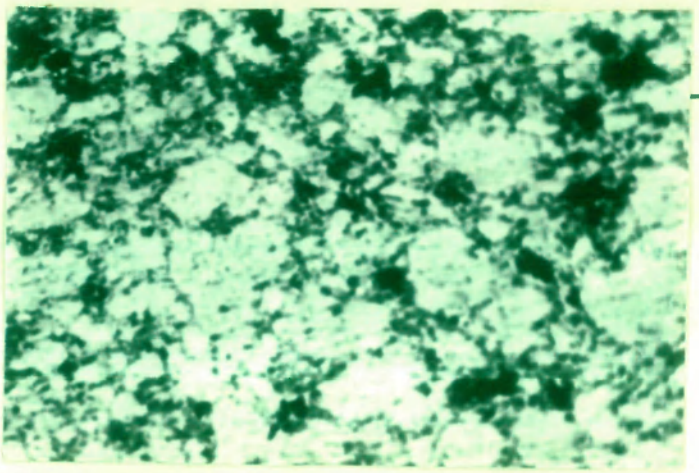

Fig. 6.22 Photomicrograph of cross-section of $Fe\text{-}10Cr_7C_3\text{-}0.1C\text{-}1.0La_2O_3$ alloy, sintered x 120

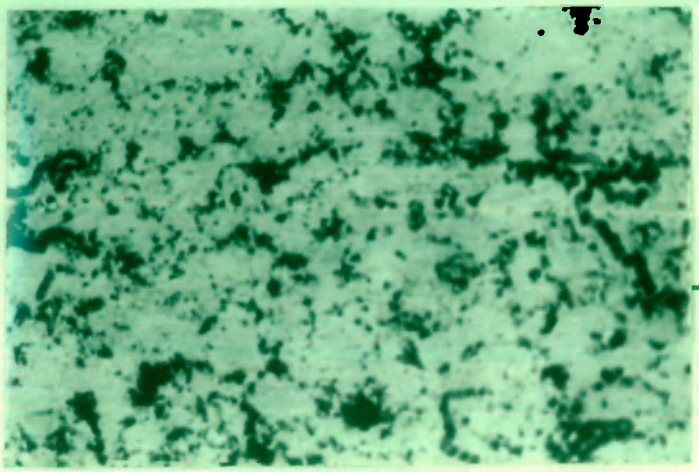

Fig. 6.23 Photomicrograph of cross section of Fe-10Cr_7C_3-0.1C-1.0Pr_2O_3alloy, sintered X 120

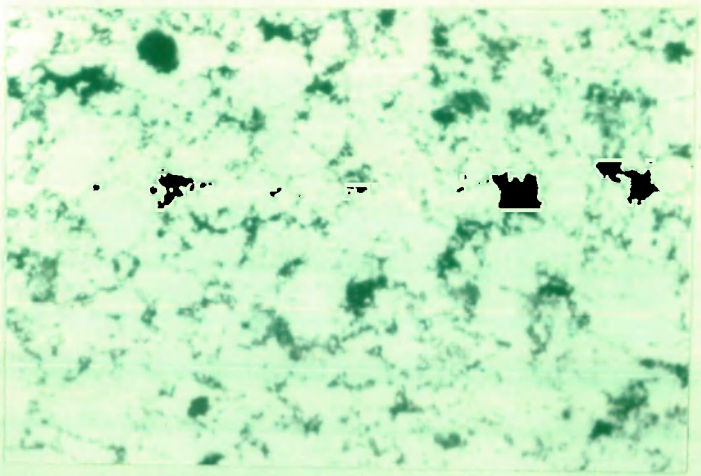

Fig. 6.24 Photomicrograph of cross-section of Fe-10Cr_7C_3-0.1C-1.0Y_2O_3 alloy, sintered. X 120

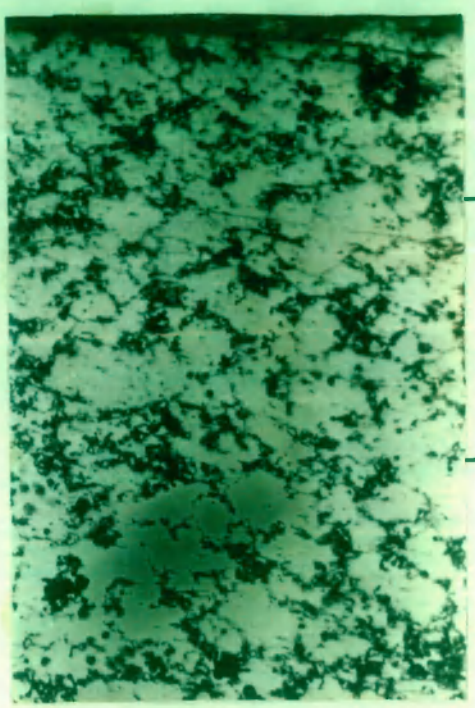

Fig. 6.25 Photomicrograph of cross-section of $Fe-10Cr_7C_3-0.1C-1.0La_2O_3$ alloy, decarburized at 900°C for 2 hrs.
X 120

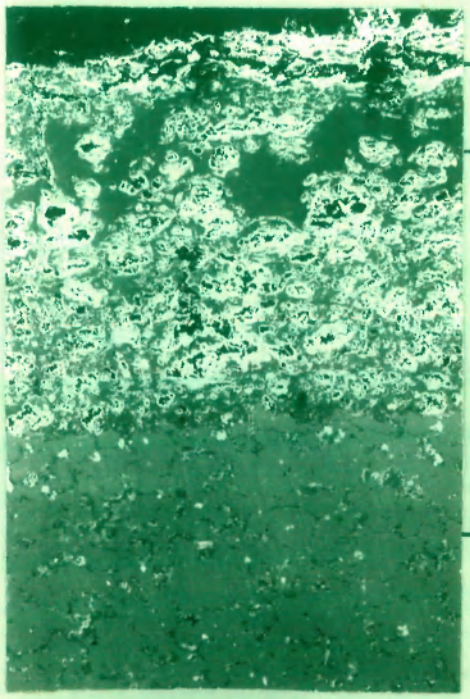

Fig. 6.26 SEM picture of $Fe-10Cr_7C_3-0.1C-1.0Y_2O_3$ alloy, oxidized at 900°C for 8 hrs.
X 100

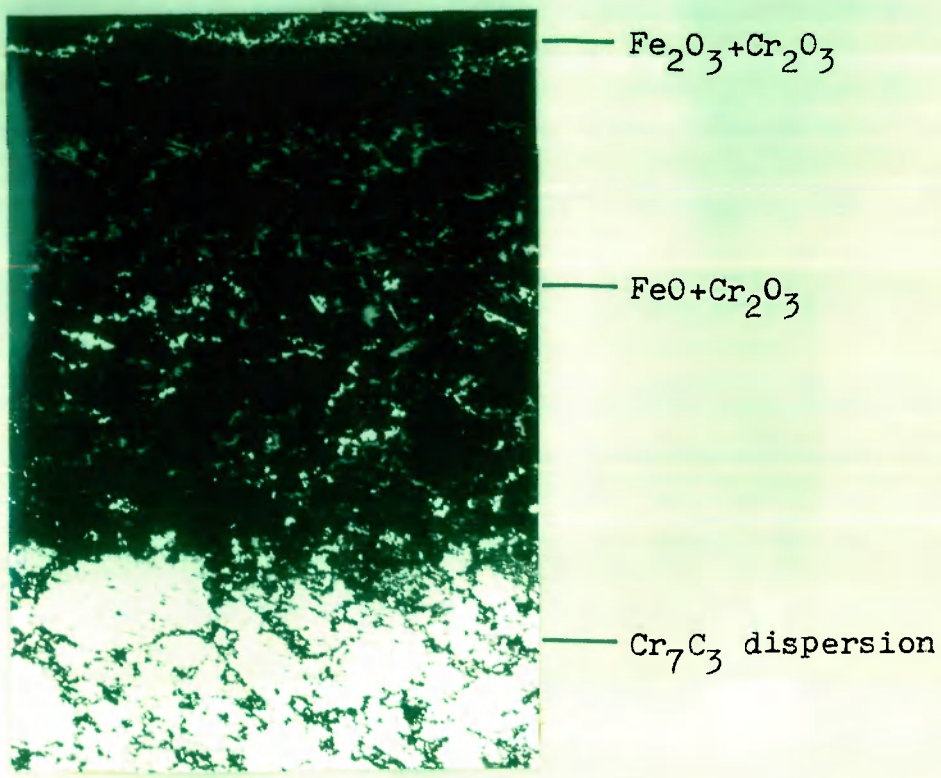

Fig. 6.27 Photomicrograph of cross-section of predecarburized Fe-10Cr_7C_3-0.1C-1.0Y_2O_3 alloy, oxidized at 900°C for 8 hrs.
X 120

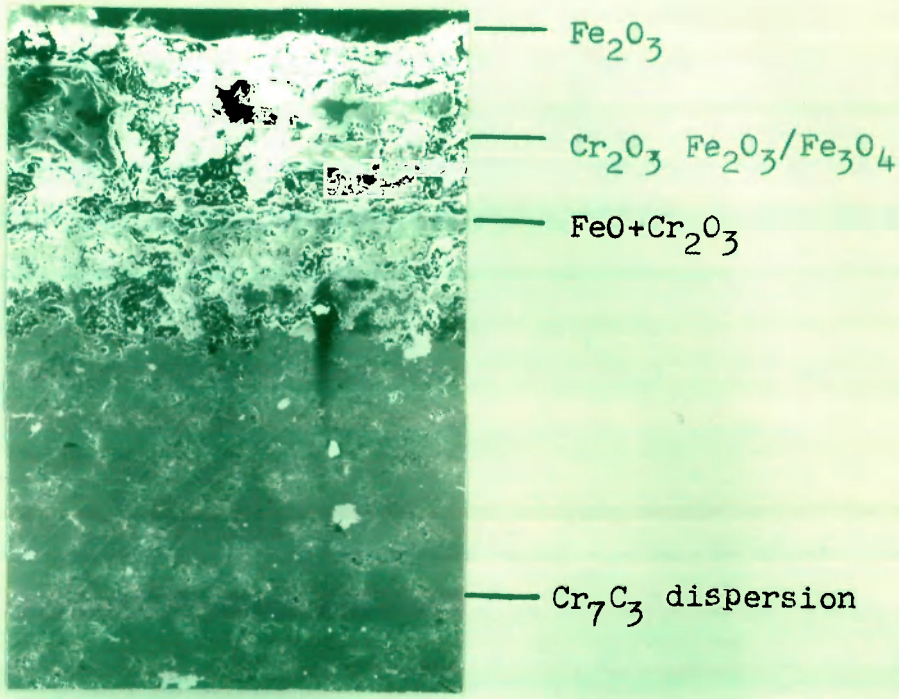

Fig. 6.28 SEM picture of Fe-10Cr_7C_3-0.1C-1.0Pr_2O_3 alloy, oxidized at 900°C for 8 hrs.
X 100

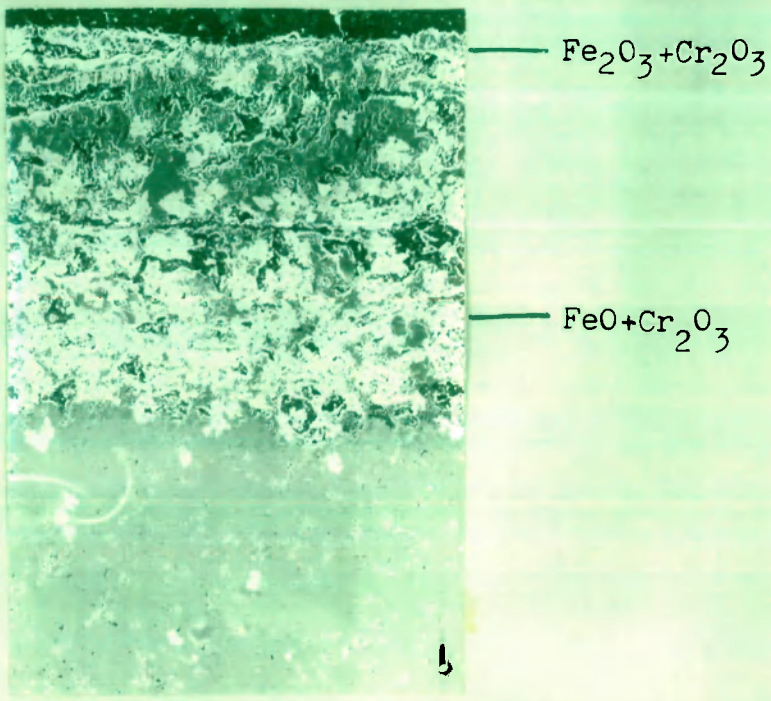

Fig. 6.29 SEM picture of predecarburized $Fe-10Cr_7C_3-0.1C-1.0La_2O_3$ alloy, oxidized at 900°C for 8 hrs.
X 100

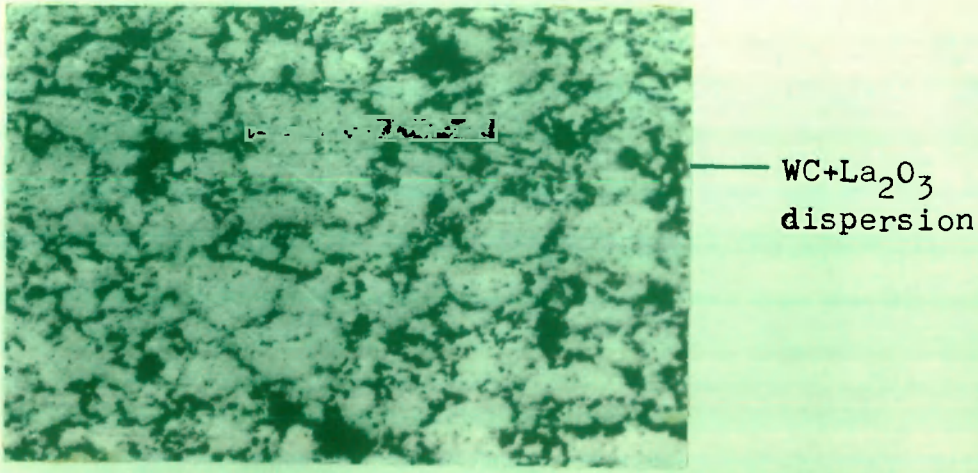

Fig. 6.30 Photomicrograph of cross section of $Fe-10WC-0.1C-1.0La_2O_3$ alloy, sintered.
X 120

in the outer and inner layers and the inner scale is largely consisted of FeO in which Cr_7C_3 is also incorporated.

6.1.2.3 Fe-10WC-0.1C-1.0RE_2O_3 Alloys

Figures 6.30-6.32 show photomicrographs of RE_2O_3-containing WC dispersed iron-base sintered alloys. The photomicrographs indicate the presence of polygonal ferrite particles along with WC particles. On decarburization the amount of ferrite phase is enhanced significantly and the carbide particles are segregated along the grain boundaries, presence of RE_2O_3 inclusions is also indicated. In the decarburized Y_2O_3-containing alloy (Fig. 6.33), some internal oxidation at the grain boundaries is also indicated. Figures 6.34 and 6.35 show scanning electron photomicrograph of Fe-10WC-0.1C-1.0La_2O_3 and Fe-10WC-0.1C-1.0Pr_2O_3 oxidized at 900°C for 8 hrs. Both the alloys show separation of the scale at the alloy interface and separation of the outer and inner scales. The inner scales are largely consisted of $FeO.WO_3$ and the outer scales contain oxides of iron. The microstructure of matrix shows segregation of WC along the grain boundaries and presence of internal FeO or $FeO.WO_3$ along with the carbides.

The scanning electron photomicrograph (Fig. 6.36) of Fe-10WC-0.1C-1.0Y_2O_3 represents typical morphology for the decarburized (H_2-H_2O) and oxidized (O_2) alloy at 900°C. The

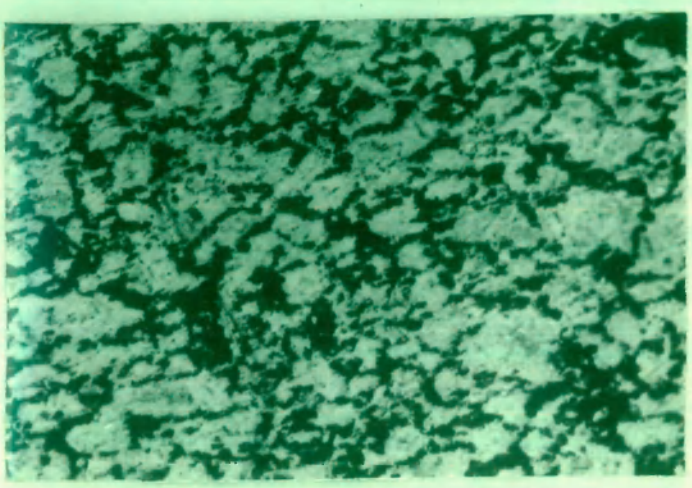

Fig. 6.31 Photomicrograph of cross-section of Fe-10WC-0.1C-1.0Pr_2O_3 alloy, sintered. X 120

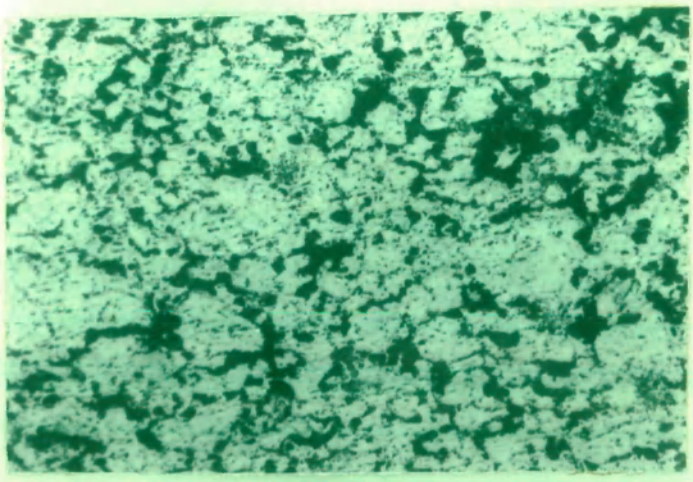

Fig. 6.32 Photomicrograph of cross-section of Fe-10WC-0.1C-1.0Y_2O_3 alloy, sintered. X 120

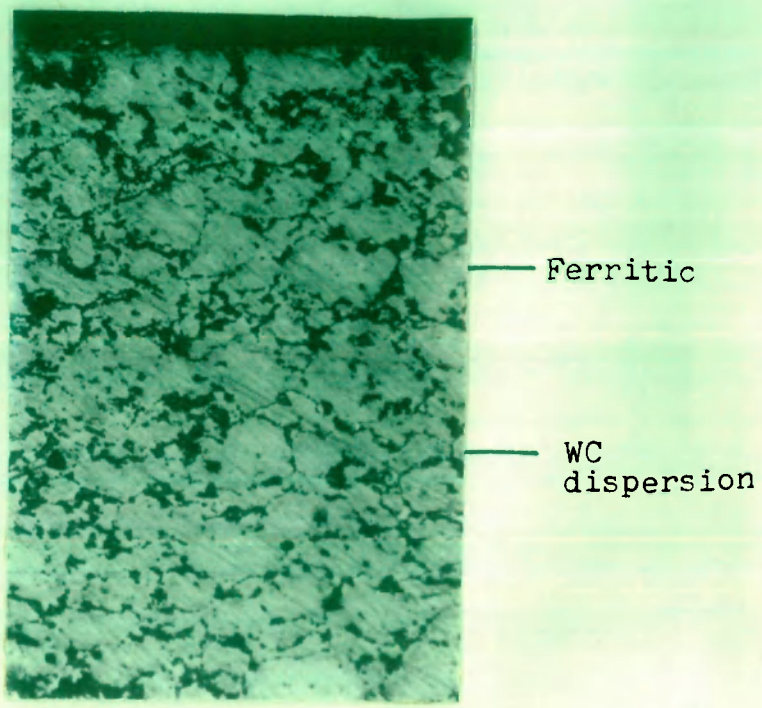

Fig. 6.33 Photomicrograph of cross-section of Fe-10WC-0.1C-1.0Y_2O_3 alloy, decarburized at 900°C for 2 hrs. X 120

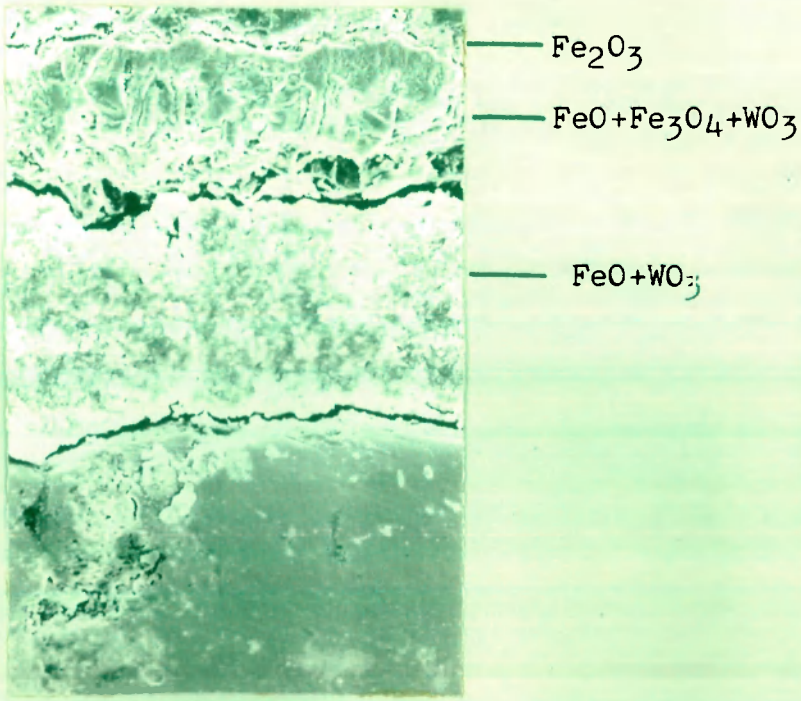

Fig. 6.34 SEM picture of Fe-10WC-0.1C-1.0La_2O_3 alloy, oxidized at 900°C for 8 hrs. X 390

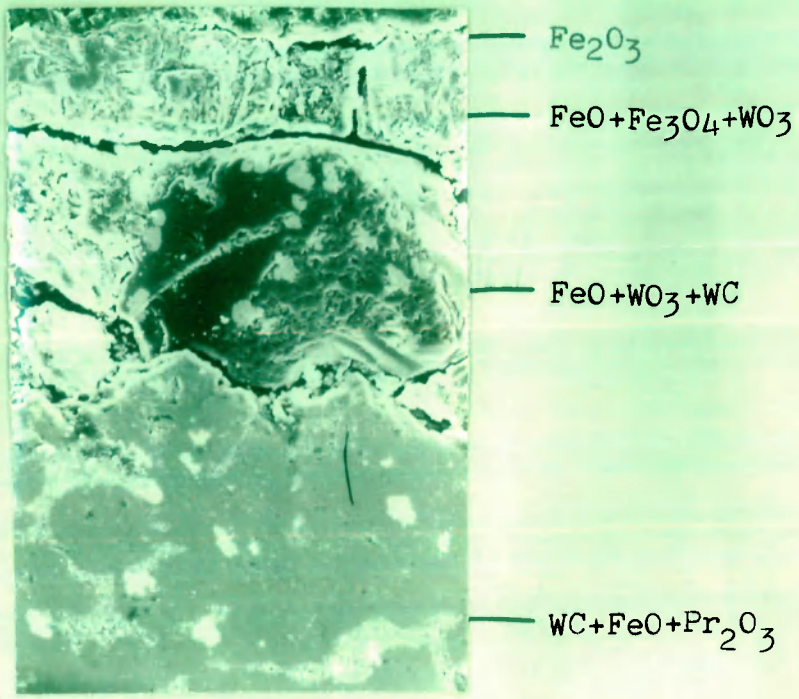

Fig. 6.35 SEM picture of Fe-10WC-0.1C-1.0Pr_2O_3 alloy, oxidized at 900°C for 8 hrs. X 390

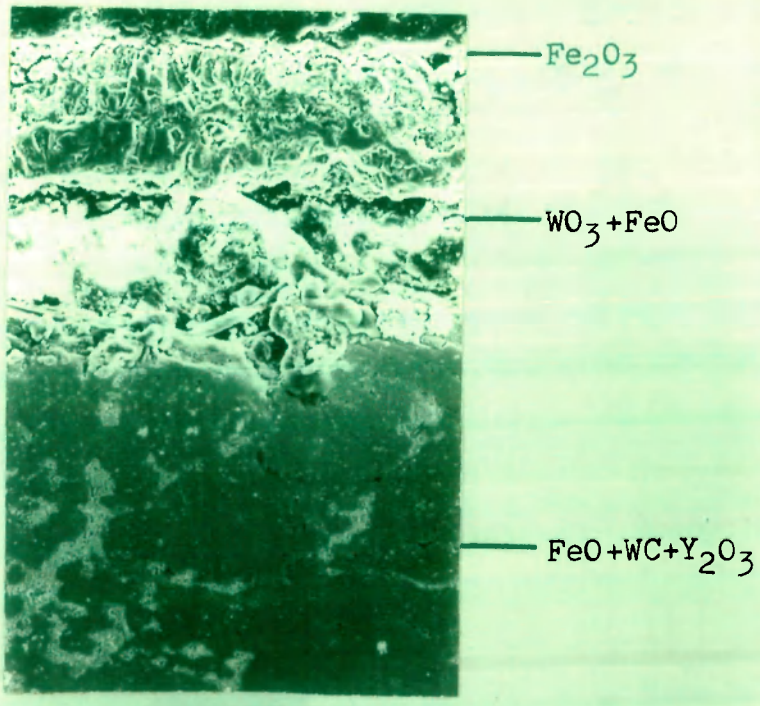

Fig. 6.36 SEM picture of predecarburized Fe-10WC-0.1C-1.0Y_2O_3 alloy, oxidized at 900°C for 8 hrs. X 300

microstructure of the matrix shows segregation of WC particles at the grain boundaries which remain undistrubed during oxidation of the decarburized alloy. The inner scales contains WO_3 or WO_3.FeO and the outer scales contain Fe_2O_3. The scales are more compact and adhered than those obtained during the oxidation of undecarburized alloys.

6.2 Discussion

Fe-10MC-0.1C-1.0RE_2O_3 sintered alloys have agglomeration of carbides at the grain boundaries. During decarburization this agglomeration remains undisturbed. On oxidation, internal oxidation of the carbide-depleted phase occurs and the oxidation product FeO is present either admixed with carbide or as a separate phase near the grain boundaries. Oxidation rates of Fe-10MC-0.1C-RE_2O_3 sintered alloys are largely dependent on the extent of internal oxidation. Thus the WC-containing alloys have relatively very little internal oxidation and have usually lowest oxidation rates. The pattern of oxidation rates of these alloys are very similar to Fe-10MC alloys, NbC-containing alloys have the highest oxidation and WC-containing lowest rate. The addition of RE_2O_3 provide more adherent and uniform oxide scales. The oxidation rates of Fe-10MC-0.1C-RE_2O_3 in undecarburized and decarburized states are much lower (about one order of magnitude) than the corresponding Fe-10MC alloys. This goes to show that the presence of RE_2O_3 play some role in restricting the oxidation

rates of the alloy. However, the oxidation rates of RE_2O_3-containing alloys are higher than 20 % Cr-containing alloys (Chapter V). It is obvious from these observations that the presence of internal Cr_2O_3 net work at the grain boundaries restricts the transportation of Fe or any alloying element and therefore, restrict the oxidation rates. In WC-containing alloys, the higher thermodynamic stability of WC towards oxidation itself plays an important role.

The influence of RE_2O_3 on the oxidation of the alloys is not fully understood, but they do play some role in reducing the oxidation rates either affecting the mobility of carbon or providing more adherent nonporous oxide scales.

CHAPTER VII

DECARBURIZATION AND OXIDATION OF Fe-10MC-0.1C-MO_2 ALLOYS

Niobium carbide (NbC), tungsten carbide (WC) or chromium carbide (Cr_7C_3) (10 wt.%) dispersed iron base alloys containing 0.1 wt. % carbon and 1.0 wt. % TiO_2 or ZrO_2 were prepared by compaction and sintering techniques. The details of experimental procedures for preparation, oxidation and decarburization kinetics and morphological studies are given in Chapter II. The sintered alloys were subjected to oxidation (1 atm. O_2), decarburization (H_2-H_2O) and oxidation of decarburized alloys at 900°C on a typical set up of Sartorious Microbalance discussed in Chapter II.

7.1 Results

7.1.1 Oxidation Kinetics

Weight gain Vs time plots for the oxidation of iron base sintered alloys of the general composition : Fe-10MC-0.1C-1.0TiO_2 or ZrO_2 (MC is NbC, WC or Cr_7C_3 10 wt. %) are shown in figures 7.1-7.3. All the alloys were oxidized in O_2(g) under one atmospheric pressure at 900°C for 8 hrs. Figures 7.4-7.6 show plots of weight gain^2 Vs time for the same alloys. In general, the weight gain Vs time plots are parabolic and weight gain^2 vs time plots are linear, indicating the diffusion-controlled growth of oxide scales. Table 7.1 lists the values of parabolic rate constant, Kp for the

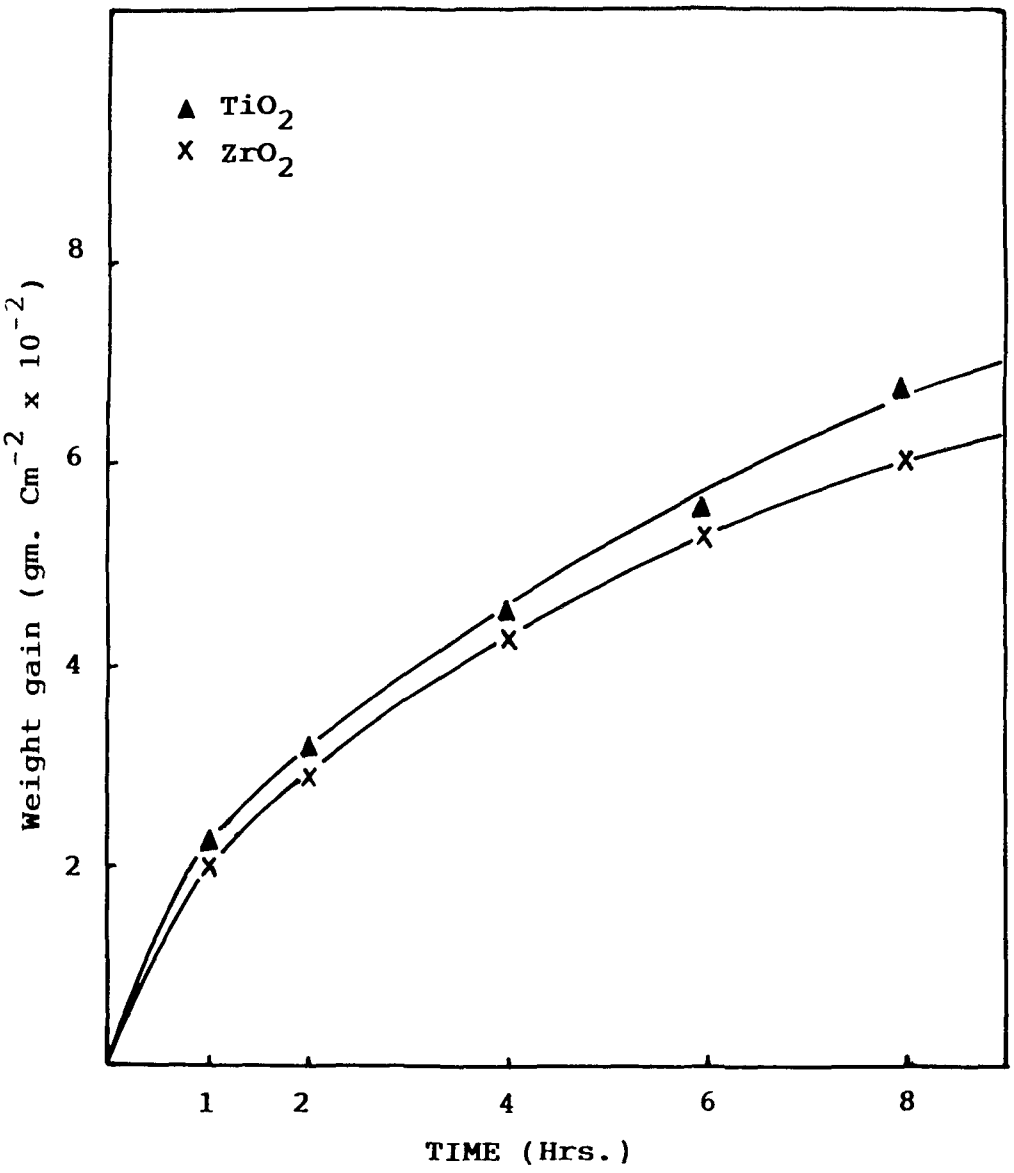

Fig. 7.1 Plots of weight gain Vs time for the oxidation of Fe-10NbC-0.1C-1.0M'O_2 alloys at 900°C.

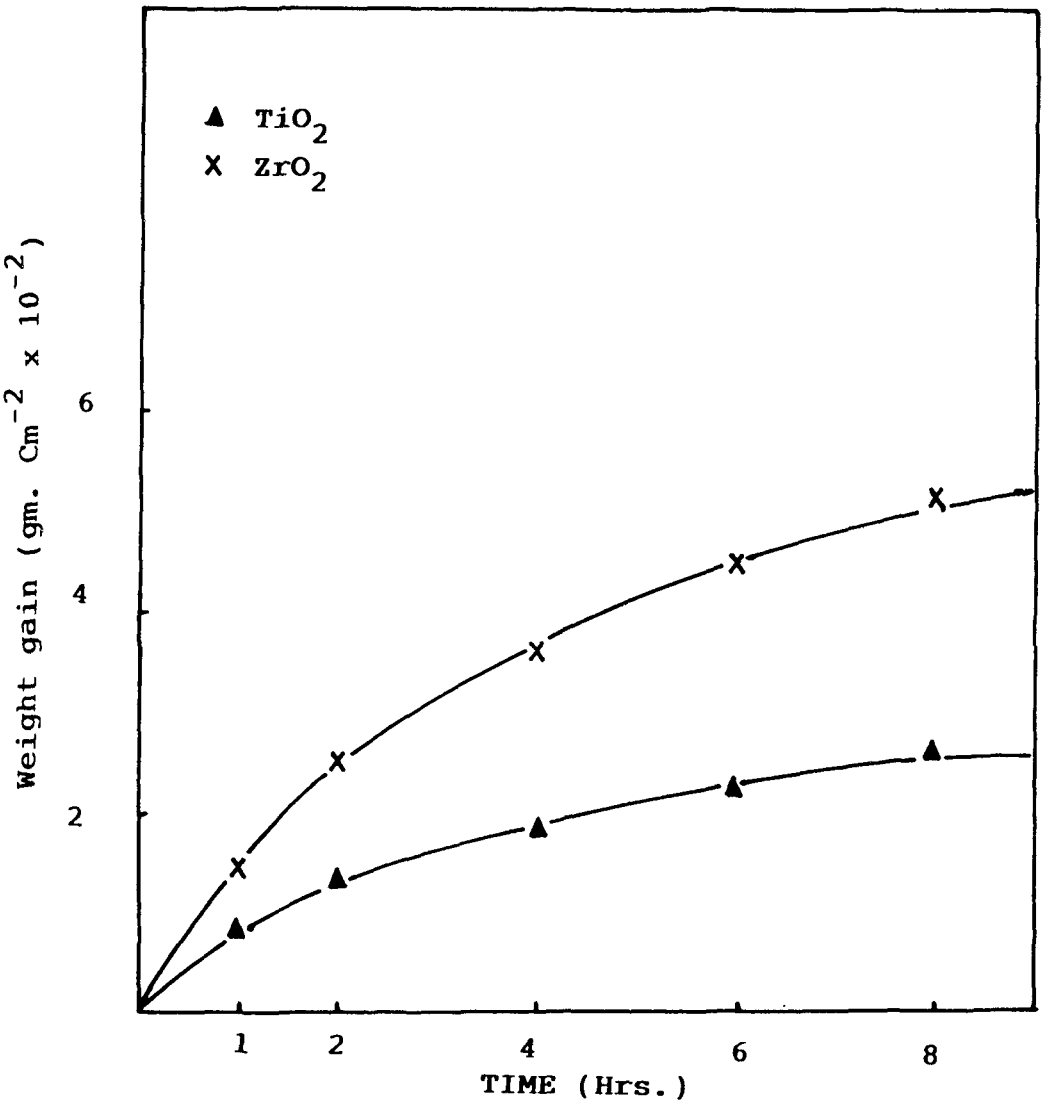

Fig. 7.2 Plots of weight gain Vs time for the oxidation of Fe-10Cr_7C_3-0.1C-1.0M'O_2 alloys at 900°C.

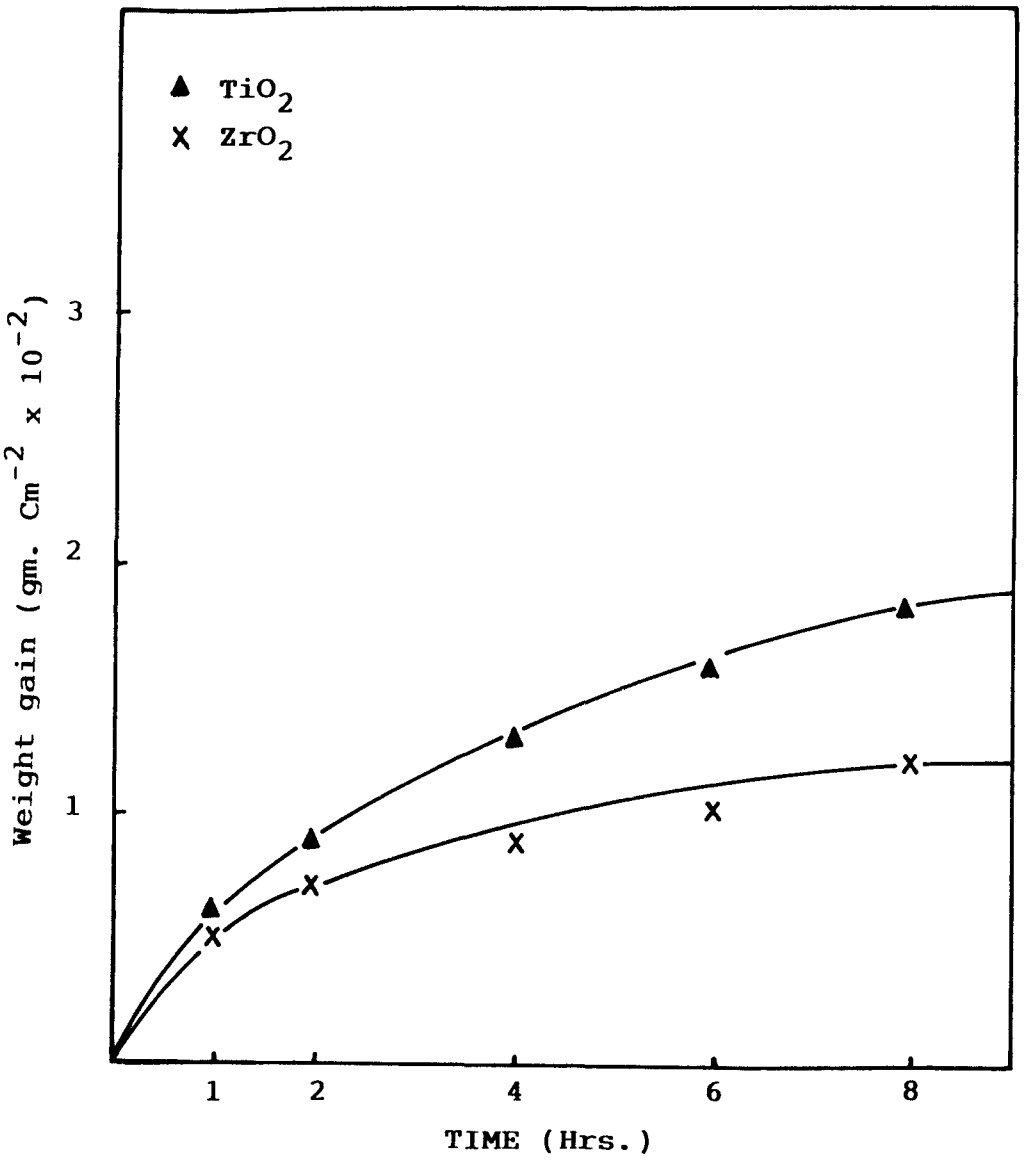

Fig. 7.3 Plots of weight gain Vs time for the odixation of Fe-10WC-0.1C-1.0M'O_2 alloys at 900°C.

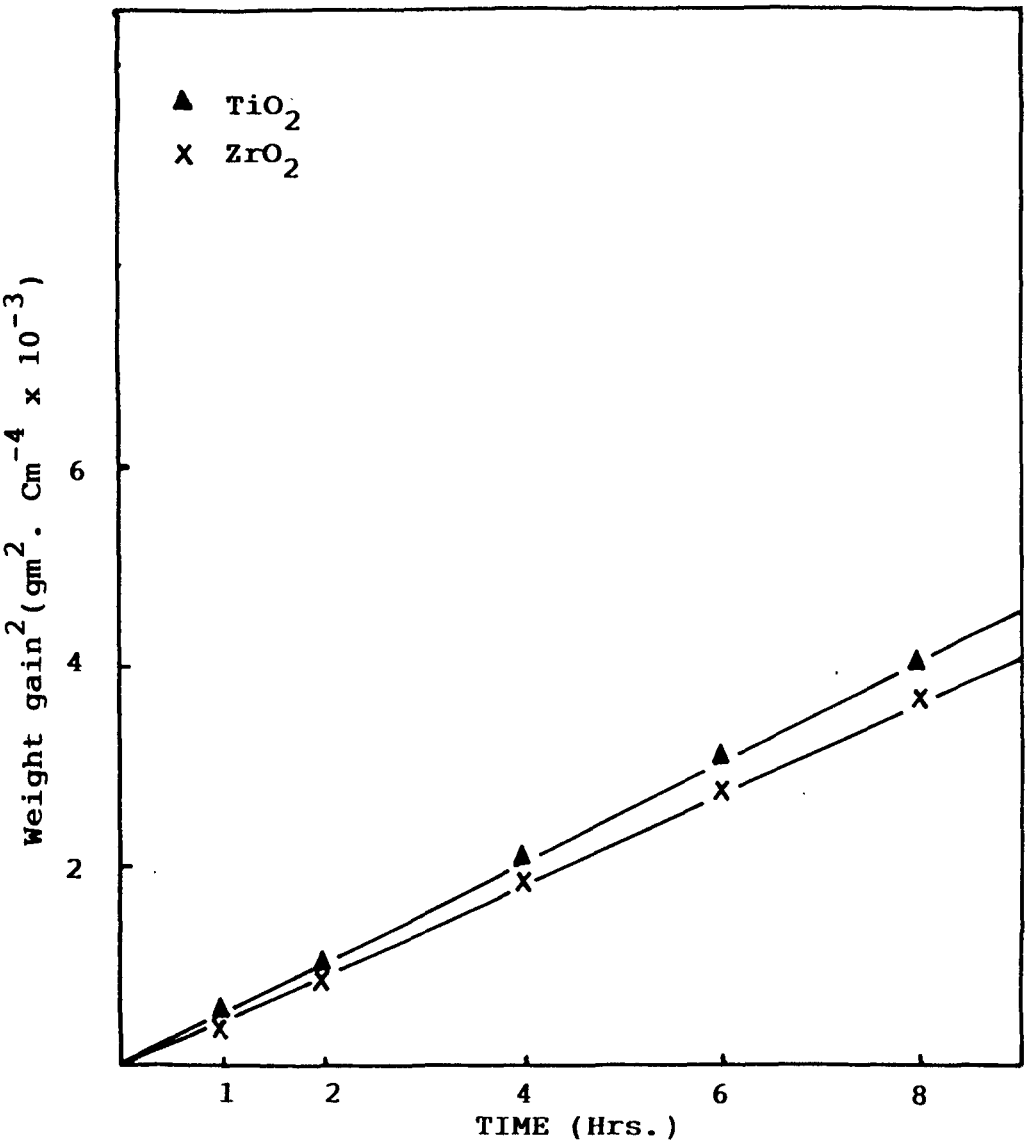

Fig. 7.4 Plots of weight gain^2 Vs time for the odixation of Fe-10NbC-0.1C-1.0M'O_2 alloys at 900°C.

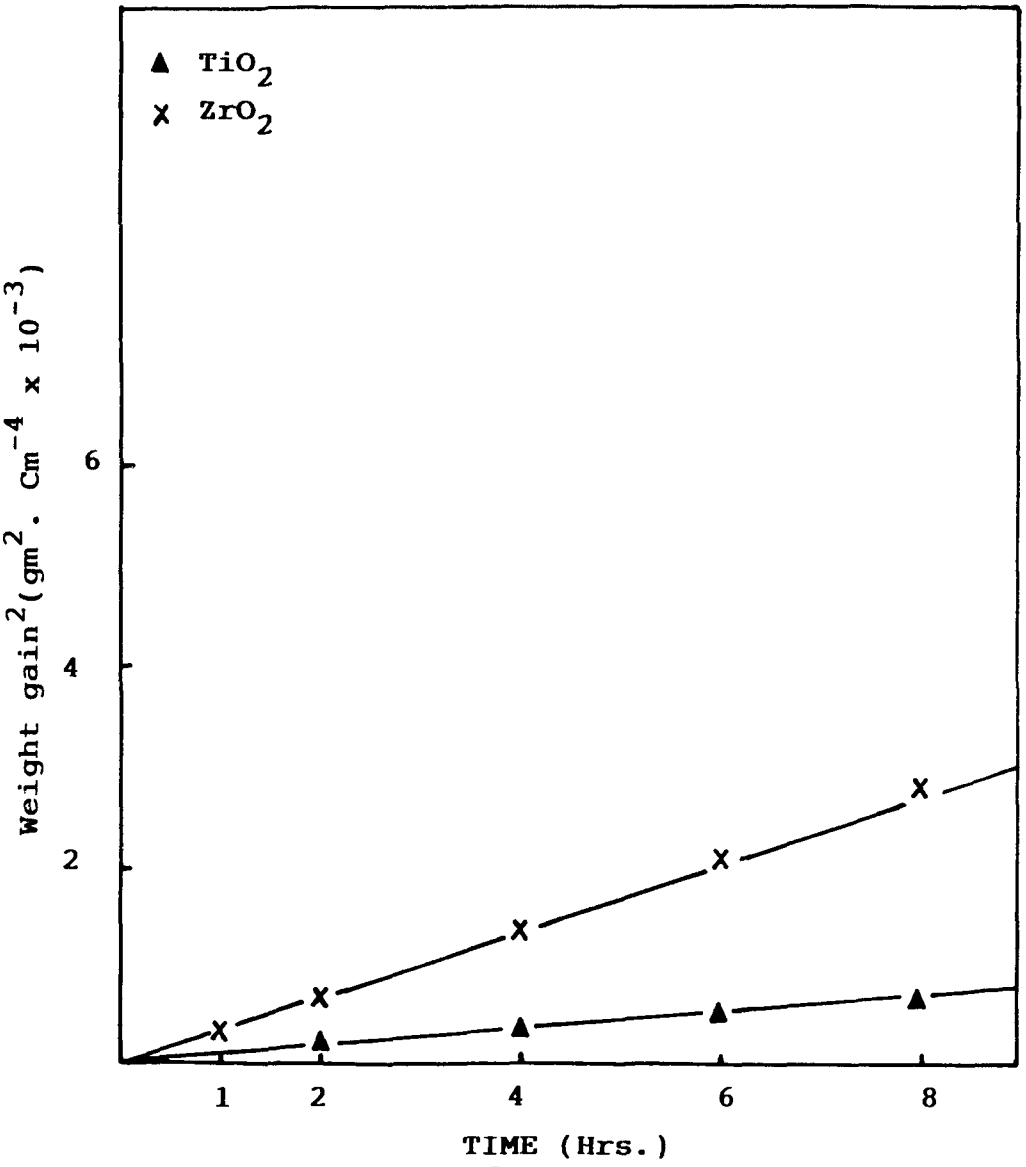

Fig. 7.5 Plots of weight gain^2 Vs time for the oxidation of Fe-10Cr_7C_3-0.1C-1.0M'O_2 alloys at 900°C.

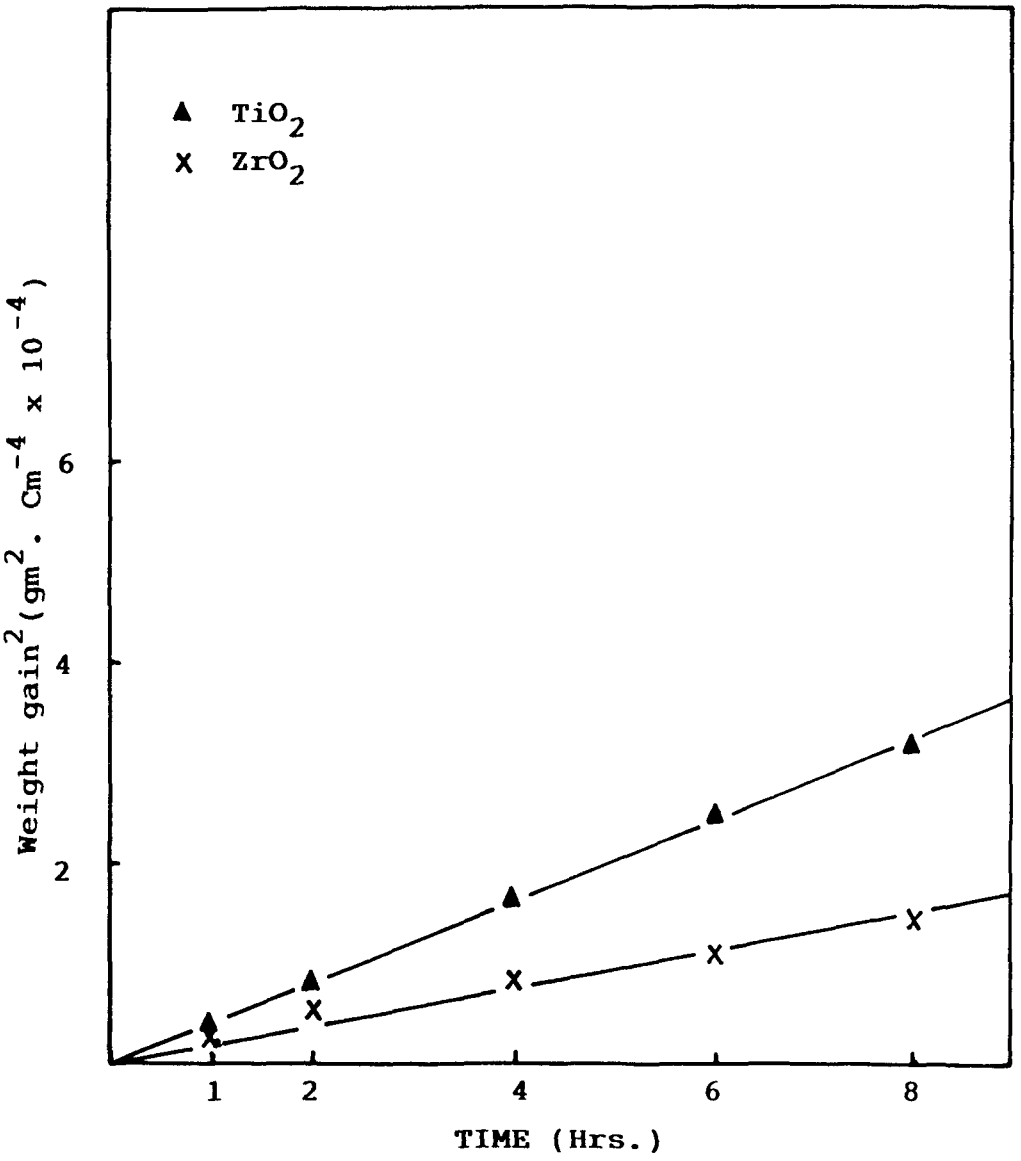

Fig. 7.6 Plots of weight gain^2 Vs time for the oxidation of Fe-10WC-0.1C-1.0M'O_2 alloys at 900°C.

oxidation of Fe-10MC-0.1C-1.0TiO_2/ZrO_2 at 900°C.

The alloys Fe-10MC-0.1C-1.0TiO_2/ZrO_2 were decarburized in wet hydrogen (H_2-H_2O) for 2 hrs. at 900°C and were subsequently oxidized in O_2(g) at the same temperature for 8 hrs. The weight gain Vs time and weight gain^2 Vs time plots are shown in figures 7.7-7.9 and figures 7.10-7.12 respectively. The decarburized alloys are also seemed to follow a parabolic rate law during oxidation indicating the operation of a diffusion controlled mechanism during oxide growth. The values of rate constant are given in table 7.1.

Table 7.1

Values of parabolic rate constants Kp for the oxidation of undecarburized and predecarburized Fe-10MC-0.1C-1.0MO_2 alloys at 900°C in $Kg^2.m^{-4}.Sec^{-1} \times 10^{-6}$.

Alloy (wt. %)	undecarburized	predecarburized
Fe-10WC-0.1C-1.0TiO_2	1.09	28.65
Fe-10WC-0.1C-1.0ZrO_2	0.49	5.40
Fe-10NbC-0.1C-1.0TiO_2	14.20	79.90
Fe-10NbC-0.1C-1.0ZrO_2	12.50	25.35
Fe-10Cr_7C_3-0.1C-1.0TiO_2	2.22	3.65
Fe-10Cr_7C_3-0.1C-1.0ZrO_2	9.40	15.30

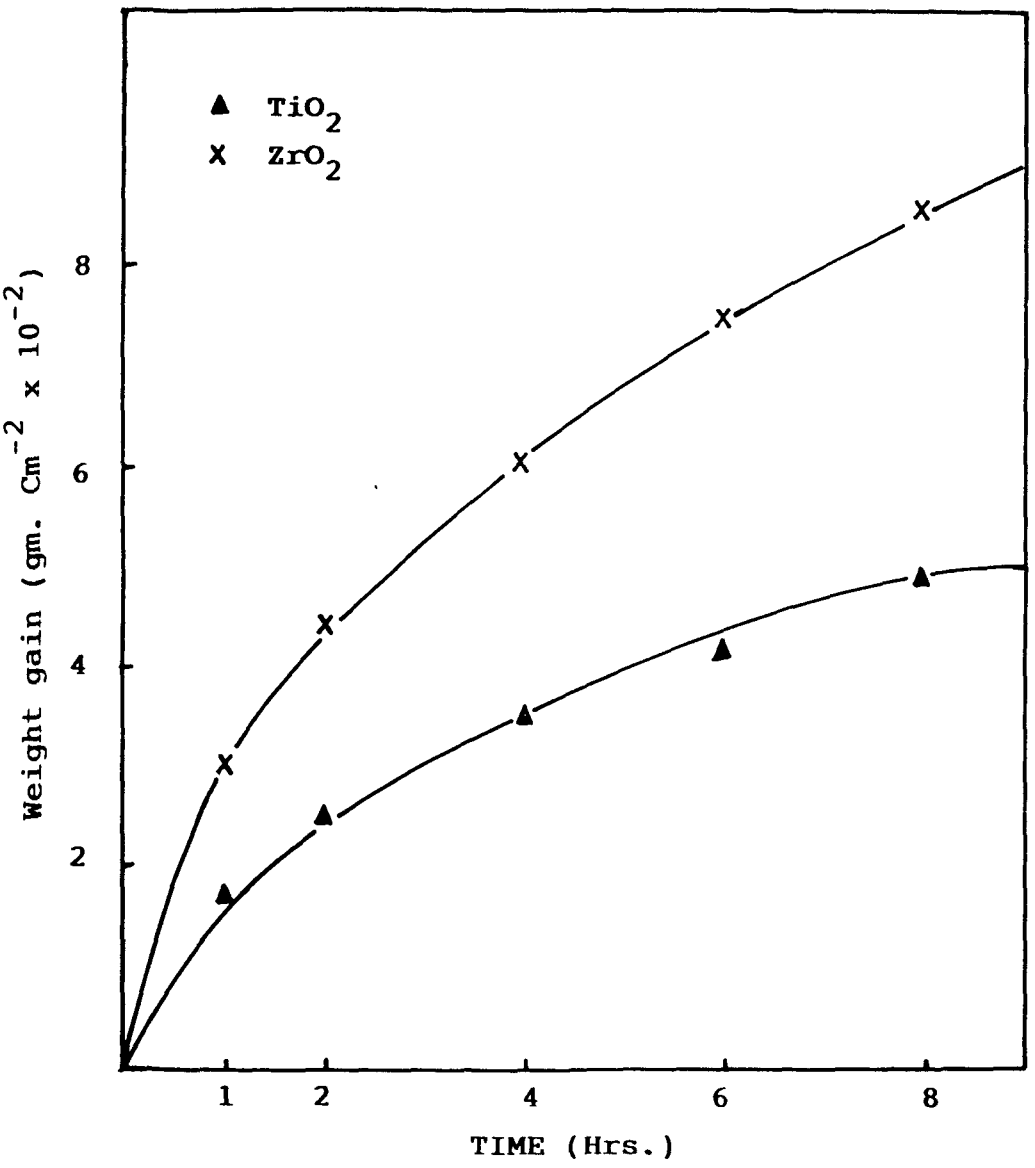

Fig. 7.7 Plots of weight gain Vs time for the oxidation of decarburized Fe-10NbC-0.1C-1.0M'O_2 alloys at 900°C.

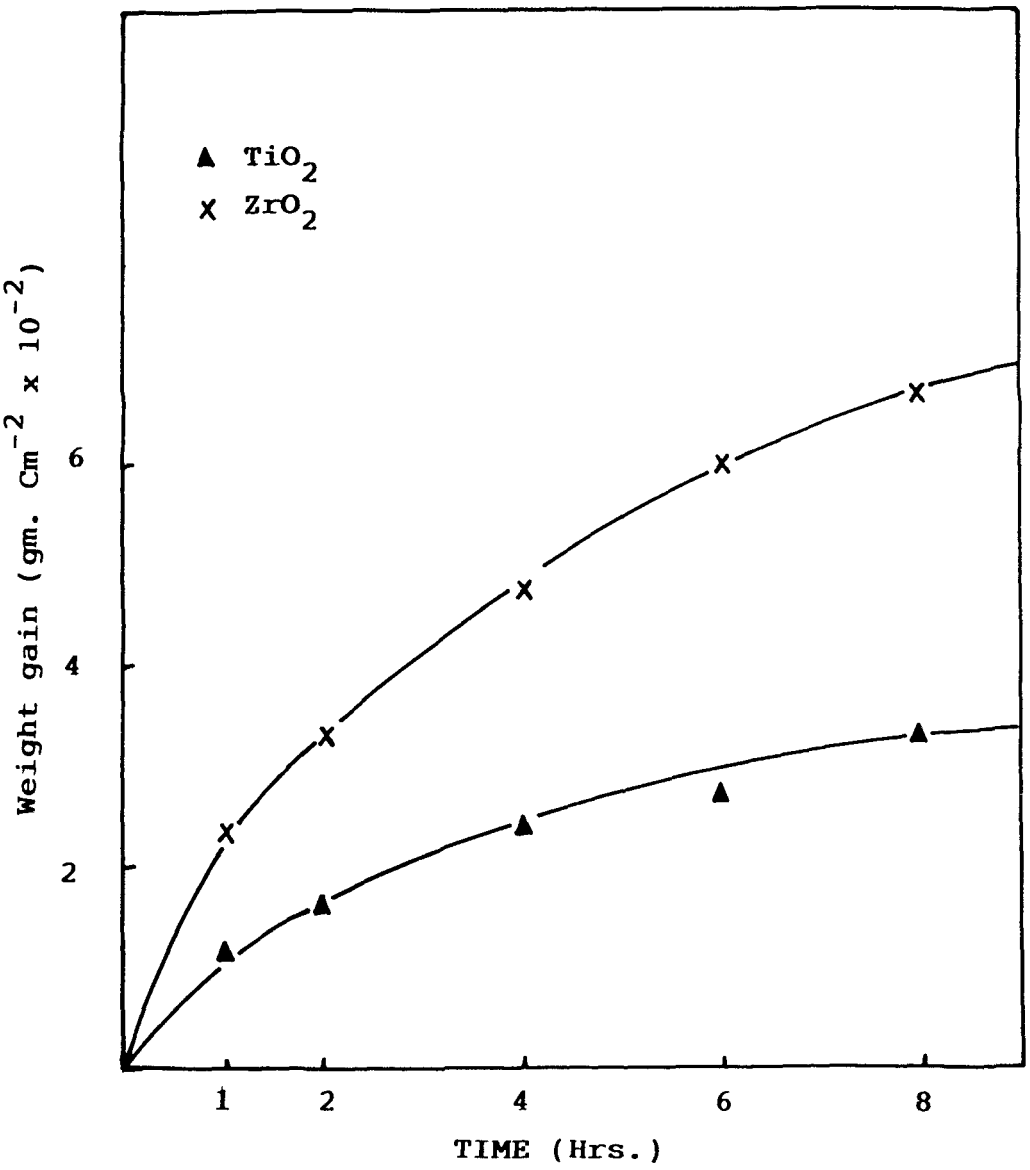

Fig. 7.8 Plots of weight gain Vs time for the oxidation of decarburized Fe-10Cr_7C_3-0.1C-1.0M'O_2 alloys at 900°C.

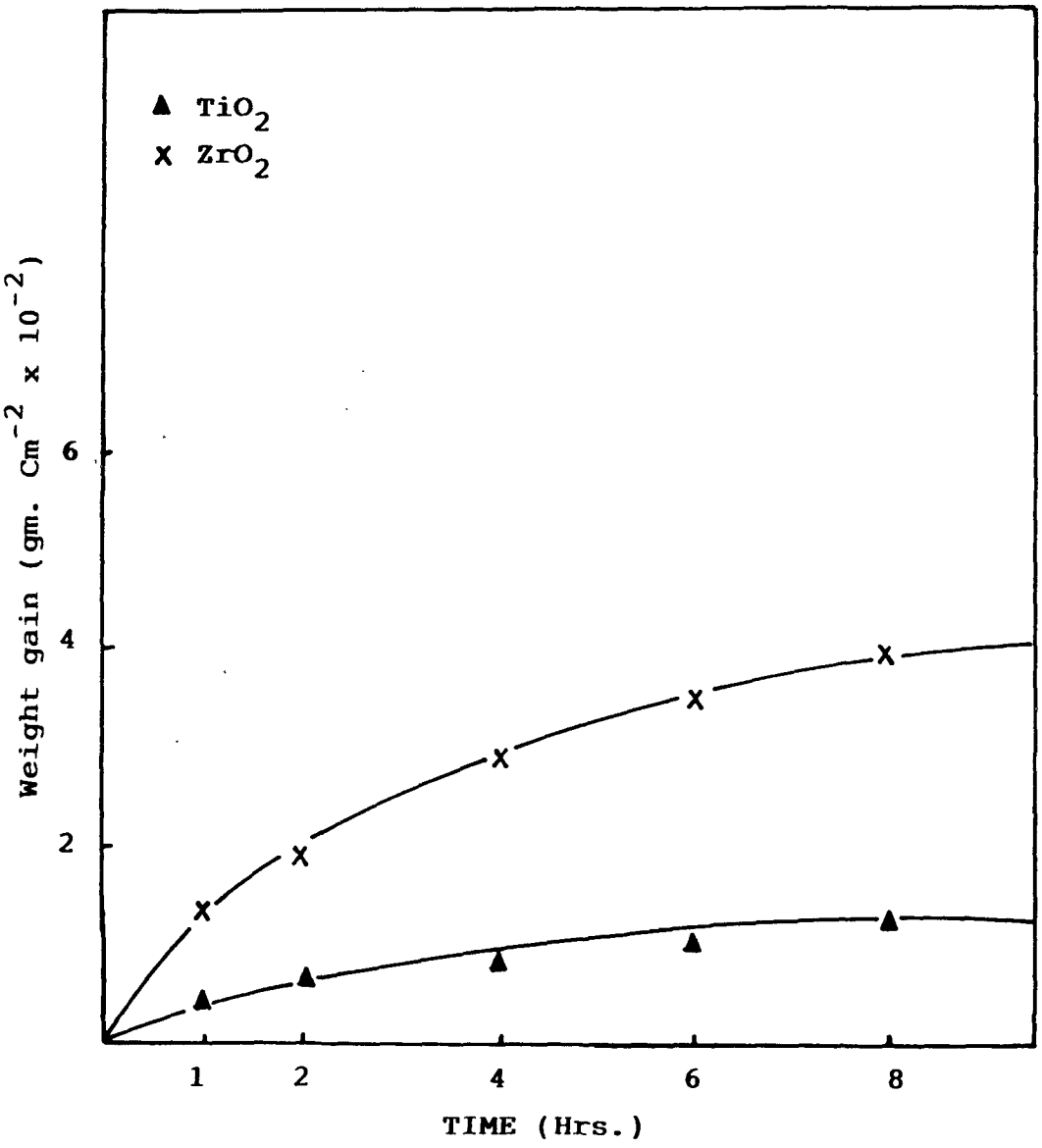

Fig. 7.9 Plots of weight gain Vs time for the oxidation of decarburized Fe-10WC-0.1C-1.0M'O_2 alloys at 900°C.

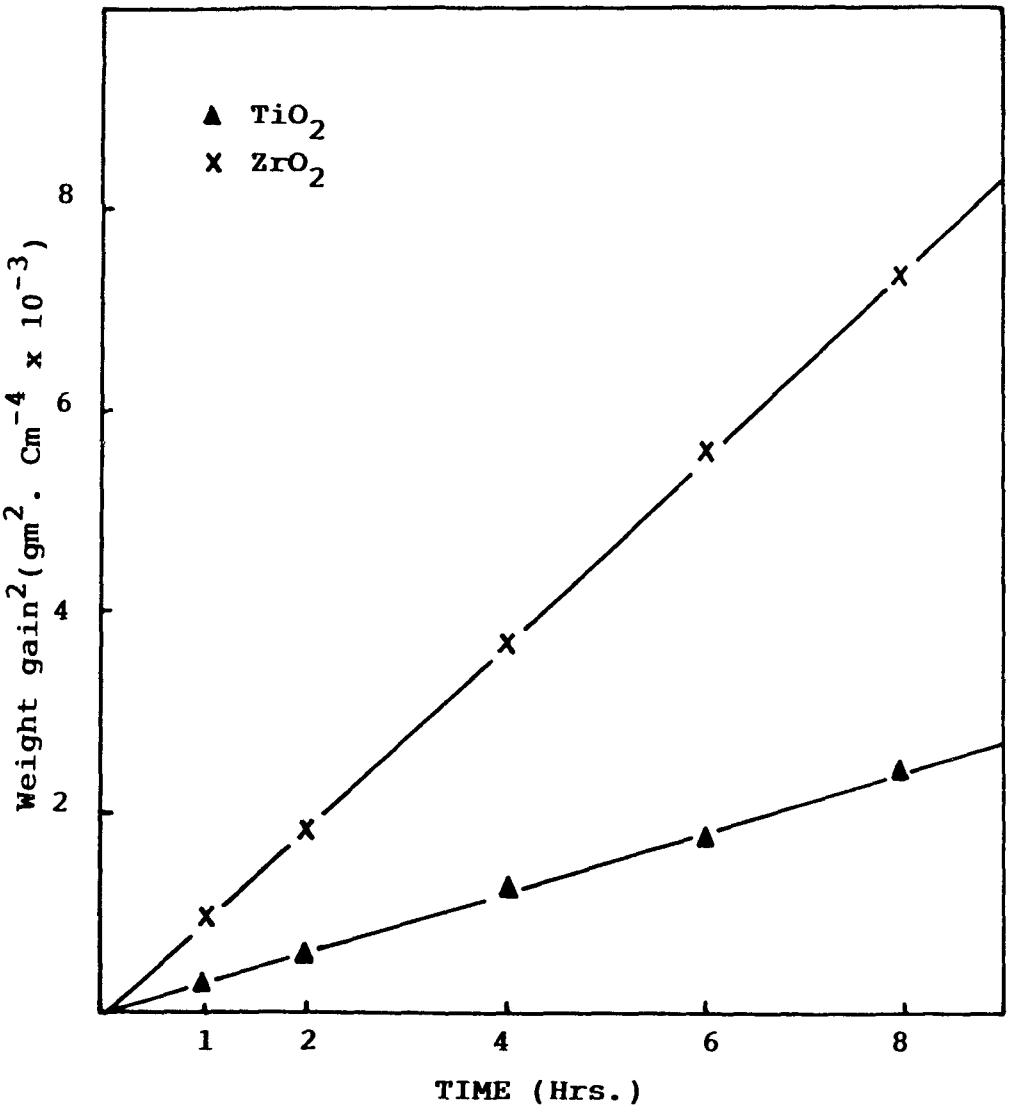

Fig. 7.10 Plots of weight gain^2 Vs time for the oxidation of decarburized Fe-10NbC-0.1C-1.0M'O_2 alloys at 900°C.

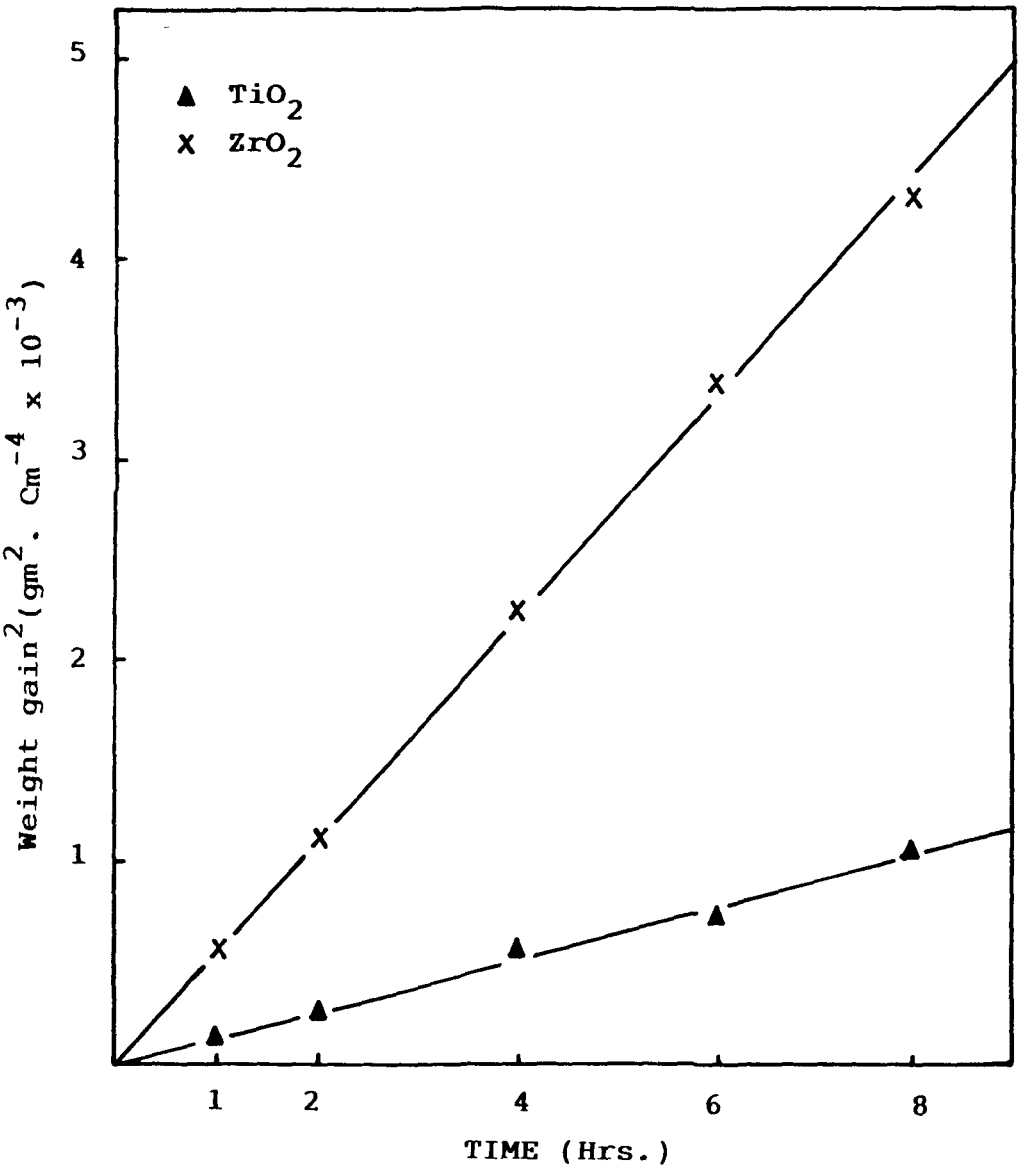

Fig. 7.11 Plots of weight gain^2 Vs time for the oxidation of decarburized Fe-10Cr_7C_3-0.1C-1.0M'O_2 alloys at 900°C.

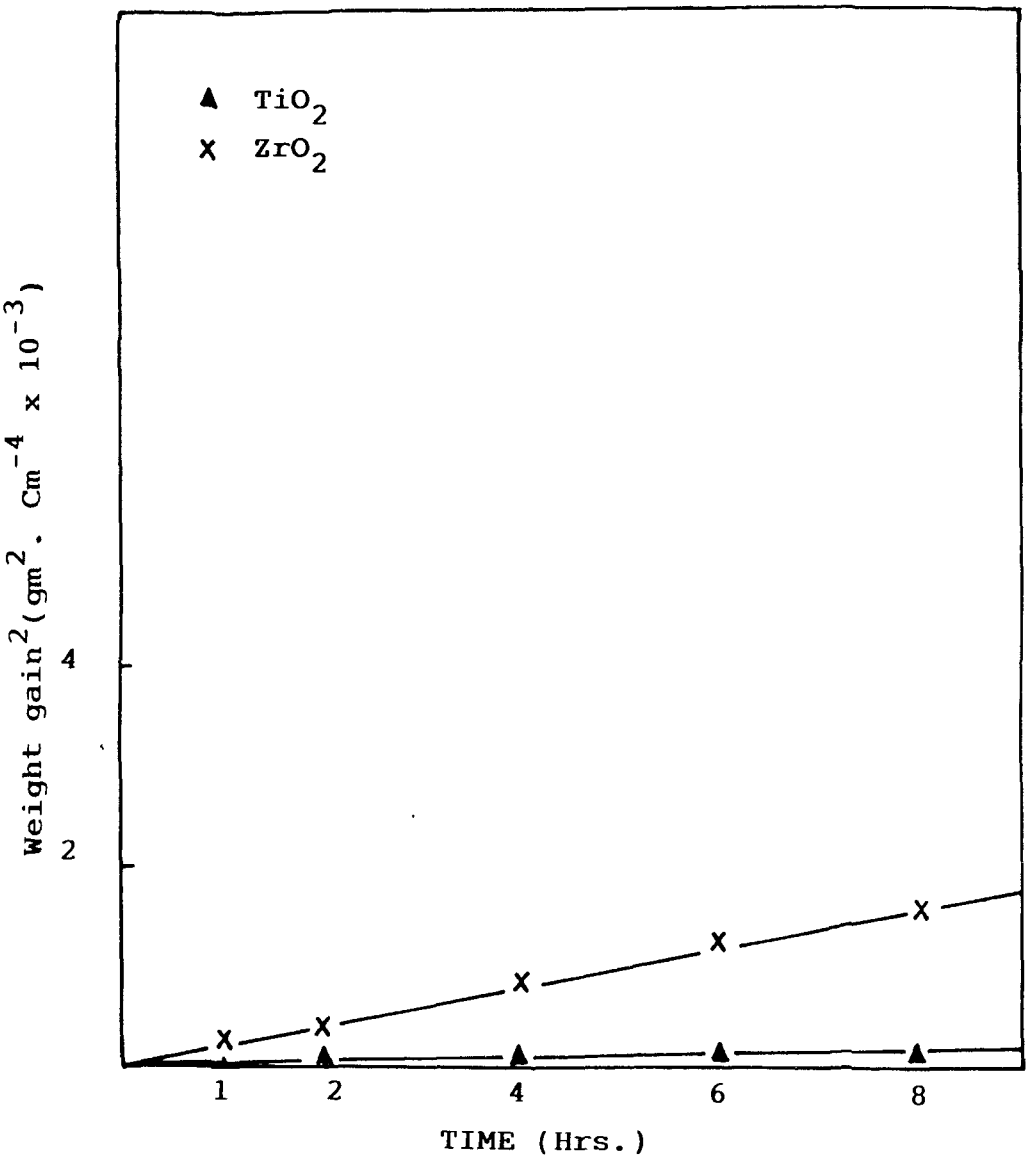

Fig. 7.12 Plots of weight gain^2 Vs time for the oxidation of decarburized Fe-10 WC-0.1C-1.0M'O_2 alloys at 900°C.

7.1.2 Metallographic Studies

7.1.2.1 Fe-10NbC-0.1C-1.0TiO_2/ZrO_2 Alloys

Figures 7.13 and 7.14 show photomicrographs of carbide-dispersed TiO_2- and ZrO_2-containing iron-base sintered alloys. Polygonal grains of ferrites are present in which carbides are present as dispersion along with TiO_2 or ZrO_2. On decarburization in H_2-H_2O at 900°C, there is no major change in the microstructure of the alloy (Figs. 7.15 and 7.16) except that it is more porous and the carbides are mainly concentrated at the grain boundaries. Figure 7.17 shows a scanning electron micrograph of TiO_2-containing alloy oxidized at 900°C for 8 hrs. The matrix contains dispersion of NbC along the grain boundaries together with FeO which is present as an internal oxide. The inner scales mainly contain FeO with TiO_2 inclusions and are fairly adherent, NbC is also incorporated with the scales. The outermost layer is mainly consisted of Fe_2O_3. A similar structure is observed in the oxidized ZrO_2-containing alloy. Figure 7.18 shows a photomicrograph of the TiO_2-containing alloy decarburized at 900°C for 2 hrs. followed by oxidation at 900°C for 8 hrs. The microstructure shows presence of a relatively thick internal FeO at or near the grain boundaries along with NbC; it is difficult to identify TiO_2 but it is certainly present in the inner oxide scales. The microstructure observed (Fig. 7.19) in case of decarburized-oxidized Fe-10NbC-0.1C-1.0ZrO_2 is almost identical to that

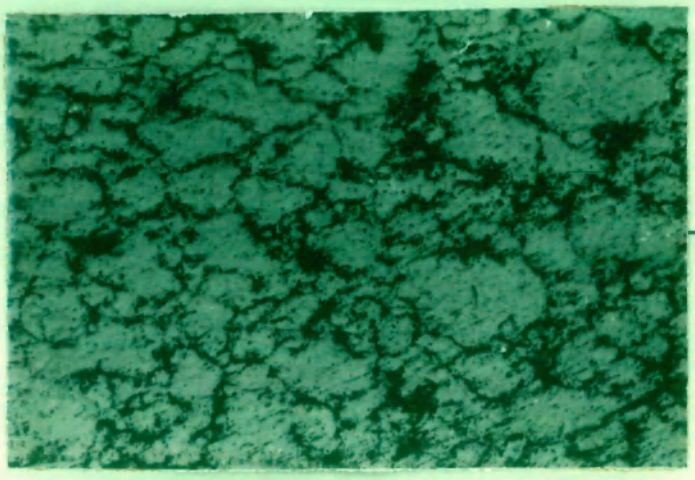

Fig. 7.13 Photomicrograph of a cross-section of Fe-10NbC-0.1C-1.0TiO_2 alloy, sintered X 120

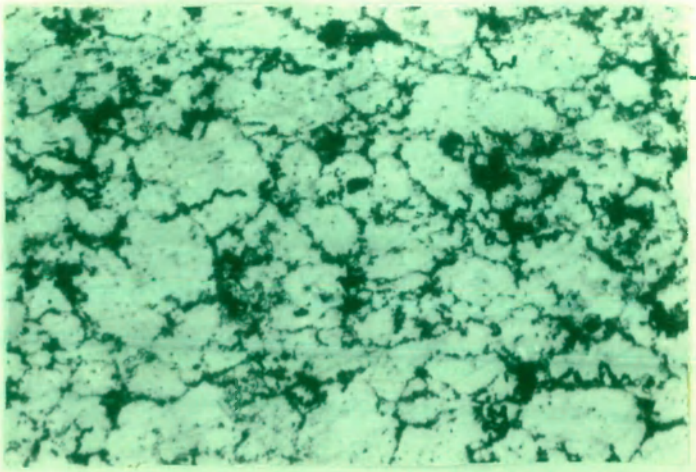

Fig. 7.14 Photomicrograph of a cross-section of Fe-10NbC-0.1C-1.0ZrO_2 alloy, sintered X 120

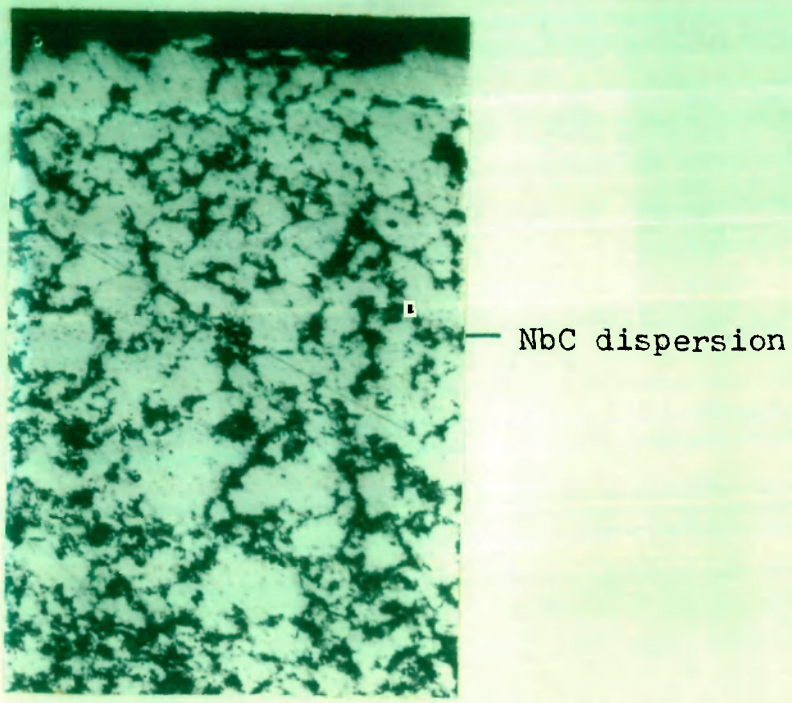

Fig. 7.15 Photomicrograph of a cross-section of Fe-10NbC-0.1C-1.0TiO_2 alloy, decarburized at 900°C for 2 hrs. X 120

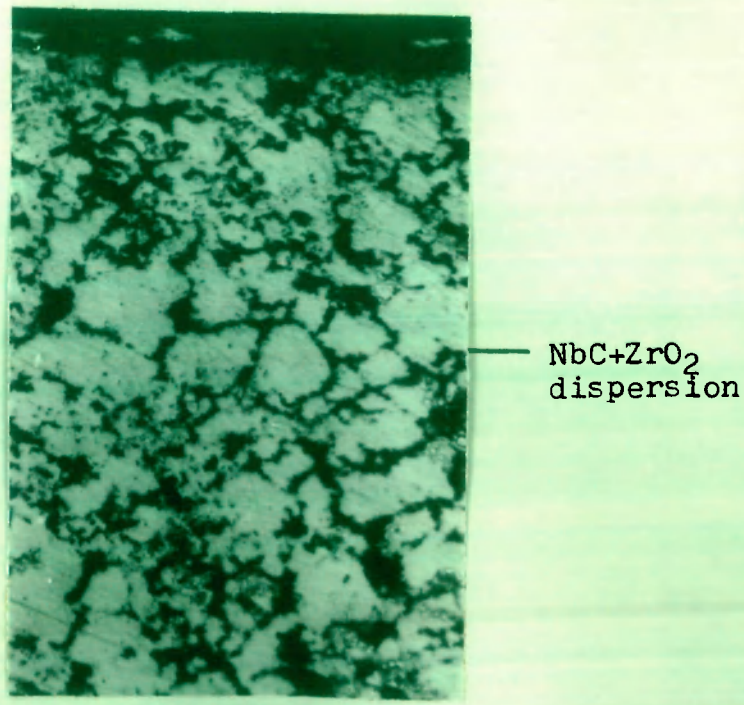

Fig. 7.16 Photomicrograph of a cross-section of Fe-10NbC-0.1C-1.0ZrO_2 alloy, decarburized at 900°C for 2 hrs. X 120

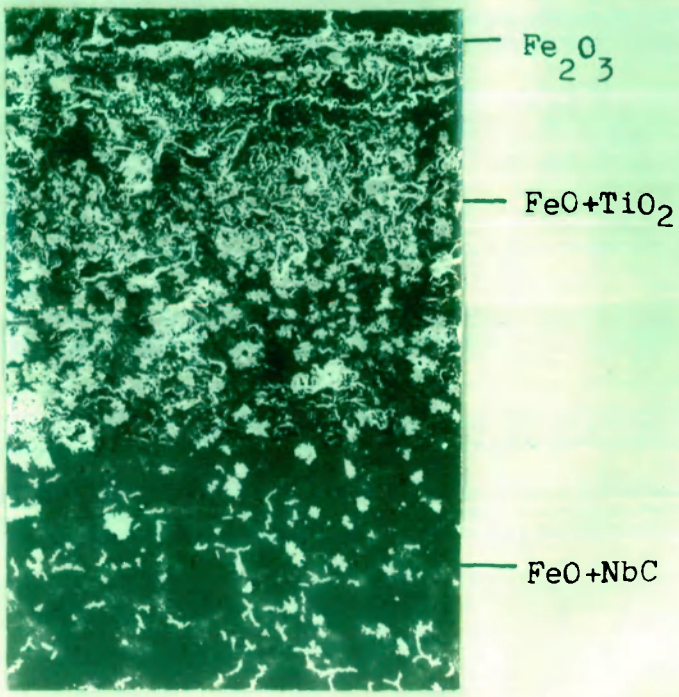

Fig. 7.17 SEM picture of Fe-10NbC-0.1C-1.0TiO_2 alloy, oxidized at 900°Cffor 8 hrs. X-100

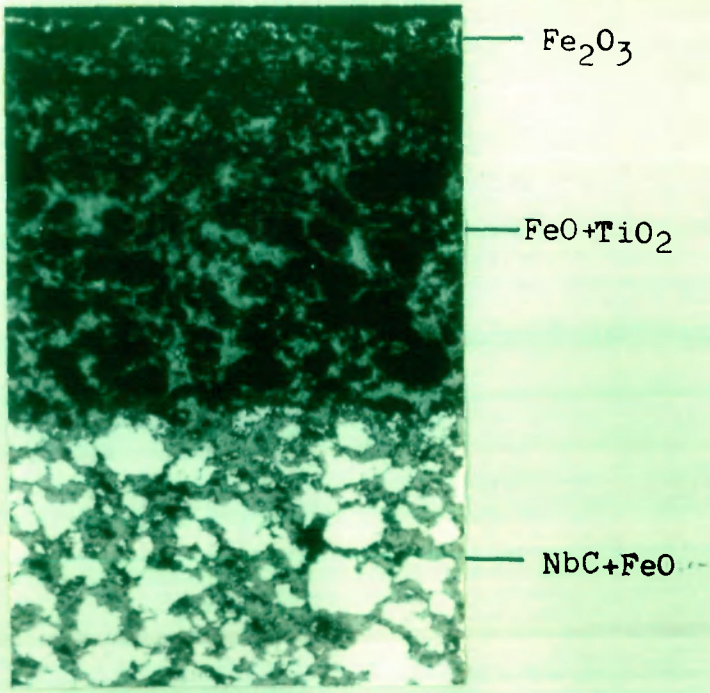

Fig. 7.18 Photomicrograph of a cross-section of predecarburized Fe-10NbC-0.1C-1.0TiO_2 alloy, oxidized at 900°C for 8 hrs. X 120

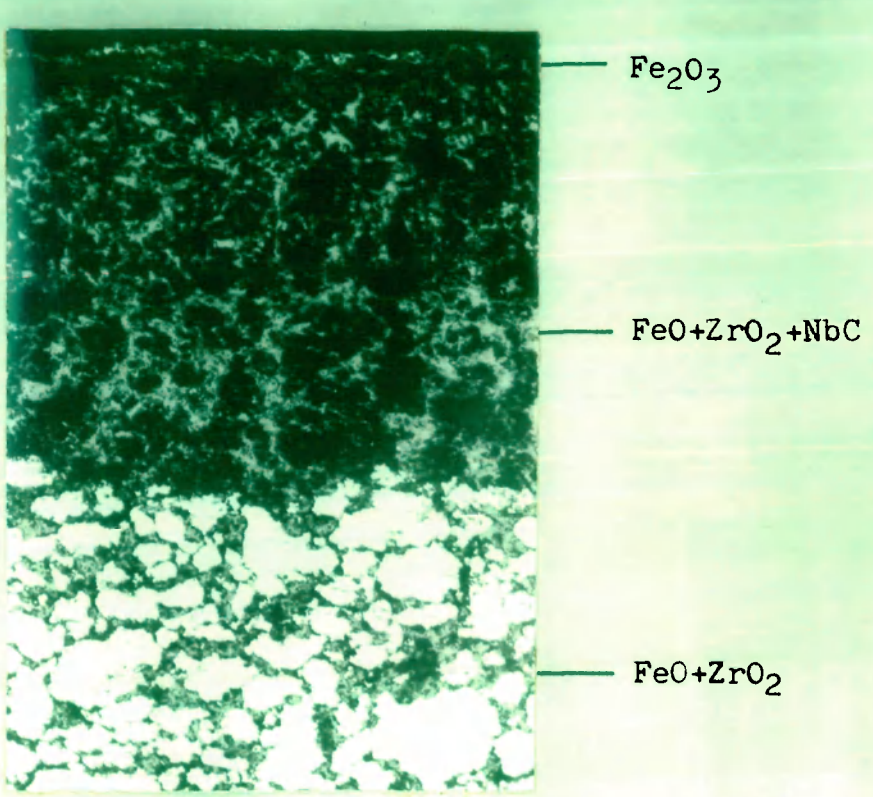

Fig. 7.19 Photomicrograph of a cross-section of decarburized, Fe-10NbC-0.1C-1.0ZrO_2 alloy, oxidized at 900°C for 8 hrs.
X 120

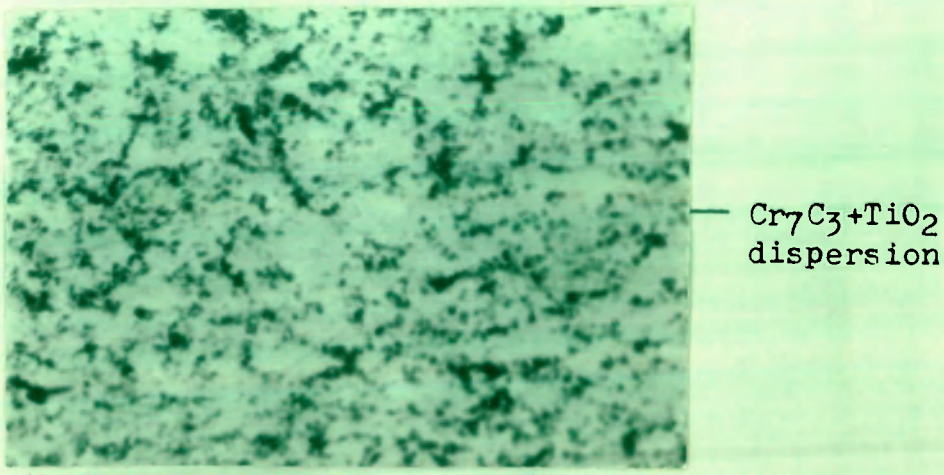

Fig. 7.20 Photomicrograph of a cross-section of Fe-10Cr_7C_3-0.1C-1.0TiO_2 alloy, sintered.
X 120

observed in case of the corresponding TiO_2-containing alloy decarburized and oxidized under similar conditions.

7.1.2.2 Fe-Cr_7C_3-0.1C-1.0TiO_2/ZrO_2 Alloys

Figure 7.20 shows a photomicrograph of TiO_2-containing Cr_7C_3 dispersed iron-base sintered alloy. The microstructure is consisted of polygonal ferrite grains containing inclusions of an external phase. The decarburized alloy shows (Fig. 7.21) the presence of white Cr_7C_3 at the grain boundaries of polygonal ferrites coexisting with another phase in the form of dark grey coloured TiO_2 grains. The microstructures of the corresponding ZrO_2-containing sintered alloy in the as-cast and decarburized conditions are almost similar. Figure 7.22 shows a scanning photomicrograph of ZrO_2-containing iron-base sintered alloy oxidized at 900°C. The microstructure indicates the presence of the clusters of ZrO_2 in the iron rich matrix along with a network of Cr_7C_3 at the grain boundaries, there is also selective oxidation of iron into FeO and Cr_7C_3 into Cr_2O_3. The ZrO_2-particles are also present in the inner scales. The photomicrograph of the same alloy under decarburized-oxidized condition (Fig. 7.23) shows the presence of carbide dispersoid at the grain boundaries along with white grains of ZrO_2 the latter are also present in the inner scale. The scanning electron photomicrograph (7.24) of TiO_2-containing alloy under decarburized and oxidized condition at 900°C, shows the

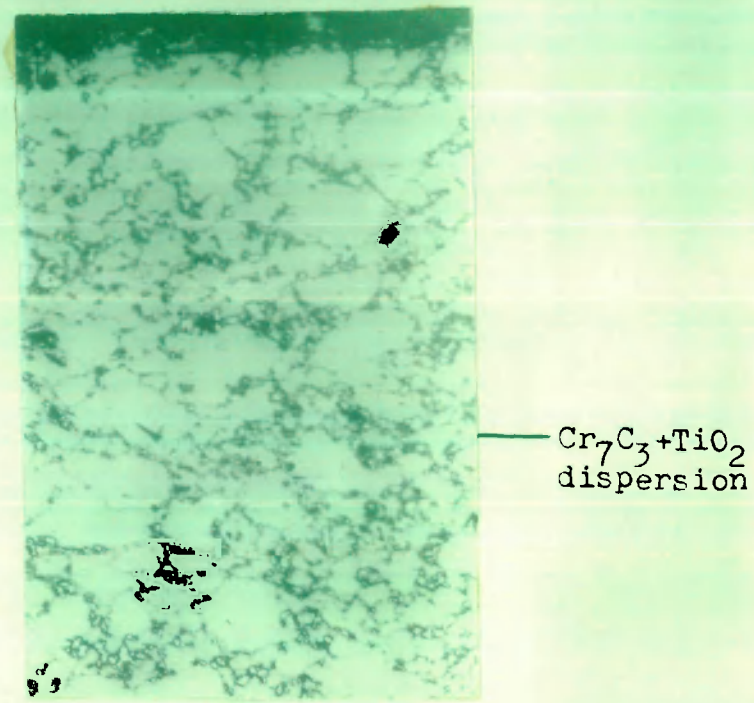

Fig. 7.21 Photomicrograph of a cross-section of Fe-10Cr_7C_3-0.1C-1.0TiO_2 alloy, decarburized at 900°C for 2 hrs.
X 120

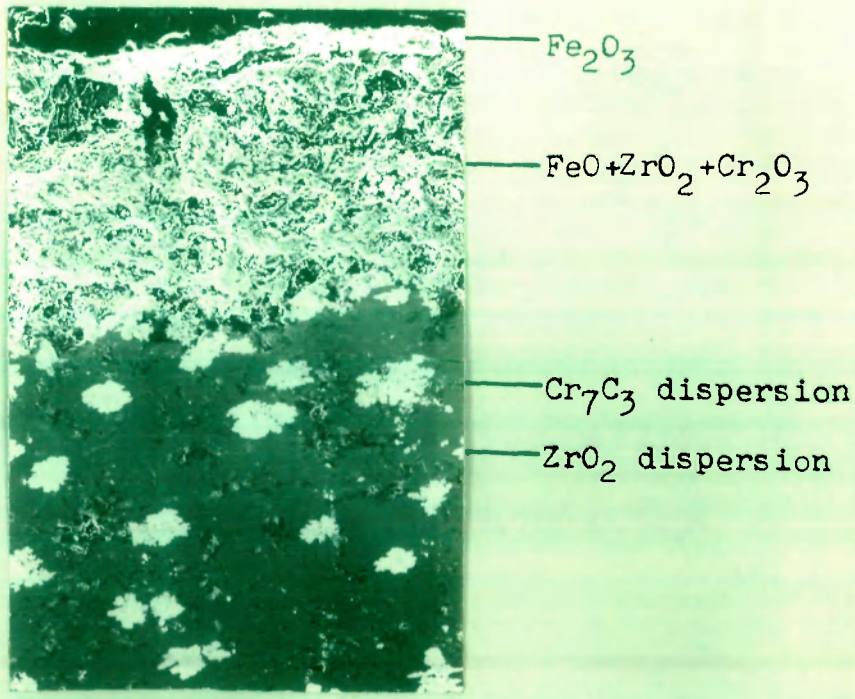

Fig. 7.22 SEM picture of Fe-10Cr_7C_3-0.1C-1.0ZrO_2 alloy, oxidized at 900°C for 8 hrs.
X 100

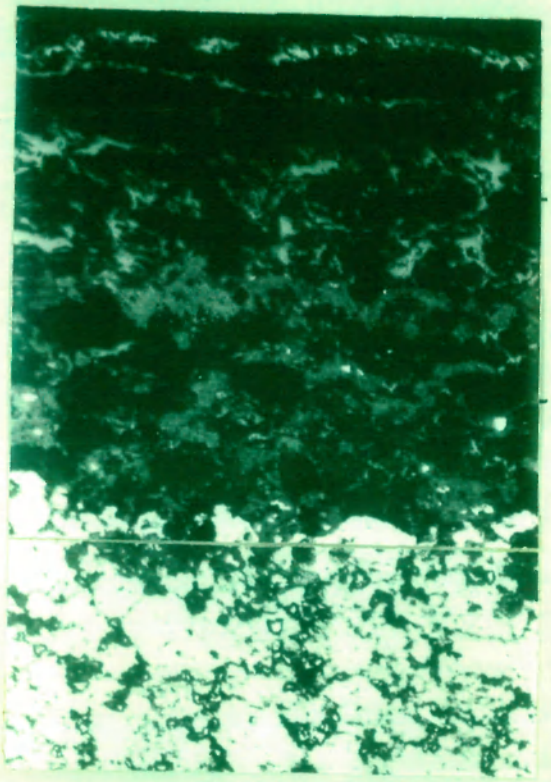

Fig. 7.23 Photomicrograph of a cross-section of predecarburized Fe-10Cr_7C_3-0.1C-1.0ZrO_2 alloy, oxidized at 900°C for 8 hrs.
X 120

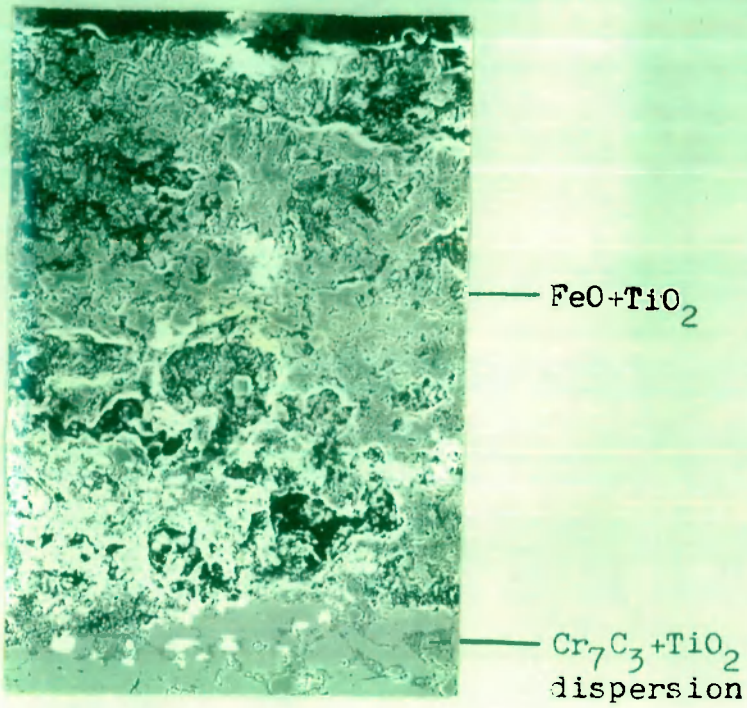

Fig. 7.24 SEM picture of predecarburized Fe-10Cr_7C_3-0.1C-1.0TiO_2 alloy, oxidized at 900°C for 8 hrs. X 100

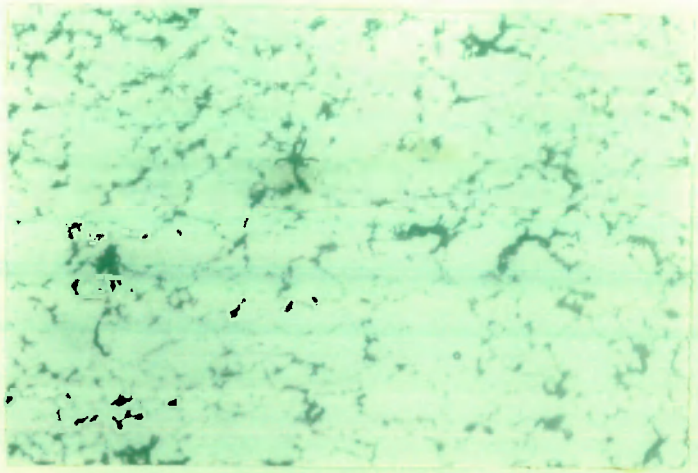

Fig.7.25 Photomicrograph of a cross-section of Fe-10WC-0.1C-1.0TiO_2 alloy, sintered. X 120

presence of a carbide net work mostly concentrated at the grain boundaries. TiO_2 is present as a white phase in the matrix and is also incorporated with the inner scales. The copious scales are continuous and adhered. The scales are predominently wustite containing inclusions of TiO_2.

7.1.2.3 Fe-10WC-0.1C-1.0TiO_2/ZrO_2 Alloys

Figure 7.25 shows a photomicrograph of TiO_2-containing WC-dispersed iron-base sintered alloy, the photomicrograph shows the presence of ferritic polygonals and the carbide particles at the grain boundaries. The alloy decarburized in H_2-H_2O shows a dispersion of coarsened WC grains at the grain boundaries along with irregular distribution of TiO_2. A similar configuration is observed in ZrO_2-containing alloys (Figures 7.26-7.27).

7.2 Discussion

The oxidation rates of undecarburized Fe-10WC-0.1C-1.0ZrO_2/TiO_2 alloys are the lowest and the corresponding NbC-containing alloys are the highest, a similar trend has been observed in Fe-10MC and Fe-10MC-0.1C-1.0R_2O_3 alloy systems. In the decarburized-oxidized state, Fe-10WC-0.1C-1.0ZrO_2 alloys have the lowest oxidation rates and Fe-10NbC-0.1C-1.0TiO_2 have the highest rates. In general, NbC-containing alloys have invariably higher oxidation rates than other carbide-containing alloys. The oxidation rates of decarburized

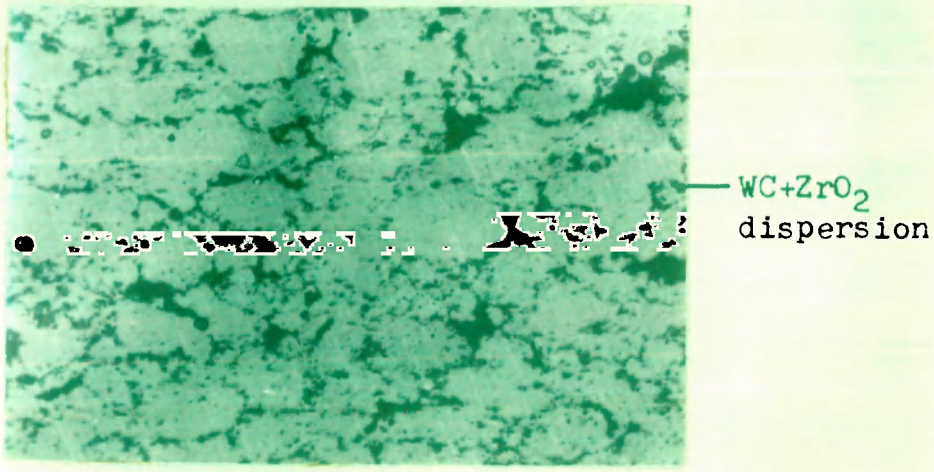

Fig. 7.26 Photomicrograph of a cross-section of Fe-10WC-0.1C-1.0ZrO_2 alloy, sintered. X 120

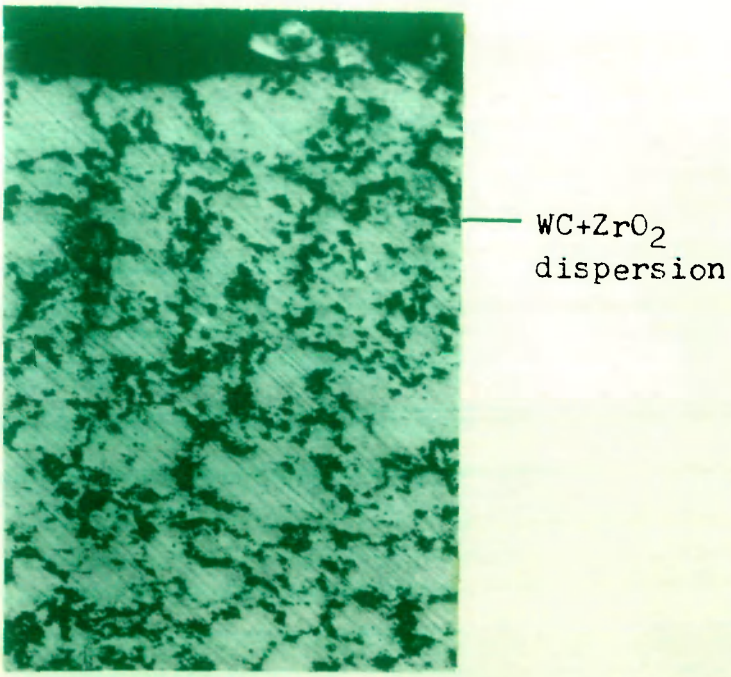

Fig. 7.27 Photomicrograph of a cross-section of Fe-10WC-0.1C-1.0ZrO_2 alloy, decarburized at 900°C for 2 hrs. X 120

alloys are significantly higher than the undecarburized alloys.

In most cases, the oxidation rates of Fe-10MC-0.1C-1.0ZrO_2/TiO_2 alloys are very slightly higher than the corresponding rare earth oxide-containing alloys (Chapter VI). However, like RE_2O_3-containing sintered alloys, ZrO_2/TiO_2-containing alloys in undecarburized and decarburized states have oxidation rates much lower (1-2 order of magnitude) than the Fe-10MC alloys (Chapter IV) and of the same order as those of Fe-10MC-0.1C-20Cr alloys.

The results of oxidation kinetic and morphology of the oxidized alloy show that like rare earth oxides, the presence of ZrO_2 or TiO_2 in the matrix greatly restricts the oxidation rates of Fe-MC alloy systems. ZrO_2 or TiO_2 inclusions act as deterent to the transport of metal during oxidation. The rare earth oxides have a slight edge over TiO_2 or ZrO_2 as far as adherent and compactness of the scales are concerned. The small difference in the oxidation rates of undecarburized and decarburized states could be attributed to the different decarburization rates of the alloys during oxidation.

CHAPTER VIII

DECARBURIZATION AND OXIDATION OF SOME INDUSTRIAL STEELS

The experimental details containing material specifications, apparatus and procedures have already been given in Chapter II.

Specimens of 15 x 15 x 1 mm size or 12.5 mm diameter and 1.5 mm thickness were cut from steel sheets or steel rods. A 0.4 mm suspension hole was drilled near the middle of one end of the specimen. The specimens were sealed in a quartz tube and annealed at 900°C for 4 hrs.

The annealed alloys were subjected to oxidation (1 atm O_2) for 6-9 hrs, decarburization (H_2-H_2O) for 2-4 hrs. and decarburization-oxidation studies at 900°C for 9 hrs. on a laboratory fabricated thermal balance.

8.1 Results

8.1.1 Oxidation Kinetics

Figure 8.1 represents weight gain vs time plots for the oxidation of low alloy steels e.g. EN-24, EN-31, EN-36, EN-9 high speed steels (6 and 18 % W), silver steel and die-steel at 900°C in 1 atm. O_2. The plots in general are parabolic as indicated by the linear nature of weight gain^2 vs time plots (Fig. 8.2). The weight gain vs time plots for the oxidation of predecarburized alloy steels are shown in Figure 8.3. In general most of alloy steels are oxidized by

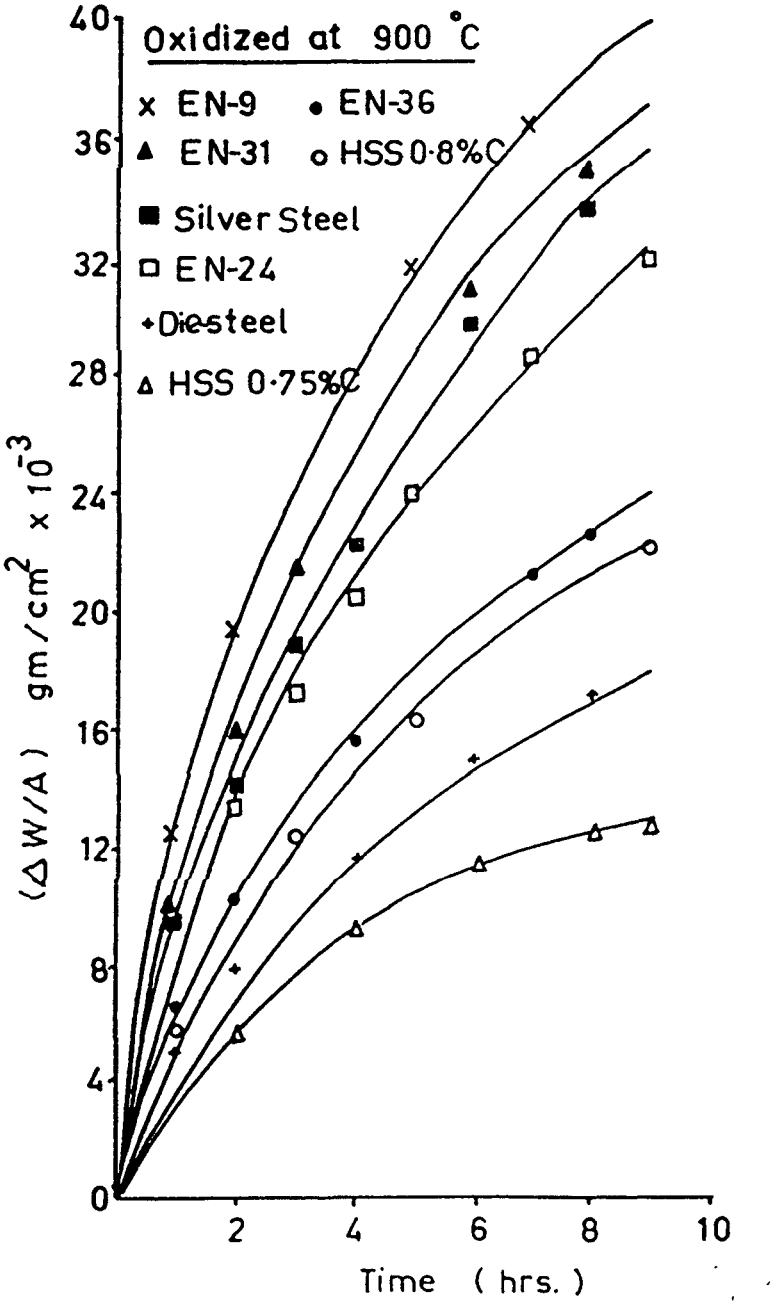

Fig. 8.1 Plots of weight gain Vs time for the oxidation of industrial steels.

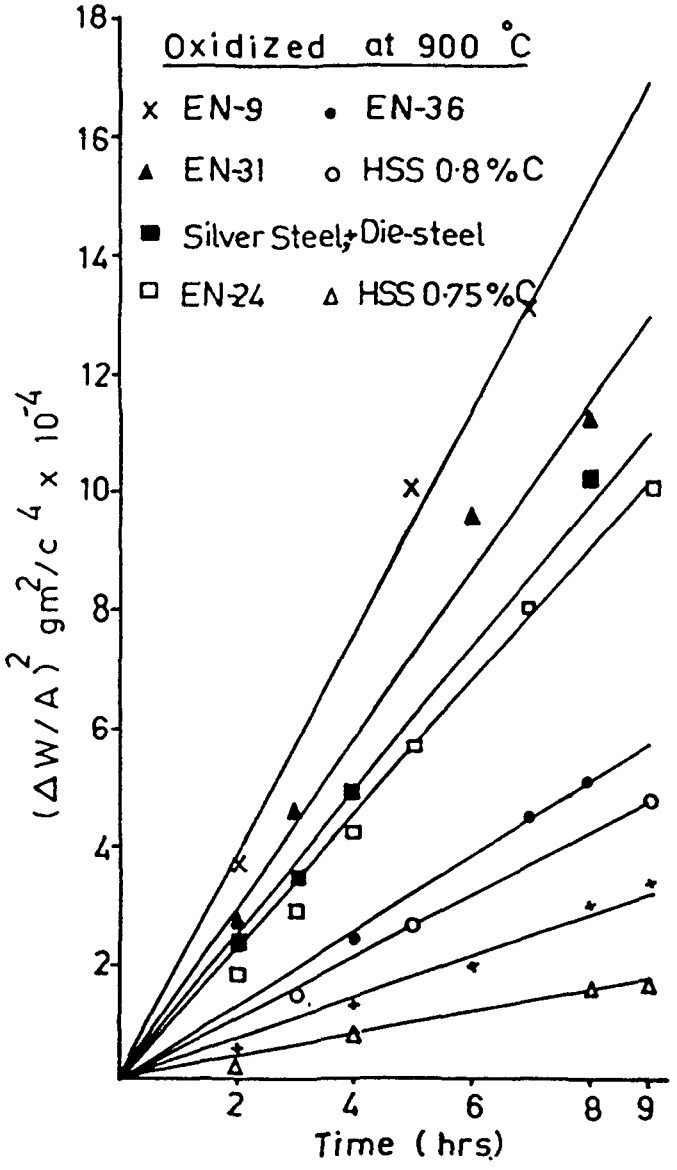

Fig.8.2 Plots of weight gain^2 Vs time for oxidation of industrial steels.

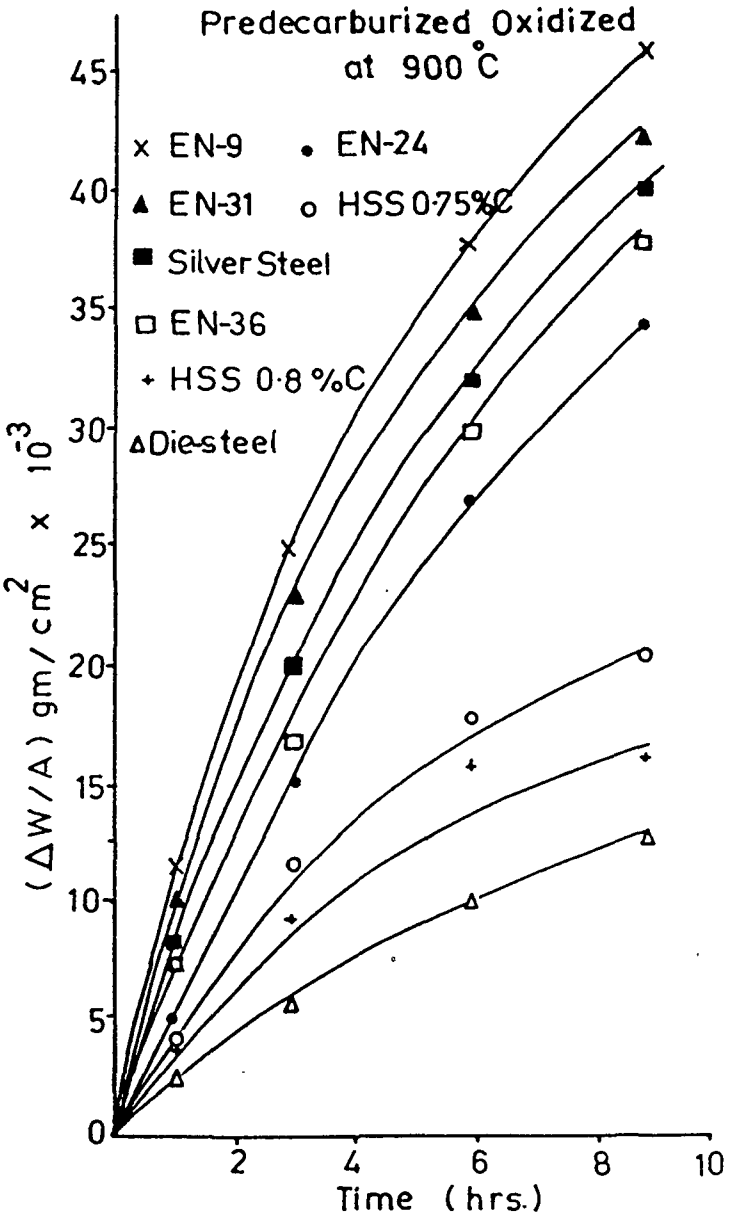

Fig. 8.3 Plots of weight gain Vs time for the oxidation of predecarburized industrial steels.

a parabolic rate law except a few as indicated by the breaks in the weight gain^2 vs time plots (Fig. 8.4).

Table 8.1 lists the values of the parabolic rate constants for the oxidation of alloy steels in as cast and decarburized condition. With a few exceptions, the oxidation rates of undecarburized alloy steels are slightly lower than the predecarburized-oxidized alloy steels. Amongst the undecarburized and predecarburized alloy steels, EN-9 has the highest oxidation rate followed by EN-31 alloy steel, high speed steel (18 % W) and die-steels showing the lowest rates respectively.

Table 8.1

Values of parabolic rate constants, Kp for the oxidation of alloys in $Kg^2,m^{-4}.sec^{-1} \times 10^{-7}$

Alloy	Plain oxidation 9 hrs.at 900°C	Decarburization and Oxidation 4 and 9 hrs. at 900°C respectively	
EN-9	51.3888	62.8333	-
EN-31	38.8888	55.555	-
Silver steel	33.3333	38.1944	54.975
EN-24	30.8333	13.8888	43.9805
EN-36	17.3611	26.0416	52.2661
HSS 6 % W	14.4472	8.68055	-
Die-steel	9.7777	4.6277	-
HSS 18 % W	5.1111	12.7305	

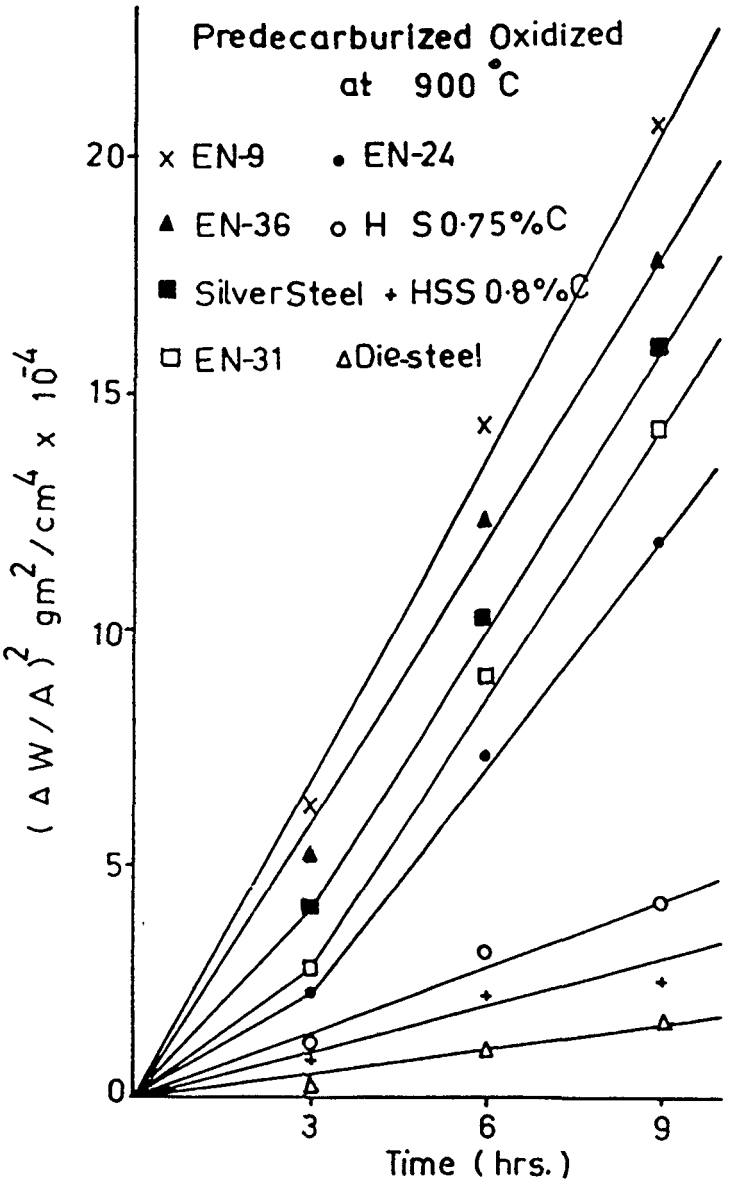

Fig. 8.4 Plots of weight gain^2 VS time for oxidation of predecarburized industrial steels.

Table 8.2 contains weight loss data for different alloy steels after 4 hr. decarburization run in H_2-H_2O atmosphere at 900°C. HSS steels show highest weight losses and EN-36 the lowest weight losses.

Table 8.2

Weight loss/area after a 4 hr. decarburization run in H_2-H_2O atmosphere at 900°C.

S.No.	Alloy	$Kg/m^2 \times 10^{-3}$	wt. loss kg x 10-6
1	EN-9	15.9	3.0
2	EN-31	49.9	7.0
3	Silver steel	24.3	5.0
4	EN-24	32.5	5.0
5	EN-36	14.7	2.0
6	HSS 6% W	45.5	10.0
7	Die-steel	14.7	3.0
8	HSS 18% W	71.2	14.0

8.1.2 Metallographic studies

Figures 8.5 to 8.15 show typical optical photomicrographs and scanning electron photomicrograph of the cross-section of decarburized and undecarburized alloy steels. All alloy steels show a well defined decarburized layer and an increase in ferrite contents of the alloys. The thickness of

the decarburized layer increases with the increase in carbon contents as evident from the photomicrographs. However a deviation is found in some cases probably due to the varying percentage of carbide formers like Ni, Cr, Mo or W.

Figures 8.16 to 8.22 show the optical photomicrographs and scanning electron photomicrographs of the cross-section of undecarburized-oxidized alloy steels. There are three different phases in the scales. In all cases the oxide scales are adhered to the matrix except in silver steel, which is due to the polishing artifacts. Figures 8.23 to 8.27 represent the optical photomicrographs and scanning electron photomicrographs of the cross-section of predecarburized-oxidized alloy steels.

The oxides formed on the alloys under these conditions are similar to those obtained in undecarburized-oxidized alloys though more thicker, porous and fragile. The porosity and fragility of the scales are perhaps responsible for higher oxidation rates.

8.1.3 Microstructure of Alloy Steels

Figures 8.5 to 8.7 show some typical microstructures of the cross sections of alloy steels in as cast condition.

A photomicrograph of diecast steel (12 % Cr - 2 % C by weight) shows the presence of white flakes of graphite and Cr_7C_3 embeded in a pearlitic matrix Figure 8.5. Silver steel (1 % C - 1 % Cr) contains a structure in which carbides of Fe

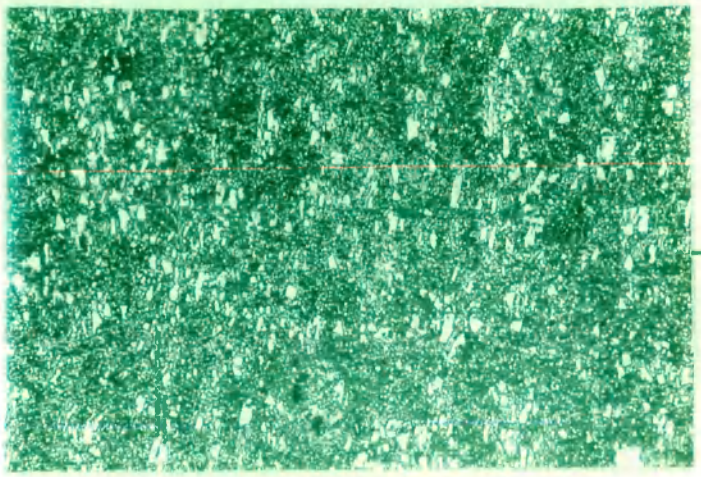

Fig. 8.5 Photomicrograph of a cross section of undecarburized die steel. X 120

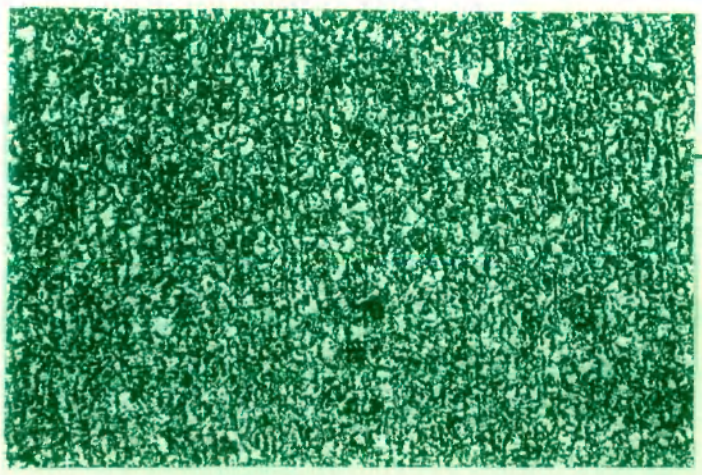

Fig. 8.6 Photomicrograph of a cross section of undecarburized EN-24 steel. X 120

and Cr are dispersed in a pearlitic matrix and EN-31 (1 % C - 1 % Cr) has Cr_7C_3 at grain boundaries in a pearlitic matrix. EN-24 (Ni-1.5, Cr-5, C-0.45) shows dispersion of spheroidal Cr_7C_3 and lamellar pearlite in a ferritic matrix (Fig. 8.6). EN-9 (0.45 % C) shows a pearlitic structure (Fig. 8.7). Mo-containing high speed tool steel (W-6, Cr-4, C-0.8, V-2 and Mo-5) in as cast condition shows a fine dispersion of the carbides of W, Mo and Cr in a ferritic matrix. 18:4:1 (W, Cr, V) high speed steel containing 0.75 % C shows a fine dispersion of carbides in a ferritic matrix. EN-36 containing 3 % Ni, 1 % Cr and 0.2 % C shows fine dispersion of Cr_7C_3 in a pearlitic matrix.

8.1.4 Morphology of Oxide Scales

8.1.4.1 Oxidized alloys

Figure 8.8 shows a cross section of silver steel decarburized in H_2-H_2O atmosphere at 900°C for 2 hrs. A well defined decarburized zone is present at the metal interface. The decarburized layer is ferritic in nature. The undecarburized matrix, contains dispersion of Cr_7C_3 in a ferritic matrix, the Fe_3C contents are considerably lowered on decarburization. A cross section of decarburized EN-31 steel shows the presence of a thin decarburized layer at the metal interface followed by a carbide rich layer. In the middle of the specimen, polygonal grains of carbides are gulfed in a ferritic matrix (Fig. not shown). Decarburized alloy steel

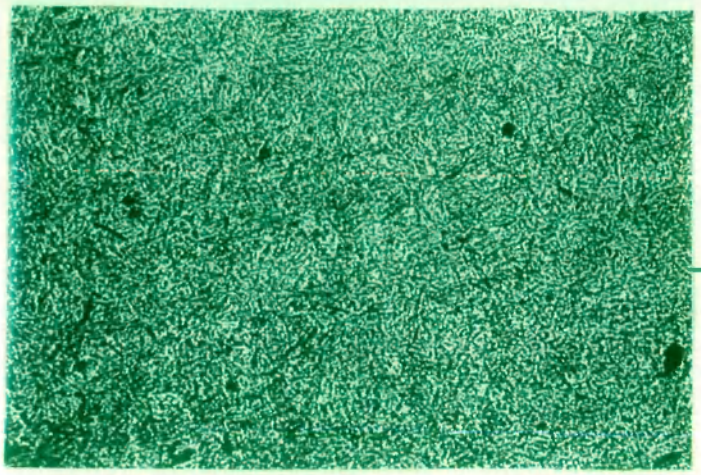

Fig. 8.7 Photomicrograph of a cross-section of undecarburized EN-9 steel. X 120

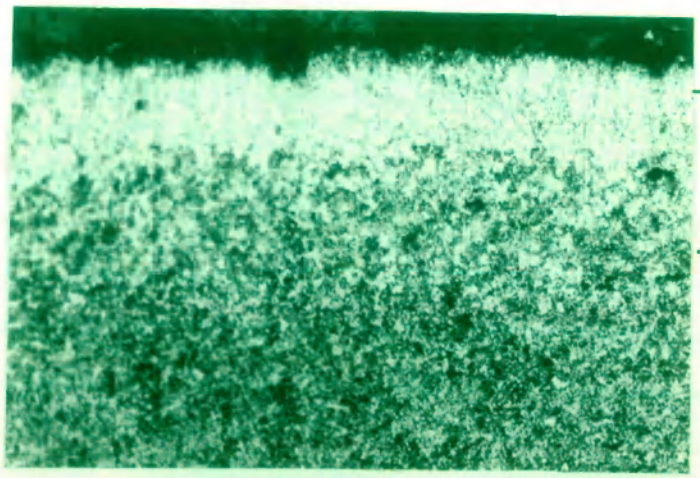

Fig. 8.8 Photomicrograph of a cross-section of silver steel, decarburized at 900°C for 2 hrs. X 120

EN-24 shows a well defined decarburized layer, the photomicrograph (Fig. 8.9) indicates extensive decarburization, the undecarburized zone contains dispersion of carbide in a ferritic matrix. Figure 8.10 shows the SEM picture of the matrix of decarburized alloy. The presence of carbide particles is clearly shown. Decarburized alloy steel EN-9 shows uniform decarburized layer at the alloy interface (Fig. 8.11). The undecarburized zone shows dispersion of cementite in a ferritic matrix. Figure 8.12 shows a photomicrograph of a cross section of decarburized high speed steel containing Mo and V. Although no well defined decarburized layer is present but there is depletion of carbide in the vicinity of alloy interface. Beyond this zone, there is a dispersion of carbides in the ferritic matrix. The microstructure of decarburized 18:4:1 (W:Cr:V) high speed steel is very similar to the low tungsten high speed steel mentioned above (Fig. 8.13). Figure 8.14 shows a cross section of decarburized EN-36 steel. On comparison with the microstructure of undecarburized alloy, it appears that some decarburization has occurred although a decarburized layer is missing. The decarburized alloy shows the dispersion of carbide in a ferritic matrix (Fig. 8.15). The decarburized die-steel shows a thin carbide depleted zone at the alloy interface. The area beyond this zone contains a dispersion of carbides in a pearlitic matrix.

Figure 8.16 shows a photomicrograph of a cross-section

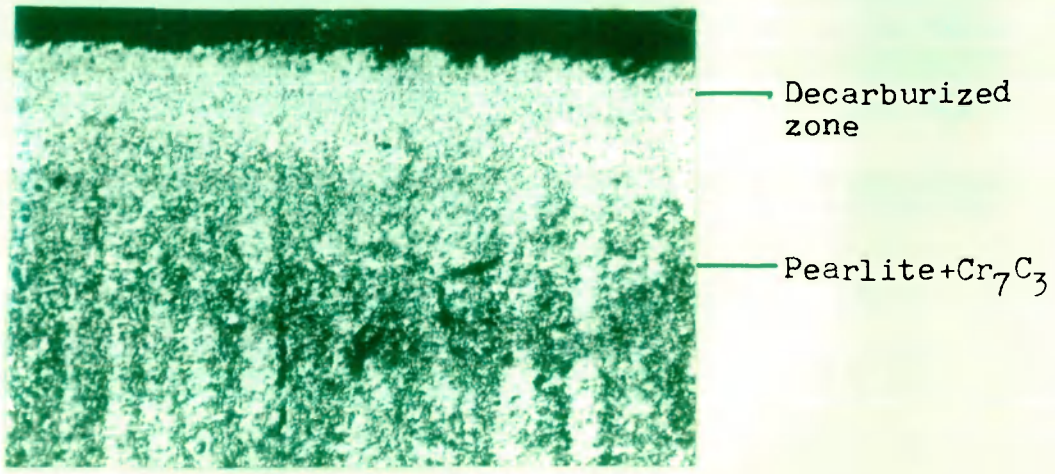

Fig. 8.9 Photomicrograph of a cross-section of EN-24 steel, decarburized at 900°C for 2 hrs. X 120

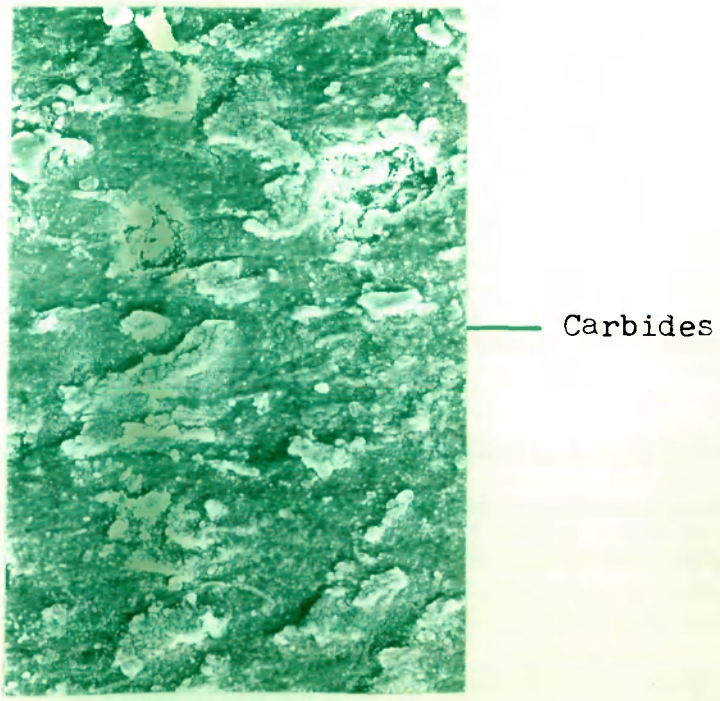

Fig. 8.10 SEM picture of EN-24 steel, decarburized at 900°C for 2 hrs. X 1000

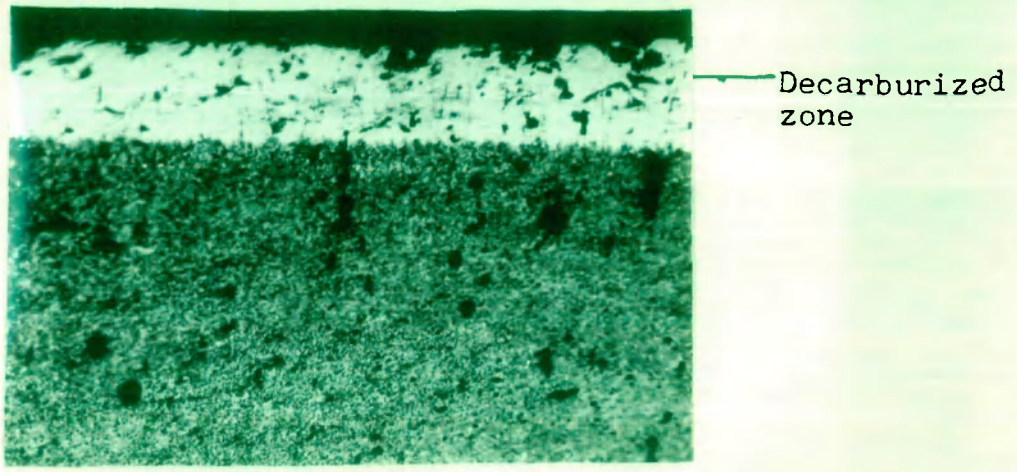

Fig. 8.11 Photomicrograph of a cross-section of EN-9 steel, decarburized at 900°C for 2 hrs. X 120

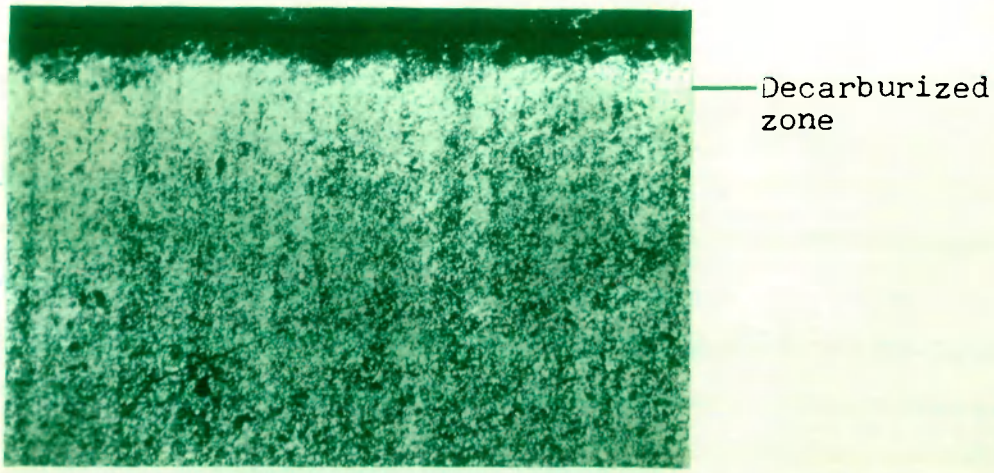

Fig.8.12 Photomicrograph of a cross-section of HSS (6-W), decarburized at 900°C for 2 hrs. X 120

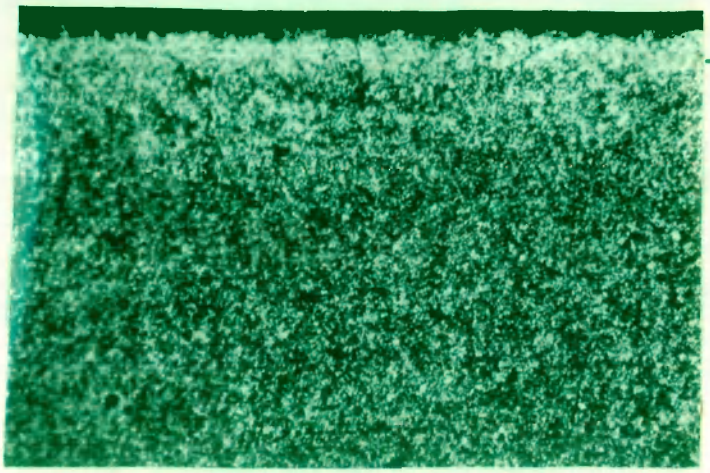

Fig. 8.13 Photomicrograph of a cross-section of HSS (18-W), decarburized at 900°C for 2 hrs. X 120

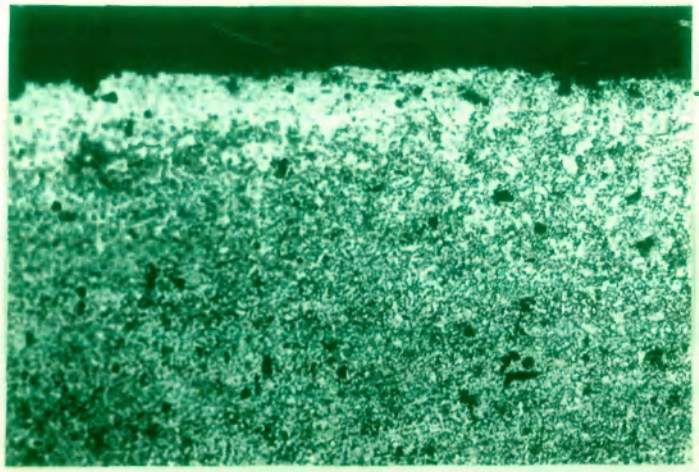

Fig. 8.14 Photomicrograph of a cross-section of EN-36 steel, decarburized at 900°C for 2 hrs. X 120

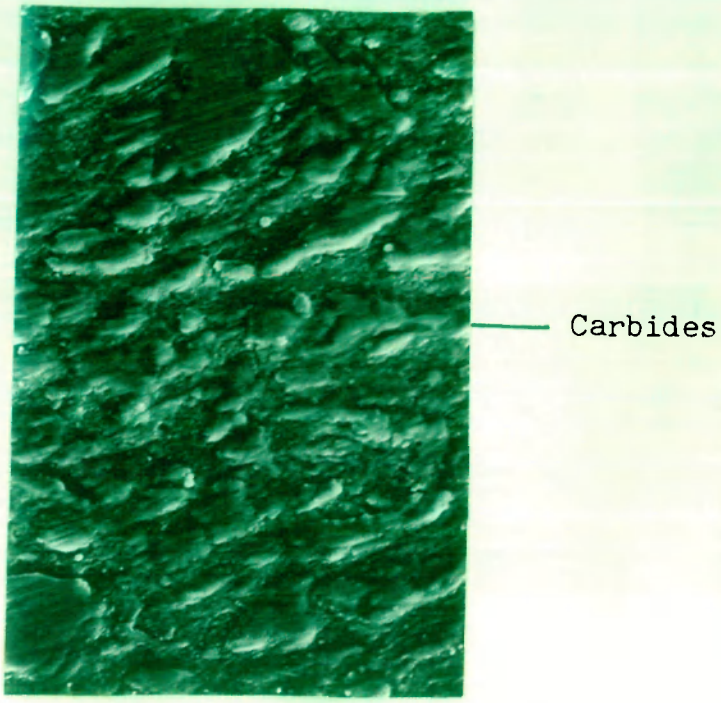

Fig. 8.15 SEM picture of EN-36 steel, decarburized at 900°C for 2 hrs. X 2000

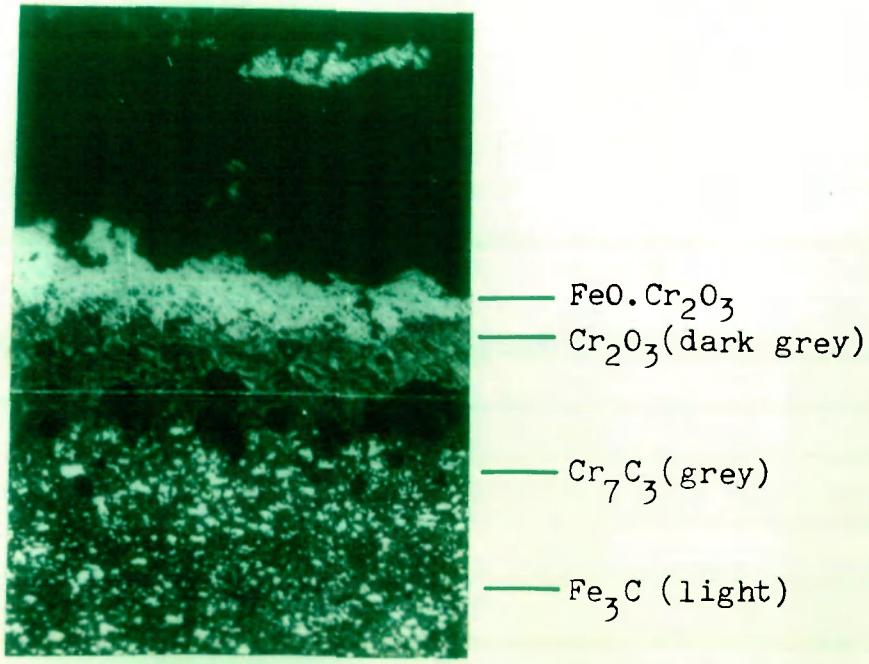

Fig. 8.16 Photomicrograph of a cross-section of die-steel, oxidized at 900°C for 6 hrs. X 60

of die-steel oxidized at 900°C for 6 hrs. The oxidized alloy contains 2-layered scales which are adhered and relatively uniform. The inner porous scales and outer scales contain Cr_2O_3 (dark grey) and $FeO.Cr_2O_3$ (light) respectively. Inclusions of FeO in the inner scales and that of Cr_2O_3 in the outer scales are also noted. The carbide dispersion remain unaffected during oxidation. Figure 8.17 shows a cross section of the silver steel oxidized in oxygen at 900°C. The alloy seems to oxidize at a rapid rate and extensive disruption of the scales occur due to decarburization. The fragmentation of the alloys is also observed. A ferritic zone containing dispersion of carbide particles is present at the alloy/scale interface. Like silver steel, EN-31 oxidizes at rapid rate and scales have similar morphologies although the substrate has a pearlitic structure (Fig. 8.18). Figure 8.19 shows a photomicrograph of oxidized EN-24. Relatively thick scales are appeared in the form of stratified layers, the inner layer contain $FeO.Cr_2O_3$ and the outer layers contain mainly iron oxides. Due to decarburization during oxidation the layers are separated providing extensive gaps in between the layers. The carbides have higher concentration at the scale/alloy interface than the middle portion of the oxidized specimen. EN-9 steel seems to oxidize by a considerably high oxidation rate and shows the inner scales are rich in chromium (Fig. 8.20). The oxidized (6W-5Mo) high speed steel forms multilayered porous scales (Fig. 8.21). The inner scales

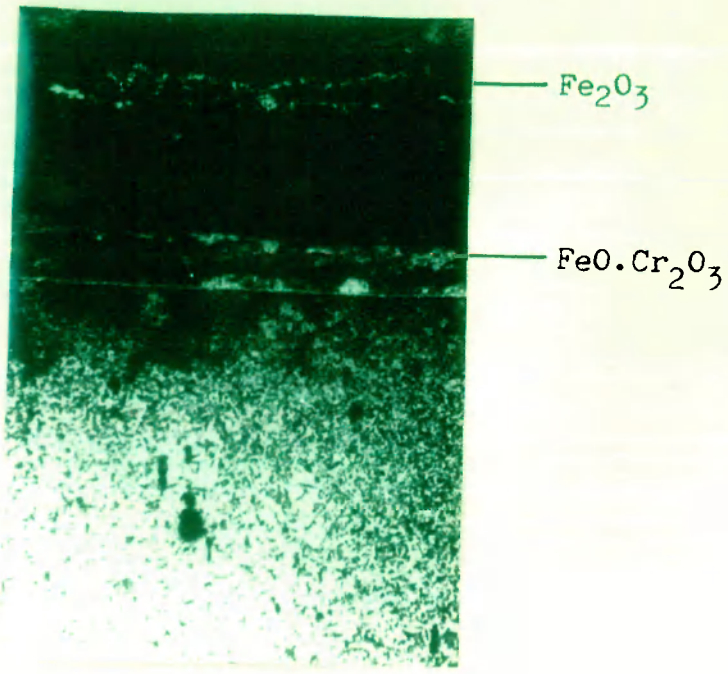

Fig. 8.17 Photomicrograph of a cross-section of silver steel, oxidized at 900°C for 8 hrs. X 60

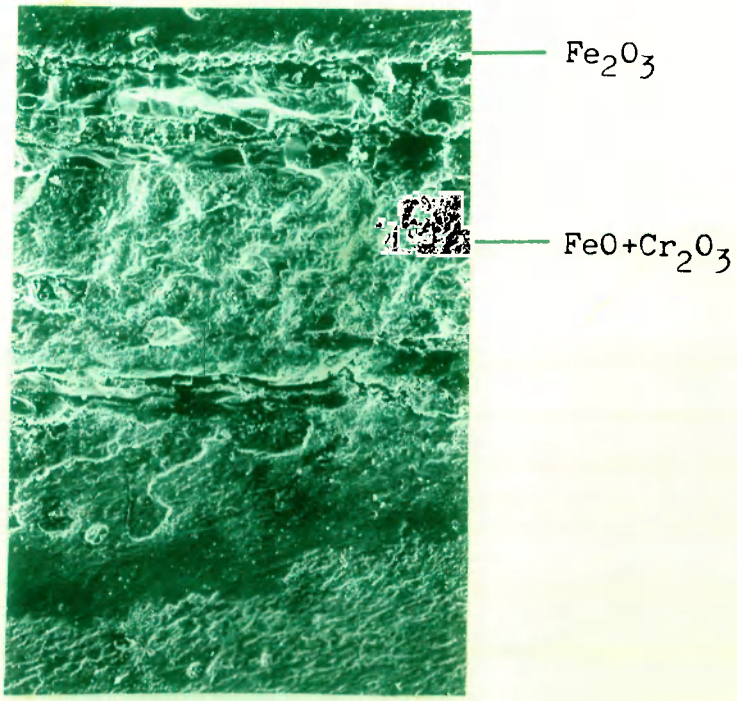

Fig. 8.18 SEM picture of EN-31 steel, oxidized at 900°C for 8 hrs.
X 200

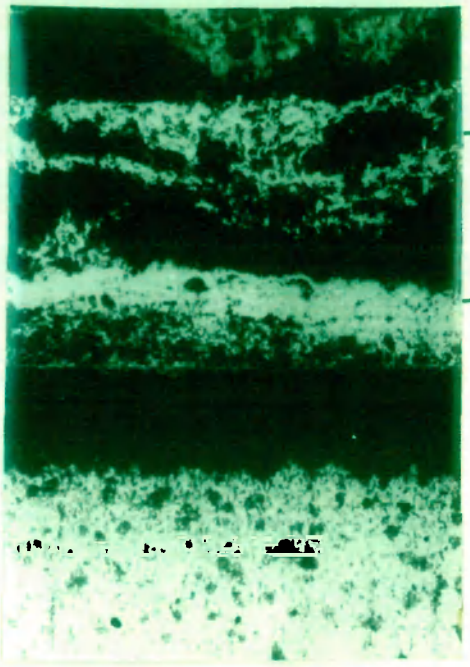

Fig. 8.21 Photomicrograph of a cross-section of HSS (6-W), oxidized at 900°C for 17 hrs. X 60

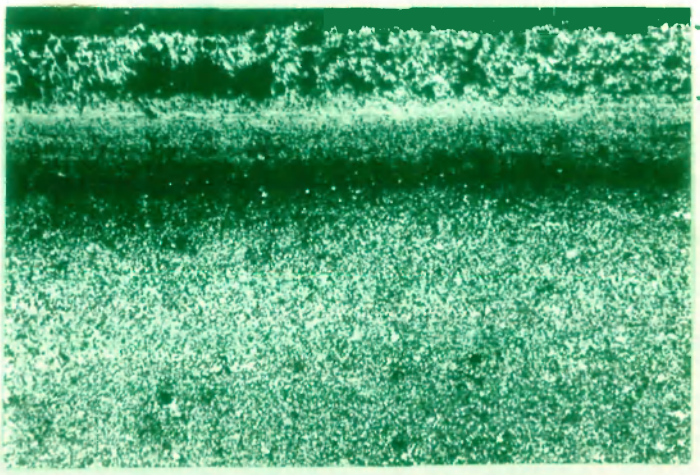

Fig. 8.22 Photomicrograph of a cross-section of HSS (18-W), oxidized at 900°C for 24 hrs. X 60

contains oxides of W, Mo, V and Cr followed by iron oxide layers containing inclusions of Cr_2O_3. The carbide density in the alloy matrix is considerably reduced on oxidation. The substrate has dispersion of spheroidal carbides in a ferritic matrix. The oxidized 18:4:1 (W, Cr, V) high speed steel shows interesting scale morphology (Fig. 8.22). The outer scales appear in the form of an uniform semi-porous oxide scale adhered to a relatively thick scale band of W_2O_3 in which Cr_2O_3 is also incorporated. This inner oxide band seems to act as barrier against oxidation. The outer scales contain FeO in which Cr_2O_3 is present as inclusions. The substrate show fine dispersion of carbides in a ferritic matrix. In EN-36 steel, decarburization during oxidation results in the fragmentation of the alloy scale moreover due to the separation of the scales the fresh alloy exposed to oxygen and oxidized at a faster rate, protrusion of alloy is observed. The matrix is ferritic with dispersion of carbides. The small voids in the substrate are perhaps inherent in the alloy during casting. The inner oxide scales are rich in Cr_2O_3 but are incorporated with Fe_3O_4/Fe, the outer most scales contain Fe_2O_3.

8.1.4.2 Predecarburized-Oxidized Alloys

Figure 8.23 shows a cross section of predecarburized oxidized die-steel. The predecarburized steel seems to oxidize at a much lower oxidation rates than the undecarburized alloy.

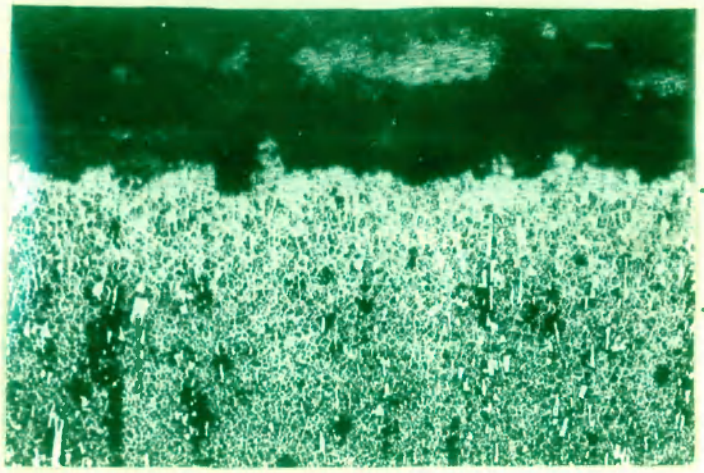

Fig. 8.23 Photomicrograph of across-section of predecarburized die steel, oxidized at 900°C for 9 hrs. X 120

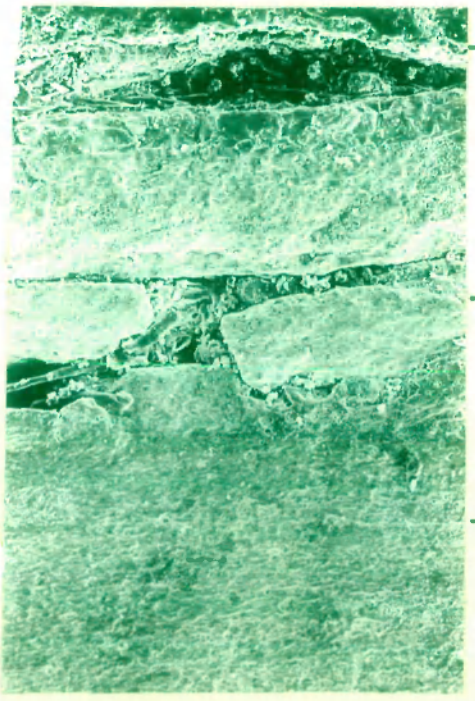

Fig. 8.24 SEM picture of predecarburized silver steel, oxidized at 900°C for 9 hrs. X 150

The scales of the predecarburized-oxidized steel are thinner and much more fragile and lost contact from the substrate during polishing. In the variety of alloy/scale interface, the substrate structure is ferritic and perhaps represent decarburized layer. This is followed by a zone which is pearlitic in nature. Both the zone contains dispersion of Cr_7C_3 and Fe_3C. Figure 8.24 represents scanning electron micrograph of a cross section of a decarburized oxidized silver steel. The substrate structure is largely pearlitic containing grey cementite in considerable portion. Due to decarburization the FeO-Cr_2O_3 porous scales are detached from the matrix, this gives rise to higher oxidation rates. EN-31 forms multilayered copious scales in which inner scales are richer in chromium and outer scales contain oxides of iron Fe_3O_4/Fe_2O_3. While comparing with undecarburized oxidized alloy, the concentration of pearlite is much lower and it has almost a ferritic structure.

During oxidation of predecarburized EN-24 alloy, the entire decarburized layer is consumed and the substrate has a ferritic matrix in which carbides are embeded. The scales are detached from the alloy as a result of decarburization during oxidation. Cr_2O_3 forms the main constitual of thick but porous inner scales, the outer layers of the external scales contain Fe_2O_3 in which NiO is incorporated (Fig. not shown). The scales on decarburized-oxidized EN-9 contain

inner layer of FeO and the outer layers contain Fe_2O_3 the middle layers which comprises the bulk of the scale contain Fe_3O_4. The alloy is oxidized profusely due to decarburization during oxidation. FeO scales formed initially are disrupted and fresh alloy is exposed to oxygen. The substrate structure is pearlitic, the decarburized layer of the decarburized alloy is totally consumed during oxidation. A uniform decarburized layer is present in the oxidized predecarburized 6W-5Mo high speed steel and this followed by a carbide dispersed ferritic matrix (Fig. 8.25). This goes to show that during oxidation, the decarburized layer present in the predecarburized alloy remains intact. Figure 8.26 shows a scanning electron photomicrograph of a cross section of the predecarburized-oxidized 18:0.75:1 (W,C,V) high speed steel. Multilayered scales in the form of band structure are formed. The inner scales shows crystals of WO_3 admixed with FeO and Cr_2O_3 this is followed by Cr_2O_3 scales the outer layers contain oxides of iron. The adhered scales are seemed to be responsible for relatively lower oxidation rates of the alloy. The matrix shows fine dispersion of carbides. The predecarburized-oxidized EN-36 forms relatively thick scales which are porous and separated from the alloy. The inner scales are richer in Cr_2O_3 and the outer scales contain Fe_2O_3 in which Cr_2O_3 is incorporated. The alloy matrix shows dispersion of carbides in a coarsened ferritic matrix. During oxidation, the decar-

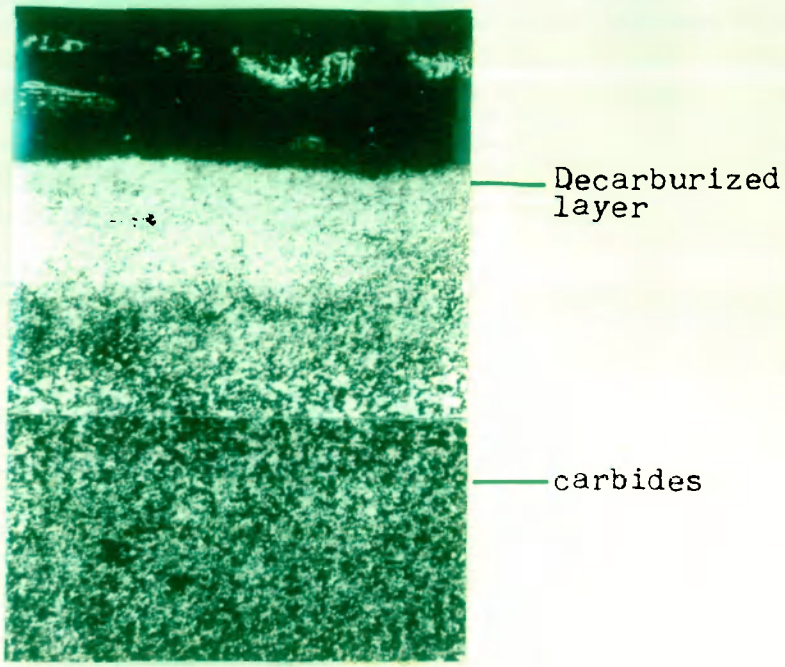

Fig. 8.25 Photomicrograph of a cross-section of predecarburized HSS (6-W), oxidized at 900°C for 9 hrs. X 120

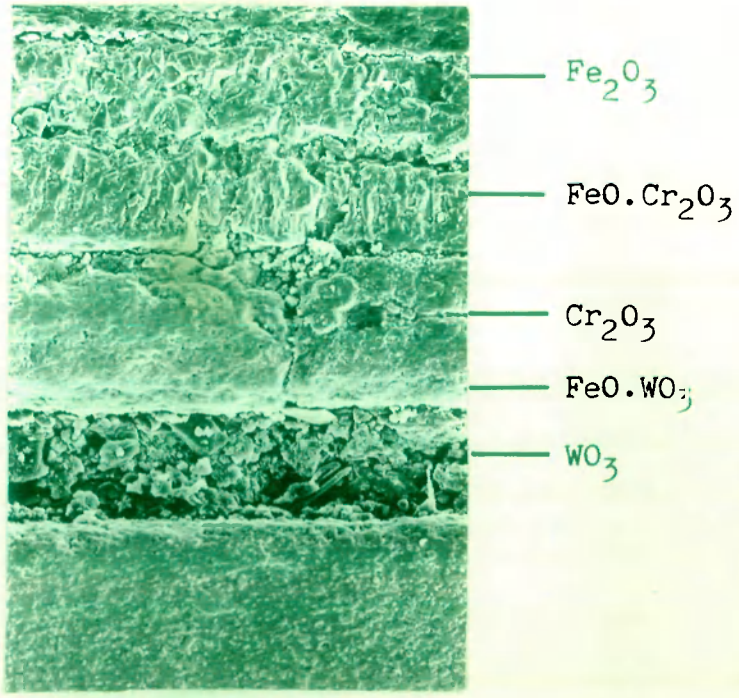

Fig. 8.26 SEM picture of predecarburized HSS (18-W), oxidized at 900°C for 9 hrs. X 400

burized layer of the decarburized alloy seems to be completely consumed.

8.2 Discussion

The oxidation of low alloy steels e.g. EN-9, EN-24, EN-31, EN-36 and silver steel, high speed tool steels (low and high tungsten) and cold die-steel in one atmospheric oxygen at 900°C proceeds by a diffusion controlled mechanism as indicated by the linear nature of weight gain^2 vs time plots. The increasing oxidation rate sequence for the different alloys is as follows :

EN-9 > EN-31 > Silver Steel > EN-24 > EN-36 > 6W-4Cr-5Mo-2V-0.8C high speed steel > cold die steel > 18W-4Cr-1V-0.75C high speed steel

18:4:1 high speed steel and cold die steel have the lowest oxidation rates and EN-9 and EN-31 have the highest oxidation rates. The alloy phase structure and the morphology of the oxide scales seem to influence the oxidation rates of the alloys. The alloy forming chromia scales and containing dispersion of carbides in the matrix have relatively lower oxidation rates. These alloys do not either undergo decarburization or to a very little extent. It has been established that the presence of carbide dispersions could restrict the mobility of carbon. Thus the high speed steels and die steel have nearly homogeneous and dense dispersion of transition metal

carbides which restricts the transport of carbon during oxidation, the Cr_2O_3 which forms the inner layer of the scale are not disrupted and largely remain adhered to the alloy surface. These two factors contribute mainly toward in declining the oxidation rates of the alloy steels. The plain carbon steel (EN-9) or low chromium steels (EN-24,-31 and-36) form copious oxide scales mainly containing oxides of iron. These alloys do not form protective chromia scales due to the presence of insufficient amount of chromium and are subjected to decarburization. The evolution of carboneous gases during oxidation results in the disruption,cracking and fragmentation of the oxide scales which eventually led to the separation of alloy and oxide scales. When the ruptured scales are separated the fresh alloy is again exposed to $O_2(g)$ and it oxidizes at a faster rate. The morphology of the oxide scales supports this view point.

Figure 8.27 shows a plot of parabolic rate constant, K_p vs (Cr+C) % for different alloys. With some exception the oxidation rate decreases with increasing (Cr+C) content, this indirectly indexed the influence of chromium carbides and other transition metal carbides on the oxidation rate of alloys. In general, plain carbon low alloy steels, high speed steels and die-steel decarburize in H_2-H_2O atmosphere at 900°C. Except high speed steels and die steel all the steels exhibit a well defined decarburized layer. The carbon losses noted during a 4 hr. decarburization run in H_2-H_2O atmosphere (Table 8.2)

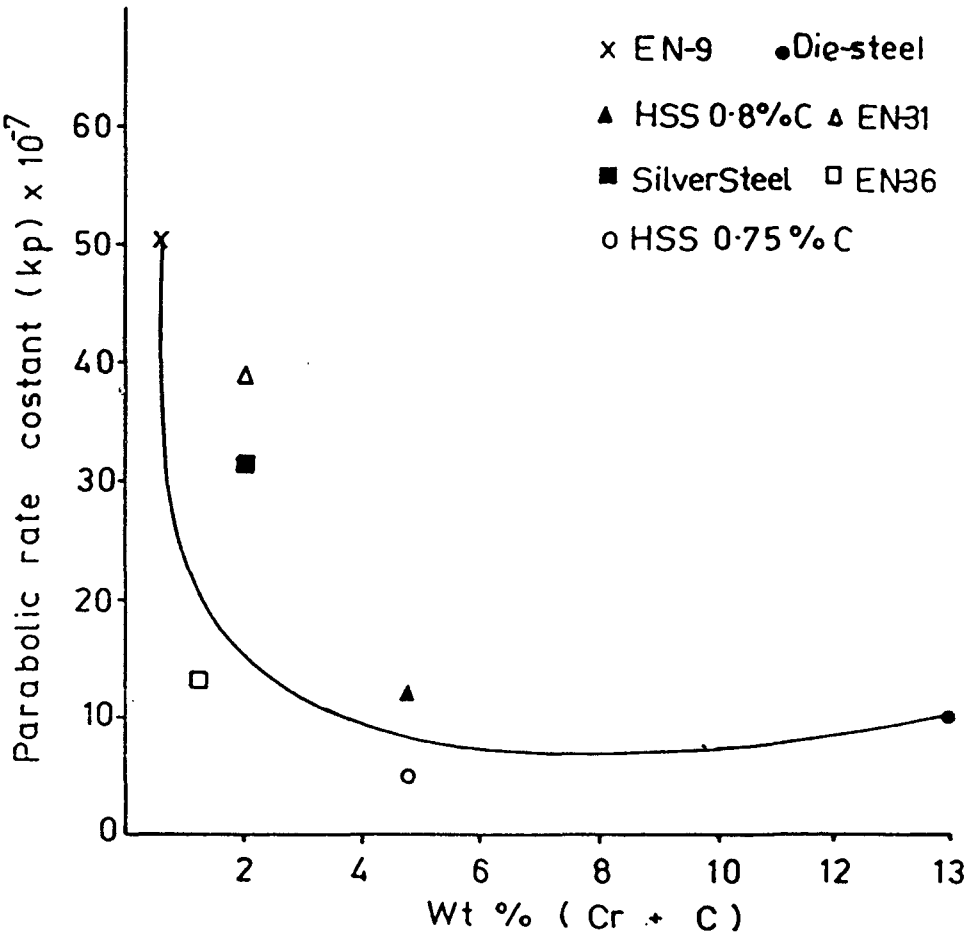

Fig. 8.27 Plot of parabolic rate constant, Kp VS (Cr+C) % for different industrial steels.

follow the sequence :

High speed steel (18 % W) < EN-31 < High speed steel (6 % W) < EN-24 < silver steel < EN-9 < EN-36 — die steel

Interestingly, although high speed steels show high carbon losses during decarburization, no well defined decarburized layer is found. During decarburization in H_2-H_2O atmospheres, the carbide dispersion net work remain uneffected but the free carbon present in solid solution or as graphite is removed as CH_4; alloys containing no or low carbide dispersion-containing matrix show well defined decarburized layer. The decarburized layer is usually ferrite containing dispersion of carbides. It means that absence of a decarburized layer is not necessarily related to the decarburization rate or carbon losses during decarburization.

Predecarburized steels follow a parabolic rate law during oxidation, however, in some cases breaks are observed in weight gain^2 vs time plots. The breaks in the oxidation kinetic curves are observed in case of EN-24, EN-36 and silver steels. The breaks in the oxidation curves can be explained on the basis of oxide scales morphology. Due to low Cr-contents and higher carbon contents, decarburization during oxidation occurs which results in the rupture of otherwise protective scales. The scales are not only separated from the alloy but also intra-separated into different layers as revealed by the

scale morphology. An interesting observation revealed during oxidation study was the presence of a well defined ferritic layer/band at the alloy/scale interface of predecarburized-oxidized high speed and die-steel which was otherwise absent from the corresponding decarburized steel. The presence of such a layer is perhaps the result of rapid diffusion of Cr and other alloying elements, which undergo oxidation and forming protective oxides. This would create a depletion in Cr concentration at the alloy/interface resulting in the formation of a ferritic zone. With some exceptions, the predecarburized alloys on oxidation follow the same oxidation sequence as that observed during the oxidation of undecarburized alloys. The oxidation rates of the decarburized alloys are slightly higher than the undecarburized alloys. This could be explained on the basis of the oxidation of decarburized layer which is ferritic in nature, the layer oxidizes at a much higher rate than carbide dispersed ferrite layer present in the undecarburized alloys. Such a behaviour has also been reported in decarburized carbide dispersed Fe-5 % M-C alloys (where M is a transition metal) which oxidize at a much higher rate than the corresponding undecarburized alloys. However, a reverse behaviour has been observed in case of carbide-dispersed iron base sintered alloys where decarburized alloys have lower oxidation rates. In sintered alloys (Chapter IV), decarburization behaviour contributes three factors responsible for lowering the

oxidation rates namely,

(i) the marked decrease in the porosity of the alloy ;

(ii) production of a homogeneous and refined matrix structure ; and

(iii) formation of a thin metal oxide film during decarburization which act as a barrier layer.

CHAPTER IX

CONCLUSIONS

The following conclusions could be drawn from the studies described in this thesis.

Chapter III [Decarburization and Oxidation of Fe-C Alloys]

(i) The decarburized steels show well defined ferritic decarburized layers, the thickness of the decarburized layer increases with increase in alloy's carbon content, exposure time and temperature.

(ii) The growth of oxides in oxidized plain Fe-C alloys or predecarburized-oxidized alloys is a diffusion controlled mechanism.

(iii) At 700°C, Fe-1.2C alloy has the highest oxidation rate and Fe-0.1C has the lowest oxidation rate. However at higher temperatures, the situation is reversed i.e. Fe-0.1C alloy has the highest oxidation rates.

(iv) At 900°C, the oxidation rate of the decarburized alloy decreases with increasing carbon content.

Chapter IV : [Decarburization and Oxidation of Fe-10MC alloys]

(i) At 900°C, the carbide-dispersed iron-base sintered alloys oxidize by a parabolic rate law and the oxidation rates for the different alloys follow the sequence

$$VC > NbC > Cr_7C_3 > TaC > MoC > TiC > WC > Fe_3C$$

(ii) The oxidation and decarburization rates of the carbide dispersed iron-base alloys are dependent largely upon the nature of the carbide. The alloys containing strong carbide formers (W,V,Mo etc.) have considerably low oxidation/decarburization rates.

(iii) The oxidation rates of the predecarburized carbide-dispersed iron-base alloys are much lower than the corresponding undecarburized alloys. This has been attributed to the presence of a protective oxide film and a more refined substrate structure of the decarburized alloys.

Chapter V : [Decarburization and Oxidation of Fe-10MC-0.1C-20Cr alloys]

(i) The alloys oxidized following a parabolic rate law indicating a diffusion controlled mechanism operating during oxidation.

(ii) The oxidation rates of Fe-10MC-0.1C-20Cr alloys are always lower, than the corresponding Fe-10MC alloys. The presence of a protective Cr_2O_3 layer seems to restricts the oxidation rates.

Chapter VI : [Decarburization and Oxidation Fe-10MC-0.1C-1.0RE_2O_3 alloys]

(i) The addition of rare earth oxides lowers the oxidation rates of Fe-10MC alloys either affecting the mobility of carbon or providing more adherent non porous oxide scales.

(ii) The oxidation rates of Fe-10MC-0.1C-1.0RE_2O_3 in undecarburized and decarburized states are much lower (about one order of magnitude) than the corresponding Fe-10MC alloys but slightly higher than the 20 % Cr-containing alloys.

Chapter VII : [Decarburization and Oxidation of Fe-10MC-0.1C-1.0MO_2 Alloys]

(i) At 900°C, all the alloys oxidized by a parabolic rate law and the oxidation rates of undecarburized Fe-10WC-0.1C-1.0ZrO_2/TiO_2 alloys are the lowest and the corresponding NbC-containing alloys are the highest.

(ii) Like RE_2O_3-containing sintered alloys, ZrO_2/TiO_2-containing alloys in undecarburized and decarburized states have oxidation rates much lower (1-2 order of magnitude) than the corresponding Fe-10MC alloys.

(iii) RE_2O_3-containing alloys have slightly lower oxidation rates than the corresponding TiO_2 or ZrO_2-containing

alloys. The former provide more adhered and compact scales and therefore, have better oxidation resistance.

Chapter VIII : [Decarburization and Oxidation of Industrial steels]

(i) Alloy phase structure and morphology of the oxide scales influence the oxidation rates of steels.

(ii) Alloys forming chromia scales and containing carbide dispersion have lower oxidation rates.

(iii) In general, with increase in Fe+C content there is a decrease in oxidation rate.

(iv) Steels containing free carbon or carbon in solid solution are much prone to decarburization than steels containing carbon in combined forms as carbide.

(v) Absence of a decarburized layer not necessarily indicates a low decarburization rate.

(vi) Decarburized alloys oxidize at a slightly higher rate than the undecarburized alloys due to the presence of a decarburized ferritic layer.

SUGGESTIONS FOR FUTURE WORK

The work presented in this thesis was mainly concerned with the decarburization and oxidation studies of carbide-dispersed iron-base sintered alloys in presence and absence of chromium or oxides of reactive elements like rare earth, Ti or Zr. The studies were first of its kind and could be the basis for the development of high temperature resistant materials derived from carbide strengthened iron-base alloys. The materials seem to have reasonable resistance against high temperature oxidation, good formability, ease of fabrication and of course, much less costlier than conventional high alloy steels, Ni or Co- base superalloys. These materials have the potentialities of applications in air craft and aerospace industries, nuclear power plants, chemical plants and energy conversion or generating units. However, more detailed studies and much more vigorous tests would be needed before these materials could be put into trial for aforementioned applications. Besides carbides and oxides, nitrides-dispersed base materials also need attention for high temperature applications.

Following are the suggestions for the future work which would be useful in case of further investigations :

(i) More detailed study of the systems already investigated fully. The studies should be focussed on the actual role of carbides during oxidation and decarburization. Applications

of techniques such as electron probe microanalysis and ESCA would be helpful in providing useful informations regarding the mechanism of oxidation.

(ii) The presence of various rare earth oxides in the alloys seems to be beneficial as far as oxidation of Fe-10MC alloys is concerned but no definite mechanism is found to explain their role satisfactorily. Therefore, further studies will be needed to investigate the role of rare earth oxides. Similarly, the beneficial role of active oxide addition such as TiO_2/ZrO_2 needs more investigation.

(iii) The alloys would be tested under simulated conditions prevailed in industrial units.

(iv) The alloys can be tested in S-containing or salt-containing environments to study the effects of sulfidation or hot corrosion.

(v) Besides, sintering technique which has been employed to fabricate the alloys used in studies described in this thesis, the carbide dispersion and/or active oxide dispersion could be achieved by diffusion casting. These alloys should also be tested in a similar ways as those adopted in case of sintered alloys.

REFERENCES

1. K. Hauffe, Oxidation of metals, Plenum Press, New York, P.I. (1965).

2. G.C. Wood and B. Chattopadhay, Corrosion Sci., 10, 471 (1970).

3. C.G. Giggins and F.S. Pettit, J. Electrochem. Soc., 118, 1782 (1971).

4. N. Pilling and R. Bedworth, J. Inst. Metals, 29, 534 (1923).

5. R.A. Rapp, Corrosion, 21, 382 (1965).

6. C. Wagner, Z. Elektrochem., 62, 722 (1959).

7. J.L. Meijering, Advances in Materials Research, 5, H. Herman, ed. (Academic Press, New York), P.I. (1971).

8. J.H. Swisher, Oxidation of Metals and Alloys, D.L. Douglass, ed., American Soc. for metals, Metals Park, Ohio, 235 (1971).

9. F. Moak, Z. Metall K., 52, 545 (1961).

10. W.W. Smeltzer and D.P. Whittle, J. Electrochem. Soc., 125, 116 (1978).

11. C. Wagner, Corrosion Sci., 5, 751 (1965)

12. J.P. Sauer, R.A. Rapp and J.P. Merte, Oxid. Met., 18, 285 (1982).

13. Y. Shida, F.H. Stott, B.W. Bastow, D.P. Whittle and G.C. Wood, Oxid. Met., 18, 93, 127 (1982).

14. J.R. Mackert Jr., R.D. Ringle, H.L. Byrd and C.W. Fairhurst, J. Dental Res., 62, 1229 (1983).

15. E.J. Felton and F.S. Pettit, Oxid. Metals, 10, 189 (1976).

16. K. Martin, M.S. Thesis, Mess. Inst. of Tech. (1983).

17. D.P. Whittle, Y. Shida, G.C. Wood, F.H. Stott and B.D. Bastow, Phil. Mag. A46, 931 (1982).

18. Y. Shida, G.C. Wood, F.H. Stoott, D.P. Whittle and B.D. Bastow, Corrosion Sci., 21, 581 (1981).

19. G. Bohm, M. Kahlweit, Acta. Met., 12, 641 (1964).

20. M. Hansen, Constitution of Binary Alloy, McGraw Hill Inc., New York (1958).

21. J. Paidassi, Nem. Sci. Rey. Metall., 54, 569 (1957).

22. A. Rahmel, Z. Elektrochem., 66, 363 (1962).

23. O. Kubaschewski, and B.E. Hopkins, Oxidation of metals and alloys, Butterworth, London (1967).

24. O. Kubaschewski and B.E. Hopkins, Oxidation of Metals and alloys (Academic Press, N.Y., 1962), p. 70.

25. A.J. Seybolt, J. Electrochem. Soc.,107, 147 (1960).

26. D. Mortimer and W.B.A. Sharp, Br. Corr. J., 3, 61 (1968).

27. M.R. Taylor, J.M. Calvert, D.G. Lees, and D.B. Meadowcroft, Oxid. Met. 14, 499 (1980).

28. P.A. Labun, J. Covington, K. Kuroda, G. Welsch, and T.E. Mitchell, Metall, Trans., 13A, 2103 (1982).

29. D. Coplan and M. Cohen, Trans. AIME, 160, 1057 (1952).

30. A.I. Kahveci and G.E. Welsch, Oxid. Met., 26, 213 (1986).

31. G.C. Wood and D.P. Whittle, Corros. Sci. 4, 263 (1964).

32. D.P. Whittle and G.C. Wood, J. Electrochem. Soc., 115, 126 (1968).

33. D.G. Bernes and J.M. Calvert, J.M. Phill. Mag., 28, 1603 (1973).

34. M. Skeldon, J.M. Calvert, and D.G. Lees, Oxid. Met., 28, 109 (1987).

35. K. Kurod, P.A. Labun, G. Welsch, T.E. Mitchell, Oxid. Met., 19, 117 (1983).

36. D.J. Gardiner, C.J. Littleton, K.M. Thomas, and K.N. Strafford, Oxid. Met., 27, 57 (1987).

37. S.H. Choi and J. Stringer, Mater. Sci., 87, 237 (1987).

38. L.B. Pfeil, U.K. Patent no. 459848 (1937).

39. L.B. Pfeil, U.K. Patent no. 574088 (1945).

40. J.M. Francis and W.H. Whitlow, Corros. Sci., 5, 701 (1965).

41. G.C. Wood and J. Boustead, Corros. Sci., 8, 719 (1968).

42. I.G. Wright and B.A. Wilcox, Oxid. Metals, 8, 283 (1974).

43. O.T. Goncel, D.P. Whittle and J. Stringer, Corros. Sci., 19, 305 (1979).

44. E.A. Gulbransen and K.F. Andrew, J. Electrochem. Soc., 106, 941 (1959).

45. E.J. Felten : ibid., 108, 490 (1961).

46. T. Nakayama and Y. Watanabe, J. Japan. Inst. Metals, 31, 385 (1967).

47. Y. Fukase, T. Nishima, K. Osozawa, and R. Nemoto, ibid, 32, 33 (1968).

48. Y. Fukase, K. Osozawa and R. Nemoto, ibid, 33, 40, 46(1969).

49. B.H. Kear, F.S. Pettit, D.F. Fornwalt and L.P. Lemaire, Oxid. Met., 3, 557 (1971).

50. F.H. Sttott and G.C. Wood, Corros. Sci., 11, 799 (1971).

51. I.A. Kvernes and P. Kofstad, J. Electrochem. Soc. 118, 1782 (1971).

52. I.A. Kvernes, Oxid. Met. 6, 45 (1973).

53. B. Lustman, Trans. AIME, 188,995 (1950).

54. S. Yajima, Y. Saito and T. Amano, DENKISEIKO, 45, 144 (1974).

55. J.K. Tien and F.S. Pettit, Met. Trans., 3, 1587 (1972).

56. J. Stringer, A.Z. Hed., G.R. Wallwork and B.A. Wilcox, Corros. Sci., 12, 625 (1972).

57. T. Amano, S. Yajima and Y. Saito, J. Japan Inst. Metals, 41, 1074 (1977).

58. J.M. Francis and W.H. Whitlow, J. Iron Steel Inst., 204, 355 (1966).

59. T. Moroishi, H. Fujikawa, and H. Makiura, J. Electrochem. Soc., 126, 2173 (1979).

60. R.G. Miner and V. Nagarajan, Oxid. Met., 16, 295 (1981).

61. J.S. Benjamin, Met. Trans., 1, 2943 (1970).

62. G.R. Wallwork and A.Z. Hed, Oxid. Met., 3, 229 (1971).

63. H.H. Davis, H.C. Graham, and I.A. Kvernes, Oxid. Met. 3, 431 (1971).

64. C.S. Giggins and F.S. Pettit, Met. Trans., 2, 1071 (1971).

65. A.U. Seybolt, Corros. Sci., 11, 751 (1971).

66. M.S. Seltzer, B.A. Wilcox and R.I. Jaffee, Met. Trans. 3, 2390 (1972).

67. J. Stringer and I.G. Wright, Oxid. Met., 5, 59 (1972).

68. I.G. Wright and B.A. Wilcox, Met. Trans., 5, 957 (1974).

69. H.T. Michels, Met. Trans. A, 7A, 379 (1976).

70. D.P. Whittle, M.E. El-Dahshan, and J. Stringer, Corros. Sci., 2, 879 (1972).

71. J. Stringer, B.A. Wilcox, and R.I. Jaffe, Oxid. Met., 5, 11 (1972).

72. R.E. Lawn, F.G. Wilson, and C.D. Desforges, J. Less Common Metals, 58, 107 (1978).

73. H. Nagai, T. Murai, and H. Mitani, J. Japan Inst. Metals, 42, 756 (1978).

74. H. Nagai, T. Murai, and H. Mitani, ibid, 42, 1138 (1978).

75. H. Nagai, H. Okabe, and E. Tsuji, ibid, 42, 509 (1978).

76. H. Nagai, T. Murai, H. Mitani, Trans. Japan Inst. Metals, 20, 299 (1979).

77. H. Nagai, T. Murai, and H. Mitani, ibid, 20, 442 (1979).

78. H. Nagai, T. Murai, and H. Mitani, ibid, 21, 563 (1980).

79. H. Nagai, Y. Takebayashi, and H. Mitani, Met. Trans. A, 12A, 435 (1979).

80 H. Nagai, T. Sawayana, S. Tetsuya and K. Shoji, Funtai Oyobi Funmatsu Yakin, 5, 34 (1987).

81. D.P. Whittle and J. Stringer, Phil, Trans. Roy. Soc. Lond. A, 295, 309 (1980).

82. A.U. Malik, Oxid. Met., 25, 233 (1985).

83. A.U. Malik and D.P. Whittle, Oxid. Met., 16, 339 (1981).

84. M. Hajuga and J. Kucera, Oxid. Met., 29, 121 (1988).

85. W.E. Boggs, J. Electrochem. Soc., 118, 906 (1971).

86. P. Pepin and L. Tertian, Metaux-Corrosion-Ind., 36, 140 (1961).

87. E. Scheill and K. Kiwit, Arch. Eisenhuttenwes, 9, 405 (1936).

88. A.U. Malik, and D.P. Whittle, Effect of Addition of alloying elements on the high Temperature Oxidation (to be published).

89. C. Upthegrove, and D.W. Murphy, Trans. Am. Soc. Steel Treat., 21, 73 (1933).

90. A. Portevin, E. Pretet and H. Tolivet, Rev. Met., 31, 101, 186, 219 (1934).

91. C.R. Austin, Trans. Am. Soc. Metals, 22, 31 (1934).

92. C.A. Siebert, ibid, 27, 752 (1939).

93. D.J. Mc.Adam and G.W. Geil, J. Research. Mat. Bur. Standards, 23, 63 (1939).

94. H.J. Engell, F.K. Peters, Arch. Eisenhuttenwes, 28, 567 (1957).

95. K. Bohnenkamp and H.J. Engell, ibid, 33, 359 (1962).

96. J.G. Billings, M.S. Thesis : Oxidation and Decarburization kinetics of iron-carbon alloys in carbon dioxide, carbon monoxide, W.W. Smeltzer, Supervisor, McMaster University, Hamiltin, Ontario (1966).

97. W.W. Webb, J.T. Norton and C.J. Wagner, Electrochem. Soc., 103, 539 (1965).

98. K. Langer and H. Trenkler, Berg-und Huttenmann Manatshefte, 110, 291 (1965).

99. A.U. Malik, Influence of Carbon on the High Temperature oxidation of Iron-Base Alloys, Ph.D. Thesis, The University of Liverpool (1975).

100. C.R. Austin, Trans. Amer. Soc. Metals, 22, 31 (1934).

101. M. Hansen and K. Anderko, Constitution of Binary Alloys 2nd ed., McGraw Hill Book Co., New York, 1958.

102. L.S. Darken, Trans. TMS-AIME, 150, 157 (1942).

103. R.P. Smith, Trans. TMS-AIME, 224, 105 (1962).

104. C. Wagner, Kinetics in Metallurgy, M.I.T., (1955).

105. C. Wagner, J. Metals, 4, 91 (1952).

106. Mechanism of Decarburization : N. Birks in 'Decarburization' I.S.I., Publication 133 (1970), pp. 1 to 13.

107. H.J. Grabke, Arch. Eisenhuttenwes, 46, 225 (1975).

108. D.N. Ghosh, Iron and Steel Making (Quarterly), No. 1, p. 36, 45 (1975).

109. P. Grieveson, Scand. J. Metallurgy, 2, 265 (1973).

110. V.H. Swisher, T.M.S. AIME, 24, 763 (1968).

111. M. Hajduga, and J. Kucera, Oxid. Met., 29, 419 (1988).

112. A. Leutgob and H. Trenkler, Arch. Eisenhuttenwes, 46, 215 (1975).

113. H.J. Grabke, K. Ohla, J. Peters and I. Wolfe, Werkstoffe und Korrosion, 34, 495 (1983).

114. M.A. Krishtal and Yu. I. Davydov, Influence of Cr and W on the diffusion and thermodynamic activity of C in Fe alloys, Cheranaya Met., 9, 133 (1965).

LIST OF PUBLICATIONS

1. A.U. Malik, Shahreer Ahmad and Sultan Ahmad,
   High Temperature Decarburization and Oxidation
   of Carbide-dispersed Iron-Base Alloys,
   Science of Sintering, 1988 (In press).

2. A.U. Malik, Shahreer Ahmad and Sultan Ahmad,
   Decarburization and Oxidation Behaviour of Fe-C Alloys,
   National Seminar on Advances in Metal Science,
   23-24 Sept., 1988, Calcutta (India).

3. A.U. Malik, Shahreer Ahmad and Sultan Ahmad,
   High Temperature Oxidation and Decarburization of low
   Alloy Steels,
   J. of Materials Science, 1988 (Communicated).

4. A.U. Malik and Shahreer Ahmad
   High Temperature Oxidation and Decarburization Behaviour
   of Carbide-dispersed, 20 % Chromium Containing Alloys,
   Steel Research, 1989 (Communicated).

5. A.U. Malik and Shahreer Ahmad,
   Effect of La_2O_3, Y_2O_3, Pr_2O_3, ZrO_2 and TiO_2 oxides
   on Decarburization and Oxidation Behaviour of Carbide-
   dispersed Iron-base Alloys (under preparation).